

University of Nottingham
UK | CHINA | MALAYSIA

Development of High-Throughput Electron Tomography for 3D Morphological Characterisation of Soot Nanoparticles

Ephraim Haffner-Staton, MSci

Submitted to The University of Nottingham for the Degree of Doctor of Philosophy, 2019

Table of Contents

Abstract vi

Acknowledgements viii

List of Publications ix

Journal Publications ix

Conference Publications ix

Equations x

Abbreviations xi

1 - Introduction 13

1.1 - Overview 13

1.2 - Background 14

1.2.1 – Soot Nomenclature 15

1.2.2 – Estimates of Soot Production 15

1.2.3 – Health and Environment 16

1.2.4 – Soot from Automotive Engines 17

1.2.5 – Context of this work 18

1.3 – Aims and Objectives 20

1.4 – Thesis Layout 21

1.5 – Contribution to Knowledge 23

2 – Literature Review 24

2.1 – Soot Formation 24

2.1.1 – Soot Formation in Internal Combustion Engines 24

2.1.2 - Chemical Pathways and Mechanisms to Soot Formation 26

2.2 – Soot Structure and Morphology 27

2.2.1 – Primary Particles and Nanostructure 28

2.2.2 – Nanoparticle Aggregate Structure 29

2.3 – Impacts of Soot 30

2.3.1 – Outside the Engine: Exhaust Soot 30

2.3.2 – Within the Engine: Soot-in-Oil 32
2.4 – Characterisation of Soot Morphology 34
2.4.1 – Low Dimensional Characterisation 34
2.4.2 – TEM Characterisation 35
2.4.3 – Electron Tomography 36
2.5 – Summary 38
3 – Experimental Methods and Facilities 40
3.1 – Transmission Electron Microscopy 40
3.1.1 – Basics of Electron Microscopy 40
3.1.2 - The specimen stage: TEM grids 41
3.1.3 – TEM at the Nanoscale and Microscale Research Centre (nmRC) 42
3.1.4 – Operation of the JEOL 2100F Transmission Electron Microscope 43
3.2 - Computational Setup for ET and Image Processing 47
3.3 - Electron Tomography 47
3.3.1 – The Projection Requirement 48
3.3.2 - Tilt-Series Acquisition (with SerialEM) 49
3.3.3 - Tilt-Series Alignment in Etomo 54
3.3.4 - Tomographic Reconstruction: the Computational Step 56
3.3.5 - Tomogram Segmentation: Producing the 3D model 60
3.3.6 - Errors of ET: Missing Wedge Elongation 64
3.4 – Soot Samples and Preparation for TEM 66
3.4.1 – FG Soot 66
3.4.2 – GTDI Soot-in-Oil 66
3.4.3 – Thermo-gravimetric Analysis (TGA) 69
3.5 - Morphological Characterisation of Soot 70
3.5.1 – 2D-TEM Morphological Characterisation 70
3.5.2 – 3D-TEM Morphological Characterisation 73
3.6 - Summary 74
4 - 2D- and 3D-TEM Morphology Characterisation of Flame-Generated Soot 75

4.1 - Introduction 76
4.2 - The FG Soot Sample 76
4.2.1 - 2D-TEM Morphology Characterisation of the FG Soot Tilt-Series 78
4.2.2 - Electron Tomography for FG soot 82
4.3 - Results & Discussion: 2D vs 3D Comparison 87
4.3.1 - Adjacent Structures in the Tilt-Series and Tomogram 87
4.3.2 – Morphological Analysis 89
4.4 – Conclusion 98
5 - Optimisation of Electron Tomography for Soot 100
5.1 - Introduction 101
5.2 - TEM Study of GTDI Soot-in-Oil 102
5.3 - Tomographic Reconstruction: WBP vs. SIRT 109
5.3.1 - SIRT: Choice of Iterations 109
5.3.2 - Reconstruction Details 110
5.3.3 - Qualitative Analysis: FG-WBP vs. FG-SIRT 111
5.3.4 - Quantitative Analysis: FG-WBP vs. FG-SIRT 115
5.4 - Tilt-Series Optimisation: Range vs. Increment 117
5.4.1 - Tilt-Series Optimisation: Qualitative Analysis 118
5.4.2 - Tilt-Series Optimisation: Quantitative Analysis 125
5.5 - Tomogram Segmentation: Effect of Interpolation 126
5.5.1 – Effect of Interpolation: Results 130
5.6 - Conclusions 137
6 - Development of Semi-Automated TEM Imaging for High-Throughput ET 139
6.1 – Introduction 139
6.2 – Automated Electron Microscopy in the Literature 141
6.3 – A Semi-Automated Procedure for Image Acquisition of Soot in TEM 144
6.3.1 - Low-Magnification Imaging and Grid Registration with SerialEM 145
6.3.2 - Medium-Magnification Montaging in SerialEM 147
6.3.3 - Image Processing of the Montage Map 151

6.3.4 - Rapid 2D-TEM Characterisation 160
6.3.5 - Communication with SerialEM for Automated Operation 164
6.4 – 2D-TEM Characterisation of GTDI Soot-in-Oil 166
6.4.1 – Application of the Automated TEM Procedure to GTDI Soot-in-Oil 166
6.4.2 – Morphological Measurements 169
6.4.3 – Primary Particle Diameter 170
6.4.4 – Aggregate Morphology 171
6.5 – Conclusions 174
7 - Assessing the Accuracy of Electron Tomography for Soot 176
7.1 - Introduction 177
7.2 – Soot-like Aggregate Models: Ground Truth 179
7.2.1 – Methodology for Accuracy Analysis 184
7.3 – Accuracy Assessment of ET: Results 186
7.3.1 - Missing Wedge Z-elongation 186
7.3.2 - Comparison of the ±80° and ±60_3° methods 188
7.3.3 - ±60_3° Reconstruction: Full Morphological Analysis 189
7.3.4 - Effect of Interpolation on Segmentation 191
7.4 - Conclusions 193
8 – 2D and 3D Morphological Characterisation of GTDI Soot-in-Oil 194
8.1 – Introduction 195
8.2 – Morphological Characterisation in 2D and 3D 197
8.2.1 – 3D Morphology Measurements 198
8.2.2 – 2D Morphology Measurements 198
8.3 – 3D Morphology of GTDI Soot-in-Oil 199
8.4 – Comparison of 2D- and 3D-derived Morphology 204
8.4.1 - Volume 204
8.4.2 - Surface Area 206
8.4.3 - Radius of Gyration 207
8.4.4 - Circularity 208

8.4.5 - Fractal Dimension....209
8.4.6 – Aspect Ratio....211
8.4.7 – Summary: 2D- vs 3D-derived Morphology....213
8.5 – Unique Outputs of 3D Reconstruction....213
8.5.1 – Variation due to Nanoparticle Orientation....214
8.5.2 – Unquantifiable Morphological Observations....216
8.6 – Conclusions....221
9 – Conclusions....223
9.1 – Future Work....230
10 - References....232
Appendix....241
A1 - Propagation of Missing Wedge Error: Fast Fourier Transforms of 2D shapes....241
A1.1 - Example-1: Circle....242
A1.2 - Example-2: Ellipses at different angles....244
A1.3 - Example 3: Nanoparticle Shape....246
A.1.4 - Summary....249
A.1.5 - References....250
A.2 - Choice of Resampling Factor in BoneJ Surface Area Calculations....251
A.2.1 - Introduction....251
A.2.2 – Results: Surface Area of Spheres as a Function of Resampling Factor....252
A.2.3 - References....253

Abstract

In this work a methodology has been developed to permit high-throughput, high-quality morphology characterisation of soot nanoparticles in 3D, using transmission electron microscopy (TEM) and electron tomography (ET). Nanoparticle morphology plays an extremely important role in determining soots contribution to global climate change, its impacts on human health, and its relation to friction and wear in engines. Morphology characterisation is thus fundamental to enabling full understanding of soot-induced phenomena and subsequent strategies for their mitigation.

Initial work employed ET for the 3D reconstruction and morphology characterisation of a flame-generated soot nanoparticle. Variability in 2D-derived measurements as a function of nanoparticle orientation was measured at up to 45%, which may be an important source of error in 2D-derived morphology measurements. Significant discrepancies of up to 36% between 2D- and 3D-derived measurements were also observed. This type of particle was particularly complex and 3-dimensional, and acted as a useful case-study for the identification of areas for possible optimisation in the 3D reconstruction process.

A sample of soot-in-oil from a gasoline turbocharged direct injection (GTDI) engine was chosen as the main focus of study in this work. This is due to both the novelty of study and potential for useful research outputs, and the difficulty of study *via* TEM due to the presence of lubricant oil. General characteristics of particulate matter in the GTDI soot-in-oil sample were understood through TEM imaging, and revealed an abundance of localised amorphous carbon structures and patches of crystalline material, in addition to typical soot nanoparticles.

Optimisation of ET was carried out by assessment of the speed and relative accuracy of a number of well-established procedures for tilt-series acquisition, tomographic reconstruction, and tomogram segmentation. It was found that the computationally efficient WBP algorithm produced data of equivalent quality to that of the theoretically more accurate SIRT algorithm, though was significantly quicker. Optimal tilt-series were acquired over ±60° ranges, in increments as large as 3°. For the final stage of optimisation, 6 nanoparticles from the GTDI soot-in-oil sample were reconstructed in 3D *via* ET. Linear interpolation was found to be useful for increasing speed while retaining accuracy in volume segmentation for producing the final nanoparticle models.

Efforts were also made to reduce the amount of time and human involvement required for nanoparticle identification and image acquisition, resulting in the development of semi-automated process for TEM imaging. Large areas of the TEM grid are automatically imaged, and then screened for structures of interest *via* an automated image processing algorithm and

a manual review process. Nanoparticles locations are then communicated to the electron microscope for subsequent 3D study. Using this semi-automated process over 4000 μm^2 of a TEM grid was imaged, resulting in identification of 271 soot nanoparticles. Additional steps were implemented for high-throughput 2D morphology characterisation, and resulted in the measurement of 523 individual nanoparticles from the GTDI soot-in-oil sample. Analysis of this data revealed similar size of soot primary particles and aggregates compared with previous studies of soot-in-oil samples, but modest aggregate sizes in comparison to exhaust and flame-generated soots.

Accuracy of ET was assessed *via* computational models of soot-like aggregates which acted as 'ground truth' (*i.e.* 3D morphology was known exactly). The soot-like models were subjected to the 3D-TEM procedure, and post-reconstruction morphology was compared to that of the original models. The results of our prior optimisation work were confirmed, and absolute accuracy of 3D-TEM for the soot-like models was shown to be extremely high (within 3.5% of original values for a range of parameters).

From the pool of 271 nanoparticles identified using the automated TEM imaging procedure, an additional 28 nanoparticles were chosen for study in 3D *via* ET. These nanoparticles were chosen to express the general extremes of visible structures, *e.g.* particularly large and complex, or small and simple nanoparticles. This total sample size of 34 nanoparticles represents the largest 3D study of soot-in-oil to date, and one of the largest 3D studies of any soot sample to date. The 3D aspect ratio of nanoparticles revealed a general tendency towards 2-dimensionality rather than strong 3-dimensionality, and overall size of nanoparticles was generally small in comparison to aerosol soot. Direct comparison of 2D- and 3D-TEM characterisation showed deviations on the order of 20-35% for some important morphological parameters (volume, surface area, circularity, aspect-ratio), though 2D-derived radius of gyrations measurements were generally accurate. Strong variability was observed across the sample of nanoparticles, and no clear correlations were drawn between particle morphology and the accuracy of 2D-derived measurements. The 3D models were used to explored the full extent of variability in the 2D appearance due to nanoparticle orientation, with an average variability in 2D area of 59%. Several nanoparticles were observed with prominent features such as rings, cavities, and arches that were not appreciable *via* typical 2D-TEM study, and may be important for greater understand of soot formation and impacts of morphology.

Acknowledgements

Firstly, I would like to thank my supervisor Dr Antonino La Rocca for his support and guidance over the last 4 years, which made a potentially difficult transition in disciplines practically seamless. In particular I am extremely grateful for the opportunities and experiences that have been afforded me during this project, which I understand are by no means typical for a PhD student.

I am also grateful for the presence of both my co-supervisors, Dr Michael Fay and Dr Chris Parmenter. In particular, I would like express my gratitude to Mike for the countless hours spent understanding the nanoscopic nature of soot through electron microscopy.

During the last 4 years I have shared the engines group office with no less than 28 different colleagues. I would like to thank them all for their contributions to a harmonious working environment. In particular I would like to thank my fellow soot researcher Sebastian for his frequent help and cooperation.

I would like to pay special thanks to my friend Ben Randall, whose own PhD studies were carried out almost simultaneously with mine. Your help, both academically and otherwise, was invaluable during the last 4 years.

To my Parents, my Brother, Hannah, and baby Ciara, thank-you for your presence, love, and support over the years.

And finally to my partner Nicole, I could not have done this without you by my side. Thank-you so much for your support, encouragement, and inspiration during this project and the years before.

List of Publications

The following publications resulted, at least in part, from work carried out during the duration of the PhD project. Those noted with '*' involved a minor contribution from myself, for all others I was the primary contributor.

Journal Publications

Orhan O., Haffner-Staton E., La Rocca A., Fay M. *Characterisation of flame-generated soot and soot-in-oil using electron tomography volume reconstructions and comparison with traditional 2D-TEM measurements*. Tribol Int. **2016**;104:272-84.

Haffner-Staton E., La Rocca A., Fay M.W. *Progress towards a methodology for high throughput 3D reconstruction of soot nanoparticles via electron tomography*. Journal of microscopy. **2018**;270(3):272-89.

* Pfau S., La Rocca A., Haffner-Staton E., Rance G., Fay M.W., Brough R., Malizia S. *Comparative nanostructure analysis of gasoline turbocharged direct injection and diesel soot-in-oil with carbon black*. Carbon. **2018**;139:342-52.

Conference Publications

Haffner-Staton E., La Rocca A., Cairns A., Mcghee M., Fay M. *Assessing the Accuracy of Soot Nanoparticle Morphology Measurements Using Three-Dimensional Electron Tomography*. SAE Technical Paper; **2019**. Report No.: 0148-7191.

Haffner-Staton E., La Rocca A., Cairns A., Fay M. *Morphological characterisation of gasoline soot-in-oil: development of semi-automated 2D-TEM and comparison with novel high-throughput 3D-TEM*. SAE Technical Paper; **2019**. Report No.: 0148-7191.

* Pfau S.A., La Rocca A., Haffner-Staton E., Rance G.A., Fay M.W., Mcghee M. *Soot in the Lubricating Oil: An Overlooked Concern for the Gasoline Direct Injection Engine?* : SAE Technical Paper; **2019**. Report No.: 0148-7191.

Equations

$$d = \frac{0.612\lambda}{NA} \tag{3.1}$$

$$N_p = k_a \left(\frac{A_p}{A_{pp}}\right)^{\alpha} \tag{3.2}$$

$$V = \frac{\pi {d_p}^3}{6} N_p \tag{3.3}$$

$$SA_1 \approx N_p \pi {d_p}^2 \tag{3.4}$$

$$C_{ov,P} = \frac{d_p - d_{ij}}{d_p} \tag{3.5}$$

$$C_{ov} = \zeta_1 . C_{ov,P} - \zeta_2 \tag{3.6}$$

$$SA_2 = SA. \left[1 - \phi . C_{ov} . \left(1 - {}^{1}/_{N_p}\right)\right] \tag{3.7}$$

$$R_g = \sqrt{\frac{\sum_{i=1}^{n_{px}} {r_i}^2}{n_{px}}} \tag{3.8}$$

$$Circ. = 4\pi \left({}^{Area}/_{Perimeter^2}\right) \tag{3.9}$$

$$3Dcirc. = 6\sqrt{\pi} \left({}^{V}/_{SA^{1.5}}\right) \tag{3.10}$$

$$x_{norm} = {}^{(x - min.)}/_{(max. - min.)} \tag{4.1}$$

$$\theta = tan^{-1} \left({}^{|\Delta y|}/_{|\Delta x|}\right) \tag{6.1}$$

$$N_p = k_f \left({}^{D_g}/_{d_{pp}}\right)^{D_f} \tag{6.2}$$

$$e_{xz} = \sqrt{\frac{\alpha + \sin(\alpha)\cos(\alpha)}{\alpha - \sin(\alpha)\cos(\alpha)}} \tag{7.1}$$

Abbreviations

ADF	Annular Dark Field
ART	Algebraic Reconstruction Technique
Au-NP(s)	Gold Nanoparticle(s)
BC	Black Carbon
BF	Bright Field
BF-TEM	Bright Field Transmission Electron Microscopy
CB	Carbon Black
CT	Computerized Tomography (*e.g.* X-ray Micro-CT)
DART	Discrete Algebraic Reconstruction Technique
DF-TEM	Dark Field Transmission Electron Microscopy
DI	Direct Injection
DISI	Direct Injection Spark Ignition
DLS	Dynamic Light Scattering
DPF	Diesel Particulate Filter
EC	Elemental Carbon
EDX	Energy Dispersive X-ray spectroscopy
EGR	Exhaust Gas Recirculation
ET	Electron Tomography
FE	Field Emission
FEG	Field Emission Gun
FFO	Fully Formulated Oil
FFT	Fast Fourier Transform
FG (soot)	Flame Generated
FOV	Field of View
FT	Fourier Transform
GDI	Gasoline Direct Inject
GPF	Gasoline Particulate Filter
GT	Ground Truth
GTDI	Gasoline Turbocharged Direct Injection
HAADF	High-Angle Annular Dark Field
HC	Hydrocarbon(s)
HR-TEM	High-Resolution Transmission Electron Microscopy

ICE	Internal Combustion Engine
NEDC	New European Driving Cycle
NTA	Nanoparticle Tracking Analysis
OC	Organic Carbon
PAH	Polycyclic Aromatic Hydrocarbons
PF	Particulate Filter
PFI	Port-fuel Injection
PM	Particulate Matter
PSF	Point Spread Function
ROI	Region of Interest
SEM	Scanning Electron Microscopy
SIRT	Simultaneous Iterative Reconstruction Technique
SNR	Signal to Noise Ratio
STEM	Scanning Transmission Electron Microscopy
TGA	Thermo-gravimetric Analysis(/Analyser)
TEM	Transmission Electron Microscopy
WBP	Weighted Back-projection
WHO	World Health Organization

1 - Introduction

1.1 - Overview

The work presented in this thesis was performed in order to develop a novel soot morphology characterisation tool. The developed methodology, which may at several points be referred to as '*3D-TEM',* utilises transmission electron microscopy (TEM) and electron tomography (ET) to facilitate full 3-dimensional appreciation of the complex, fractal-like structure of soot nanoparticles. This endeavour reflects doubts over the accuracy of traditional morphology characterisation *via* TEM, which arise primarily due to the lack of depth perception in 2D projections. Accurate characterisation of morphology is important because of the defining role it plays in the behaviour of soot in a variety of environments. This includes significant contributions to the greenhouse effect and snow-ice melting, death and disease in humans and animals, alteration to ecological systems and marine habitats, and increased wear and reduced efficiency in automotive engines. Soot morphology is also strongly dependent on the conditions of the combustion environment in which the soot is formed. As such, the characterisation of soot nanoparticle morphology is an extremely important means by which to enhance understanding of soot formation and the intricacies of its behaviour and interactions in different physical and chemical environments.

The aim of this work was to adapt established techniques for electron tomography to the unique challenge of soot nanoparticles. Though in no way limited to this type of sample, this work has a particular focus on 'soot-in-oil' (soot entrained within engine lubrication oils) from gasoline direct injection (GDI) engine. There were two main reasons for this choice. Firstly, GDI exhaust soot and particularly soot-in-oil is relatively under-studied compared with diesel soot, despite rapid growth in market share in recent years. Additionally, lubricant oil is a strong contaminant in TEM and ET, and thus presents a higher degree of difficulty for study in comparison to essentially all other types of soot. A GDI soot-in-oil sample is there a topic with ample opportunity for novel research outputs, and ensures any developments should be easily applicable to whatever soot samples we may desire to study in future.

While use of ET is widespread in the study of biological structures (*e.g.* cellular structures, viruses, *etc.*) and materials (*e.g.* embedded nanoparticles, catalysts, and highly porous materials), its application to soot is challenging due to a number of distinct features of soot samples. This includes complexity and non-conformity of structures, high numbers of individual measurements needed, challenging preparation

due to presence of oil, nanoscopic size (generally <500 nm), and low contrast in TEM due to light-element composition (predominantly carbon, hydrogen, oxygen).

Optimisation of ET in terms of speed and quality was a key factor of this work. In order to be a viable technique, *3D-TEM* must offer significant advantages *vs.* the current state-of-the-art in terms of quality of morphology characterisation, but must also remain competitive in terms of speed and throughput. In this regard, different strategies to apply ET to soot were explored and compared, including both existing and novel techniques. Sample preparation for TEM imaging, image acquisition schemes, tomographic reconstruction algorithms, and image segmentation protocols were carefully considered and evaluated. Additionally, work was carried out to assess the accuracy of the technique through development of computational models of soot-like structures. Finally, the foundations were laid for the methodology to permit semi-automated screening of soot samples so that identification of structures of interest could be achieved with minimal human involvement.

The methodology that has been developed represents the most advanced morphological characterisation tool for soot that exists to date. It has progressed significantly further than the achievements of the few previously published introductory studies exploring ET for soot. *3D-TEM* is now in a position to begin to challenge traditional 2-dimensional characterisation techniques. Hopefully, with further development over the coming years this technique can be used to assist the understanding of numerous soot-related phenomena, especially the relationship that exists between soot and engine lubricant oil performance.

1.2 - Background

Soot is the black particulate by-product of the incomplete combustion of hydrocarbon fuel (diesel, gasoline, butane, *etc.*) and carbonaceous biomass (wood, plant matter, food waste, *etc.*). Soot takes the form of nanoscopic particles with complex 3-dimensional structures, which are often described as being ‘fractal-like’ in their morphology. Depending on the perspective/discipline in which soot is being discussed, terms such as particulate matter (PM), black carbon (BC), carbon black (CB), brown carbon, elemental carbon (EC), and organic carbon (OC) may all be used to refer to what is predominately the same, or a very similar, material.

1.2.1 – Soot Nomenclature

The different terms listed above are used to describe nuances between 'soots' as they exist in different physical (and abstract) environments. The term 'particulate matter' is widely used in studies related to internal combustion engine (ICE) emissions and encompasses a range of aerosol species that are emitted alongside soot, such as ash, liquid organic droplets, and secondary particulates derived from nitrates (NOx_x) and sulphates (SO_x) [1]. In studies of atmospheric aerosols and their relation to radiative forcing and climate change, 'black carbon' is used to refer to a combination of combustion-derived chars and soot that possess high potential for absorption of light [2]. In contrast, 'carbon black' refers to soot produced in a commercial process *via* pyrolysis or combustion of hydrocarbons, for use in tyres, inks, and numerous other enterprises [3]. Similarly to black carbon, 'brown carbon' refers to soot-like material that plays an important role in climate effects in the atmosphere. While black carbon includes typical soot nanoparticles, brown carbon describes large, amorphous carbon spherules that possess different light and radiation absorption properties [4]. 'Elemental carbon' makes reference to the fact that soot-like materials are predominately carbon in their elemental composition (>80%), and may be used to refer to char-like aerosols (from pyrolysis of biomass and coal, predominantly) as well as soot (which is flame-derived). Typically it represents solid-phase carbonaceous aerosols below temperatures at which they decompose in air (~550°C) [5]. Often used in atmospheric studies, 'organic carbon' refers to molecular hydrocarbon species that form alongside soot during combustion (or those derived from unburnt fuels) that are incorporated into, and onto the surfaces of the 'elemental carbon' framework of soot (*i.e.* the solid, nanoparticle phase). In many cases, BC is considered as a combination of EC + OC, and EC/OC ratios are commonly measured for aerosol soot samples [6]. In this work, 'soot' will be used as the generic term, and any specific sample types will be described where appropriate.

1.2.2 – Estimates of Soot Production

Published figures describing the global production of soot-like materials can vary depending upon the definitions of soot used, and the sources taken into account. In many cases, soot or BC emissions may not be directly included, but rather incorporated as part of total particulate number or mass measurements. Popular definitions of total particulate matter include size specific bands such as PM_{10}, $PM_{2.5}$, PM_1, and $PM_{0.1}$, which refer to particles smaller than 10, 2.5, 1, and 0.1 μm respectively. In such cases,

soot contributes to each band to a different degree, with a greater relevance to PM_1 and $PM_{0.1}$ specifically [7]. Figures tend to be calculated in a bottom-up approach, extrapolating based on datasets of international and national emissions and energy usage statistics, for example based on figures of yearly fuel consumption and records of vehicles types.

A widely referenced figure from Bond *et al.* in 2004 used such an approach, and put global BC emissions from a variety of sources within a range of 4.3 - 22 Tg $year^{-1}$ [8]. Global contributions from combustion of biomass, fossil fuels, and biofuel were put at 42%, 38%, and 20% of the overall total respectively, though on a regional scale these contributions varied greatly. While in typical 1st world regions (*e.g.* Japan, Europe, and North America) diesel engines contribute around 70% of total BC, in the 3rd world it is combustion of biomass and solid fuels that dominates. The authors of that study conceded that calculations are troubled by important uncertainties. These relate primarily to estimations of combustion using out-dated technologies, and the amount and type of fuel burnt in biomass combustion. Accordingly, this is more significant when calculating contributions from developing nations [9]. A more recent publication by Klimont *et al*. provided an assessment of particulate emissions over the last 3 decades, and incorporated a number of emission sources that had previously been ignored [10]. This study broke down emissions into both size-specific (e.g. PM_{10}, $PM_{2.5}$ *etc.*) and type-specific (BC and OC) categories. Results indicated that over a 20-year period from 1990-2010, global particulate emissions had remained relatively constant, though contributions from specific regions had changed significantly. While PM emissions from typically 1st world nations decreased from around 30% to 15% of the total, emissions from Asia in general had risen from roughly half to over two-thirds of the total. Global BC emissions were estimated to have risen from 6.6 Tg $year^{-1}$ in 2000 to 7.2 Tg $year^{-1}$ in 2010, and accounted for up to 50% of total transport PM.

1.2.3 – Health and Environment

Regardless of its origin, soot is likely to cause problems in practically all environments into which it can penetrate. Perhaps the most important and well-publicised effects of soot are in relation to human health and global climate change.

A 2016 report by the World Health Organization (WHO) considers ambient air pollution to be the single biggest environmental risk to human health [11], playing a role in 1 in 9 deaths globally in 2012. In particular, PM is known to be associated with respiratory and cardiovascular disease [12, 13], where particulate size is an important consideration

for the degree of impact. PM is also an important cause of environmental degradation, contributing to altered ecological balance in water systems and reducing diversity of ecosystems [13].

Because of the prominence of these issues, numerous regulations and control schemes for PM emissions have been put into place over the years. The World Health Organization has created a variety of guidelines in relation to air pollution in different scenarios [14], and include particular focus on particulate emissions [15]. These kind of regulations are also usually implemented on a national level, such as the National Air Quality Objectives in the UK [16] which includes limits on exposure to PM_{10} and $PM_{2.5}$. Despite these efforts, recent work by the European Environment Agency has found that as much as 81% of urban populations may be exposed to $PM_{2.5}$ above WHO limits [17].

Atmospheric soot, often referred to as Black Carbon in this context, is extremely important in relation to the greenhouse effect and global climate change. In fact, it has been calculated that BC is second only to CO_2 in terms of radiative forcing effects [9], and is known additionally to contribute to snow-ice melting *via* deposition in polar regions [18]. Reduction of BC emissions is a key target for abatement of climate change, as the short-lived nature of atmospheric soot in comparison to gaseous species such as CO_2 means benefits may be much more quickly realised [19].

1.2.4 – Soot from Automotive Engines

As mentioned, the major source of soot in regions such as the UK, Europe, and North America is automotive ICEs, in particular diesel-powered vehicles. Given that my PhD project has been carried out as part of the Nottingham Powertrain research group, these sources have been our most direct concern in relation to soot.

Though soot production from diesel engines has a long history, significant production of soot from gasoline engines is a relatively recent development. A major reason for recent focus on PM emissions from ICEs actually stems from increasingly stringent controls on efficiency and emissions of other pollutants (a comprehensive guide to worldwide regulations on vehicle emissions can be found at [20]). To increase efficiency, modern engines adopt strategies such as direct injection (DI) and turbocharging. However, this has resulted in increased levels of soot production, particularly for gasoline engines [21]. Though use of particulate filters for soot capture are widely used for diesel, and are becoming more prominent for gasoline engines, their use is associated with an increase in fuel consumption by up to 5% [22]. Similarly,

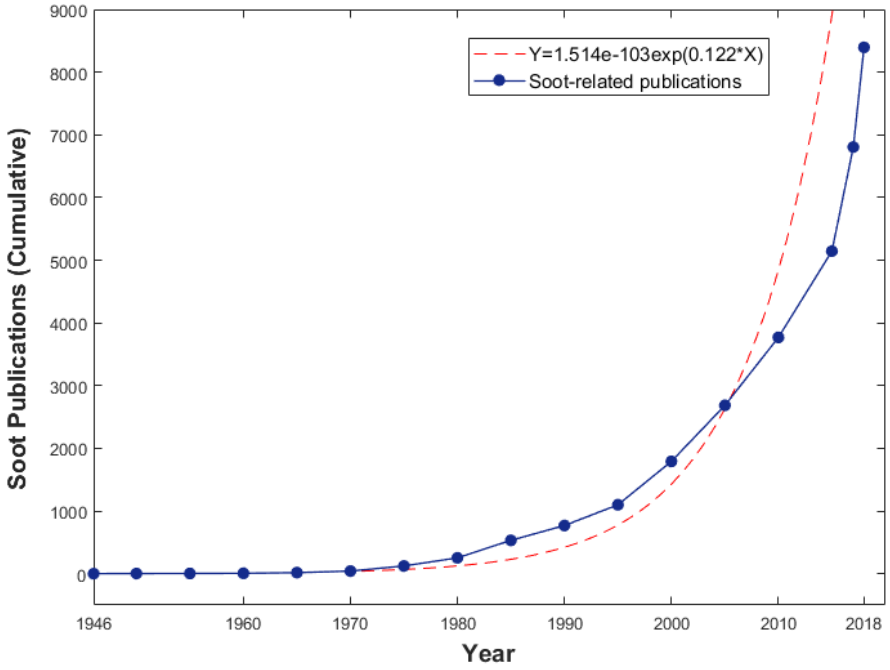
technologies adopted to decrease gaseous emissions can have a similar effect. Exhaust gas recirculation is a commonly used method for reducing NO_x emissions, but in diesel engines can result in a so-called "soot-NO_x trade-off" [23]. In response to this increased sooting tendency of modern engines, European Emissions Standards have limited mass of PM emissions since 1993 for diesel, and 2009 for gasoline engines. More recent iterations of the EURO regulations, for example EURO-VI introduced in 2014, have limited particle number concentration as well.

Even in the event of *perfectly* designed particulate filters, emitted soot is not the only concern. Soot can also entrain within the engine lubricant oils, where it is known to degrade the lubricating properties of oil and increase wear [24, 25]. Despite extensive research (see following chapter, section-2.3.2), the precise relation between soot and oil is as yet not well understood. This is particularly so for gasoline engines, in which soot-loading in oils significantly increases with use of technologies such as direct injection [21]. Increased oil viscosity is of great concern, as use of low-viscosity oils is key to reduce friction losses and increase engine efficiency [26, 27].

Though hybrid and electric vehicles are ever increasing in popularity, diesel consumption is still expected to increase by up to 85% over the next 20 years, with gasoline consumption predicted to decrease only moderately, by around 10%, over the same period [28]. As such, soot-based research related to ICE can expect to be an important area of research for the foreseeable future. Based on the Scopus database of publications since 1946, the rate of increase of publications including "soot" as a keyword is almost twice that of the scientific literature in general, highlighting the growth of research in this area (see figure-1.1).

1.2.5 – Context of this work

Given the nature of my research group, the native focus of this study is on soot from automotive ICEs. The main impetus for developing a morphology characterisation tool is the observation that soot morphology plays an important in soot-mediated phenomena. Examples include toxicity to humans [29], radiative properties in the atmosphere [30], and coagulation of nanoparticles [31]. In some cases, authors have even explicitly stated that improved morphological characterisation could yield improved understanding of, for example, viscosity behaviour of sooted lubricant oils [32], and the relationship between soot and ash formation during engine cold-starts [33]. Characterisation of soot morphology permits understanding of these phenomena and subsequently intelligent design of systems to abate soot-related effects.



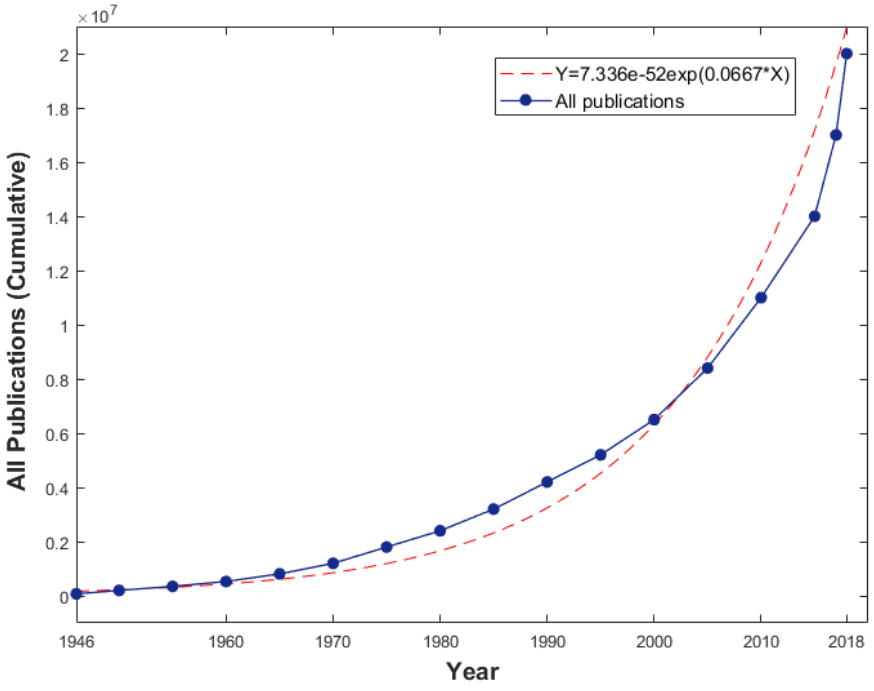


Figure-1.1: Plots of the growth in number of publications contained in the Scopus database from 1946 to 2018. Above shows all publications including key-word "soot", while below is all publications in general. Exponential fittings show rate of growth of soot publications (0.122) is almost twice that of the scientific literature in general (0.0667).

Prior to this work, the study of soot nanoparticles in 3D *via* electron tomography has been employed on only a small number of occasions, as a means to improve understanding of radiative forcing of soot by improving morphological characterisation [34-36]. During the course of this project, two more 3D soot studies have also been published [37, 38]. In all of these works, the authors highlight improvements in morphological characterisation both in quantitative and qualitative terms. Higher quality of morphological measurements resulted in strong deviations in predictions of light-scattering *vs.* simplistic morphology [34, 36], and qualitative appearance of particles lead to predictions relating to soot formation mechanisms [38].

At the inception of this project, however, methodologies for ET study of soot nanoparticles were simply not quick enough to be practical. Characterisation of a soot sample generally requires several hundred individual measurements [39], yet the full 3D reconstruction requires ≥1 day per nanoparticle [40]. As such, this project was focussed on optimisation of ET so that the benefits of improved morphological characterisation in 3D could be realised in a practice. Though this work is generally carried out in the context of soot from ICE engines, and the main sample studied is from the oil of a GDI engine, it is most certainly not limited to this field. Given that the aim of the project is to develop a *tool* or *methodology* for soot characterisation, much of the work undertaken could easily be applied to other soot species, and even any nanoparticles vaguely similar to soot in their size and appearance in TEM.

1.3 – Aims and Objectives

The overall aim of this work is to develop a high-throughput methodology for high quality morphology characterisation of soot nanoparticles in 3D. To achieve this, the following objectives were identified:

- Develop a procedure to enable routine TEM observation of soot-in-oil nanoparticles in spite of the contamination from lubricant oil. This was achieved through development of a solvent extraction technique devoid of centrifugation or ultra-sonication.
- Quantify uncertainty in traditional 2D-TEM morphology characterisation relating to orientation of nanoparticles on the TEM grid.
- Optimise the major steps of the electron tomography procedure in terms of speed and accuracy. This was carried out through direct comparison of commonly available methods when performed on the same data set

- Optimisation of TEM imaging. Identification of sufficient quantities of suitable soot structures was streamlined *via* development of a semi-automated image acquisition and screening procedure. Reduction in direct human involvement was a major target of optimisation.
- Assess accuracy of 3D reconstruction of soot. A simple aggregation simulation was performed to create soot-like models with exactly known 3D morphology. The 3D-TEM procedure was applied, and post-reconstruction morphology was compared to that of the original models.

Upon completion of these objectives a final additional aim was to use the technique to characterise a real soot-in-oil sample in 2D and 3D. Soot was extracted from the oil of a gasoline turbocharged direct injection (GTDI) engine, and 34 nanoparticles were characterised in both 2D *via* TEM and 3D *via* ET. This data was used to compare 2D- and 3D-derived morphology directly, and describe the typical morphology of nanoparticles in that sample both qualitatively and quantitatively. A secondary output of this work was a methodology for high-throughput 2D-TEM morphology characterisation, and the same soot-in-oil sample was characterised *via* measurement of 524 nanoparticles in 2D.

1.4 – Thesis Layout

This thesis contains 9 chapters in total. Chapters 2 and 3 contain the literature review and experimental details, respectively. Chapters 4-8 are the main working chapters of the thesis, while chapter 9 contains the final discussions and conclusions. The appendix also includes two short sections that are referred to in the main text. It was decided that these sections detracted from the flow of main chapters, so were separated for the sake of the overall narrative.

The literature review aims to provide a holistic overview of soot to provide deep context for the work carried out. This includes details on soots formation, structure, and impacts, as well as details on methods of study of soot nanoparticles. It also describes the most relevant works in the literature, particularly those that also employ ET.

Chapter 3 details the experimental equipment employed and the samples studied, as well as describing operation of TEM in relation to soot study and fundamental details on the processes involved in electron tomography.

This work includes a total of 4 ‘results’ or ‘working’ chapters, which are summarised in figure-1.2 below.

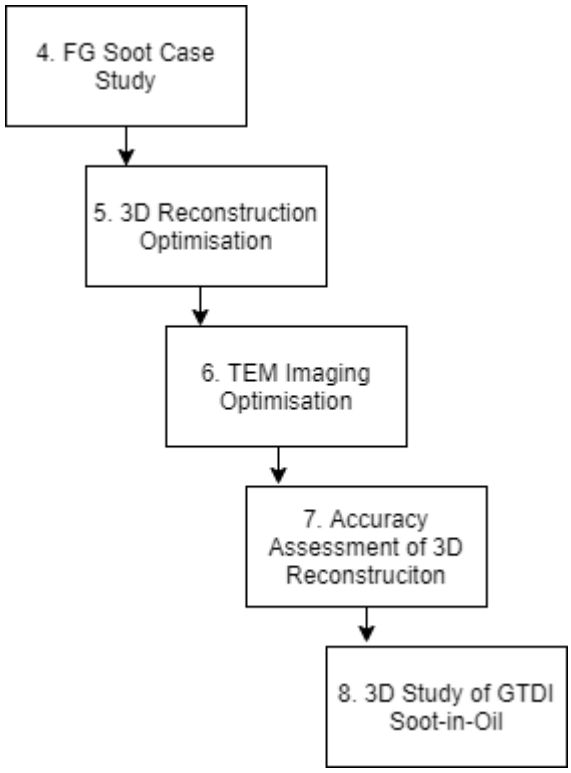


Figure-1.2: A flow-chart showing the arrangement of the 4 results chapters

The first working chapter (chapter 4) contains details on the use of ET and TEM for a ‘case-study’ of flame-generated soot. This chapter contains discussions on sources of error in traditional 2D characterisation of soot morphology, as well as comparison of 2D- and 3D-derived morphological result. This work is used to identify the areas in which improvement is required to achieve the goals of the project.

Chapter 5 describes the assessment of various methods for tomographic reconstruction of soot in terms of speed and quality. The result is an optimised ET methodology that saves significant time while retaining accuracy of volume reconstruction. Chapter 6 follows on from this optimisation, targeting improvements to the speed and ease of imaging *via* TEM. A methodology is developed to greatly increase automation in identification of nanoparticles for 3D study and reduce bias in these selections. The GTDI soot-in-oil sample is also characterised *via* typical 2D-TEM methods.

Chapter 7 details the assessment of the accuracy of volume reconstruction by electron tomography. A set of soot-like aggregate models is created *via* a simple aggregation

model, and used a ‘ground truth’ by which to determine the propagation of reconstruction artefacts.

Chapter 8 is the final results chapter, and describes the use of the optimised procedure for TEM imaging and ET to perform the most extensive 3D study of a soot-in-oil sample to date. In studying 34 individual nanoparticles, results are provided on the comparison of 2D- and 3D-derived morphology, the range of morphology in a quantitative sense, and qualitative observations of morphology facilitate only by 3D study.

A final chapter of conclusions brings together all the outputs of this work, and details the achievements and opportunities for further work.

1.5 – Contribution to Knowledge

The work contained in this thesis provides a practical route towards full-scale 3D morphological characterisation of soot. To the authors knowledge, this work represents the first attempt at developing ET into a practical tool for soot study, as well as the most extensive 3D study of soot-in-oil and possibly any single sample of soot nanoparticles to date.

Through both 2D and 3D study, this work provides qualitative and quantitative descriptions of soot extracted from the oil of a GTDI engine, a topic on which there are only a few examples available in the literature [21, 41]. The effect of nanoparticle orientation on typical 2D-derived morphology is quantified for this sample, as is the discrepancy between 2D- and 3D-derived morphology. Assessment of the accuracy of tomographic reconstruction of soot-like models is also performed for the first time.

The optimised methodology for 3D morphology characterisation of soot was developed for study of a GTDI soot-in-oil sample, but is by no means limited to this. Study of aerosol soot, carbon black, diesel exhaust and soot-in-oil can all benefit from advanced morphological characterisation. The technique could also be extended to other light-element nanoscopic species that appear similarly to soot in TEM.

2 – Literature Review

This chapter details a review of the literature in regards to the formation, structure, and impacts of soot, as well as state-of-the-art methods of soot study. The aim is to present a thorough and well-rounded description of soot from a bottom-up perspective so as to provide the reader with sufficient context for the work carried out in this thesis.

2.1 – Soot Formation

In the introduction, the basic principles of soot formation were described. Oxidation of hydrocarbon and carbonaceous fuels forms carbonaceous particulate matter, *i.e.* soot, when there is insufficient presence of oxygen. So-called incomplete combustion can arise in many different scenarios, *e.g.* forest fires, internal combustion engines, candle flames, *etc.* The focus of soot study in the Powertrain research group at the University of Nottingham is on that produced by internal combustion engines. For the reasons stated in the introduction, this project also has a particular focus on GDI soot-in-oil, which is soot produced by automotive gasoline direct injection engines that has transferred to the lubricant oil film of the engine.

In this section, the findings of published work regarding the formation of ICE soot will be detailed and discussed. First, details on the modes of operation in automotive ICEs that lead to soot formation will be presented, followed by the chemical pathways and mechanisms that cause soot to be formed under such conditions.

2.1.1 – Soot Formation in Internal Combustion Engines

Production of soot is a well-known phenomenon for diesel engines, and while traditionally insignificant for older gasoline engines it has become a growing concern with the increased usage of direct injection technology. As mentioned, soot is formed when incomplete combustion takes place due to lack of oxygen during the combustion. These ‘anaerobic’ conditions within the engine cylinders can arise for a number of different reasons.

One of the most important causes of soot formation in diesel and gasoline engines is the presence of fuel-rich zones within the cylinders which arise due to non-homogeneous mixing of fuel and air (together known as the *charge*) prior to ignition [41-43]. Older

gasoline engines made use of carburettors or port-fuel injectors (PFI) to ensure homogeneous mixing of fuel and air prior to injection, but modern diesel and gasoline engines tend to use *direct injection* of fuel instead. Direct injection has been employed because greater control over injection timing and pressure has enabled improvements to both efficiency and performance [44]. However, direct injection of fuel into the cylinder allows less time for vaporisation and mixing with air, and is known to lead to higher levels of particulate emissions [42, 45]. Though injection timing can be altered to allow longer mixing periods, Williams *et al.* observed that mixing of the charge occurred to a similar degree regardless of the injection timings used in their study [46]. Maricq *et al.* observed that particulate emissions of a direct injection spark ignition (DISI) engine even increased as injection timing was advanced [47], when theoretically there would be more time for mixing. They suggested that soot may form due to direct thermal decomposition or 'charring' of liquid fuel droplets, as well as from combustion of fuel-rich zones.

As described above, liquid fuel droplets can form when there is insufficient time for fuel vaporisation and mixing, such as during late fuel injection timings and high speed load conditions [47]. However, droplets may also form due to condensation at low engine temperatures during 'cold-start' conditions. Cold-start refers to the initial period of engine operation when pre-ignition temperature is low, which has been defined as < 23 °C [33]. In this regard, Peckham *et al.* observed that soot formation was most prominent during the first 200 seconds of a test cycle for a 1.6 L GDI engine from a passenger vehicle. Badshah *et al*. studied cold-start particulate emissions during the New European Driving Cycle (NEDC) test for over 20 vehicles, comprising a mix of PFI, GDI, and diesel technology. For most gasoline engines they observed that Euro-VI particle limits for the entire test cycle were exceeded within the first 12 seconds of a cold-start [33]. In their recent study of exhaust soot from a GDI engine [48], Bogarra *et al.* measured peak particle number concentrations of 1.4×10^8 cm^{-3} during a cold-start, which "dropped an order of magnitude after 140 seconds of the engine warming up".

In a similar vein, soot formation also occurs due the combustion of films and pools of liquid fuel in the combustion chamber. In DI engines, the geometry of the fuel injection is designed to achieve fuel-air mixing in the cylinders, due the lack of pre-mixing [49, 50]. A common strategy for both diesel and gasoline engines is wall-guided injection [51, 52], where mixing is promoted by deflection of the fuel spray off the piston. In GDI engines another common strategy is air-guided injection [50], where turbulent intake air promotes directional mixing. Depending on the mode of operation employed, the fuel spray can impinge on the walls of the cylinder [49, 53], or on top of the piston [54]

leading to presence of liquid fuel in these areas, and subsequent soot formation during combustion.

Direct fuel injection in automotive ICEs has been extremely useful for meeting efficiency and emissions targets in recent years. However, improvements in power output, thermal efficiency, and NO_x, CO, and hydrocarbon (HC) emissions tends to come at the cost of increased soot production [23, 55].

2.1.2 - Chemical Pathways and Mechanisms to Soot Formation

The works referenced in the previous section consider soot formation in ICEs from a top-down perspective, but for full appreciation of soot formation the processes must also be considered from the bottom-up. A vast amount of research has been carried out over the last several decades to understand soot formation in terms of chemical mechanisms and pathways.

The main stages generally agreed upon as those that govern the formation of soot are: formation of polycyclic aromatic hydrocarbons (PAHs) from precursor molecules, nucleation to form particles, surface growth from the vapour phase, coagulation of particles, and oxidation acting to decompose the soot [56]. Though it is useful to consider these processes in the order stated above to understand a single nanoparticle formation, in reality they all occur simultaneously during combustion. According to a series of complex chemical reactions, soot nanoparticles are produced within milliseconds [57].

During the initial stages of combustion a number of small molecular and radical species form from the breakdown of the longer-chain fuel molecules. In regards to initiating soot formation, one of the most important of these ‘precursor’ molecules is considered to be acetylene [56, 58]. Other small hydrocarbon radical species are present alongside acetylene, and radical reactions occur to produce small aromatic molecules such as benzene and naphthalene [56, 59]. Some authors have considered that these small aromatic molecules may be more accurately thought of as soot precursors rather than acetylene [60]. Polymerisation reactions continue and large macro-molecules with extended aromatic character (known as polycyclic aromatic hydrocarbons or PAHs) are formed [56, 59].

Next, the nucleation of large PAHs occurs and the first soot particulates of several hundred [61], or several thousand [62] atomic mass units emerge from the vapour phase. In general, the formation of these incipient particles is not currently well understood

[59, 63], but recent work by Johansson *et al.* has suggested a possible mechanism for nucleation and subsequent surface growth [64]. This mechanism involves radical chain-reactions creating covalent bonds between small molecules (such as acetylene) to form PAH radical species stabilised by their aromatic character. Similar radical reactions are expected to be able to covalently bind aromatic and aliphatic species to form large PAHs and the nascent particles. Finally, the mechanism predicts presence of radical reaction sites on particles as important for surface growth of vapour phase species that are otherwise too small to directly condense on the particle. Another widely considered mechanism for surface growth of particles by addition of small vapour phase molecules is *via* hydrogen abstraction carbon addition reactions [65]. Surface growth is considered to be the major contributor to mass of soot nanoparticles [66].

Concurrent with surface growth and nucleation, coagulation of the initial particle species occurs, resulting in a decrease in overall particle number but an increase in particle size [66]. The coagulation (or coalescence) of multiple small particles, alongside continued surface growth, results in the formation of the characteristic soot primary particle [67]. Primary particles are approximately spherical with diameters around 20-50 nm [68], and constitute the basic structural unit of soot nanoparticles. The final formation process is the aggregation of primary particles *via* their collision, creating the typical fractal-like chain structures of soot nanoparticles [57].

Of course, these processes occur in a high-temperature environment in the presence of oxygen, and the soot itself is carbonaceous and therefore combustible. As such, oxidation reactions pervade the formation processes and act to reduce overall soot size and mass. Prior work has observed that O_2, CO_2, H_2O, and NO_2 species all contribute to oxidation of soot [69]. Additionally, the reactive cylinder conditions act to reduce the elemental diversity of soot *via* the elimination of functional groups containing hetero-atoms. So-called carbonisation increases the relative carbon content of soot as well as its crystallinity [56].

The structural characteristics of soot depend strongly on the balance of the formation and oxidation process, and as such can vary greatly depending the source. The next section details typical structural features of soot nanoparticles.

2.2 – Soot Structure and Morphology

Soot nanoparticles, often referred to as agglomerates or aggregates, have a complex, branched morphology resulting from the chain- or cluster-like aggregation of sub-units

known as primary particles. The size of soot nanoparticles typically ranges from 50-500nm, though this is strongly dependent on the formation conditions [68, 70-72]. The term 'mass fractal' is often used to describe soot agglomerates [73-75] due to their resemblance to self-similar fractal patterns, though self-similarity in soot is often only true over very small distances.

2.2.1 – Primary Particles and Nanostructure

The structural sub-unit of soot nanoparticles are the 'primary particles', which are approximately spherical and possess a structure comprising an inner core and outer shell [41, 70, 76]. The inner core generally has diameter around 10 nm and consists of several small carbon spherules with diameters of 3-4 nm, surrounded by carbon layers in a distorted, flexible structure [76]. The presence of spherules relates to the formation of the primary particles *via* the coagulation of the nascent soot particles [67]. An outer layer of similar thickness is formed from a concentric "onion-like" arrangement of short graphitic "micro-crystallites", perpendicular to the radius [76, 77]. The micro-crystallites are short lengths of graphitic carbon, consisting of 2-5 layers of sp^2-hybridised carbon in a hexagonal honeycomb arrangement, and are around 1 nm thick and 3.5 nm wide [76].

Mean primary particle diameters are usually in the range of 20-50 nm, and size and morphology have been seen to vary depending on the source, and between works. For example, La Rocca *et al.* found a mean diameter of 36 nm for GDI soot-in-oil, with an additional 5 nm thick amorphous layer observed on the surface of the particles [41], whilst a typical 2-layer structure and a mean diameter of 20 nm was found for soot taken from diesel engine oil [70]. Lapuerta *et al.* observed a mean of 25 nm within a narrow range in their study of exhaust soot from a diesel engine [71], whilst Devlin *et al.* [78] and Clague *et al.* [68] each found a mean of 40 nm for a similar soot source. In their study of diesel exhaust soot from a Euro IV compliant engine, Su *et al.* observed small primary particles with diameters in the range 3-15 nm, where the particles consisted of only an inner core; the lack of an outer layer perhaps due to the higher extent of oxidation exhaust soot is subject to [79]. By comparison, carbon black primary particles were 20-30 nm in diameter. Lee *et al.*, in their study of diesel engine particulates, found that primary particle size varied over the range 28.5 to 34.4 nm as engine conditions were altered [80], and Lu *et al*. found primary particles in the range 23.8-28.5 nm in a similar study [81]. When considering soot formed from diffusion flames of different blends of ethanol and gasoline, Maricq observed primary particle diameter to increase

from 19 nm to 44 nm as the ethanol fraction decreased from 85% to 0% [82]. Wentzel's 2003 study compared diesel exhaust soot with soot created from spark discharge of graphite [83], and while diesel primary particle diameter was fairly typical at around 23 nm, so-called "Palas soot" was much smaller at around 7 nm.

Despite significant variation in size between different samples, primary particle size has been considered to be effectively monodisperse within a particular diesel soot sample [71, 84, 85]. Some work, however, has observed significant variation in primary particle size for soot from gasoline engines. For example, in their study of GDI exhaust soot Liati *et al*. [86] observed primary particle diameters in the range 4-55 nm. A similarly large range in primary particle diameter was also observed by Seong *et al*. in their study of the effect of engine operating parameters on the morphology of GDI soot [87].

2.2.2 – Nanoparticle Aggregate Structure

The spherical primary particles aggregate to form fractal-like nanoparticles, sometimes termed secondary particles, in the form chains and clusters. The size and morphology of aggregates depends on the source of the soot, but in general particles are in the range of 50-1000+ nm in length. Aggregate sizing *via* TEM is less common to observe in publications compared with primary particle sizing, but when present can be seen measured *via* methods such as mass particle size analysis or TEM (see section 2.4.1).

In their TEM study of soot-in-oil [41], La Rocca *et al*. found the mean skeleton length of soot-in-oil from a GDI engine to be 153 nm, and skeleton width to be 59 nm. This was slightly larger than mean skeleton length and width for soot from diesel engine oil [70], which were measured as 132 nm and 49 nm respectively. GDI soot-in-oil saw 9% of particles with length over 300 nm, whilst soot from diesel engine oil saw 90% of particles under 200 nm long. Imposing a condition that particles with aspect ratio >2.5 be considered chains, and <2.5 as clusters, GDI oil soot possessed slight excess (54%) of clusters, whilst diesel oil soot had the same level of excess in favour of chains. Clague *et al*. (also employing TEM) observed differences in mean particle size for soot taken from 2 engine oils with different dispersant abilities [68]. The better dispersed soot had an average size of 150 nm, with a maximum of around 400 nm, whilst the poorer oil saw average size of 210 nm, with some particles over 500 nm. In their study of diesel exhaust soot, Park *et al.* observed particles ranging from 50 to 300 nm in size [84]. Uy *et al.* compared diesel and gasoline soot with carbon black using a range of analytical techniques including TEM [21]. While carbon black agglomerates could reach several microns in size, GTDI soot was sub-micron in size and diesel soot agglomerates were

observed with lengths in the range of 100-700 nm. As previously mentioned, Seong *et al*. studied effects of engine operation on GDI soot formation [87]. Their measurements of radius of gyration showed that advanced injection timing increased aggregate size from around 66 nm to 90 nm, and that retarded timing was concurrent with increased ratio of smaller particles.

La Rocca *et al.* [70] recently observed that the method of imaging particles could also affect the size of particles due to the experimental handling required. High resolution TEM imaging (HR-TEM) of oil soot required ultracentrifugation to achieve sufficient separation from the oil phase, as engine oil is a contaminant in electron microscopy [41, 88]. This was seen to increase mean agglomerate skeleton length by more than double, and width by almost 70% compared to soot particles from the same sample prepared for and imaged by standard TEM. Ultrasonic bathing reduced agglomerate size, but not to the original size observed in standard TEM.

2.3 – Impacts of Soot

As described, production of soot is in balance between the formation and oxidation processes. Due to the ongoing oxidation, a fraction of the soot produced is simply decomposed within a single stroke of the piston. However, that which survives can follow two different paths: emissions from the engine with the exhaust gases, or entrainment within the lubricant oil film.

2.3.1 – Outside the Engine: Exhaust Soot

Of the soot that survives oxidation, most is emitted from the engine alongside the exhaust gases that include CO_2, H_2O, CO, NO_x, and various hydrocarbons. Reduction of CO, NO_x, and HC emissions is commonly achieved using three-way catalytic filters in gasoline engines, while use of oxidative catalysts for CO reduction and exhaust gas recirculation (EGR) for NO_x reduction is common in diesel engines [89]. Since their first commercial application in diesel vehicles in 2000 [90], many automotive engines are now fitted with filters to remove particulates as well. So-called diesel particulate filters (DPFs), and more recently gasoline particulate filters (GPFs) [91], operate as high surface area, porous ‘traps’ that retain particulates whilst allowing gaseous species to pass through. Filtering of particles is achieved through simple sieving based on size, adsorption onto the walls over the long path-length, and so-called ‘cake’ filtration where

subsequent particulates build thick layers on the filter over time [22]. Eventually, high levels of accumulation mean filters need to be 'regenerated' by combustion of the soot on the filter. While particle filtering efficiency can be greater than 99% once cake-filtration occurs [92], increases in backpressure reduce engine efficiency and subsequently fuel economy can decrease by 2-5% [22].

Particle filtering efficiency has been observed to be inconsistent over different particle size ranges [92], and particle production has been seen to increase by an order of magnitude during filter regeneration [93]. While strict particulate emission regulations mean that PFs are now incorporated into most diesel passenger vehicles, market share of gasoline PFs as of 2018 has been estimated at only around 10% [94]. As such, significant quantities of soot and other particulates are still emitted from automotive ICEs worldwide. As an aerosol, soot is well-known for its negative effects on human health, as well as its significant contribution to ecological damage, the greenhouse effect, and global climate change.

In relation to their effect on human health automotive exhaust emissions have been researched extensively, such that that this section can serve only as a brief snapshot of the state of current understanding. In general though, it has been considered that cancer, and respiratory and cardiovascular illnesses are the primary forms of disease due to soot [95]. In their 2011 study, von Klot *et al.* observed that soot exposure could trigger acute myocardial infarction, and related soot exposure to time spent outdoors and in traffic [96]. When exposing mice to diesel exhaust emissions, Nejad *et al.* observed an increase in neurovascular inflammation and a 'compromised' function of the blood brain barrier [97]. Similarly, Barath *et al.* observed 'impaired vascular function' and airway inflammation due to soot exposure, and noted that the extent of the effects changed as a function of engine operating conditions [98]. Separate studies have also observed that both the fractal morphology of soot [99], and its hygroscopic properties [100] were related to depth of penetration within human lungs. It has also been observed that the increased surface area of the nanoparticles is linked to increased toxicity in humans [29].

In their extensive review of the role of carbon nanoparticles in climate systems, Bond *et al.* concluded that soot was second only to CO_2 in terms of its contribution to radiative forcing [9]. In the stratosphere, soot nanoparticles are known to be involved in complex interactions with radiation [35, 36, 101], resulting in a net positive contribution to the greenhouse effect [102] through absorption of visible light. Soot has also been linked to increased snow and ice melting due to deposition on these surfaces and consequent heating *via* light absorption [18], which also contributes to climate warming through

altering the albedo of the planet. Again it has been seen that the fractal morphology, quantified *via* the fractal dimension, plays a role in determining the refractive properties of soot [30], and similarly can be used to understand the Brownian coagulation of soot in atmospheric models [31].

Further examples of the effects of soot is in its concentration in surface waters [103], where the surface soot particles behave as active sites for adsorption of waterborne biological species, altering the microbial balance. Similarly, soot has also been observed to alter distribution of other pollutant species in water systems by acting as sites for adsorption of organic molecules [104]

Study of soot (including the specific effects of nanoparticle morphology) is an extremely important topic of research in wide variety of disciplines, and as concerns over health and climate effects continue to increase it is only likely to become more important.

2.3.2 – Within the Engine: Soot-in-Oil

A small percentage of the soot produced in the cylinders becomes entrained within the engine lubricant oil, either *via* blow-by gases passing the piston rings [105], or *via* a thermophoretic mechanism into the oil film on the cylinder walls [106, 107]. So called 'soot-in-oil' is a well-known phenomenon for diesel engines, where it has been observed that structure and morphology is generally similar to exhaust soot and carbon black [21, 68]. Recently, work has begun to be published regarding GDI soot-in-oil, for which numerous novel structural and morphological features have been observed [21, 41, 108]. This includes presence of localized amorphous structures, crystalline areas related to wear elements, and amorphous layers at the primary particle level.

The effects of soot entrainment within the lubricant oil of automotive vehicles have been the subject of extensive research since the 1970s. These studies primarily focus on the observation of the changes in friction [109-114], viscosity [24, 32, 114, 115], and wear [115-120] in the presence of soot. Although in general it is acceptable to state that soot leads to decreased lubricant performance, a precise understanding of the soot-oil relationship has not yet been achieved. For example, though in the majority of cases increased soot causes an increase in wear [111, 112, 116, 120, 121], it is not universally so [113, 122]. In terms of viscosity, soot increasing viscosity is the predominant finding [32, 115, 123] but there are exceptions [114]. In terms of friction, there is a more even split as to whether increased soot causes an increase [109, 110, 112, 124], or decrease

[109, 111-114, 125] in friction coefficient. These apparent contradictions are due in part to distinct differences in the experimental setup of different studies. This includes choice of oil (fully formulated oil [21, 126], base oil [127], or base oil + selected additives [113, 115, 116]), source of soot (genuine soot-in-oil from engine operation [21, 32], exhaust soot [113], or carbon black [112, 114]), level of soot contamination, and method of experimentation (*e.g.* various geometries of surfaces in contact, lubrication regime, contact material, temperature, operating speed *etc.*) amongst numerous others.

In many studies of the effect of soot on oil, the only metric used to describe entrained soot is the percentage by weight [24, 109-114, 116, 117, 119, 121, 125], commonly determined using thermogravimetric analysis (TGA) [32, 128]. Such a simplistic parameter ignores the defining characteristic of soot; that it is in the form of nanoscale agglomerate particles that have complex fractal 3-dimensional morphology. This may be part of the reason for the lack of coherence in results on the soot-oil relation. A study that perfectly embodies this notion is that by Liu & Nemoto [109], where different oil formulations laden with 3% soot see coefficient of friction both increase and decrease as a function of temperature. In response to the inconsistent relationships that are observed between soot and oil, several authors have concluded that the 'state' of soot in oil is a more important factor than simple concentration [24, 32, 111, 128]. In this sense, 'state' refers to properties such as particle size [120], total soot surface area [32], level of agglomeration [24], and surface reactivity [112].

When more detailed characterisation of the soot is carried out, it often leads to more nuanced and in-depth relations observed between soot and oil properties. For example, Bardasz *et al*. observed that while viscosity increases tended to depend on soot concentration, there was no direct correlation [32]. Instead, total soot surface area [32], and particle size [118] (related to level of agglomeration) showed strong correlation to viscosity increase, and the authors noted that more accurate understanding of morphology would improve any observed relations. In their 2010 study, Antusch *et al*. concluded that wear properties of sooted oils could not be interpreted from soot concentration alone, as physico-chemical properties including morphology and surface reactivity were more significant [111]. In a simulation study of soot-in-oil suspensions, Zeidan *et al.* concluded that soot-loading rate of oil is intrinsically linked to particle morphology and in-turn lubricant viscosities [129]. In their study of diesel engine lubricant oil, Covitch observed that alongside soot concentration, soot agglomerate size played a role in altering lubricant oil viscosity [130]. Asango *et al.* [128] observed how experimental viscosity measurements for soot-laden oils deviated from the predictions

of both Einstein's [131], and Brinkman's viscosity equations [132], and suggested that both concentration and size distribution of soot played a role.

In a similar vein, studies of nanofluids (a term often used to described fluids with entrained nanoscopic particles, fundamentally similar to suspension of soot in lubricant oil) have often observed the impact of morphology on physical properties such as viscosity and thermal conductivity. For example, the viscosity of liquid-solid suspensions has been observed to have a dependence on the shape and size of the entrained nanoparticles [133], which strongly affects solid-solid interactions within suspensions. In their 2018 study, An *et al.* observed that particles of higher *sphericity* (*i.e.* more spherical) experience less inter-particle friction, and thus lead to smaller viscosity increases [134]. Sphericity has also been used to account for the effect of nanoparticle shape on thermal conductivity of heterogeneous materials since the 1960s [135]. Ghozatloo *et al*. observed that modification of common rheological equations for liquid suspensions by addition of a shape factor term (similar to aspect ratio) resulted in a closer fit *vs.* experimental viscosity measurements for several nanofluids [136]. And in 2003, Wang *et al.* developed a model for predicting thermal properties of nanofluids using input from fractal geometry of nanoparticles [137].

Based on the observations in both this section and the previous section, the morphology of soot is clearly very important in terms of determining the extent of soot related effects. As such, soot morphology has been determined frequently in the literature using a variety of different techniques. These will be discussed in the following sub-section.

2.4 – Characterisation of Soot Morphology

Determination of the shape and structure of both individual nanoparticles and soot samples as a whole can be carried out using range of different techniques and equipment, depending on the needs and interests of the researcher.

2.4.1 – Low Dimensional Characterisation

Soot morphology characterisation in its most basic forms can be carried out without direct observation of the structures of individual nanoparticles. There exist a number of somewhat similar techniques that measure average size and size distributions of nanoparticles in-situ in terms of an 'equivalent diameter'.

The size of aerosol soot nanoparticles is commonly determined using electrical mobility measurements [138-140]. This technique involves adding electrical charge to aerosol particles, and observing their rate of movement through a medium in response to an applied electric field. Particle size is determined because, for example, larger particles will move more slowly than smaller particles.

Two similar techniques that measure soot size in liquid suspensions in terms of 'hydrodynamic diameter' are nanoparticle tracking analysis [141, 142], and dynamic light scattering [109, 128, 143, 144] (NTA and DLS respectively). In both of these methods, instruments track the Brownian motion of particles in suspension as a means to calculate their number concentration and size distribution. Hydrodynamic diameter refers to the effective diameter of the particle during dynamic motion in suspension. DLS records fluctuations in the overall intensity of scattering of an incident laser beam, and relates the rate of fluctuation to the Brownian motion of particles in the sample *via* an auto-correlation function. Hydrodynamic diameter is derived from the relationship between particle size and speed in Brownian motion. By contrast, NTA records laser scattering by individual particles and tracks movement through a field of view in real-time to determine the Brownian motion and hydrodynamic diameter.

These types of techniques can be performed rapidly and in-situ, and resulting diameters and size-distributions are generally based on measurements of statistically significant quantities of particles. However, in comparison to the known fractal structures of soot particles this information is clearly very limited, and often more detailed methods of characterisation are preferred.

2.4.2 – TEM Characterisation

Due to their nanoscopic size, the direct visualisation of soot nanoparticles can only be achieved with ultra-high resolution techniques such as transmission electron microscopy. Many of the studies already mentioned in this literature review have opted to use TEM as a means to study the morphology and nanostructure of soot. A description of the basic operation of TEM in relation to soot study is provided in the following chapter, section-3.1.4. TEM allows direct imaging of soot nanoparticles, albeit in 2D, so provides greater detail on morphology in comparison to the methods mentioned in the previous section.

Electron microscopy was first developed in the 1930s [145], and has been used to study soot since at least the 1940s [146]. The technique has been used to study a wide variety

of soot and soot-like materials including carbon black [68], brown carbon [4], flame-generated soot [147], diesel exhaust soot [84] and soot-in-oil [70], gasoline exhaust soot [148, 149] and soot-in-oil [21, 41], aviation soot [150], and soot from marine vehicles [151].

TEM is commonly used for measurement of primary particle diameters [150] and overall aggregate size [152], generally involving the study of around 50-500 individual nanoparticles and primary particles [39, 152]. However, TEM images only provide 2D projections of what are known to be 3-dimensional structures. As such, 3D morphology cannot be measured directly but must instead be inferred from what *can* be measured in 2D. Correction factors of some form must be derived that link real 3D morphology with the observed and measured 2D morphology. In this regard, measurements of aggregate area and mean primary particle diameter are commonly used to determine the number of primary particles constituting an aggregate based on a combination of simulated and real aggregate data [73, 75]. The number of primary particles may then be used to infer volume [153], surface area [154, 155], and fractal dimension [75, 83] of a nanoparticle. Alternatively, parameters such as fractal dimension [156], radius of gyration [157, 158], circularity [159], and skeletal length [160] are simply measured in 2D, with the no direct attempt to infer 3D morphology. In section-3.6.1 of the following chapter, and various points within chapter-4, more detailed discussion of morphological characterisation by these methods can be found.

Details of the graphitic nanostructure of primary particles, as discussed earlier in this chapter, can be quantified in terms of properties such as length, tortuosity, and separation by using high-resolution TEM imaging (see section-3.1.4.3 for further details) [108, 147, 161]. Such information has been used to understand soot formation processes [162], and make predictions on the reactivity of nanoparticles [163].

2.4.3 – Electron Tomography

In an effort to perform morphological characterisation in even greater detail, electron tomography has been used to study soot nanoparticles on a small number of occasions in the literature. Electron tomography uses multiple 2D TEM images of a nanoparticle to recreate the original nanoparticle volume in 3D. Electron tomography can permit direct determination of 3D morphology without need for empirical correlations and the associated uncertainties.

Electron tomography was initially developed in the late 1960s by David DeRosier and (eventual Nobel Laureate) Sir Aaron Klug, and was first used for the 3D study of a bacteriophage virus [164]. Following in this direction, ET has primarily been used for the study of biological samples such as viruses and cellular sub-structures [165], but has also been widely adapted for materials science in recent years too (many useful examples of the application of ET can be found in the introduction of Fernandez' work entitled *"Computational Methods for Electron Tomography"* [166]).

Prior to 2016, ET had only been used for soot study by van Poppel *et al.* [34], Adachi *et al.* [35, 36], and members of my own research group [40]. More recently, work including ET study of soot was also published by Okyay *et al.* [37] and Baldelli *et al.* [38].

For van Poppel [34], the emphasis for the use of ET was understanding radiative forcing by atmospheric soot, for which predictive models tend to consider soot only as spherical particles. Based on the results of their study, they considered that traditional predictions of soot ageing were up to 16 times too long, leading to significant overestimations of the 'global burden' of soot. However, they also predicted that the implication of 3D morphology for light-scattering properties of soot could be even more significant for predictions of the impact of soot on climate.

Following on from the work of van Poppel, Adachi and co-workers were also concerned primarily with the climate effects of soot [35, 36]. In particular, they considered that traditional 2D-TEM morphology characterisation was inadequate for determination of fractal morphology. They observed significant deviations between 2D- and 3D-derived morphology, and significant variability in 2D-derived morphology depending on the angle at which a nanoparticle was observed. Their calculations of light-scattering by soot was up to 30 times larger when incorporating 3D-derived morphology compared with a typical spherical model of nanoparticles.

In 2016, Okyay *et al.* performed a variation of electron tomography using scanning electron microscopy (SEM) instead of TEM [37]. Their purpose for soot study was the thermal conductivity of soot in industrial combustion processes, for which they were aware nanoparticle morphology played an important role. Again, they were particularly concerned with inaccuracies in 2D fractal dimension calculations, and were of the opinion that SEM offered simpler sample preparation in comparison to ET *via* TEM. Their study primarily focussed on the development of the methodology rather than calculations based on 3D morphology.

Most recently, Baldelli used electron tomography for the study of soot produced from flames [38]. Their primary concern was more fundamental, in terms of validation of 2D-derived soot morphology and potential implications of 3D morphology as opposed to a specific soot-related process. They paid particular attention to the variability of 2D-derived morphology as a function of particle orientation, similar to the work of Adachi and that performed in this thesis. Based on their results, they considered that 2D-derived primary particle diameter and aspect ratio were not strongly affected by nanoparticle orientation, though measurements of area varied by around 30% on average. By using ET, they observed ring-features in the 3D models of nanoparticles that were not appreciable *via* typical 2D-TEM study. They reflected that such observations were potentially useful for understanding soot formation processes, suggesting that it indicated that bonds between primary particles were somewhat labile early during soot formation.

Despite these promising results, the use of ET for soot study has remained effectively at an 'introductory study' stage. In short, electron tomography is simply too slow to facilitate the study of a statistically significant number of individual nanoparticles that would be needed to characterise a particular sample. This is because ET requires many individual TEM projections to be acquired for each nanoparticle, additional constraints which particles are suitable for study, and time required for computations and production of the 3D model (these are discussed in detail in the following chapter, section-3.3). Regardless of benefits in accuracy *vs.* 2D-TEM and other techniques, ET as it stood at the beginning of this project was not a viable option for a real application. The aim of this work is to narrow the gap in throughput between 2D- and 3D-TEM, and make ET a legitimate alternative for soot study.

2.5 – Summary

The aim of this literature review was to provide a detailed account of the state of the understanding of soot in general, and appreciation for the wide scope of soot-related research carried out at present. With a particular focus on soot from automotive engines, historical and contemporary research was presented relating to soots formation, structure, and impact in a range of environments. Where relevant, the role of morphology in soot-related phenomena was highlighted, given the relevance to the work in this thesis. Particular attention was also paid to the relationship between soot and oil given the main soot-sample studied in this work was soot-in-oil from a GTDI vehicle.

Also discussed were various techniques for the characterisation of soot morphology and structure, especially TEM. Finally, the burgeoning field of ET study of soot was discussed to place this work in its most immediate context.

The topics discussed in this chapter clearly demonstrate that morphological characterisation of soot is not only relevant, but extremely important in numerous applications. In particular the benefits of 3D soot study from the perspective of other researchers make evident that ET is an effective tool for enhanced soot characterisation.

3 – Experimental Methods and Facilities

The following chapter details the facilities available at the University of Nottingham to perform TEM and ET on soot, and the nature of the soot samples studied in this work. A brief explanation is given on the TEM operation in relation, and the theory and process of tomographic reconstruction is explained. Finally, details on the morphological characterisation performed on soot are provided.

3.1 – Transmission Electron Microscopy

3.1.1 – Basics of Electron Microscopy

Transmission electron microscopy is an ultra-high resolution imaging technique widely used to study nanoscopic structures in fields as diverse as medicine [167, 168], biology [169], materials science [170], and nanotechnology [171, 172]. Basic TEM imaging operates under the same principles as optical light microscopy, in which an incident beam from an illumination source is transmitted through a thin specimen and produces a projection. While in optical microscopy visible light is the illumination source, in TEM an electron beam is used to facilitate extremely high levels of magnification. The *de Broglie* wavelength of an accelerated electron is much shorter than that of visible light and can be shorter than that of X-rays too, being on the order of around 2-3 pm under typical TEM conditions. In microscopy, shorter wavelengths in the illuminating beam enable higher resolution imaging to be performed. By 'resolution' what is meant is the smallest distance that can exist between two points at which they still appear as individual points; above the resolution limit they would appear to merge into a single point. The theoretical relation between wavelength and resolution is described by Ernst Abbe's equation:

$$d = \frac{0.612\lambda}{NA} \qquad \textbf{(3.1)}$$

Where d is resolution, λ is wavelength, and NA is numerical aperture (a measure of the range of angles over which the microscope can accept/emit the illuminating beam). Due limitations in the focussing capacity of the lenses used, resolution in TEM is restricted to around 1 Å (1×10^{-10} m) in practice.

3.1.2 - The specimen stage: TEM grids

Samples for TEM are prepared on so-called grids. TEM grids generally take the form of 3 mm diameter disks made of a metallic mesh (copper, nickel, and gold are common grid materials), which is illustrated in figure-3.1. Different mesh sizes are available, containing anywhere between 50 to 600 individual squares over the 3 mm disk. At '300 mesh', each square is around 40 x 40 μm in size. The grid mesh is coated with a *support film*, which is the substrate onto which the sample (*e.g.* soot) is deposited. There are a wide range of different support films available depending on the nature of the sample under study. Common support films include formvar (a thermoplastic resin), and holey amorphous carbon films. An example of the latter is shown in figure-3.2. The support film must be strong enough to support the sample and span the gaps of the mesh, yet must also be as transparent as possible under the electron beam to minimise obscuring the structures of interest. In many cases, larger specimens may simply span the holes of the metallic mesh, or those of a holey/lacey carbon film. In this case the background to the specimen is only the vacuum of the microscope, which provides the least possible contrast. However, smaller structures such as soot nanoparticles are much smaller than the holes of even a holey carbon film (generally <500 nm in length). In order to properly support these nanoscopic structures, an additional support film may be deposited on top of a holey/lacey carbon mesh. For our studies of soot we used 300 mesh copper grids coated with lacey or holey carbon, also coated with a few additional layers of graphene oxide. The graphene oxide is extremely thin (<1 nm per layer) and provides minimal contrast under the TEM beam, so is an ideal support for the soot nanoparticles. Example images of the grids used in this work are provided in figures 3.1 and 3.2.

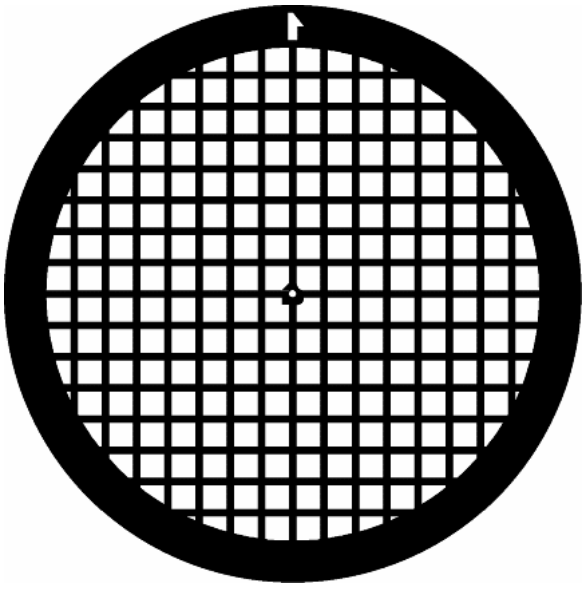
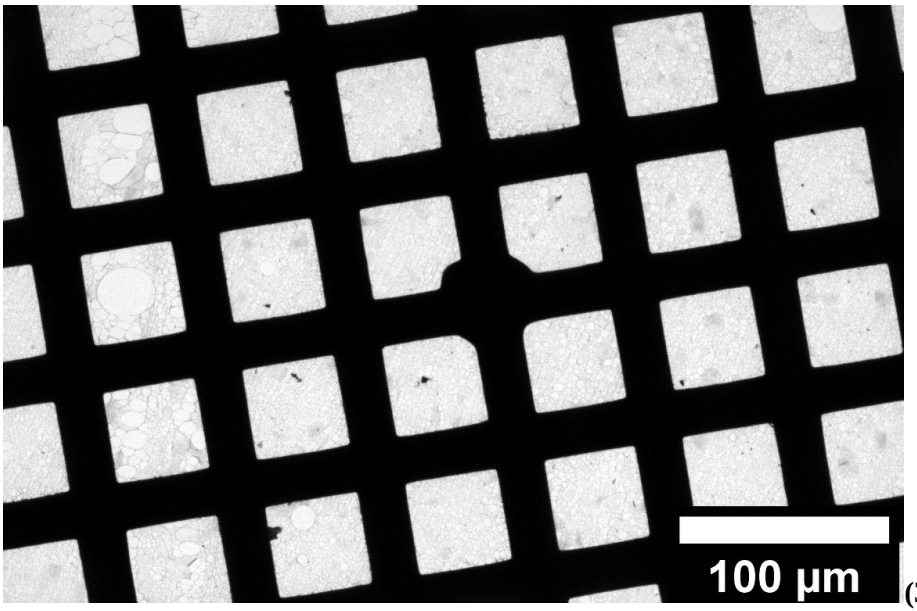
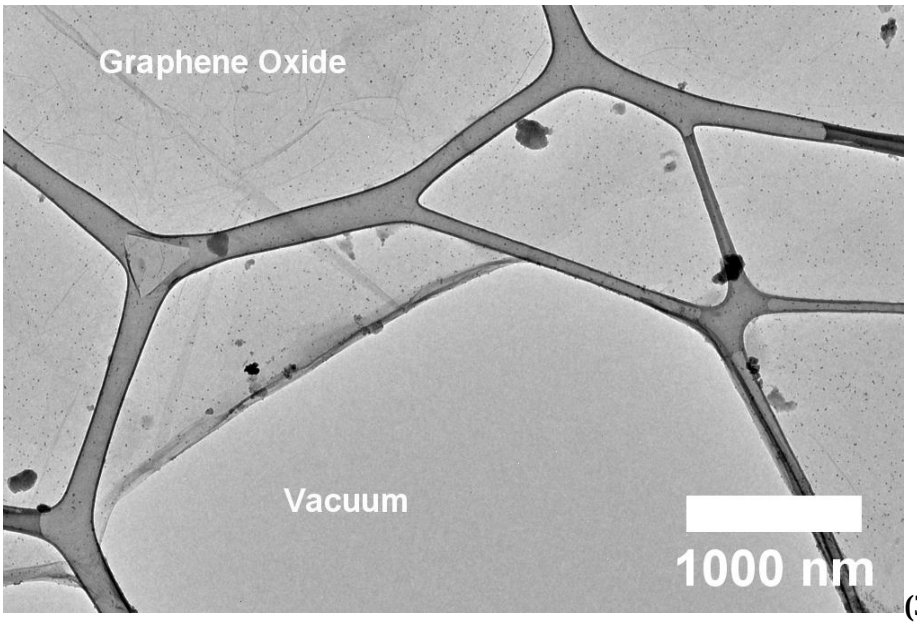


Figure-3.1: Graphical representation of a TEM grid. Actual diameter = 3mm.



(3.2a)



(3.2b)

Figure-3.2: (a) low magnification (x50) TEM image of TEM grid, (b) x2000 magnification TEM image with lacey carbon support (darker 'netting'), graphene oxide, and a breakage in the GO (contrast due to vacuum of the microscope)

3.1.3 – TEM at the Nanoscale and Microscale Research Centre (nmRC)

All TEM work in the thesis was performed at the nmRC at the University of Nottingham, under microscope operation by Dr Michael Fay (my PhD co-supervisor). The nmRC is a cross-disciplinary facility at the University of Nottingham that hosts over 20 instruments to facilitate the imaging and analytical investigation of materials from a wide range of scientific disciplines. All images included in this thesis were acquired using a JEOL 2100F Field Emission Electron Microscope. This microscope uses a field emission gun (FEG) to produce a highly stable electron beam, enabling

extremely high resolution and high contrast. The TEM is capable of operation at both 100 kV and 200 kV accelerating voltages, though soot imaging was performed exclusively at the higher voltage. While lower accelerating voltage can provide higher contrast and lesser damage to carbon bonds, the higher voltage is the default of FEG-TEM operation and permits high-resolution imaging for thicker samples. The microscope is fitted with a Gatan Orius CCD camera, producing images 2004 x 1336 pixels (px) in size. Gatan's own software, *Digital Micrograph*, was used to control image acquisition. Energy Dispersive X-ray (EDX) spectroscopy capabilities are integrated into the microscope, and can be performed directly during imaging.

Tilt-series acquisition was controlled using the open-source software SerialEM [173]. This software was developed for tilt-series acquisition, and can interface with a range of microscope setups. The software manages the tilting of the TEM grid during image acquisition for ET, and tracking of structures as they move due to the rotation of the grid. SerialEM also permits a variety of other types of microscope control and is used in later sections of the thesis for systematically imaging large areas of the TEM grid automatically (chapter-6).

3.1.4 – Operation of the JEOL 2100F Transmission Electron Microscope

3.1.4.1 - Producing the Electron Beam: Field Emission

The JEOL 2100F microscope produces the electron beam *via* Field Emission (FE), which is one of two main sources of electron beams used in TEM, the other being thermionic sources. In comparison to thermionic sources, field emission produces a more intense electron beam with a more discrete range of wavelengths (often described as being *monochromatic*), though the equipment is generally more expensive.

Field emission operates by applying an electric potential between an ultra-fine needle tip (commonly containing Tungsten, *e.g.* ZrO/W), and an anode. The small size of the tip (approx. ≤ 0.1 μm diameter) generates an extremely strong electric field, which acts to lower the work function (the amount of energy required to ionise an electron) of the tip material. The lowered work function allows electrons to *tunnel* from the energy levels of the source atoms to the vacuum of the microscope, thus creating the electron beam.

A potential applied at a second anode is used to accelerate the electron beam and control its initial path, and this two-anode system is together known as a Field-Emission gun (FEG). Most TEM work is usually performed at accelerating voltages of 100-300 kV,

though different voltages may be more appropriate for different types of samples. At 100 kV, the electrons in the beam travel at around 63% of the speed of light. Information in this sub-section is based upon that found in "*Transmission Electron Microscopy: A Textbook for Materials Science*" by Williams and Carter [174].

There are a number of different interactions that can occur when the high-energy electron beam is incident on the specimen. Almost all contain a wealth of useful information, and can be detected and measured using different techniques. In the following sub-section, three key interactions that were used to study the soot samples in this work are discussed: direct transmission for bright field imaging (BF-TEM), X-ray emission for energy dispersive X-ray spectroscopy (EDX), and the combination of scattered and transmitted electrons for high resolution TEM (HR-TEM).

3.1.4.2 – Bright Field Imaging (BF-TEM)

The most simplistic interaction that may occur between the incident beam and the sample is a non-interaction; electrons may be transmitted directly through the specimen without interacting with any of its atoms, or altering their original path of travel. These electrons that are unaltered from their original path are collectively known as the *direct beam*, and it is used to perform bright-field TEM imaging. This imaging mode is directly analogous to a standard optical microscope. In thicker and/or denser areas of the specimen, the direct beam is attenuated as interactions with the specimen deflect electrons from their original path and so away from the camera. Transmission of the electrons is more likely to occur in thinner and less dense areas of the specimen, as there is simply less material for the electron beam to interact with. In BF-TEM, regions of the specimen that interact with the electron beam more strongly appear darker, and areas that interact less strongly appear lighter. An example BF-TEM image of a soot nanoparticle is given in figure-3.3.

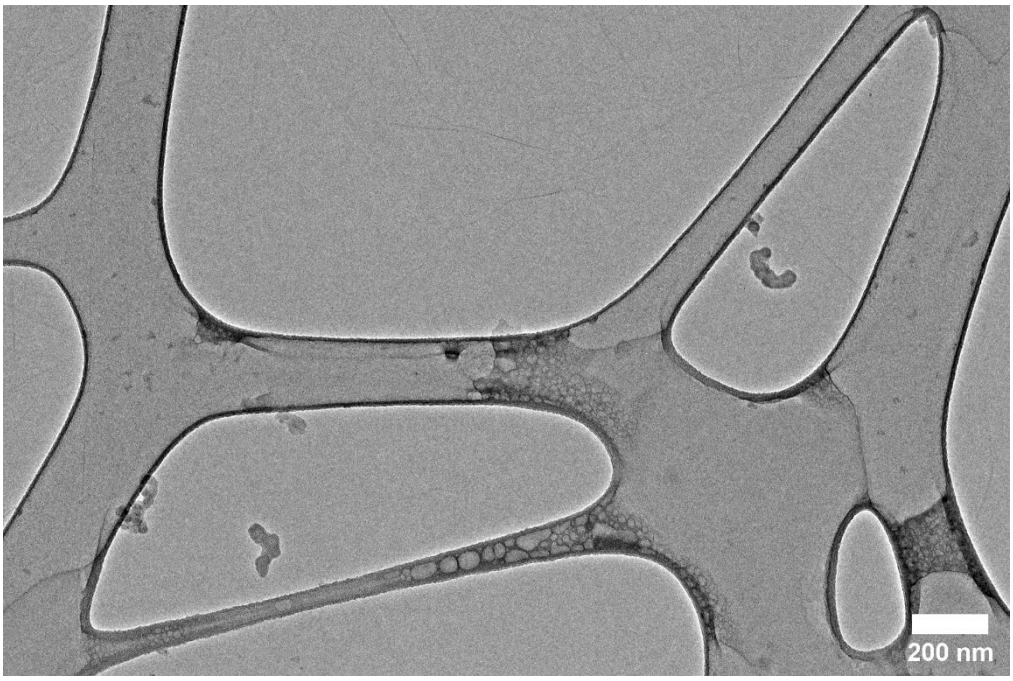


Figure-3.3: A x10,000 magnification BF-TEM image showing typical contrast of soot nanoparticles against graphene oxide film (2 nanoparticles are present)

3.1.4.3 - Scattered Electrons: EDX and HR-TEM

When electrons are not transmitted through the specimen, one of the most important type of interactions that may occur is scattering. Scattering occurs when the incident electrons interact with the atoms and molecules of the specimen and are deflected from their original path. Due to the wave-particle duality of electrons, this can be thought of both as a negatively charged particle interacting electrostatically with the electron cloud (negative) and nucleus (positive) of the specimen atoms, and as a wave being diffracted by a grid of slits and obstacles. A great deal more information on scattering processes can be found in the textbook by Williams and Carter [175].

Elastic scattering occurs when the electrons are deflected but do not impart any of their energy into the specimen atoms, and continue travelling at the same speed. Elastically scattered electrons are primarily used to produce diffraction patterns, which can provide a great amount of detail on the crystalline nature of the sample. The precise arrangement of atoms in a crystal lattice results in a precise pattern of scattering of the electron beam, and thus a diffraction pattern can be used to identify a particular crystalline material. Another prominent use of the elastically scattered electrons is in high-resolution imaging. HR-TEM uses both the direct beam and the elastically scattered beam to produce an image of the sample. An extremely complex pattern of constructive and destructive interference occurs between the scattered and direct beams, and produces an

image by so-called *phase contrast*. This type of contrast is not so intuitively described and there exists many detailed descriptions of the process, for example that contained in [175]. Simply put, the interference that occurs produces a representation of the arrangement of atoms and molecules that is present in the sample. Where the specimen contains highly ordered crystalline materials the high-resolution image will show a series of ordered ridges or points. Where the specimen material is amorphous, no such pattern will emerge and the image will appear 'noisy' and random. It should be noted that what is observed is *not* the actual contours of the atoms and molecules, but a second-hand representation of where they occur. Example HR-TEM images of crystalline and amorphous materials (both observed in soot samples) are given in figure-3.4.

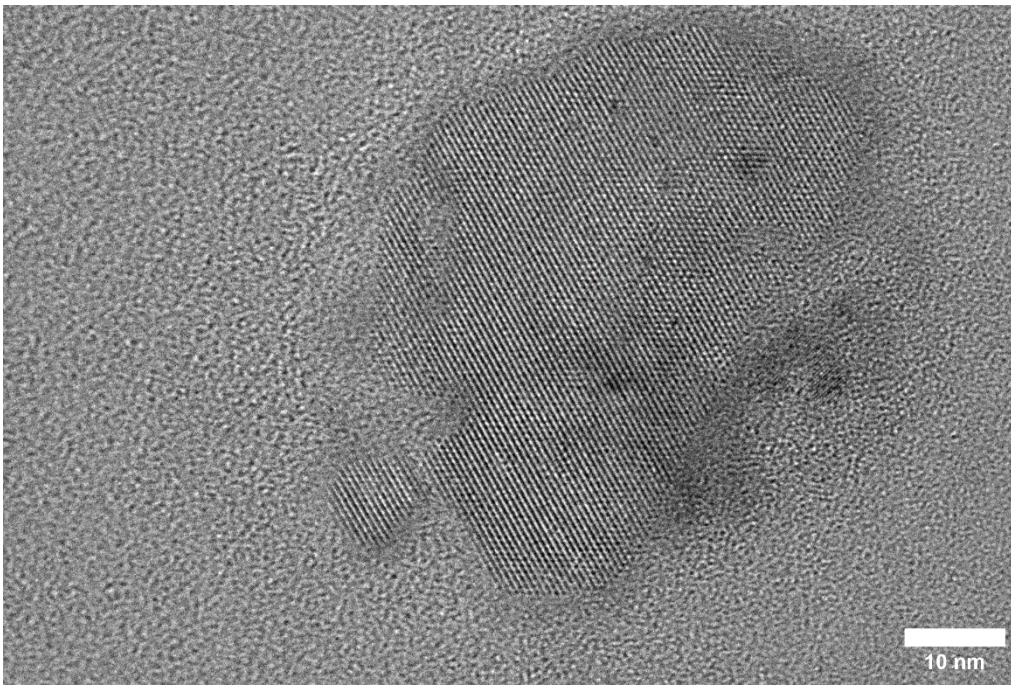


Figure-3.4: A high-resolution TEM image of a crystalline material observed in a GTDI soot-in-oil sample (see chapter-5 for more details). Note highly ordered ridges within the contours of the globular structure.

Inelastic scattering occurs when there is an exchange of energy between the electron beam and the atoms/molecules of the specimen. This exchange of energy is the source of many characteristic emissions of photons and electrons from the specimen which contain extremely useful information on the material present. One such emission made use of in this work is that of *characteristic X-rays*. The incident electrons are extremely high energy and are able to ionise core electrons from atoms in the sample (these so-called *secondary electrons* can also be detected). This creates a 'hole' in the core energy

levels of the atom, leaving it in a high-energy and unstable state. To gain stability, an electron in a higher energy level in the atom will *relax* to fill the core level. By moving closer to the nucleus this electron gains energy, which then must be released. One way in which the energy can be released is by the emission of a photon. This photon will have energy/wavelength that corresponds to the difference in energy between the higher energy-level (from which relaxation occurred) and the core energy-level. These photons are therefore characteristic of the energy levels in the atom, and are used to identify the species of atoms present on the surface of the specimen.

3.2 - Computational Setup for ET and Image Processing

Image acquisition for electron tomography was performed using SerialEM [173]. This software permits control of electron microscope image acquisition and is useful for acquiring multiple images of structures from a range of different angles, and imaging large areas of the TEM grid.

The software chosen to perform tomographic reconstruction was Etomo [176]. This was based on the results previous investigations by members of the Powertrain Research Group prior to my PhD. Possible alternatives included TomoJ [177] and Tomo3D [178], but these had been judged to be slower and less user-friendly. A modified version of image processing software *ImageJ* [179], known as *Fiji* (Fiji Is Just ImageJ) [180], was chosen to perform handling of both 2D and 3D data, including tomogram segmentation. ImageJ and Fiji are open-source and offer great flexibility to install plugins created by other users, and to create bespoke macros and functions. Possible alternatives for 2D and 3D data visualization could have been Avizo [181] or Amira [182], though these are not open-source and required purchase of licenses. All computational work relating to image processing and tomographic reconstruction was carried out on a Lenovo PC with a 3.50 GHz Intel Xeon E5-1620v3 processor (8 CPUs) and 32 GB RAM, using a 64-bit version of Windows 10.

3.3 - Electron Tomography

Electron tomography is a technique used to recreate 3D volumes of objects from a series of standard 2-dimensional TEM images. The first step in ET is to produce multiple 2D TEM projections of a single object acquired from different viewing angles; this is

known as a *tilt-series*. The tilt-series of projections is then used to create a 3D volume known as a *tomogram*. The tomogram is a 3D volume that contains the information from which a model of the object under study can be made. Details in this section are based on those found in [165], and [166, 183].

The basic principle of ET is the same as that used in other forms of tomography such as magnetic resonance imaging (MRI) and computerised tomography (CT) scanning, which are extremely common in medical applications. These different techniques use different protocols to acquire their 2D projections, and accordingly different arrangements of projections may be sampled. For example, in MRI the different projections are acquired by moving the 'camera' rather than tilting the specimen.

The underlying theory of tomographic reconstruction is known as either Fourier slice, projection slice, or central slice theorem. Fourier slice theorem states that a *complete* set of projections of an object contains within it the information required to fully recreate the object in 3D. This is because the 2-dimensional Fourier transform (FT) of a projection represents a slice of the 3-dimensional FT of the object, taken at the angle the projection was acquired.

The 2D-FTs of the set of projections can thus be combined to represent the 3D-FT of the original object, and so in theory an inverse-FT will reveal the objects original structure. Though the theory dictates use of the Fourier domain for calculations, as will be discussed shortly not all tomographic methods compute all the FTs mentioned in Fourier slice theorem.

3.3.1 – The Projection Requirement

The definition of *projections* in the Fourier slice theorem is an important nuance, and leads to what is known as the *projection requirement* for tomography [184]. A projection is a representation of an object onto some kind of screen, and in our case this would be a 3D soot nanoparticle represented as a 2D image on the TEM detector screen *via* the electron beam. The projection requirement is that the input for tomographic reconstruction (*e.g.* tilt-series) is a true projection of the object, such that it 'monotonically' represents some physical property of the object. This essentially means that the contrast in the projection (*i.e.* how 'intense' structures appear) needs to be directly related to the property of the specimen that is dictating the levels of contrast.

In BF-TEM, the property that creates the different levels of contrast is scattering of the electron beam by the atoms of the specimen. As has already been discussed electrons

are more strongly scattered by denser or thicker objects, and as such a weaker BF signal will be detected directly in-line with such structures in the TEM images (resulting in darker regions of pixels). Contrast in TEM derived from these types of interactions is known as *mass-thickness contrast*. As long as mass-thickness is the dominant mechanism of contrast then the projection requirement is met, as thicker objects lead to weaker signal and *vice versa* (the signal is a monotonic function of mass-thickness). This will be the case for thin specimens made primarily of amorphous (*i.e.* non-crystalline) material.

There are, however, cases in which the projection requirement will not be met in BF-TEM. For strongly crystalline structures, diffraction of the electron beam by the crystal lattice will be stronger than scattering due to the thickness/density of the material. This so-called *diffraction contrast* is not directly related to the amount of material the electron beam passes through, and as such the projection requirement is not met. Methods of enabling tomographic reconstruction of objects that do not meet the projection requirement in BF-TEM have also been developed. A prominent example is Z-contrast tomography, which utilises a mode of TEM imaging known as annular dark field (ADF) [184]. In ADF mode, atoms of higher atomic number (also known as the *Z-number*) appear in greater contrast that 'lighter' atoms. For example, structures made of lead will appear much darker than structures made of carbon, regardless of how much thicker the carbon structure may be. This type of contrast formation does essentially fulfil the projection requirement, as contrast varies as a function of Z-number. Z-contrast tomography is particularly useful for studying metallic structures which would appear completely opaque in BF-TEM, and structures for which diffraction contrast dominates in BF-TEM mode [184].

3.3.2 - Tilt-Series Acquisition (with SerialEM)

The first step of tomographic reconstruction is to acquire the set of 2D projections from which the 3D volume will be produced. In ET this set of projections is produced by tilting the TEM specimen holder whilst acquiring images, and is known as a tilt-series. A tilt-series contains projections from different viewing directions, which present different 2D representations of the true 3D morphology of the object. To establish an axial system for describing the tilt-series, the TEM grid is considered the XY-plane and the direction of the perpendicular electron beam is the Z-direction/axis (see figure-3.5).

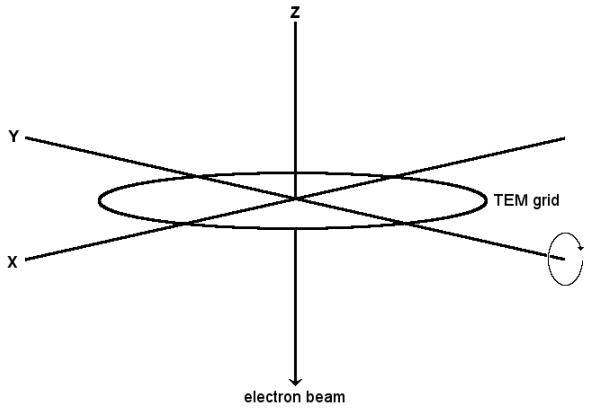
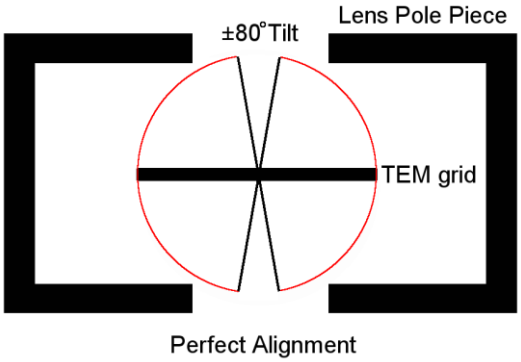
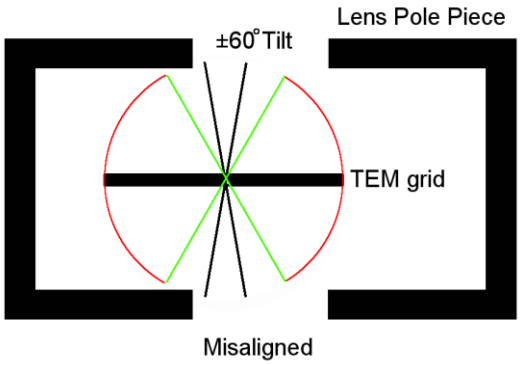


Figure-3.5: Diagram showing typical single-axis tilting, with denotation of axes used in this work.



(3.6a)



(3.6b)

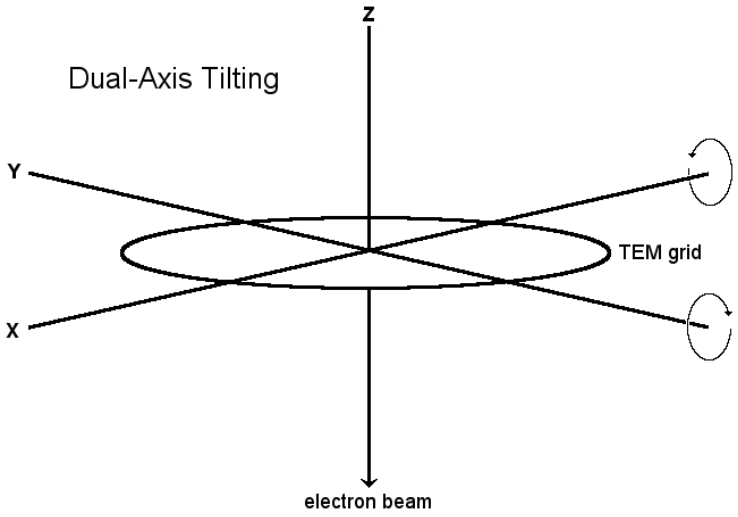
Figure-3.6: (a) showing ideal alignment of TEM grid within a microscope lens, where ±80° tilt-range is possible. (b) shows exaggeration of misaligned and limiting of tilt-range due to contact with lens material that would occur

A standard specimen holder for tomography tilts the TEM grid about a single, fixed axis in the XY-plane (see figure-3.5). Though the position of this *tilt-axis* in the XY-plane is arbitrary, for the sake of continuity it will be designated as the Y-axis. A standard tomography holder for TEM has a theoretical maximum tilting limit of ±80° tilt, but in most cases a ±60° tilt is the practical limit. The tilt-range is limited by the proximity of

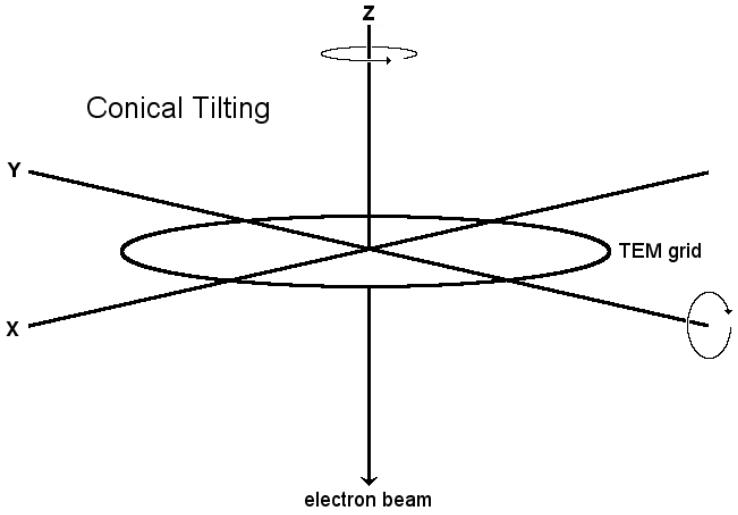
the TEM grid to the edge of the microscope that surrounds it, as the microscope cannot operate if contact is made. In theory, there is enough space for the TEM grid to complete a ±80° tilt within the objective lens of the microscope. Unfortunately, the slightest mis-alignment of the specimen holder or slightest bending of the fragile specimen stage will reduce the operational range to a maximum of ±60° in most cases. An illustration is provided in figure-3.6. The angle increment between subsequent tilt-series images can be varied according to the needs of the user, and is typically within the range of 1-10°. According to Fourier slice theorem, a greater angle range and smaller increments between images should result in a more accurate reconstruction. This is because such a tilt-series more closely adheres to the Fourier slice theorem, which describes a *complete set of projections*. In this regard more advanced schemes of tilt-series acquisition are possible, but require more specialised (and expensive) specimen holders and result in greater beam dosage to the sample due to the greater number of images acquired. *Dual-axis* tomography holders permit acquisition of two perpendicular tilt-series; both are in the XY-plane, rotated by 90° about the Z-axis with respect to one another. A dual-axis tilt-series thus samples a greater range of the *full set* of projections described in Fourier slice theorem. Another technique used to acquire a greater range of projections is so-called *conical tilting*. A conical tilt holder can be tilted in the XY-plane like a standard single-axis tomography holder, but also rotated 360° about the Z-axis. At chosen angles of tilt about the XY-plane, a full 360° tilt in the Z-axis can be performed, further increasing the 'completeness' of the tilt-series. The geometry of the tilt-series is an important consideration for so-called *missing wedge elongation*, an artefact of ET that acts to stretch the reconstructed volume in the Z-direction compared to the original object. This will be discussed in greater detail shortly (section 3.3.6). Details provided in this paragraph are taken from [185]. Illustrations of dual-axis and conical tilting are provided in figure-3.7.

The process of tilting the TEM grid to acquire the set of projections places constraints upon which structures on the grid are suitable. At high angles of tilt, structures of interest can become obscured by overlapping adjacent objects. Inclusion of other structures within the tilt-series will render them unusable past the point at which they appear. In particular, structures situated close to the edges of the grid bars can become obscured by the copper mesh at higher angles of tilt. An example of this is provided in figure-3.8, where visibility of the grid bars ruins contrast of the tilt-series images. Also, if structures are present in too high concentrations they can obscure one another. The transparency of soot nanoparticles under the electron beam means that it is often hard to tell whether

overlapping agglomerates are indeed individuals or part of a single larger structure, so high concentrations of sample on the grid are best avoided.



(3.7a)



(3.7b)

Figure-3.7: (a) diagram showing dual-axis tilting geometry, and (b) conical tilting geometry

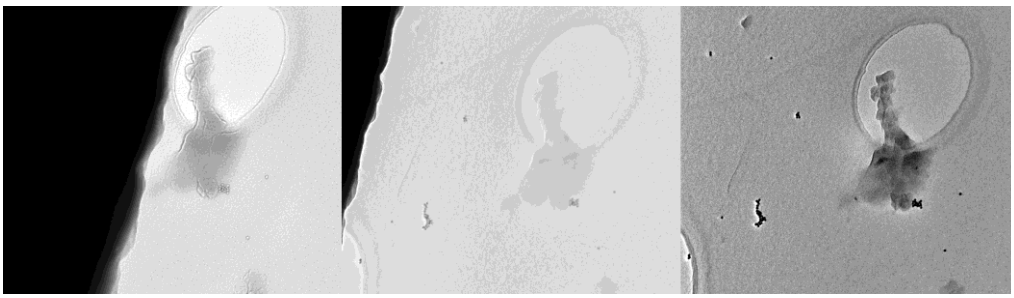


Figure-3.8: A sample of 3 TEM images from a tilt-series, increasing in angle from right to left. As angle increases, the copper bars of the mesh become visible and strongly distort the image contrast and quality

An additional consideration in tilt-series acquisition is alignment of the images. Due to the extremely small size of structures that can be studied with TEM, the mechanical limitations of the tilting mechanism can cause relatively large shifts in the image position to occur between tilt increments. While traditionally tilt-series were acquired by manually performing tilting, alignment and image capture at each increment there now exist software that can automate the process, for example SerialEM which was used in this work [173]. A key technique used to ensure good alignment in both the tilt-series is to add so-called *fiducial markers* to the TEM grid. Fiducial markers are easily identified reference points used to align the images, and in TEM gold nanoparticles are commonly used. Gold nanoparticles (Au-NPs) are approximately spherical, and can be produced with well-defined diameters in the range of 5 to 100+ nm. Gold is extremely dense and is not transparent to the electron beam, thus appearing completely opaque in BF-TEM images. This combination of well-defined size and shape, and high-contrast appearance makes them ideal for use as fiducial markers. The gold nanoparticles can be automatically tracked by tilt-series acquisition software and used to approximately align images in the tilt-series. They are also tracked in the computational reconstruction process, and used to produce more the finely aligned tilt-series used to create the 3D volume (see section-3.3.3). An example of gold nanoparticles in a TEM image is given in figure-3.9.

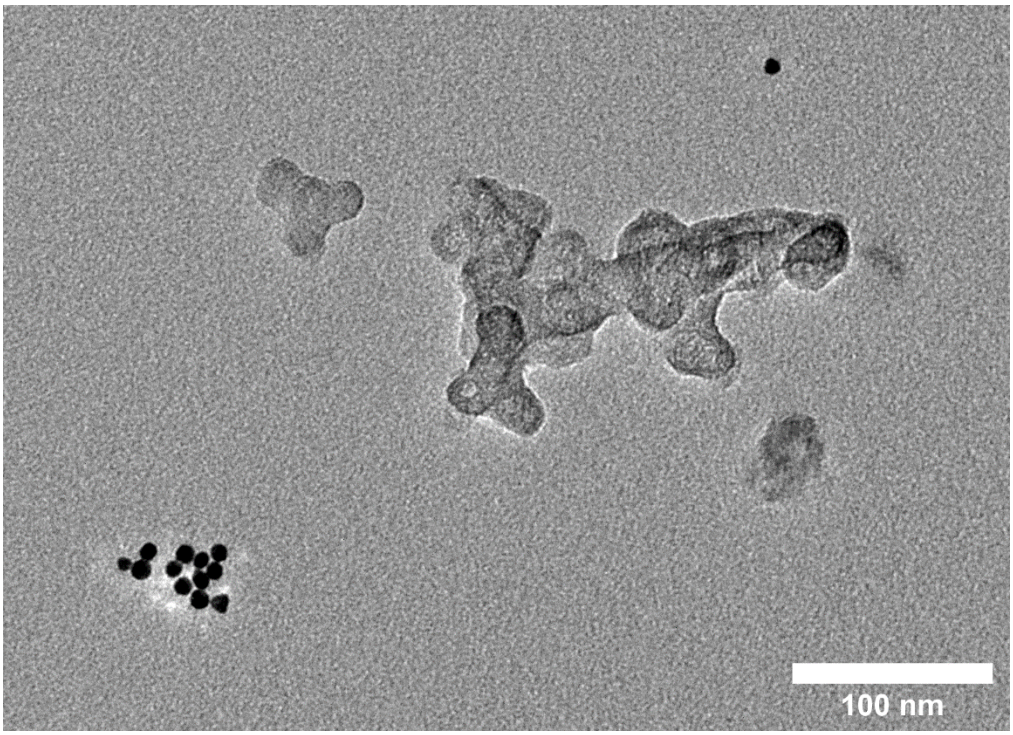


Figure-3.9: BF-TEM image showing a cluster of gold nanoparticles to the lower-left of two soot nanoparticles (one large, and one very small). A single gold nanoparticle is visible to the upper-right of the image.

Once suitable particles have been found, the tilt series of images can then be collected. Single-axis tilt series can contain as many as 100-200 images, and take up to an hour to complete depending on the tilt-range and increment sizes. The large number of images required exposes the soot samples to high beam dosage, which can be problematic for soot-in-oil samples. Residual oil can cause severe contamination of the image, obscuring regions of interest [41], meaning quality tomographic reconstruction is no longer possible. As such, high-quality sample preparation on the TEM grid is of great importance for tilt-series acquisition. TEM grid preparation is discussed in more detail in a later section of this chapter (section 3.5.2).

Tilt-series files are exported from SerialEM as*.*mrc* image stacks (given the extension *.*st* by SerialEM). The *.mrc file type is the standard in ET for storing tilt-series and tomograms, and is named after the Medical Research Council UK lab in which it was developed [186]. Details of the scale of the images, approximate size of the fiducial markers, and angle of the tilt-axis are required. These can be retrieved automatically from files produced by SerialEM, otherwise must be entered manually. The approximate range and increment size of the tilt-series must also be entered. Etomo offers functionality to exclude specific images of the tilt-series from the reconstruction, which can be useful if some kind of error or corruption has occurred

As mentioned earlier, tomographic reconstruction is performed in Etomo. The details of the ET procedure with this software will be provided in the following sections.

3.3.3 - Tilt-Series Alignment in Etomo

The first step of the computational reconstruction process is to load the tilt-series files into Etomo. The software is able to read image stack files in various formats, including *.*tiff*, *.*mrc*, *.*st*, and *.*dm3* (the native file-type of Digital Micrograph). Etomo is able to perform dual-axis reconstruction as well as standard single-axis reconstruction. Details must be entered for the scale of the images, the approximate angle of the tilt-axis, size of the tilt-range, and increment between images.

Prior to the computational reconstruction, the images of the tilt-series must be finely aligned. As mentioned earlier, mechanical imperfections of the TEM machinery and limitations of the automated tracking in SerialEM mean that the original tilt-series images are not perfectly aligned. Alignment of the tilt-series is key to achieving high-quality tomographic reconstruction. Reconstructions from a misaligned tilt-series will be subject to significant blurring of the structures of interest, a significant problem when the goal is quantitative morphological characterisation.

First, an automated cross-correlation is used to calculate an estimate of both the angle increment and XY-displacement that occurs between each pair of images in the tilt-series. Cross-correlation determines the degree of similarity between pairs of images, essentially comparing the colour values of each pair of corresponding pixels. The displacement between images is determined by shifting the images relative to one another to maximise similarity. After the displacement in the XY-plane and tilt-axis have been determined, the images are then shifted by the appropriate amount into an improved alignment.

Alignment of the tilt-series is then further refined by tracking of the Au-NP 'fiducial markers'. In the un-tilted image of the tilt-series the user must identify gold nanoparticles to be tracked. In Etomo the selection of nanoparticles can be performed either manually or automatically, and the Etomo guide suggests at least 8 fiducial markers for a good alignment. Though theoretically more markers will result in a better alignment, it risks a lengthier process due to inaccuracies in automated tracking that need to be corrected manually (see next paragraph). Practice with Etomo throughout this project has indicated that as few as 5 nanoparticles results in acceptable alignment. An ideal selection of fiducial markers is distributed as evenly as possible around the structure of interest. Due to the movement of the background film that occurs with tilting, fiducial markers towards the edge of the field of view (FOV) may not be visible at higher angles of tilt. Additionally, those close to adjacent structures may become somewhat obscured at high tilt-angle, though generally the denser gold will be visible through semi-transparent carbon matter (this can be seen in figure-3.9). Due to these constraints, it was generally easier to manually locate nanoparticles to ensure an ideal distribution and minimal corrections. The chosen distribution for the flame-generated particle studied in chapter 4 can be seen in figure-3.10. Note the non-ideal arrangement of the Au-NPs around the soot structure of interest due to uneven distribution and overlap of gold and soot. Despite this, alignment was successful with no major issues.

Once identified, fiducial markers are tracked through all the images of the tilt-series. Based on the approximate alignment from cross-correlation, fiducial marker position is predicted by Etomo. In instances of large shifts between subsequent images or obscuring of nanoparticles by adjacent matter, this tracking may be inaccurate as the predicted position is too far from the real nanoparticle position. The user must then manually correct positions until all nanoparticles are accurately located in all images of the tilt-series. Typically, picking and then tracking/correcting 5-10 fiducial markers through 121 images of a tilt-series requires <10 minutes of direct interaction from the user, per tilt-series.

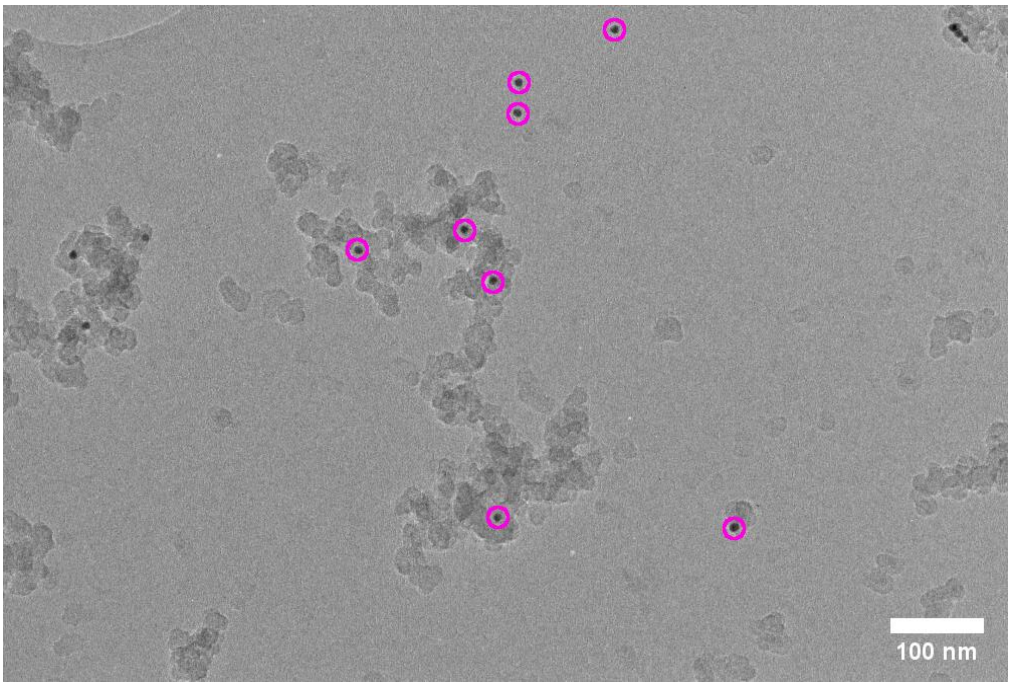


Figure-3.10: Choice of gold nanoparticle makers for alignment of a tilt-series. Note that 4 of the gold makers are visible through the main soot nanoparticle.

So-called markerless alignment methods also exist, though were not used in this work. These methods employ existing features on the grid as fiducial markers, rather than rely on additional materials such as Au-NPs [187]. For soot, the low contrast of carbon-on-carbon makes tracking of features too inaccurate.

3.3.4 - Tomographic Reconstruction: the Computational Step

Once a finely aligned version of the tilt-series has been created, the computation can be performed to extract the 3D information. Though the original theory underpinning tomography calls for an inverse Fourier transform to be applied to the tilt-series data, in practice this is not always carried out. In many applications, the data set of the 2D projections is too large to be efficiently computed in terms of Fourier transforms. The most widely used reconstruction methods currently are instead based on *back-projection* and *iterative methods*. Both these subsets of algorithms consider the reconstruction problem in terms of 'real' space rather than 'Fourier space' [166].

Back-projection methods are considered to be a direct 'real-space' analogue of the Fourier method. Instead of considering the combination of the 2D-FTs of the projections to create the 3D-FT of the object, back-projection considers direct combination of the projection images to create a 3D volume containing the object. One of the simplest and

most widely used methods is known as weighted back-projection (WBP), and will be used as an example to describe how back-projection reconstruction works.

To help understand back-projection, it is useful to recall the projection requirement for tomography; that the input data for tomographic reconstruction were true projections. This is true in the case of BF-TEM of non-diffracting samples, and means that thicker/denser objects appear darker in the projections and *vice versa* with lighter objects. In BF-TEM, the electron beam passes through the 3D structure of the specimen, and creates a 2D projection on the detector screen. In back-projection this process is effectively reversed; rather than projecting through a 3D object onto a 2D screen, the 2D signal is spread back through an empty 3D volume. A simplified version in *(n-1)* dimensions is given in figure-3.11. The images of a tilt-series are arranged around the empty volume according to their angle of acquisition, and their content is back-projected through the volume at that angle. Because the TEM images met the projection requirement, when the back-projections coincide with one another in the prepared volume they rebuild the original structures; darker regions in the projections superimpose to create darker regions in the 3D volume, and similarly lighter regions superimpose less strongly.

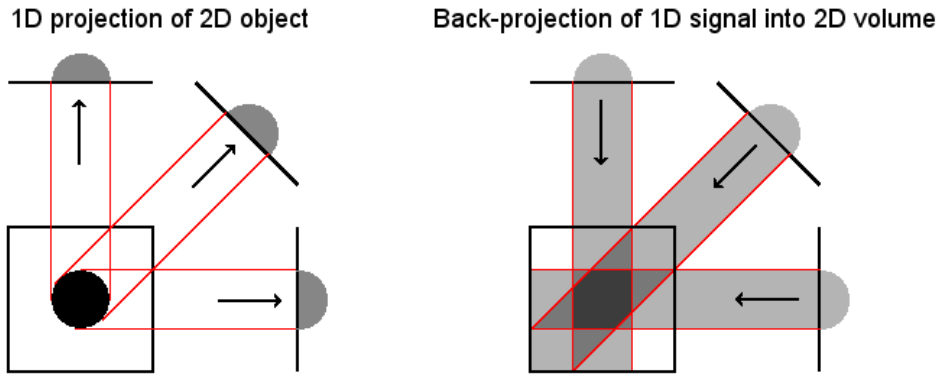
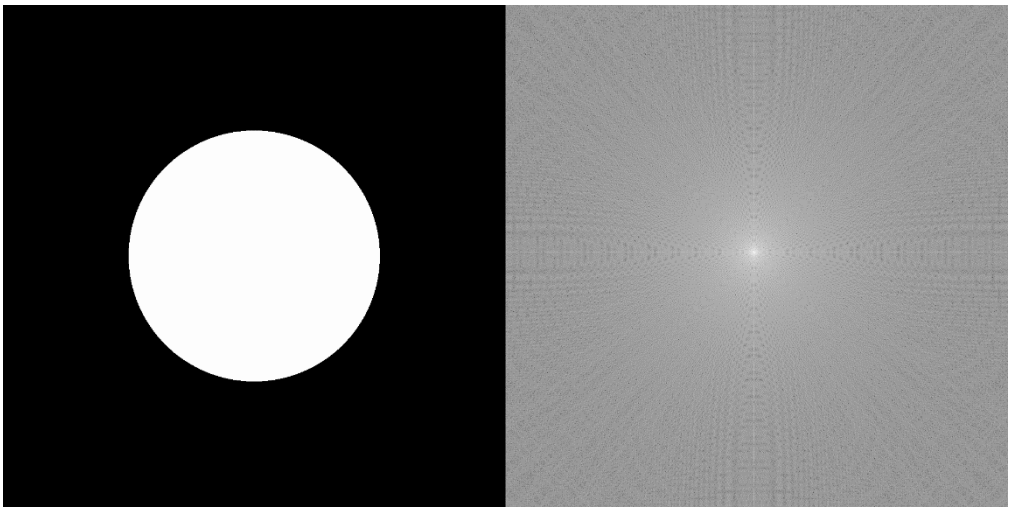


Figure-3.11: A simplified 2-dimensional representation of back-projection. The left image shows the forward projection (imaging), and the right image shows the back-projection (reconstruction)

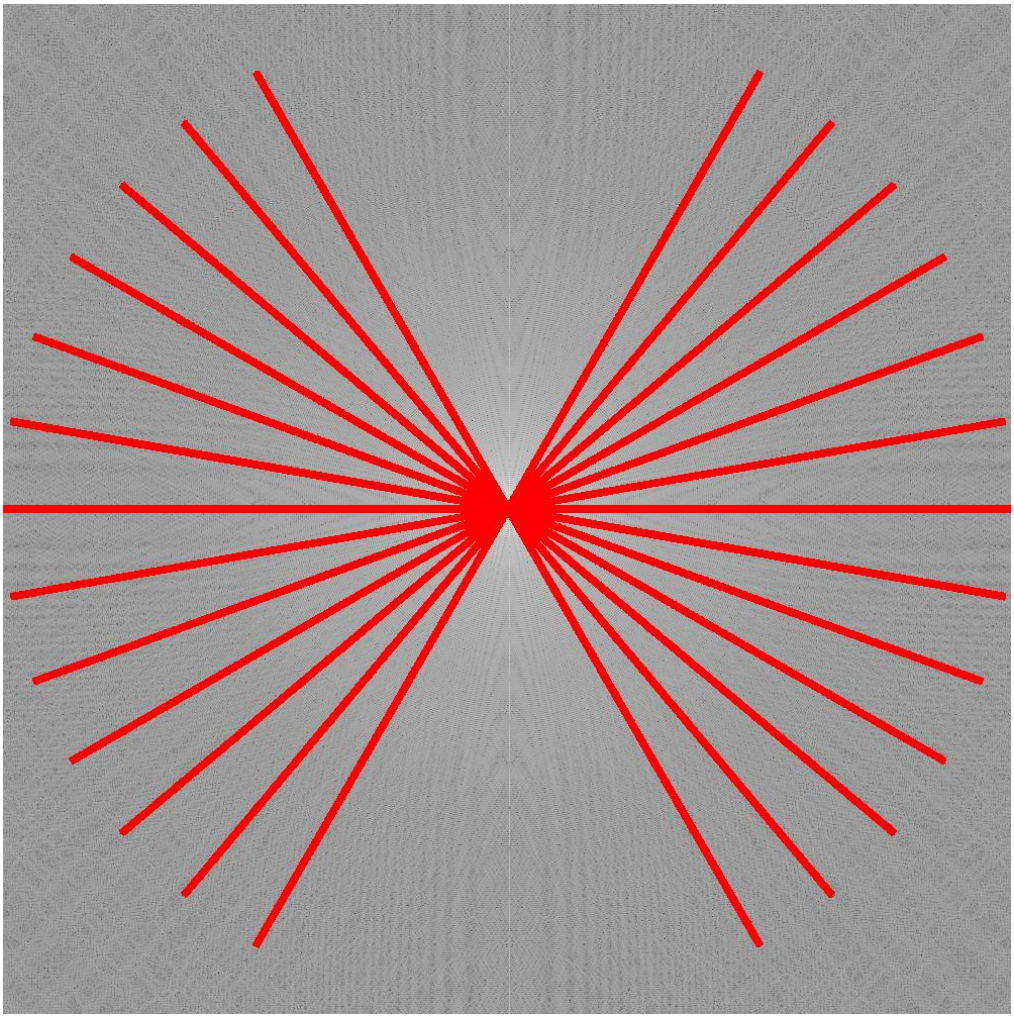
What results is a 3D volume that is *completely* filled with the overlapping back-projections, and this is known as a *tomogram*. However, as the name suggests the back-projection is not the only part of the process. A weighting (sometimes also described as *filtering*) is an additional process that is required to reduce blurring in the tomogram and ensure that the edges of the object can be distinguished. Blurring in simple back-projection (*i.e.* without filtering or weighting) is inherent, and it relates back to the Fourier slice theorem. Towards the centre of the 3D-FT, the vectors that represent the

2D projections are more closely packed and cover a greater proportion of the space in the FT. This is represented in 2D in figure-3.12. Further from the centre the slices diverge, and they less completely sample the space of the FT. In the Fourier domain, the central areas represent the low frequencies, and the outer areas represent the higher frequencies. Therefore, our set of projections (unless the angular increment between them is infinitesimal) more densely sample the lower frequencies of the FT. The lower frequencies of the FT correspond to the smooth surfaces of the object, whereas the higher frequencies correspond to the sharper edges and details of the object. Thus, the combination of our back-projections will result in a highly blurred reconstruction of the original object, as the fine edges are underrepresented. Filtering or weighting is performed to reduce the blurring, and is achieved by applying a high-pass feature to repress the contribution of the lower frequencies. The high-pass filtering is performed on the FTs of the projections *via* a ramp filter, and so the overall order of the WBP process is as follows: Acquire 2D projections, create FTs of projections, filter FTs, inverse FT to produce filtered projections, back-projection into empty volume, production of tomogram.

Iterative reconstruction is another branch of the widely used real-space reconstruction methods. While usually more computationally expensive than back-projection, these methods can be more effective when the quality and quantity of projection data is limited. The general principle of iterative reconstruction is that first, an estimate of the tomogram is produced. The 3D tomogram data is projected back into 2D to simulate the original projection data (*i.e.* the tilt-series images). The simulated and original projection data is compared, and the error between them is used to refine the tomogram. This process is repeated in an iterative process in order to minimise the difference between the real and simulated projection data. Different iterative techniques employ different schemes by which to refine the tomogram and minimise the difference between the projections. One of the most widely used versions is the simultaneous iterative reconstruction technique (SIRT). In the limit of infinite iterations, the SIRT method is in theory perfectly accurate. The SIRT method includes the equivalent of two back-projections per iteration, and as such SIRT reconstruction with 10 iterations would be expected to take around 20 times longer than WBP reconstruction [166]. General descriptions of back-projection and iterative methods were made using a combination of information from the works of Fernandez [166, 183], Frank and co-authors [165], and online materials from the creators of the ASTRA toolbox [188, 189]



(3.12a)



(3.12b)

Figure-3.12: A 2-dimensional representation of the relative sampling of high and low frequencies in the FFT of a 2D object. Above shows a 2D circle and its FFT. Below shows the same FFT image with vectors superimposed to represent a typical ±60° tilt-range. Note how towards the centre a greater proportion of the image is covered by these vectors

Other iterative methods, such as algebraic reconstruction techniques (ART), are also fairly common. In its simplest form, ART differs from SIRT as it updates the tomogram by considering only a single simulated projection per iteration, rather than the whole set of projections simultaneously [190]. In practice this method is quicker, but exact reconstruction in the extent of infinite iterations is no longer guaranteed. This is because poor quality input data can skew the resulting tomograms. A recently developed algebraic method is known as the discrete algebraic reconstruction technique (DART) [191, 192]. This method incorporates prior knowledge of the grey-levels of the different components of the original object. DART then guides the reconstruction towards only containing these discrete grey-levels by performing segmentation in each iteration. Across subsequent iterations, homogeneous regions of the tomogram are retained, and reconstruction focuses on refining the borders between them. This method was assessed to produce superior results for several datasets, though a pre-requisite is the existence of discrete grey-levels within the specimen. As both soot nanoparticles and the supporting graphene oxide film are primarily carbon in nature, their appearance under the electron beam is very similar. This means we are unable to assign discrete grey-levels to the components of the image (e.g. soot and background film) and this method would not be suitable for our samples. Other examples of advanced reconstruction algorithms, again unsuitable for soot study, can be found in the works of Goris [193] and Chen [194].

Regardless of the method used, the final result of tomographic reconstruction is the tomogram. This is a filled 3D volume that contains information on the structure of the original object. However, as the TEM projections of the tilt-series contain both the structure of interest and the background support material, the background supporting material is also present within the tomogram. As such, the structure of interest must be 'sculpted' from the tomogram in a process known as segmentation.

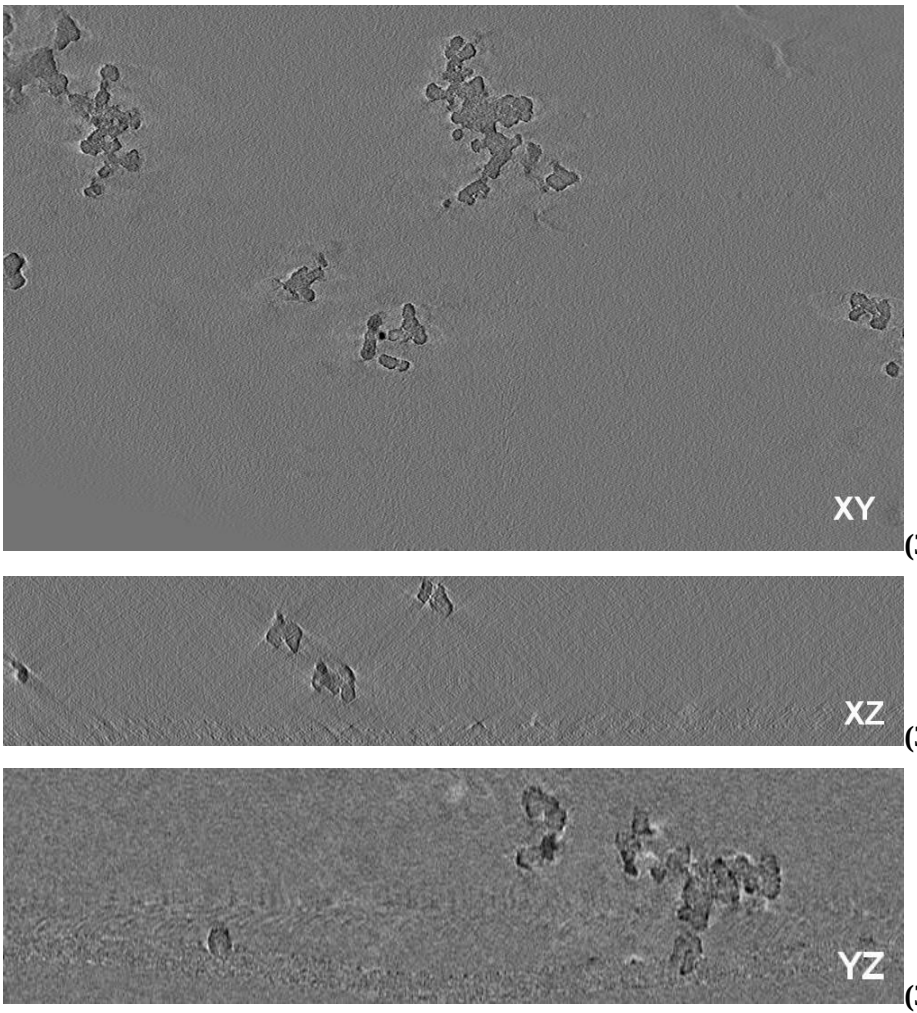
3.3.5 - Tomogram Segmentation: Producing the 3D model

To enable quantitative analysis of 3D-TEM data, models of the structures of interest must be created from the bulk tomogram data. Segmentation is the process by which the voxels of the tomogram that correspond to particle matter are defined from those that represent the background or adjacent structures. The combination of all particle voxels result in a 3D model that can be characterised in terms of its morphology. This step is extremely important as the accuracy of segmentation directly determines the morphology of the produced 3D models. Tomograms are produced by Etomo in the

form of image stack files, and these can be handled in image processing software such as ImageJ. They may also be directly 3D rendered in appropriate software, though will require some level of transparency to be applied to the *voxels* (the 3D equivalent of pixels) else will appear only as an opaque polygon.

Segmentation is usually performed by arranging the tomogram into a series of 2-dimensional slices, rather than handling it in 3D. Each slice of the tomogram will be 1 voxel thick in the 3rd dimension, though the user can choose which of the principle axes is considered the *3rd dimension*. The tomogram can be viewed either top-down (observing the XY-plane), or side-on (observing either the XZ- or YZ-plane). Generally, the top-down approach offers the most intuitive representation of the tomogram. Due to the typical scale of soot structures and the size of the TEM camera, the Z-depth of the tomogram is usually the smallest dimension, so the top-down approach also considers the fewest individual slices. An example of different viewing schemes is given in figure-3.13.

To create a 3D model, every single 2D slice of the tomogram must be segmented. Depending on the size of the tomogram and the complexity of the structure of interest, this can potentially be extremely time consuming. High resolution tomograms of large structures can be several hundred slices thick, and the task is effectively the equivalent of several hundred individual particle characterisations *via* 2D-TEM. Ideally this task would be handled automatically, though in practice the only widely applicable technique is manual segmentation *via* image processing software. While production of automated tomogram segmentation methods is not unknown [195-197], these tend to be produced on an *ad hoc* basis by research groups for their particular samples of interest. A generally applicable automated segmentation method does not yet exist as the appearance of tomograms is too strongly variable, and generally possess a low signal to noise ratio (SNR) [166].



(3.13a)

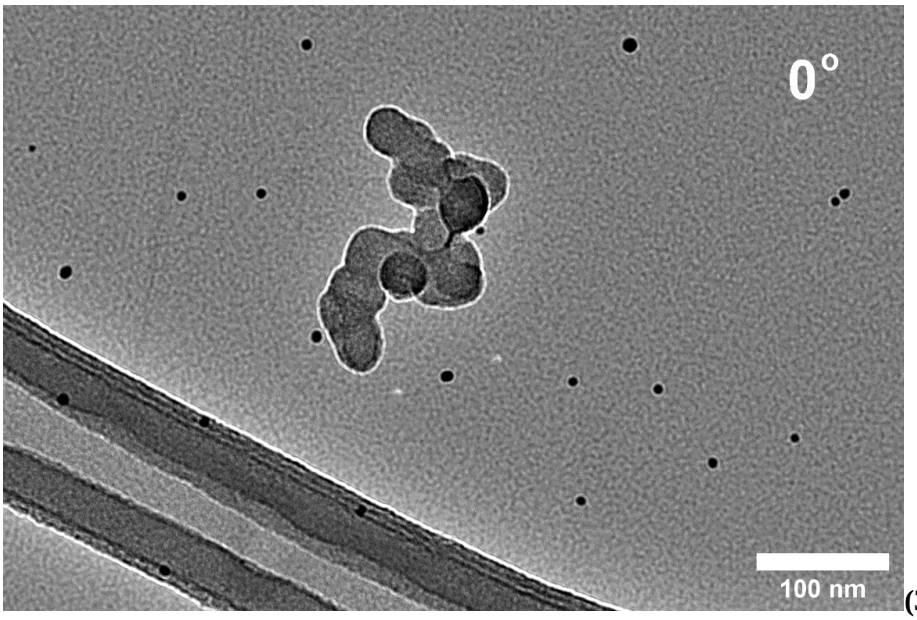
(3.13b)

(3.13c)

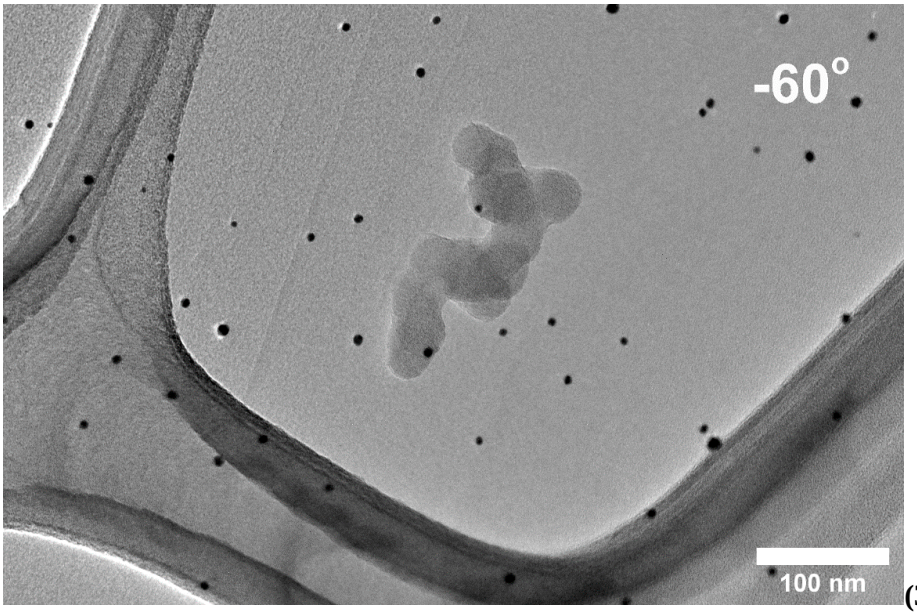
Figure-3.13: Example of the differences in visual appearance of a tomogram when viewing (a) the XY-plane, (b) the XZ-plane, and (c) the YZ-plane. Note the visibility of fanning effects in the XZ-plane view.

The appearance of tomograms depends on the quality of the input data (the tilt-series), and the propagation of reconstruction artefacts. Together these two factors govern contrast, noise, edge definition/blurring, and extent elongation and fanning effects in the tomogram. Standard TEM images of soot are subject to strong variation depending on factors such as the cleanliness of samples, size of soot nanoparticles, TEM operating voltage, thickness of the TEM support film, and quality of the TEM camera. While in some instances soot may be defined quite clearly from the background material, in other cases they may be hard to distinguish from parts of the carbonaceous support film. Appearance of TEM projections can also vary through the tilt-series due to the change in thickness of the specimen at high angles. An example of variability in TEM appearance of the same soot nanoparticle within a tilt-series is provided in figure-3.14. To some degree, the quality of the tilt-series limits the quality of the tomogram. However, these effects are also acting in combination with the reconstruction artefacts

that arise due to the algorithms used and also the missing wedge (discussed in the next section, 3.3.6). The effect of tilt-series acquisition scheme, increment between images, tilt-range *etc.* will all affect the degree of reconstruction artefacts such as fanning, blurring, and missing-wedge elongation. As such, tomograms are subject to strong variability in their appearance even for similar samples, meaning manual image processing is often the only easily applied segmentation methodology.



(3.14a)



(3.14b)

Figure-3.14: (a) showing the un-tilted (0°) TEM image of a soot nanoparticle, and (b) showing the -60° image from the same tilt-series

Manual segmentation through image processing software such as ImageJ/Fiji is carried out in exactly the same way as for 2D-TEM characterisation of soot. Usually, a brush tool is chosen to highlight pixels that are defined from the background by their darker

colour (lower grey-level). An additional difficulty of tomogram segmentation is that only a cross-section of the entire structure is visible. As such, in the presence of numerous adjacent structures it can be difficult to identify darker regions that *only* pertain to the structure of interest. Complex 3D structures mean that connected regions in 3D are not always clearly connected in 2D, and this issue is usually most prominent towards the bottom of the tomogram near to the TEM support film. This issue can increase the likelihood of errors, and increase the time that is required to create an acceptably segmented tomogram.

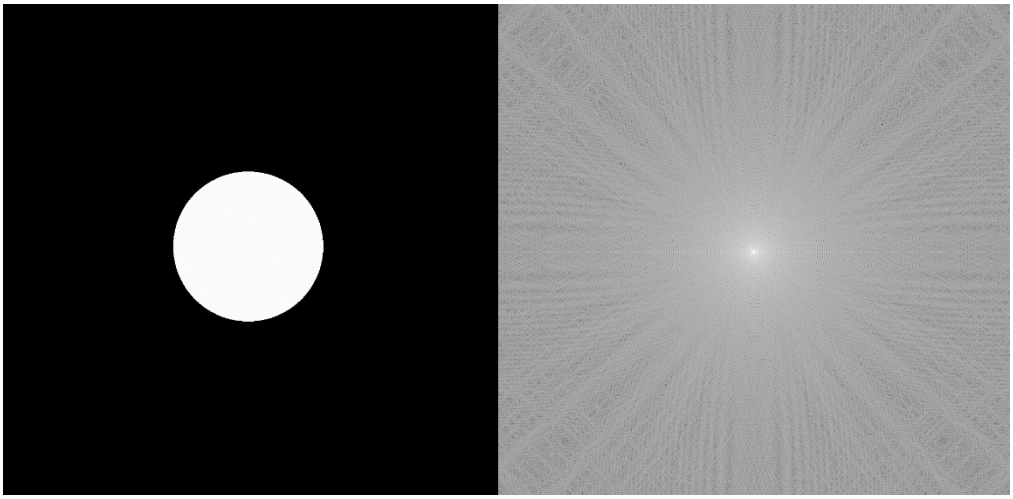
Once all individually slices of the tomogram have been segmented, the results are combined. The standard procedure is to binarized each slice, so that all voxels relating to the particle are white, and all other voxels are black. Binarized 8-bit image stacks can then be used directly as 3D models files, though they can be trimmed to reduce the amount of blank information in the files in the slices.

3.3.6 - Errors of ET: Missing Wedge Elongation

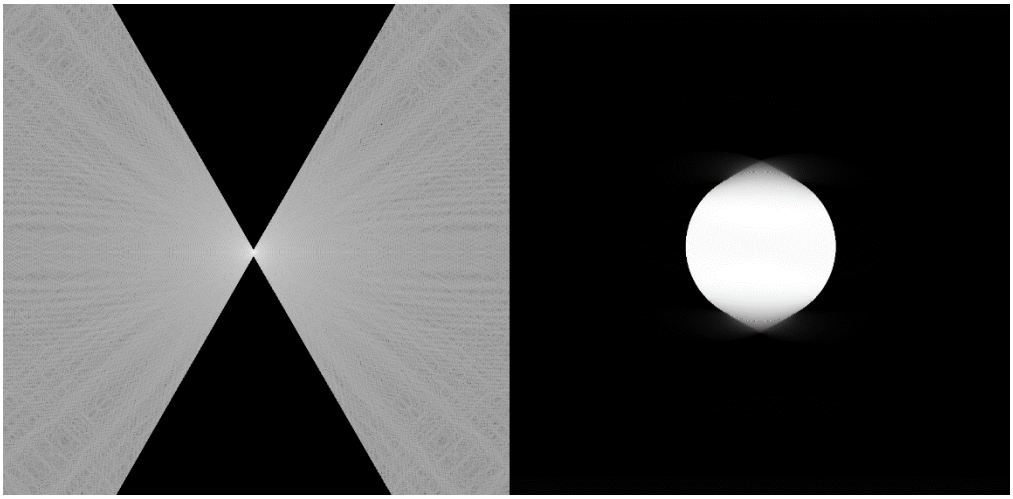
As described earlier, the appearance of the tomogram is highly dependent upon the input data and reconstruction method used, and is susceptible to poor image quality in the form of noise, low contrast, and blurring. One of the most important sources of errors and image degradation in tomographic reconstruction are image artefacts relating to the so-called *missing-wedge*. The term 'missing wedge' refers to the fact that real tilt-series data does not fulfil the requirements of Fourier Slice Theorem in almost all cases. While Fourier slice theorem describes a *full set of projections*, the reality of TEM image acquisition is generally a ±60° range of images acquired over a single tilt-axis. When presented graphically (figure-3.15), a typical single-axis tilt range only partially samples the full range of projection angles, leaving a wedge-shaped gap in the direction of the electron beam.

If we consider this in terms of the 3D-FT of the object, we do not possess information on how the object appears in the Z-direction. The consequence is that during reconstruction the information that we *do* possess gets spread out through the regions of space where we *don't* possess information; this occurs perpendicular to most extreme angles of the tilt-series. Essentially, at each point in the tomogram the information ceases at the limits of the tilt-range, and the back-projection rays continue to travel through the tomogram volume perpendicular to this angle. This effect is most prominent where the back-projection rays are stronger (*i.e.* corresponding to particle matter rather than background), and interference of these rays can cause dark patches to occur in

regions where particle matter does not truly exist. Within the bulk of a particle, these erroneous back-projection rays are not prominent as they as masked by the strong *real* back-projection interference. However, at the very extents of the particle in the direction of the missing wedge, these effects become apparent as they are present amongst weaker interference of background materials back-projection rays. In appendix section-A.1, these effects are observed to be more prominent when applied across greater areas, *e.g.* where the object is broad and smooth at its outermost extent in the Z-direction. For structures that terminate in complex or sharp points in the Z-direction, the missing wedge applies only over a small area and so the overall elongation is small.



(3.15a)



(3.15b)

Figure-3.15: Graphical representation of a missing wedge in 2D, and associated elongation. Above images show 2D circle and its FFT. Below images show deletion of missing wedge from the FFT, and subsequent elongation to the circle when an inverse FFT is performed. Note these figures are repeated in appendix section-A.1.

The propagation of these errors can also be observed when viewing a tomogram from different planes, as in figure-3.13. The reason for this is that although the XY-plane is viewed in TEM images, in single-axis reconstruction the tilt-axis is only along the Y-axis. As such, there is asymmetry in how the 3D FT of the object is sampled in X and Y. When viewing the XY-plane (top-down), the fanning effects primarily occur horizontally through the slice, perpendicular to the Y-axis. When viewing the XZ-plane the profile of the missing-wedge can most clearly be seen as the view is along the tilt-axis. Both fanning effects and Z-elongation are most prominent from this direction, and in figure-3.13b the 'X' shape of the tilt-series limits can be seen around the edges of the particle matter. From the YZ-plane view, the fanning effects propagate along the vertical axis (Z-axis in absolute terms) but are not particularly clear to see.

Other sources of error in ET reconstruction include the variable quality and anisotropy of images of the tilt-series, which slightly alters the nature of the projections of the 3D structure. Even in the case of very small or no missing wedge, errors could arise from interference of back-projection rays that does not represent the real structures. This could, for example, be caused by the fact that high tilt-angles require the electron beam to travel through more material, altering the contrast and resolution in comparison to untilted or low-angle images.

3.4 – Soot Samples and Preparation for TEM

Two samples of soot were studied in this work: a flame-generated (FG) soot, and a soot-in-oil sample extracted from a gasoline turbo direct injection (GTDI).

3.4.1 – FG Soot

The first soot sampled studied was a case study of a single FG soot nanoparticle. This sample of soot had already been prepared for TEM prior to the start this PhD project, and at no point are conclusions or insights drawn on the nature of its formation. Further details on this sample are provided in chapter-4.

3.4.2 – GTDI Soot-in-Oil

Used lubricant oil was drained from the sump of a modern 1.4 L 4 cylinder GTDI engine. This engine was equipped in a passenger vehicle operating under real driving conditions in primarily urban and extra-urban environments, with cylinder deactivation enabled. The oil used was a 5W-30 grade fully formulated synthetic oil (FFO). The soot-laden oil was sampled after a period in which the vehicle covered 20,284 km. Thermo-

gravimetric analysis (TGA) was used to determine soot concentration in the used oil, which was found to be 0.56 % by weight (details of the TGA protocol used are provided at the end of this chapter, section-3.5.3).

Prior study of both diesel and GDI soot-in-oil with TEM had been carried out by members of the Nottingham Powertrain research group [40, 41, 70, 198]. The typical sample preparation methods have been described in those works, but is also provided here for clarity. Soot-in-oil samples are challenging for TEM study as lubricant oil is known to be a severe contaminant under the electron beam [40]. The high-energy electron beams essentially destroys the long-chain polymers present in the oil producing a haze of amorphous carbon material that obscures structures of interest.

In the past centrifugation has been employed to remove oil from the soot [68], though prior work has revealed that such methods change the morphology of nanoparticles [70]. Aggregate size was observed to increase after centrifugation as measured by particle sizing methods. As such, gentler methods of oil removal were sought. This was achieved by performing dilution of the oil in heptane. Lubricant oil is soluble in heptane due to their compatible low polarities, and the solvent is much less viscous and possesses a much lower boiling point. This acts to remove oil adsorbed onto the surface of the soot by dilution and subsequent evaporation.

Dilution of oil in heptane is generally performed in ratios of 1:20 to 1:60, depending on the concentration of soot in the oil. Only very small quantities are required for deposition onto the TEM grids, typically < 50 μL, so only a small amount of oil needs to be collected. Gentle agitation of the used oil is carried out prior to dilution in case of any settling. Previous work has observed that appropriate levels of dispersant in fully formulated lubricant oils maintain soot size distribution for as long as 12 months [118].

Deposition of soot onto the TEM grid was performed using 10 μL micropipette, with a maximum droplet size of 5 μL to prevent oversaturation of the grid. Several droplets of the diluted oil sample are typically deposited onto a TEM grid, where they are allowed to sit for a short while before wicking away of the liquid with filter paper. The sample is wicked away rather than allowed to evaporate as the drying of the droplets will drag the particulate matter of the sample together. Wicking helps to prevent oversaturation of small areas of the grid with particle matter.

Further removal of oil contamination is carried out by ‘washing’ the TEM grid with several droplets of diethyl ether. This solvent is extremely volatile, and so wicking of the liquid is carried out immediately after deposition to prevent drying effects. Typically, 5-20 μL of diethyl ether washing is performed.

TEM grids are further prepared by exposure to a high-vacuum at approx. $1x10^{-6}$ Bar. The nmRC at Nottingham possesses specific equipment for the low-pressure pumping of TEM specimen holders. Ideally, this is carried out for at least several hours prior to TEM imaging. The preparation of soot-in-oil samples for TEM imaging is summarised in figure-3.16.

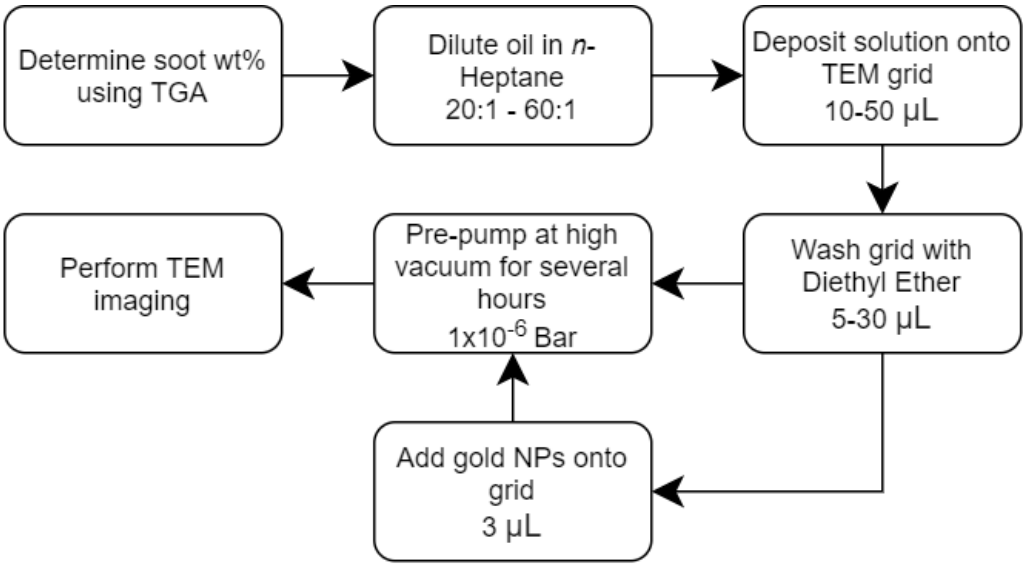


Figure-3.16: Flow chart representing typical preparation of soot-in-oil samples for TEM imaging

Due to their nanoscopic size, deposition of soot nanoparticles onto the TEM grid is largely uncontrolled. Although the exact same experimental procedure may be carried out, grids produced may be of varying quality in terms of soot concentration. Oil samples with such low soot percentages are particularly difficult to prepare, as weaker dilutions are required to provide sufficient quantity of soot onto the TEM grid. However, weaker dilutions mean that oil is less effectively removed from the soot nanoparticles and thus the samples are more prone to beam damage occurring. In turn, this requires greater amounts of washing with diethyl ether, and so it becomes more likely that soot material can be washed off the support film. This can lower the concentration of soot on the grid to the point where location of nanoparticles becomes very difficult and time consuming.

To some degree trial-and-error preparation of TEM grids is required, but prior knowledge of soot concentration in the oil *via* TGA is extremely useful for helping guide the choice of an appropriate dilution ratio. The concentration measurement provided by TGA was used to guide use of a 1:30 dilution in heptane.

The final grid preparation protocol used for the GTDI soot-in-oil sample in this work was:

- dilution in heptane at 1:30 (0.5 mL oil to 15 mL solvent)
- deposition of 30 μL of diluted oil onto the TEM grid (with wicking)
- washing with 15 μL diethyl ether to further remove oil contamination (with wicking)
- exposure to high vacuum (approx. $1x10^{-6}$ Bar) for several hours prior to TEM imaging

3.4.3 – Thermo-gravimetric Analysis (TGA)

Soot concentration in the used oil was measured using thermo-gravimetric analysis on a TA Instruments Q500 analyser. The methodology was adapted from the ASTM D5967-08 test standard and has previously used by members of the Nottingham Powertrain research group [142]. A platinum TGA pan was dosed with 20 μg (±0.5 μg) of used oil and loaded into the analyser. Nitrogen gas was used to purge the combustion chamber of oxygen prior to analysis. All gas flow-rates were set to 100 mL min^{-1}. The sample was held under nitrogen at room temperature for 20 minutes before heating to 50 °C at a rate of 5 °C min^{-1}. After a short isothermal stage at 50 °C, the sample was again heated at a higher rate of 50 °C min^{-1} until the chamber reached 550 °C. Heating rate was then decreased to 20 °C min^{-1} and continued until the chamber reached 650 °C. Up until this point, the high temperature in the chamber has removed all volatile material, including oil and fuel traces, through evaporation, but the solid phase of the oil (soot and ash) remains. The use of inert flow gas means that the soot is not combusted. After the temperature reached 650 °C, the gas flow was switched from N_2 to air and heating continued at 20 °C min^{-1-} until a final temperature of 750 °C was reached. This period of high temperature and continued heating in air allows the soot phase to combust. The balance of the TGA records the change in mass of the sample over time, and the rapid mass loss that occurs alongside the N_2/air switchover is used to determine weight percentage of soot in the oil. Once reaching the final temperature, the sample is held at 750 °C for 5 minutes before the test concludes and the chamber temperature is reduced to room temperature. For the GTDI soot-in-oil sample used in this work, soot concentration was determined as 0.56% by mass.

3.5 - Morphological Characterisation of Soot

The purpose of TEM and ET study of soot in this work is to permit morphological characterisation of the soot nanoparticles. As mentioned, calculation of morphological parameters was carried out using Fiji. This section details the methods used to calculate the parameters considered in this work.

3.5.1 – 2D-TEM Morphological Characterisation

Based on soot morphological studies found in the literature, the following parameters were measured from 2D-TEM images in this work: projected area (A_p), number of primary particles (N_p), Volume (V & Vol), surface area (SA), radius of gyration (R_g), fractal dimension (D_f), circularity (circ.), Feret diameter, and primary particle diameter (d_{pp})

The initial step of 2D characterisation is segmentation of particles from the TEM background, carried out manually in Fiji. This isolates pixels representing the particle from those of the background, and is used to measure the area occupied by the nanoparticle as well as certain shape descripting measurements. An automated process for 2D-TEM image segmentation is described in chapter-6.

In order to estimate the number of primary particles comprising the nanoparticles, a mean primary particle diameter of the sample must first be determined. For the FG soot nanoparticle, this was measured solely *via* the images of the tilt-series. For the GTDI soot-in-oil sample, both tilt-series data and standard 2D-TEM images were used. Previously, Kondo *et al.* had considered the effect of the human operator on the uncertainty of 2D-TEM image segmentation, including measurements of primary particle diameter [39]. Experienced operators showed only a small degree of variation in their selections, with identification of primary particles only occurring where clearly visible. Where possible, the methods described in that work were followed. The values measured for the FG soot and GTDI soot-in-oil samples are discussed in chapter-4 and chapter-6 respectively.

Number of primary particles (N_p) was inferred according to the methods of Neer & Koylu [75] using equation-3.2, where A_p is the 2D area of the whole nanoparticle, and A_{pp} is the area that an average-sized spherical primary particle would occupy in a 2D projection. The pre-factor k_a, and exponent α take the values 1.15 and 1.09 respectively, and account for the unseen 3D extent of the particle. These coefficients were determined

by Koylu *et al.* based on 2D-3D morphology comparisons for a combination of simulated soot aggregates and real flame-generated soot [73]. Simulated aggregates were created to qualitatively mimic flame-generated soots from diffusion flames. Individual and pairs of primary particles were connected in random orientations, with no overlap. Aggregates were created with N_p = 20-1000, and were limited in terms of fractal dimension ($1.7 < D_f < 1.8$) to match prior experimental observations. Known N_p was compared to measured 2D area in order to derive the relation between them. Following this, real flame generated soot was imaged *via* TEM over ±45° range. Angled images were used to determine N_p by manual inspection, and compared against the 2D area. Close agreement was found between simulated and experimental data, leading to derivation of the constants in equation-3.2.

Simplified nanoparticle volume (V) [199], and surface area (SA_1) are estimated by multiplying N_p by the volume and surface area of the average-sized spherical primary particle (equations 3.3 and 3.4), with no primary particle overlap taken into account.

Surface area inclusive of primary particle overlap (SA_2) was also estimated based on the methods presented by Brasil *et al.* [154], and by Bau *et al.* [155]. In this methodology, a coefficient ($C_{ov,P}$) is measured for the overlap of primary particles in 2D-TEM projections (equation-3.5), where d_p is the average primary particle diameter, and d_{ij} is the distance between the centres of pairs of overlapping primary particles. From 60 measurements of our sample, the average d_{ij} was determined as 27 nm. An additional overlap coefficient, C_{ov}, is calculated *via* equation-3.6, where ζ_1 and ζ_2 are equal to 1.1 and 0.2 respectively. Finally, an estimate of 3D surface area is calculated using equation-3.7, where ϕ is an empirically determined constant equal to 1.3. For the GTDI soot-in-oil sample, equation-3.6 revealed C_{ov} as a small negative value, and was adjusted to 0 to cooperate with equation-3.7 for surface area (surface area should not be greater than the no-overlap value, SA_1). For the FG soot sample, the tilt-series images were not sufficiently high-resolution to calculate primary particle overlap. A value of 0 for C_{ov} results in both methods for calculating surface area being equivalent.

Radius of gyration (R_g) was determined *via* a pixel-based method demonstrated by, amongst others, Lapuerta *et al.* [157]. The distance from each pixel to the centre of mass is measured (r_i) and used alongside the total number of pixels (n_{px}) in equation-3.8.

Circularity was measured directly in Fiji based on area and perimeter values, according to equation-3.9. Circularity is used as a measure of complexity as it provides a value of 1 for a perfect circle, and values move towards 0 for a 1-dimensional line. Thus more

clustered soot nanoparticles possess higher values, and more complex and branched structures possess lower values.

Fractal dimension was determined using two methods. The first was the so-called box-counting or Minkowski-Bouligand method. This is a general purpose method developed for true fractal structures (such as the Sierpinski carpet). This method is common for fractal dimension measurements of individual soot nanoparticles [156, 200]. This method counts the number of boxes required to cover the area occupied by the nanoparticle as a function of the size of the boxes. A log-log plot of number of boxes against the reciprocal of the box size, for which the slope gives the fractal dimension. The choice of the sizes of boxes tested was guided by the work of Lottin *et al*. [156]. In this method, maximum box-size for accurate measurements is considered to be close to the scale of the irregularities of the structure. For a soot nanoparticle this is the primary particles, so maximum box-size is set equal to the primary particle diameter (20 nm). The minimum box-size in Lottin's work was around 10-20% of the maximum box size, and by also considering the suggestion of Wozniak [200] was set to 2 pixels (equivalent to around 10% of primary particle diameter in the scale of the tilt-series).

The second method used to calculate fractal dimension was a soot-specific iterative method developed by Lapuerta *et al.* [157]. In this method hypothetical arrangements of primary particles leading to extreme values of D_f (D_f=1 and D_f=3) were considered, and a curve was created to describe the D_f values of intermediate cases. A shape factor was included to better match the shape of the potential interpolation between extremes to that of experimental findings. There are several assumptions made in this method, including that all primary particles are considered perfectly spherical, and the 2D radius of gyration is equivalent to the 3D-R_g value. Primary particle diameter, radius of gyration, and area must also be taken from 2D projection as an initial step. As opposed to box-counting methods, the establishing of extreme conditions means this method does in fact attempt to provide a value for the fractal dimension of the 3D particle, using values measured from the 2D projections. For this work, a Matlab script to calculate D_f *via* this method was produced based on the description of the method provided in [157].

$$N_p = k_a \left(\frac{A_p}{A_{pp}}\right)^{\alpha} \quad \textbf{(3.2)}$$

$$V = \frac{\pi {d_p}^3}{6} N_p \quad \textbf{(3.3)}$$

$$SA_1 \approx N_p \pi {d_p}^2 \quad \textbf{(3.4)}$$

$$C_{ov,P} = \frac{d_p - d_{ij}}{d_p} \quad \textbf{(3.5)}$$

$$C_{ov} = \zeta_1 . C_{ov,P} - \zeta_2 \quad \textbf{(3.6)}$$

$$SA_2 = SA. \left[1 - \phi . C_{ov} . \left(1 - {}^1/_{N_p}\right)\right] \quad \textbf{(3.7)}$$

$$R_g = \sqrt{\frac{\sum_{i=1}^{n_{px}} {r_i}^2}{n_{px}}} \quad \textbf{(3.8)}$$

$$Circ. = 4\pi \left({}^{Area}/_{Perimeter^2}\right) \quad \textbf{(3.9)}$$

$$3Dcirc. = 6\sqrt{\pi} \left({}^{V}/_{SA^{1.5}}\right) \quad \textbf{(3.10)}$$

3.5.2 – 3D-TEM Morphological Characterisation

The 3D particle models resulting from ET were characterised in terms of volume, surface area, radius of gyration, fractal dimension, and a 3-dimensional equivalent of circularity.

Volume and surface area were directly extracted from 3D volume reconstructions using the *BoneJ* plugin for Fiji [201]. Volume was simply determined from the number of voxels that comprise the model. The surface area was determined based on a production of a triangular surface mesh covering the surface. This calculation requires choice of a resampling factor, effectively smoothing the surface of the model to fit the triangular mesh. The choice of resampling factor balances speed against accuracy, and is described in a separate section in the appendix (section-A.2).

Radius of gyration was calculated *via* a 3D analogue of the pixel-based method used in 2D characterization (equation-3.8), as performed by other authors in ET study of soot [36]. This was performed using a self-produced macro for Fiji.

For comparison with 2D-derived shape complexity measurements, a 3D equivalent of the circularity parameter was derived. A relationship between volume and surface area was establish to produce values of 1 for a perfect sphere, and to move towards 0 for purely 2-dimensional (flat) objects. This is analogous to the ratio of area and perimeter

used in the 2D calculation. The calculations for this parameter are given in equation-3.10. This parameter is very similar to the *sphericity* parameter of Wadell [202], but due to slight differences in the calculation, and for the sake of clarity, our parameter will be referred to as *3D-circularity*.

The 3D-D_f was calculated *via* cube-counting in Fiji using the BoneJ plugin. This is a direct 3D equivalent of the box-counting method used in 2D. In BoneJ, the set of cube sizes is automatically chosen based on the size of the model, and must be manually reduced to comply with Lottin's guide to box sizes [156]. As for 2D box-counting, D_f was determined *via* the slope a log-log plot of the number of cubes *vs.* the size of cubes required to enclose the nanoparticle.

3.6 - Summary

This chapter has detailed fundamentals of the operation of both TEM and ET with specific relation to the work performed in this thesis. The use of these techniques was described with regard to the equipment available for use at the University of Nottingham. Details have also been provided on the soot samples studied and their preparation for TEM imaging *via* solvent dilution and thermo-gravimetric analysis, as well as details on the methods used for soot characterisation in both 2D and 3D.

4 - 2D- and 3D-TEM Morphology Characterisation of Flame-Generated Soot

This chapter details the initial usages of TEM and ET in this project. A case-study of a flame-generated soot nanoparticle was used to develop expertise with both TEM image processing and the tomographic reconstruction process. Traditional 2D morphology characterisation is performed on a range of images throughout the ±60° tilt-series, and is used to provide an example of variability in 2D-derived measurements as a function of projections angle. Measurements of area, number of primary particles, volume and surface area varied by 40-45% compared with the mean values, and measurements of circularity varied by up to 69%. Fractal dimension as determined *via* box-counting methods was insensitive to the angle of projection, while an alternative iterative method provided more variable values as was expected. The nanoparticle morphology was also characterised in 3D using the model produced by ET. A comparison of 2D- and 3D-derived measurements found significant deviations between the two. While the 2D method underestimated 3D-volume by around 36%, surface area was on average overestimated. Fractal dimension was underestimated by 2D methods, with a similar scale of deviation (~20-30%) as seen in previous works. Deviations between 2D- and 3D-circularity were 18% on average, while 2D-R_g was reasonably accurate at only 8% difference. The work carried out in this chapter highlights doubts by previous authors over efficacy of 2D measurements of single projections of soot nanoparticles, due to strong variability in 2D measurements with projection angle. This work was also useful for identify areas of the ET process that could be optimised.

The work included in this chapter was adapted from a journal publication, and was presented in-part at the 20th ETH Conference on Combustion Generated Nanoparticles in Zurich (2016):

Orhan O., Haffner-Staton E., La Rocca A., Fay M. *Characterisation of flame-generated soot and soot-in-oil using electron tomography volume reconstructions and comparison with traditional 2D-TEM measurements*. Tribol Int. **2016**;104:272-84.

4.1 - Introduction

As described in the literature review, ET has previously been used for soot study by both our own group and other research groups [34-36, 40]. To date, however, there has been little in the way of follow-up work. This is almost certainly due to how slow ET is compared to typical 2D characterisation. Currently, ET cannot compete with 2D-TEM regardless of improvements in quality. A practical 3D characterisation tool needs to be quick enough so that the advantages in quality are tangible and the technique can be a viable alternative. Thus, the aim of this thesis is to develop a 3D-TEM methodology for soot morphology characterisation that is both high quality *and* high-throughput. The main focus of this work will be in relation to optimisation and accuracy of 3D-TEM.

The work in this chapter describes the first forays into the use of electron microscopy and tomography for soot. These initial explorations are carried out using a simple case-study sample of flame generated (FG) soot that had been prepared prior to the start of the project. This sample eliminated the necessity of sample preparation that is known to be somewhat tricky for soot-in-oil samples [41], which were to be the main focus of my project. As such it offered an ideal data set with which to practice performing both traditional 2D-TEM and ET-derived morphology characterisations. This section also contains a small investigation into the effect of nanoparticle orientation on 2D-TEM characterisation.

4.2 - The FG Soot Sample

The first sample studied was a pre-prepared flame-generated (FG) soot nanoparticle. The sample was pre-prepared in the sense that it had already been deposited onto a TEM grid prior to the start of the project, and was made available by Dr Michael Fay at the nmRC. The grid had been prepared for tomography by addition of gold nanoparticles in a heptane suspension. The Au-NPs were acquired from MP Biomedicals, and were approximately spherical with an average diameter of 10 nm (±3 nm). As described in the literature review section, these nanoparticles are extremely high contrast in BF-TEM due to their extremely high density. Their well-defined size and shape is useful for acting as fiducial markers, meaning they are used to track the position of images and align them. Several Au-NPs can be seen in figure-4.1, which shows the FG soot nanoparticle in a standard BF-TEM projection.

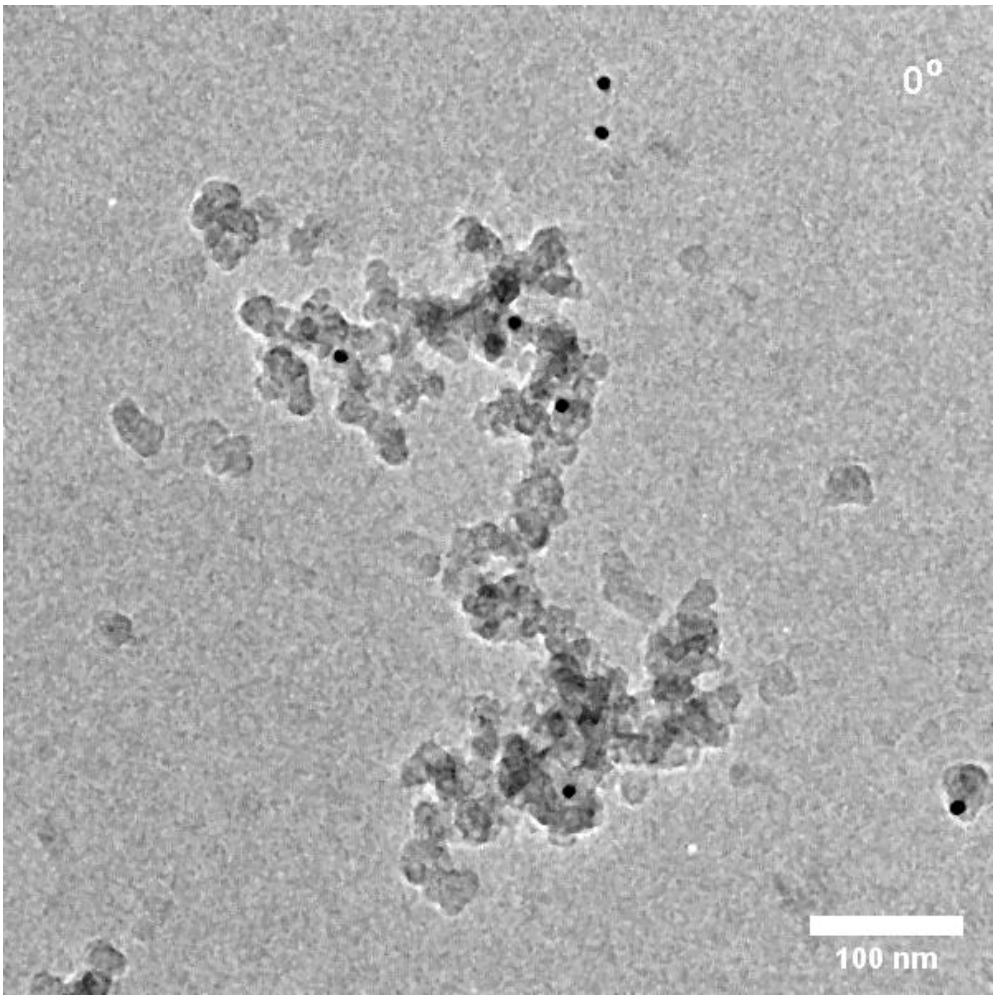


Figure-4.1: The flame-generated soot nanoparticle in an un-tilted BF-TEM image

This particular structure was chosen primarily due to its interesting 3-dimensional structure which included a prominent arch joining two complex and bulky bases. Additionally this structure had an acceptable distribution of gold nanoparticles in the locale, and lack of significant overlap with adjacent structures. For this FG soot particle, a tilt-series had been acquired over a ±60° range in 1° increments (121 images total). The images had been binned by a factor of 2, and were 1000 x 668 pixels in size (*cf.* the native size of the camera; 2004 x 1336 pixels). The image scale was 1.068 nm per pixel. As the sample had already been prepared and tilt-series already acquired this represented an ideal practice data set for ET, leaving only the computational steps of the process.

4.2.1 - 2D-TEM Morphology Characterisation of the FG Soot Tilt-Series

Prior to the use of ET, standard 2D-TEM morphology characterisation was carried out for the FG soot nanoparticle. This would enable us to gain insight into the kind of discrepancy that exists between 2D- and 3D-derived methods for this nanoparticle. This is important, as the emphasis for 3D characterisation is uncertainty in the accuracy of 2D soot characterisation.

Typically, morphological characterisation of soot is carried out *via* 2D-TEM imaging. However, the measurement of morphology from 2-dimenisonal projections of what are known to be complex, 3-dimensional structures has many potential sources of error. In some instances, fundamentally 2-dimensional parameters may be measured and it is assumed the 2D-3D difference is not significant. Examples include calculation of fractal dimension *via* the box-counting method [156, 200, 203], and radius of gyration *via* a pixel-based method [157, 204]. Authors have observed and predicted significant differences between 2D- and 3D-derived values for these parameters. In their 1995 work, Koylu *et al.* observed that on average 3D-R_g was 24% greater than 2D-R_g [73], while Rogak *et al.* predicted 2D-3D differences of 10-20% in terms of fractal dimension [74]. Alternatively, relationships may be used which attempt to correlate observed 2D properties with real 3D morphology. Such a method that has gained wide-spread use is the determination of the number of primary particles comprising an aggregate from the area it occupies in a 2D projection [73, 75]. This method (equation-3.2) does not account for real primary particle size distributions as the simulation involves only spheres of the same size (a problem discussed in depth by Morán *et al.* [205]), and all primary particles are assumed perfectly spherical. Correction factors are included to account for the 3D nature of the particle, but are partially based on simulations that do not account for primary particle overlap or realistic appearance of soot in TEM images. Even if a method to correlate 2D and 3D morphology were well calibrated, its general application to different samples is limited since the morphology of soot nanoparticles is so strongly dependent upon their formation. As might be expected given these considerations, previous 3D study of soot *via* ET has already observed significant differences between 2D- and 3D-morphology [34, 36].

It was also decided that 2D-TEM characterisation should be carried out over a range of images included in the tilt-series, rather than just the untilted image that would be used in standard characterisation. It has been acknowledged by several authors in the field that the appearance of soot nanoparticles varies strongly depending on the angle of projection (also described as ‘viewing direction’ or ‘orientation of the particle’) [36, 38,

73, 206]. This variability due to orientation has been considered to act almost as an uncertainty on 2D-derived measurements. For example, in their study using ET to determine optical properties of soot Adachi *et al*. considered that use of single TEM projections yields results that were arbitrary given they depend so strongly on projection orientation. They considered that use of single 2D projections could lead to uncertainties in models of soot atmospheric lifetime and associated light scattering and absorption. More recently, Baldelli *et al*. studied FG soot using both ET and TEM [38]. While they observed that primary particle measurements were not dependent upon angle of projection, 2D projected area measurements varied by approx. 30% across a tilt-series. They acknowledged that when using 2D methods, it is unclear whether differences in morphological measurements between particles is due to real differences in 3D structure or simply due to orientation effects. This a key consideration for the validity of 2D-derived characterisation. It is the differences between individuals of a sample that provide information on the state of soot in that sample. This in turn is the information used to try and understand how morphology is directing behaviour and producing effects in certain environments. If it is unclear whether the measured characteristics of a sample are real or simply artefacts of the measurement process, then it undermines the characterisation process.

Image processing was performed using Fiji, where pixels relating to the particle matter were manually identified and stored as regions of interest (ROIs). As described in the experimental section, this process is most generally performed manually, though in certain studies authors have developed bespoke automated methods [160, 207-209]. This 2D segmentation was carried out every 4° over the tilt-series, resulting in 31 measurements. Care was taken to consider each image from the tilt-series on an individual basis, as if it were only the image available. The different angles of the tilt-series reveal 3D information on the morphology of the structure, such as whether overlapping structures are connected to the main feature or not (this is discussed in more detail in section-4.3.1). As the purpose of this part of the study was to estimate errors in typical 2D-characterisation, efforts were made to ensure that ROI selections mimic those in a typical study where angled projections are not available.

An example of different ROI selections over the tilt-series are shown in figure-4.2, highlighting strong variability in the 2D appearance of this nanoparticle. The FG soot nanoparticle was characterised in terms of a number of morphological parameters. Firstly, it was necessary to determine the mean primary particle diameter (see the following paragraph for details of this procedure). The parameters that could be directly measured from the 2D images were: area, circularity, radius of gyration *via* pixel-based

method, and fractal dimension *via* box-counting. The box-set used was based on the work of Lottin *et al*. [156], where maximum box-size for accurate measurements is considered to be close to the scale of the irregularities of the structure. For a soot nanoparticle this is the primary particles, so maximum box-size is set equal to the primary particle diameter (20 nm). The minimum box-size in Lottin's work was around 10-20% of the maximum box size, and by also considering the suggestion of Wozniak [200] was set to 2 pixels (equivalent to around 10% of primary particle diameter in the scale of the tilt-series). The 2D area and mean primary particle diameter (see next paragraph for details on d_{pp} measurements) were then used according to the methods given in section-3.6.1 to derive the following 3D parameters: number of primary particles, volume, simple surface area (without overlap), and fractal dimension *via* Lapuerta's iterative method. The most widely used method of calculating fractal dimension, using the mass-fractal power-law relationship [75], is not applicable in this case as it meant to be used based on a sample of data rather than for individual nanoparticles.

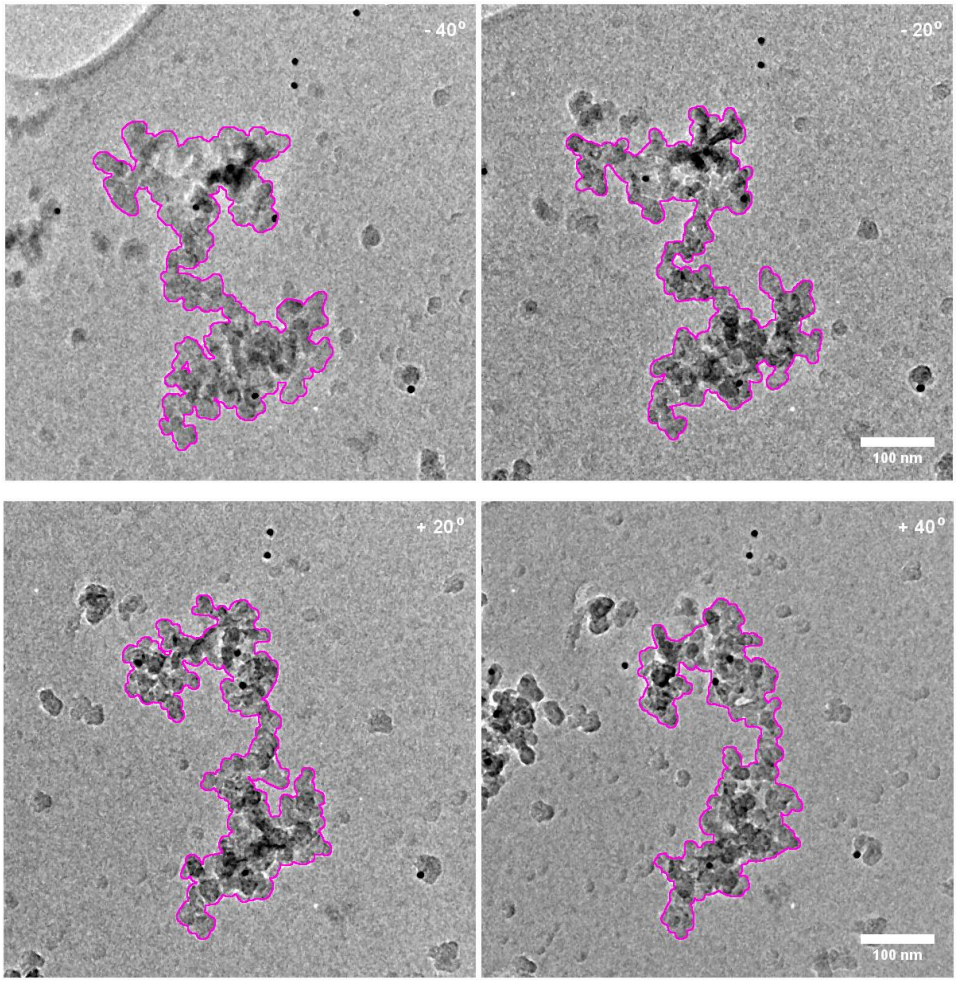


Figure-4.2: These images show the FG soot nanoparticle at various angles throughout the tilt-series. From top-left clockwise: -40°, -20°, +40°, +20°. Scale bars measure 100 nm in length.

Though in typical 2D characterisations the mean primary particle diameter is determined from a number of different nanoparticles in the sample, in this case only the particles visible in the tilt-series were available to be considered. The untilted image from the tilt-series was used to measure primary particle diameters, resulting in 33 individual measurements. Previous studies has indicated suitability of single projections for primary particle sizing [38]. The majority were single measurements per primary particle, though a small number contain two roughly perpendicular measurements over the same particle. This was only possible for the most clearly visible particles, following the protocol for reliable primary particle sizing described by Kondo *et al*. [39]. Due to the fact the tilt-series images were binned, the resolution is not ideal for measurement of primary particle diameters. The relatively coarse scale makes it difficult to discern anything but the most clearly visible primary particles. Additionally, overlap of primary particles is almost impossible to determine meaning that the overlapping surface area measurements (see experimental section-3.6.1) could not be performed, as the required overlap parameters could not be determined. The chosen primary particle measurements superimposed on the untilted image are shown in figure-4.3, and a histogram of the measured diameters is provided in figure-4.4. The histogram suggests a log-normal distribution, with the modal interval (based on 6 bins, *via* the Freedman-Diaconis rule [210]) between 17.8 and 20.4 nm. The mean diameter was calculated as 20.2 nm, and 20 nm was used in the calculations to derive the 3D parameters.

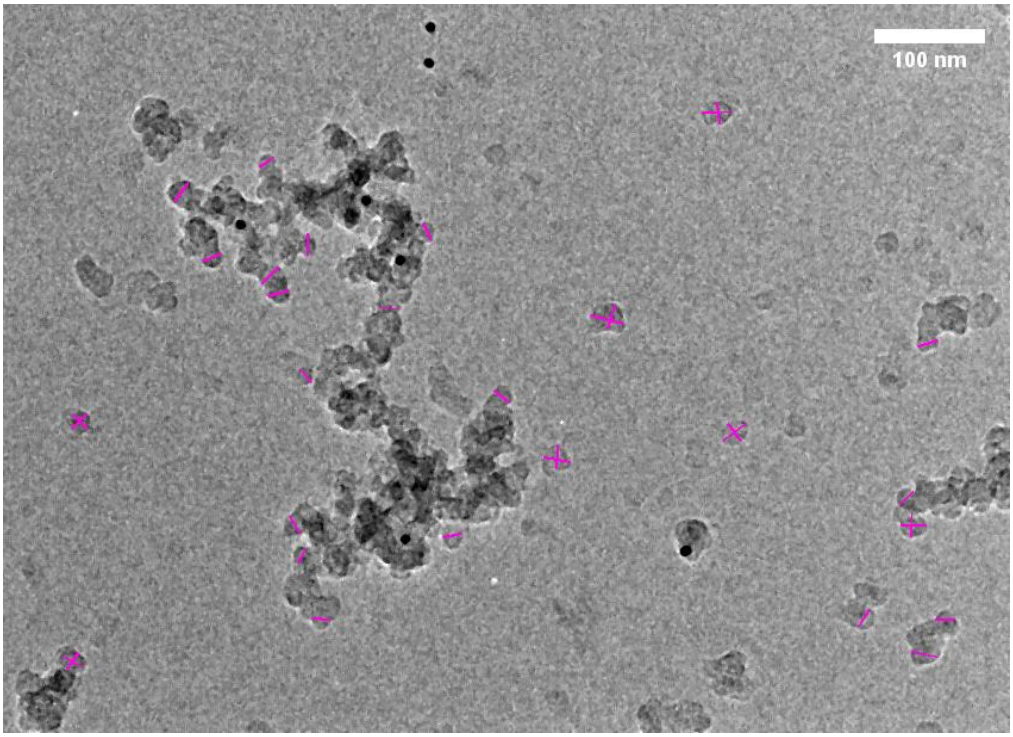


Figure-4.3: An example of the measurements of primary particle diameter for the FG soot sample, with vectors shown in pink.

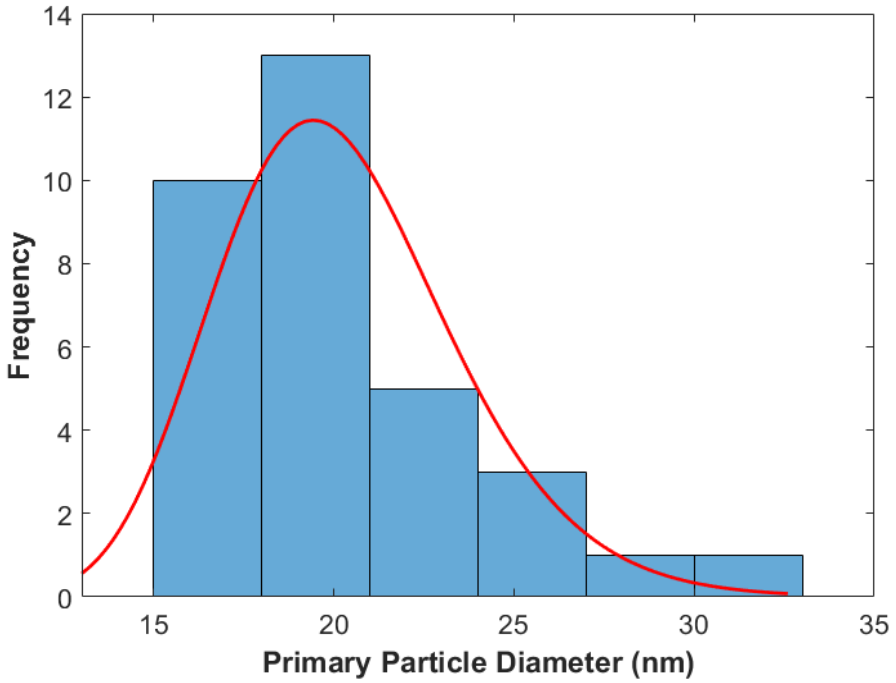


Figure-4.4: A histogram showing the (log-normal) size-distribution of primary particle diameters in this sample. Modal interval was between 17.8 and 20.4 nm, and the mean diameter was 20.2 nm.

4.2.2 - Electron Tomography for FG soot

The FG soot nanoparticle was reconstructed using the Etomo software, created by Mastronard *et al.* [176]. All 121 images of the tilt-series were included in the computation, corresponding to a file size of 158 MB. The software permits exclusion of any images from the computation if desired, *e.g.* if corruption of the image occurs or the displacement is very large, but this was not needed or used. Weighted back-projection was used to perform the computational step, as it is one of the simplest methods and was readily available in the software.

As described in the experimental section, alignment of the tilt-series is carried out first using simple image cross-correlation, and then refined using positions of the fiducial markers. An example of the chosen fiducial markers is given in figure-4.5. Though the number of markers chosen was towards the lower limit suggested by the Etomo guide, alignment completed with no major issues. The errors in alignment were well in-line with those suggested in the Etomo guide. A small number of manual corrections to fiducial marker position was required, but the entire alignment procedure completed within 5 minutes.

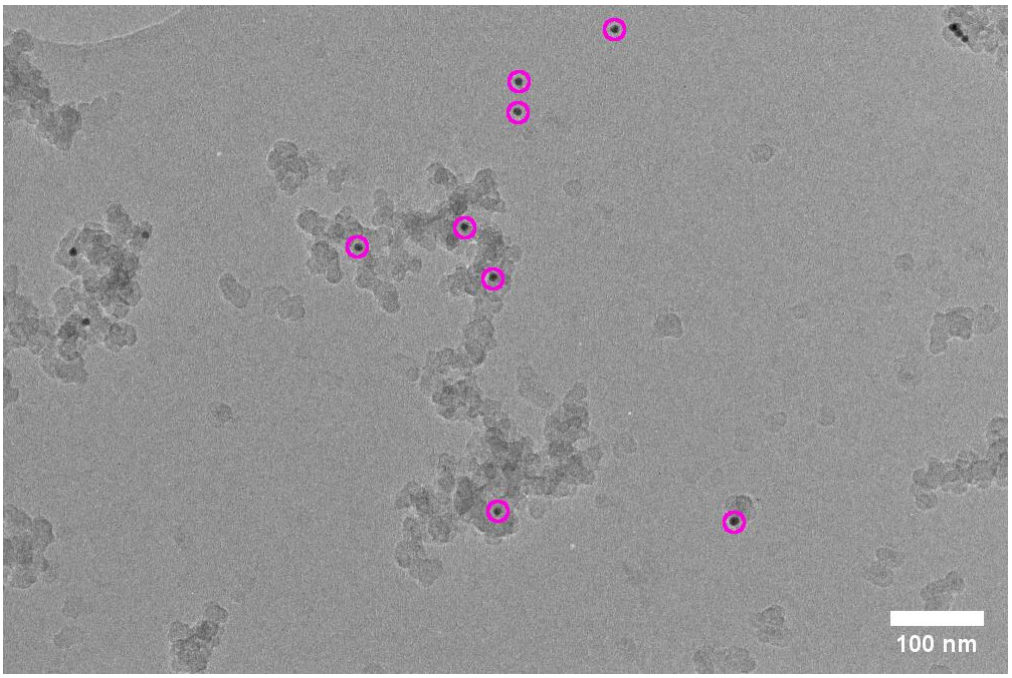
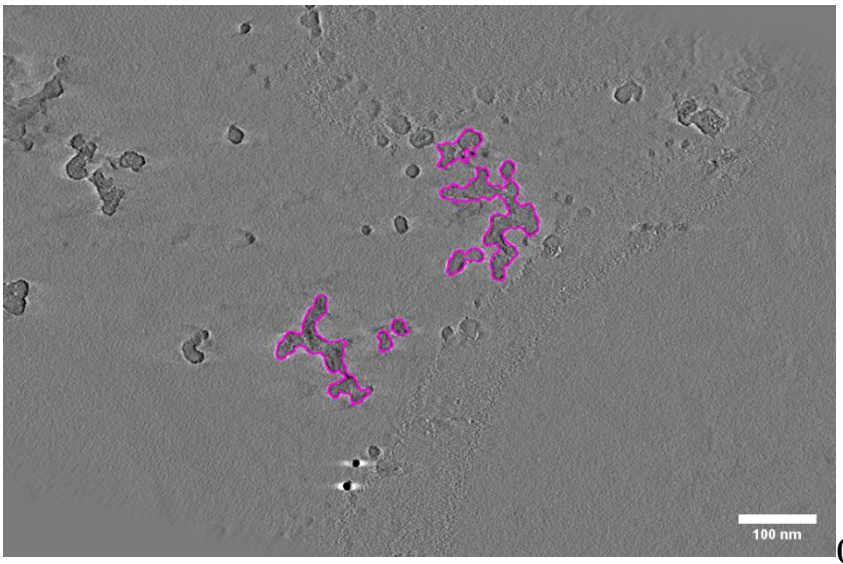


Figure-4.5: The fiducial markers chosen for fine-alignment of the FG soot tilt-series in Etomo.

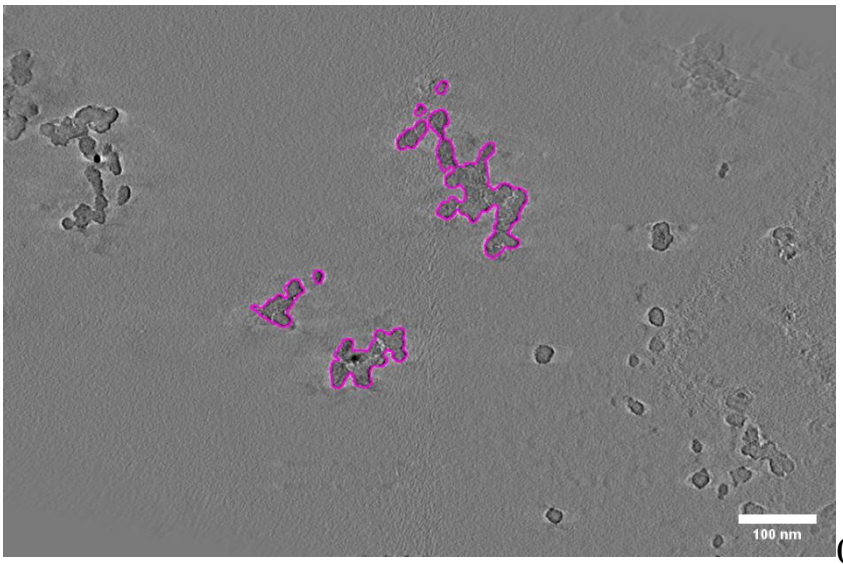
Etomo permits creation and viewing of temporary 'rough' tomograms for refining the positioning of the 3D reconstruction in 3D space. This is useful for limiting reconstruction of empty space, which can increase the size of tomogram files and the time required for the computation. The final chosen tomogram size was 300 slices in the Z-direction (perpendicular to the TEM grid), with a degree of 'padding' above and below the nanoparticle. In the XY-plane, the tomogram was simply the same size as the tilt-series images (1000 x 668 pixels).

The computational step that produces the tomogram completed in around 30 seconds, and was performed using all default settings. Details of the computer specifications are given in the experimental section-3.2. The raw tomogram (designated as 'FG-WBP') was 391 MB in size. This image stack was trimmed in size in X, Y, and Z to limit the volume of undesired material in the tomogram. The resulting tomogram contained 190 slices in the Z-direction, significantly reducing the file size (302 MB).

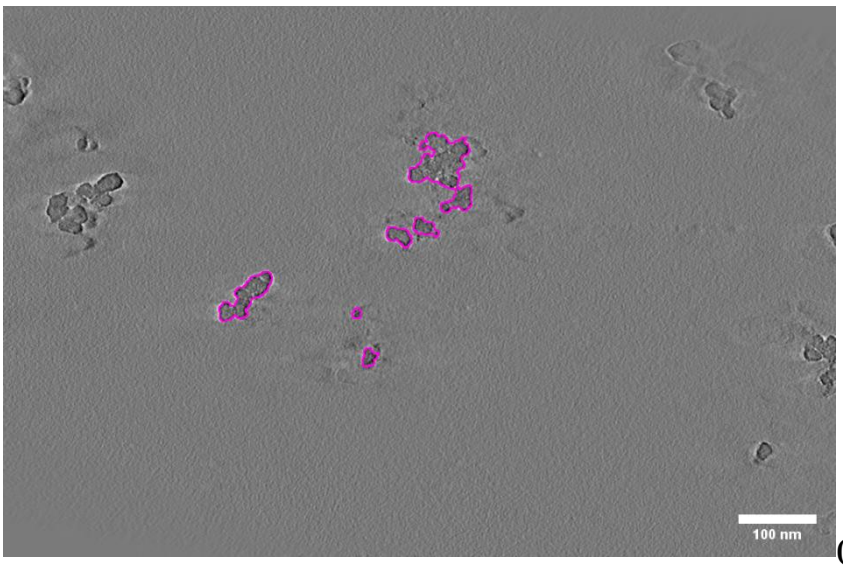
Segmentation of the tomogram was performed manually in Fiji, with the tomogram arranged into slices presenting the XY-plane (see experimental section-3.3.5 for more details). A brush tool was used to select the desired regions of the image, and selections for each slice were saved using the built-in *ROI Manager* tool. This process is exactly the same as that used to identify soot in 2D-TEM images, only that multiple 2D segmentations are created. Figure-4.6 shows several slices from the FG-WBP tomogram, and associated ROI selections.



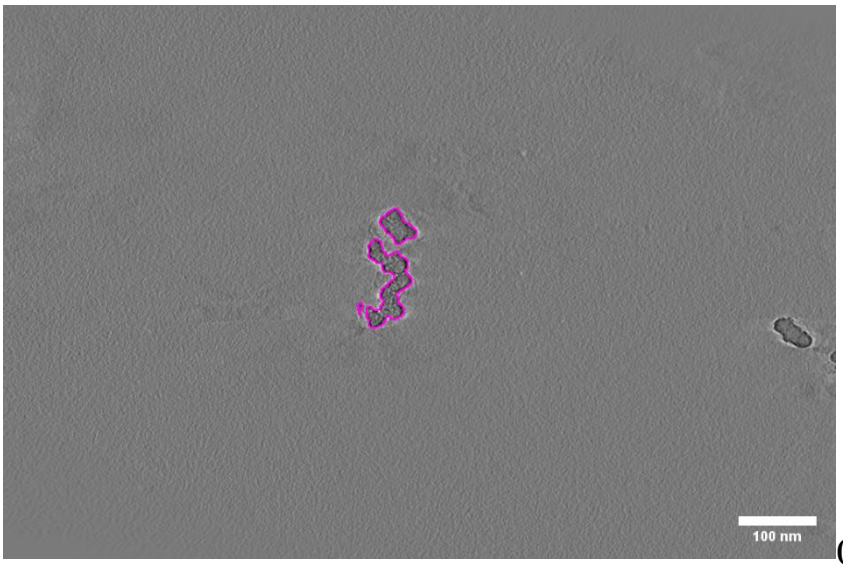
(4.6a)



(4.6b)



(4.6c)



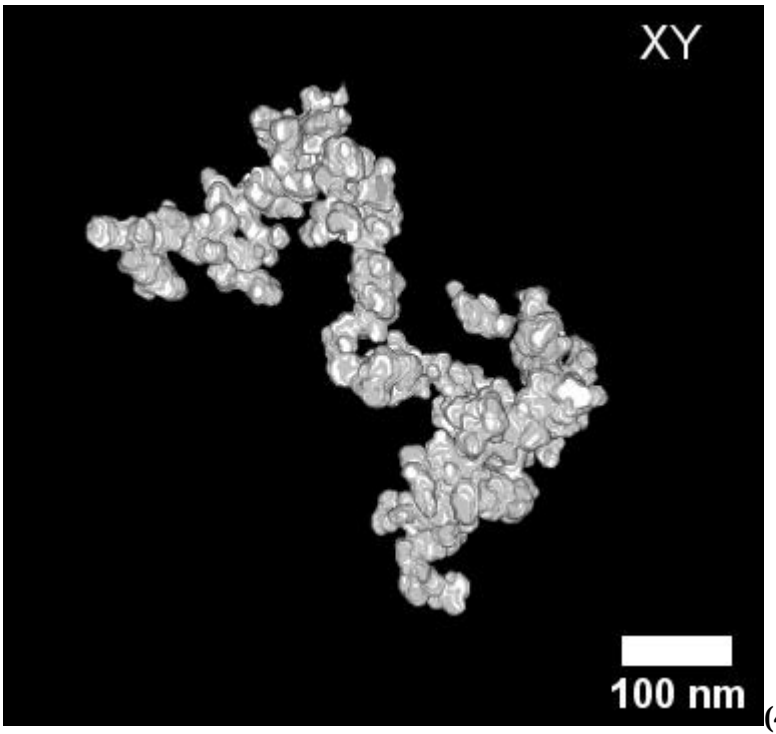
(4.6d)

Figure-4.6: These images shows 4 slices from the FG-WBP tomogram, taken from different heights. The ROI selections of the relevant particles matter are superimposed on the images.

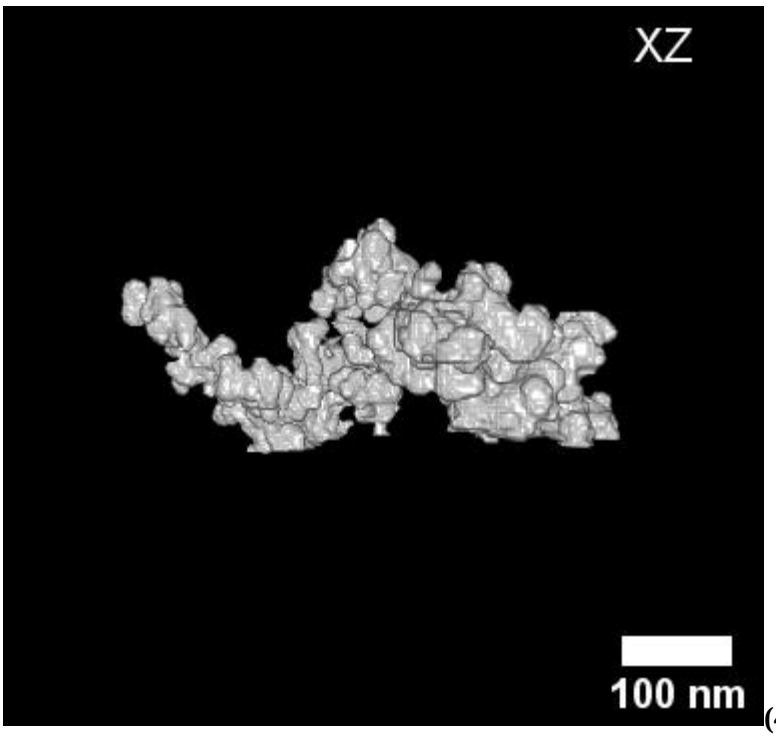
As can be seen, not all of the darker pixels in the tomogram slices are selected. Only those that pertain to the same nanoparticle are selected, as all other matter belongs to separate structures. The first two images in figure-4.6 (*a* and *b*) show the lower sections of the tomogram, which are closer to the TEM grid. This is closer to the adjacent soot-like structures that present (these can also be seen surrounding the structure of interest in figure-4.1) on the TEM grid, and thus more unselected matter is visible. As only cross-sections of the tomogram are viewed, it is not always obvious which areas of matter are connected at other depths. The presence of adjacent structures makes it significantly more difficult to correctly identify regions of interest. It is necessary for the user to repeatedly scroll forwards and backwards through the tilt-series to identify interconnected areas, which increases the time required for this process. The last two images of figure-4.6 (*c* and *d*) are around 200 nm vertically above the TEM grid, so the smaller adjacent structures are not visible and do not hamper segmentation.

Due to the large number of slices involved, manual segmentation of the tomogram took 144 minutes in total, an average of around 45 seconds per slice. This tomogram is actually towards the upper limits of difficulty for segmentation of soot. This is due to the presence of numerous adjacent structures as well as its large size, complex shape, and particularly its 3D nature. This amplified the difficulty of identifying connected regions of particle between slices and the extent to which selections changed between subsequent slices, increasing the time required for ROI selections to be made and confirmed.

Following completion of segmentation, all ROI selections are combined and 'binarized'. All pixels within the ROI selections (*i.e.* the particle) are coloured white, and all other pixels are coloured black. The result is a binary 8-bit image stack that can be handled as a 3D model. 3D renderings from different viewing directions are shown in figure-4.7, as produced using UCSF Chimera [211].



(4.7a)



(4.7b)

Figure-4.7: 3D renderings of the FG soot nanoparticle produced in UCSF Chimera.

The FG soot nanoparticle was measured in terms of volume, surface area, radius of gyration, 3D-circularity, and fractal dimension. Volume, surface area, and fractal dimension were measured using the BoneJ plugin for ImageJ. Volume was simply determined from the number of voxels, while surface area was determined based on a production of a triangular surface mesh covering the surface. This calculation requires choice of a resampling factor, effectively smoothing the surface of the model to fit the triangular mesh. Choice of this parameter for soot is discussed separately in the appendix section-A.2. For the FG soot nanoparticle, a resampling factor of 2 was chosen based on the typical scale of primary particles in the aggregate. Fractal dimension was calculated using a cube-counting method, with a cube-set based on the findings of Lottin's 2013 work [156]. Briefly, as for the 2D box-counting method for Df the minimum cube-size was set to around 10% of the primary particle diameter (2 nm), and the maximum cube-size was set to close the primary particle diameter of 20 nm. Radius of gyration was calculated *via* a self-produced macro for Fiji, and was a direct 3-dimensional extension of the 2D method used by previous authors [157]. As described in the experimental section, 3D-circularity is a direct 3D analogue to the 2D shape factor *circularity*. 3D-circularity accounts for the complexity of the morphology of the particle in terms of a ratio of its volume and surface area.

4.3 - Results & Discussion: 2D vs 3D Comparison

4.3.1 - Adjacent Structures in the Tilt-Series and Tomogram

An interesting observation during tilt-series characterisation was how at different angles, adjacent soot material could appear to be either connected/disconnected to the main structure. As soot is partially transparent in BF-TEM, when adjacent material overlaps the main structure it is very difficult to discern whether the particle is truly connected or not. This can be illustrated by considering the appearance of the FG soot nanoparticle at -12° and at 4° in the tilt-series, shown in figure-4.8. At the negative angle the highlighted adjacent structure, a small particle of possibly 2 or 3 primary particles combined, is positioned underneath the main structure and considered connected. However, just a few degrees in the positive direction this structure emerges from underneath the particle, and would be excluded from ROI selection. In the untilted image, this adjacent structure sits very much on the edge of the main aggregate and its inclusion or exclusion would be purely down to the choice of the user. Very similar observations of overlapping but non-connecting structures were made very recently, in

the work of Baldelli *et al.* [38]. They also noted how in standard single-projection imaging it is unclear whether structures are genuinely attached or not.

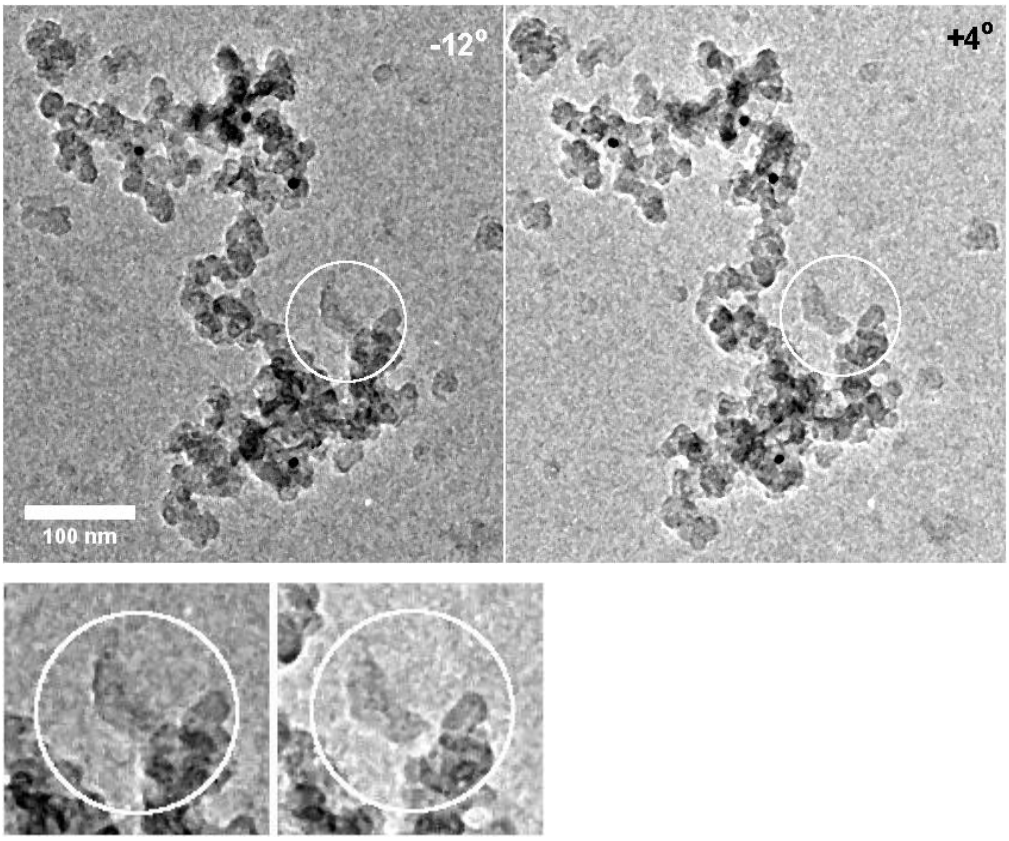


Figure-4.8: Example tilt-series images of the FG soot nanoparticle, where adjacent soot material appears as either connected or disconnected from the main structure.

Such effects are another potential concern for standard 2D-TEM, as with only a single projection it would not be possible to observe the true nature of such an arrangement of particles. This could lead to potentially erroneous measurements of morphology. Realistically, this problem would likely be avoided by preparing the TEM grid with a lower concentration of soot. This would make it less likely for structures to overlap, though this cannot always be avoided as deposition of soot is largely uncontrolled.

In 3D-TEM the tilt-series allows us to visualise the particle in 3D, and higher angles can be used to determine whether adjacent particles are connected or not. This knowledge was utilised during the segmentation of the FG soot nanoparticle, as the initial segmentation actually included the adjacent structure shown in figure-4.8. Due to the close proximity of the adjacent structure, inaccuracies of the reconstruction (blurring primarily) caused the two structure to appear connected. As it happened, only the most tenuous of connections linked this section to the main particle in a single slice of the

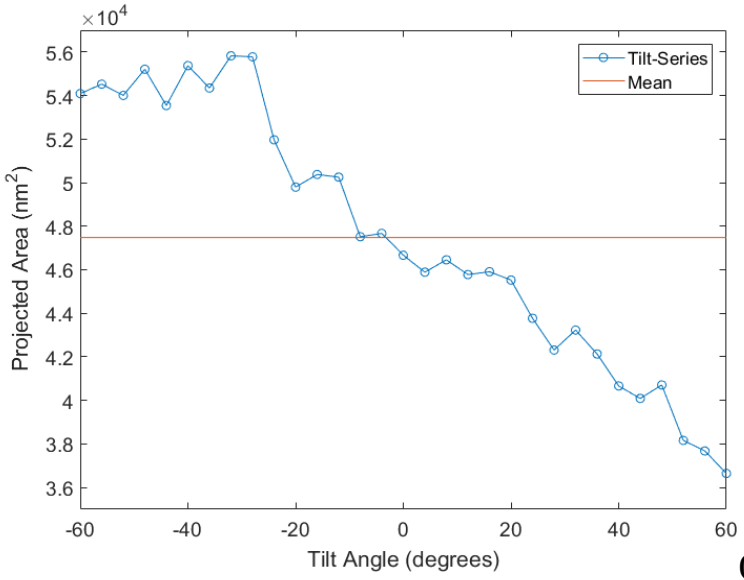
tomogram. By observing the tilt-series, it was clear this structure was not attached, and the tomogram segmentation could be edited to remove this section. Of course, as for standard 2D-TEM the most effective remedy is simply better grid preparation to ensure low likelihood of particle overlapping. However, in some cases it may be unavoidable and as such it is useful to be able to utilise the tilt-series to advise edits to the initial segmentation.

4.3.2 – Morphological Analysis

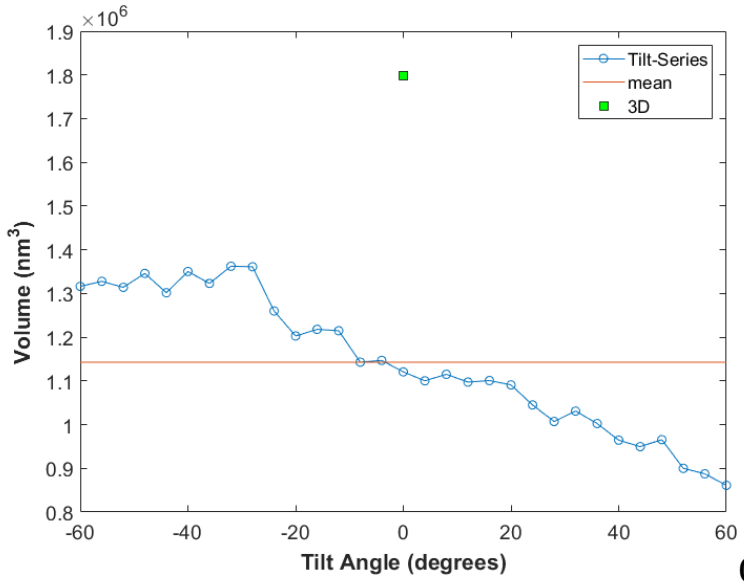
The FG soot nanoparticle was characterised in terms of morphology *via* typical 2-dimensional methods across 31 different projection angles, and *via* 3D-methods using a reconstructed model. Scatter plots were produced to visualise how different morphological properties varied as the viewing angle in TEM changed, and 3D-derived values were inset into these plots (figure-4.9). Mean values across the tilt-series, and their deviation *vs.* 3D-derived values are included in table-4.1.

	Volume (nm^3)	**Surface Area (nm^2)**	**Radius of Gyration (nm)**	**Fractal Dimension (box-count)**	**Fractal Dimension (iterative)**	**Circularity**
3D	1,797,700	303,700	149.1	2.47	2.47	0.114
2D-mean	1,142,800	342,800	136.9	1.83	1.95	0.093
2D-3D discrepancy	36 %	-13 %	8 %	26 %	21 %	18 %

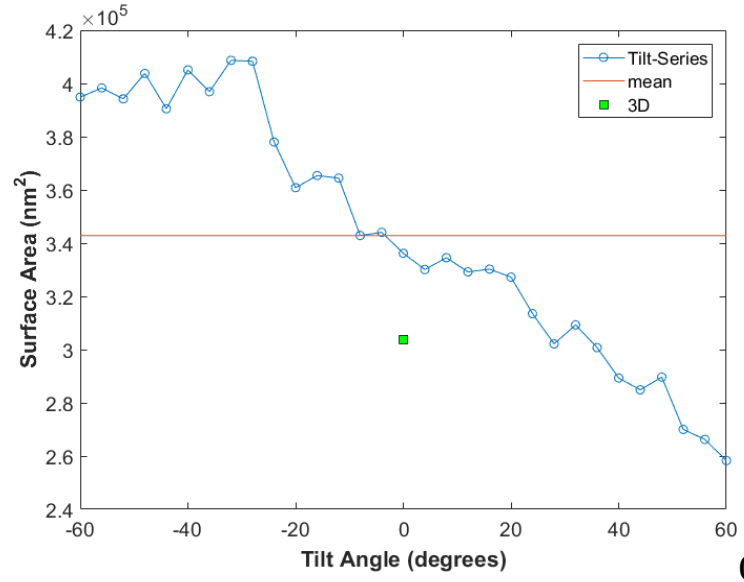
Table4.1: Showing the 3D-derived and mean 2D-derived values for several morphological parameters. Also shown is the discrepancy between the two methods, calculated as a percentage of the 3D-derived value.


×10^4
Tilt-Series
Mean
Projected Area (nm^2)
Tilt Angle (degrees)

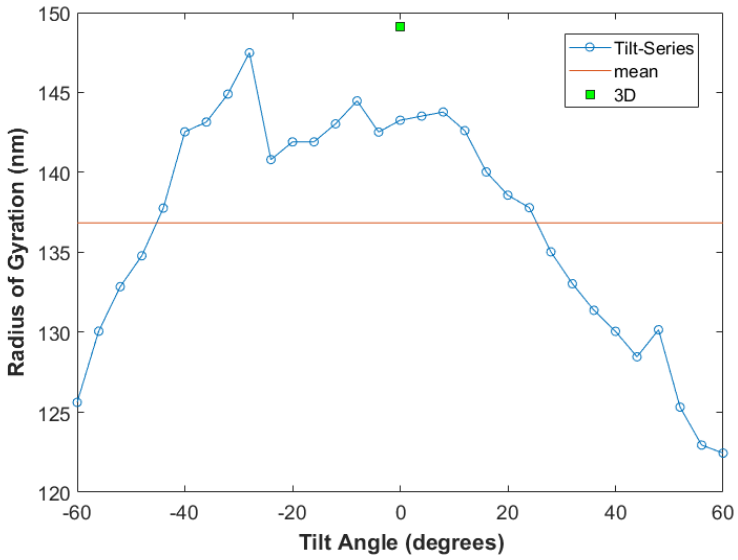
(4.9a)


×10^6
Tilt-Series
mean
3D
Volume (nm^3)
Tilt Angle (degrees)

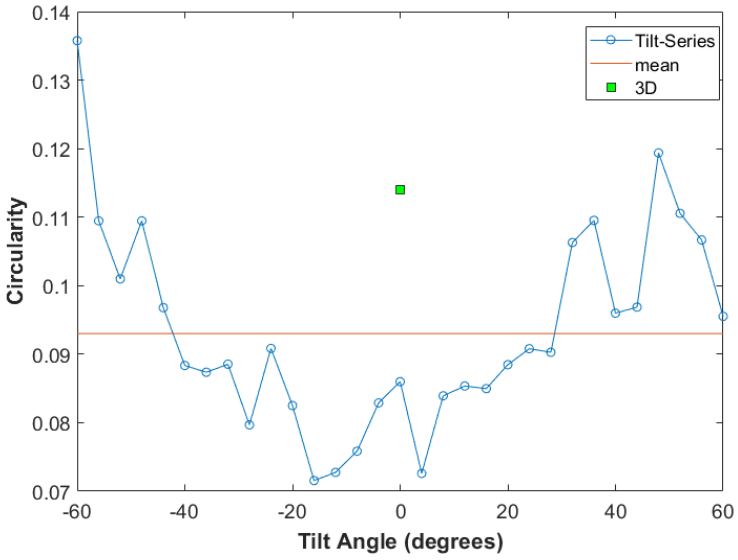
(4.9b)


×10^5
Tilt-Series
mean
3D
Surface Area (nm^2)
Tilt Angle (degrees)

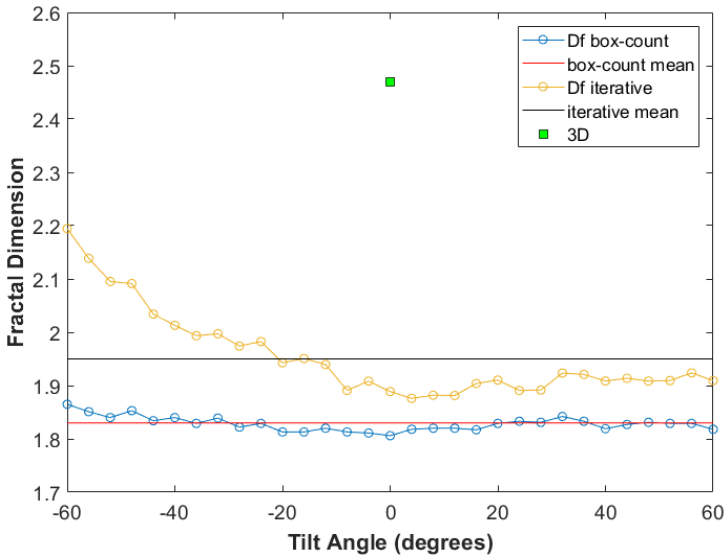
(4.9c)



(4.9d)



(4.9e)



(4.9f)

Figure-4.9: Scatter plots showing the variation in 2D-derived morphological measurements as a function of the viewing angle in the tilt-series. Also included are the single 3D-derived measurements and the mean of the 2D-derived measurements.

4.3.2.1 – Area, N_p, Vol, and SA: Variation over the Tilt-Series

Firstly, the parameters A_p, N_p, V, and SA can essentially be grouped together when considering their variability. The measured 2D area is used in equation-3.2 to calculate a value for N_p. As such their variability is almost identical (figure-4.9a-f), only showing a small deviation due to the use of the exponent α (= 1.09). Volume and surface area are derived directly from N_p and thus show identical variability over the tilt-series.

For these 4 parameters, a significant degree of variation was observed over the tilt-series. The range of results measured was ≥40% of the size of the mean value, and the variation was asymmetric over the tilt-series. The exact form of this variation is dependent upon the particular 3D structure of the nanoparticle, and would be different depending on the particle studied. By chance, the apparent morphology at the extreme negative angles (-60° to -30°) presented the largest areas, resulting in the largest measured values of these parameters. From -30° to +60° there was a somewhat linear decrease in the 2D area occupied by the nanoparticle, though this decrease was not smooth.

The use of ET allowed us to compare 3D-derived morphology with the 2D-derived results from the tilt-series. The A_p property is purely 2-dimensional, so has no direct relation to the 3D derived results. Similarly, it was not possible to directly determine N_p from the 3D model. In some studies, including Koylu's which derived the values of k_a and α used in equation-3.2 [73], it was apparently possible to determine N_p visually from a series of angled TEM images (not unlike a tilt-series). However, it was not the case for the FG soot nanoparticle. The resolution and contrast did not allow for all individual primary particles to be clearly discerned. Indeed, from the experienced gained in TEM imaging of soot is seems unlikely for this ever to be a *routinely* achievable measurement. Only for the most well-defined particles in ideal TEM projections would this ever be possible. The examples provided in Koylu's work show extremely branched nanoparticles with essentially no multi-particle connections or clusters [73].

4.3.2.2 – Vol: 2D vs 3D

Firstly, it can be seen in figure-4.9b (and table-4.1) that all 2D-derived measurements of volume were underestimated in comparison to 3D-derived volume. The mean volume measurement across the tilt-series was 36% smaller than the 3D-volume. This result suggests that the 2D method has significantly underestimated the bulk of the FG soot

nanoparticle. This may be through either overestimation of the extent of primary particle overlap, by underestimation of the unseen 3D-extent of the particle, or both. These two factors are governed by the use of the pre-factor k_a and the exponent α. The data shown in this section is useful as an example of what degree of uncertainty may be associated with the 2D-TEM methodology, but remains unaccounted for.

4.3.2.3 – SA: 2D vs 3D

In contrast to the underestimations in volume measurements, the 2D-TEM method was seen to overestimate surface area *vs.* the 3D-result for the around three-quarters of the total tilt-range. Only the orientations from around +30° to +60° resulted in surface area measurements that were smaller than the 3D-SA. Due to the fact that different orientations resulted in both underestimation and overestimation, on average the 2D-method was only 13% larger than the 3D-SA. An overestimation is not entirely unexpected, as the simple method use to calculated the 2D-derived SA made no attempt to account for the overlap of the primary particles. As such, internal surfaces of the primary particles that are not accessible in reality are included in the calculation, resulting in a gross overestimation. Despite the mean 2D-SA being relatively close to the 3D-derived result, the lack of incorporation of any overlap factors mean that this is almost certainly simply down to chance and would be unlikely to retain this closeness for an ensemble of nanoparticles. In any case, due to the strong variability in the 2D-SA, a large number of orientations still resulted in a significant deviation *vs.* the 3D-SA.

4.3.2.4 – R_g: 2D Variation and 2D vs 3D

Figure-4.9d shows the variability in the radius of gyration over the tilt-series. A first observation from this plot is that the shape does not entirely mimic that seen for A_p, V, SA, and N_p. Radius of gyration can be thought of as a measure of complexity, taking into account the distribution of the particles matter around its centre of mass. Highly branched particles that extend further outward from the centre of mass will exhibit higher R_g values than those that cluster close to the centre, even when their projection area is significantly smaller. As such, the form of the R_g variation is not directly related to that of projection area, and we observed more parabolic variation over the tilt-series. For example, a sharp decrease in R_g from around -40° to -60° is concurrent with a relatively steady value of projection area. The parabolic shape of the plot implies that the particle appears more clustered at the higher angles. The degree of variability in R_g

was not as large as that seen for the previously discussed parameters. The range of results was still fairly significant however, at around 18% of the size of the mean value.

In comparison to the 3D-R_g, the 2D method resulted in an underestimation in every image across the tilt-range, though at just 8% on average this was smaller than that seen for volume. It is unsurprising that the 2D-methodology resulted in an underestimation, as the method makes no attempt to account for the unseen 3D extent of the particle. The pixel-based method is a purely 2-dimensional parameter, and incorporation of the voxels in a 3rd dimension would be expected to increase the value. The 8% average underestimation seen here is significantly lower than that measured by Koylu *et al.*in their 1995 work [73], which saw an average 24% underestimation in 2D. However, it is not clear what method is used to calculate radius of gyration in that work, and calculations were performed on simulated aggregates rather than real nanoparticles. A potential cause of the relatively high accuracy of 2D-R_g may be due to the aspect ratio of the nanoparticle. Despite significant 3-dimensional character, and the Z-depth of the particle being in excess of 200 nm, the particle is much larger in the XY-plane. This is emphasised in a 3D-rendering of the particle in a minimum bounding box (figure-4.10).

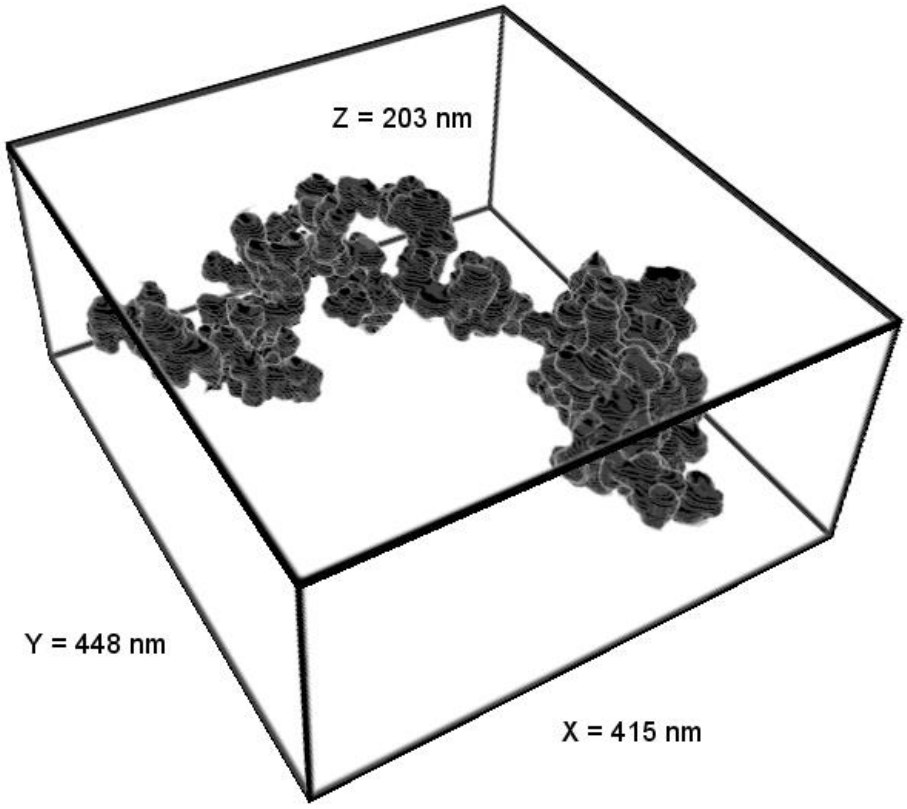


Figure-4.10: A 3D render of FG soot in a minimum bounding box.

The XY-plane Feret diameter is 461 nm (the maximum distance between any 2 points of the structure), so is large in comparison to the maximum Z-depth of 203 nm. This means that the contribution to the voxel-based 3D-R_g value is primarily from the XY-plane, which is the only contribution in the 2-dimensional method. For particles with a smaller XY:Z ratio it is expected that the 2D-3D difference in R_g will be more prominent, and *vice versa* for more 2-dimensional nanoparticles.

4.3.2.5 - D_f: Box/Cube-counting and Lapuerta's Iterative Method

In spite of the strong variation in many of the other parameters measured, D_f calculated *via* the box-counting method barely changed across the tilt-series. The range of results measured was only 3% of the size of the mean Df value, showing the parameter to be apparently insensitive to significant changes in particle morphology. This insensitivity was in contrast to the findings of Wentzel *et al*. [83], who observed fractal dimension *via* box-counting to vary by up to 20% across different orientations of the same nanoparticle. However, these results are in agreement with those of Lottin *et al*. [156], where only 2% variation was observed when considering projections angles of a single nanoparticle from -68° to +62°. Given the lack of variability, there was no obvious pattern to the variation and results simply varied by small amounts close to the mean value.

Lottin considered this insensitivity indicative of the fact that single projection angles were particularly suited to fractal analysis *via* this method [156]. However, given the large deviations variations in many of the other parameters, it seems prudent to question the efficacy of this parameter for describing nanoparticle morphology. If D_f is supposed to describe particle complexity, then surely such large changes in apparent morphology should be reflected in variation in values of the Df. In fact, the range of results measured was only 2% of the size of the full range of possible Df values, which should be $1 < D_f < 3$. Another factor of concern for D_f *via* box-counting is the choice of box-set. It is well-established that box-set can significantly affect the values measured, and was partially the reason for Lottin's study [212]. They calibrated the box-set choice through creation of a soot-like true-fractal pattern of known D_f, establishing the box-set choices employed in this thesis. However, in some studies the choice of box-set is neither thoroughly rationalised or even described at all [203].

By comparison, Lapuerta's iterative method [157] for fractal dimension showed more significant variation across the tilt-series, with the maximum range of results equal to 16% of the mean value. The shape of this variation was also asymmetric, in contrast to the relatively formless variation *via* box-counting. The largest $D_{f\text{-Iterative}}$ values were

observed at the largest negative angle (-60°), and decreased relatively linearly to a low plateau from around 0° to +60°. All values of $D_{f\text{-Iterative}}$ were universally higher than those measured *via* box-counting. This is not surprising, as while the iterative method was developed specifically to considered soot nanoparticle morphology, the box-counting method is purely 2-dimensional and fundamentally cannot provide a value > 2.

As mentioned, both R_g and D_f can be considered as measures of the complexity of a soot nanoparticle as they consider the distribution of a particles mass in comparison to its centre of mass. In theory, branched aggregates and clustered aggregates would result in different values in both parameters. The relationship between R_g and D_f in particular should be approximately inverse, as radius of gyration values are higher for branched structures, whereas D_f is lower for branched structures (and vice versa with clustered structures). By normalizing the data according to the minimum and maximum values in the range for the tilt-series (equation-4.1), and plotting normalized values alongside one another we could visualise the relationship between R_g and D_f by both methods (figure-4.11).

$$x_{norm} = {(x - min.)}/{(max. - min.)} \quad \textbf{(4.1)}$$

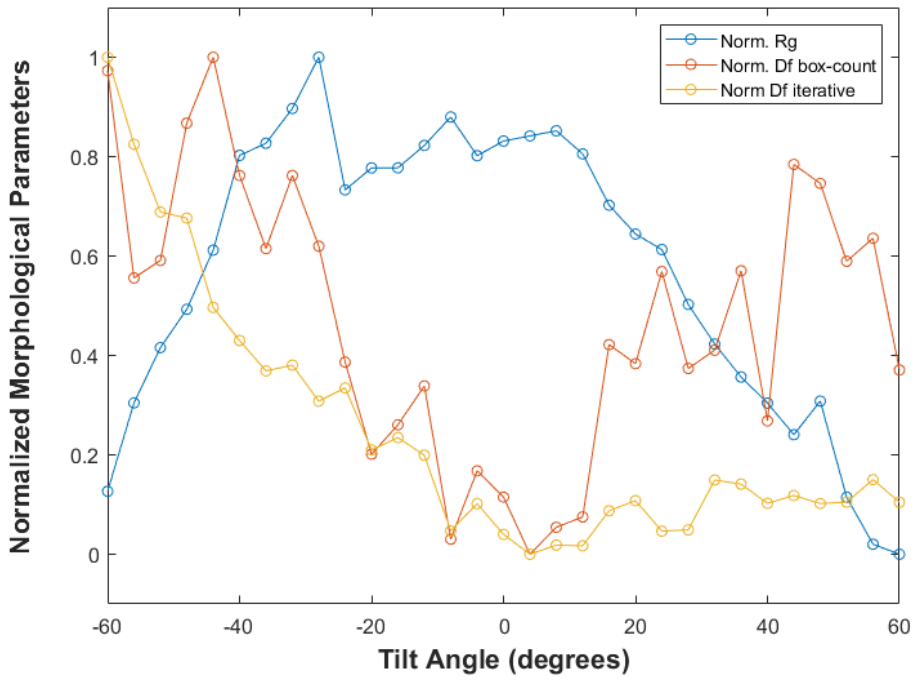


Figure-4.11: Plot comparing the normalised variation of fractal dimension and radius of gyration measurements as a function of tilt-angle

The normalised $D_{f\text{-iterative}}$ plot is somewhat inverse to the $y = -x^2$ shape of the radius of gyration plot, but this behaviour does not hold over the whole tilt-series. While from -60° to around 0° increasing R_g is concurrent with decreasing D_f-iterative, the positive half of the tilt-series see $D_{f\text{-iterative}}$ plateau while R_g decreases. The normalised $D_{f\text{-box}}$ plot is quite strongly variable, which stems from the normalisation of a very small range of results effectively exaggerating the variation of the original $D_{f\text{-box}}$ data. Overall, a roughly inverse relationship is observed *vs.* radius of gyration, but strength of the relation is hampered by the variability mentioned. Additionally, this is not particularly meaningful as in absolute terms the sensitivity of the $D_{f\text{-box}}$ method was very low. While not too useful in a quantitative sense, this small set of data at least indicates that both R_g and D_f appear to be representing nanoparticle complexity in their intended way.

The 3D-D_f was calculated *via* cube-counting in Fiji using the BoneJ plugin. In BoneJ, the set of cube sizes is automatically chosen based on the size of the model, and must be manually reduced to comply with Lottin's guide to box sizes [156]. As for 2D box-counting, D_f was determined *via* the slope a log-log plot of the number of cubes *vs.* the size of cubes required to enclose the nanoparticle. The 3D-D_f was determined as 2.47, which was 26% larger than the mean $D_{f\text{-box}}$ value, and 21% larger than the mean $D_{f\text{-iterative}}$ value. The increased accuracy of the iterative method is somewhat expected given the concerning lack of sensitivity in the $D_{f\text{-box}}$ results, and the fact that box-counting makes no attempt to infer the 3D morphology of the nanoparticle. The box-counting method produced values slightly greater the range of underestimation expected by Rogak *et al.* (10-20% *vs.* 3D-Df) [74], but within the 30% underestimation predicted by Tence *et al.* [213]. Comparatively, the iterative method slightly outperformed box-counting, but was still significantly underestimating 3D-D_f.

4.3.2.6 – Circularity: 2D Variability and 2D vs 3D

Circularity has been included in this work as an additional measure of complexity for the fractal nanoparticle morphology. Circularity can be considered somewhat of an analogue to the fractal dimension parameter. In 2-dimensions, circularity considers how similar the shape of an object is to a circle, by considering the ratio of its area and perimeter (equation-3.9). A perfect circle provides a value of 1, and the parameter moves towards 0 for a 1-dimensional line, hence the similarity to the 1-3 scale for fractal dimension. This method was extended to 3-dimensions by considering the ratio of the 3D analogues of area and perimeter, *i.e.* volume and surface area respectively (equation-

3.10). A factor was introduced to calibrate a perfect sphere to possess a *3D-circularity* of 1, and provide a value of 0 for a perfectly 2-dimensional object.

Variability in 2D-circularity over the tilt-series was the strongest seen for any of the measured parameters. The range of results measured was equal to 69% of the size of the mean circularity over the tilt-series. The form of this variation was approximately parabolic ($y = x^2$), and inverse to the variability seen for the radius of gyration ($y = -x^2$). This is an expected result, as circularity should produce higher values for more clustered particles ($\rightarrow$1, as they are likely more spherical in shape overall), and lower values for branched particles ($\rightarrow$0, as they are similar in shape to a circle). This is illustrated in the plot showing normalised circularity and normalised R_g as a function of tilt-angle (figure-4.12). This is similar as to what was seen for D_f, though the relationship appears to hold more strongly for circularity. The average circularity measured over the tilt-series was 0.093, which underestimates the 3D-circularity value (0.114) by 18%.

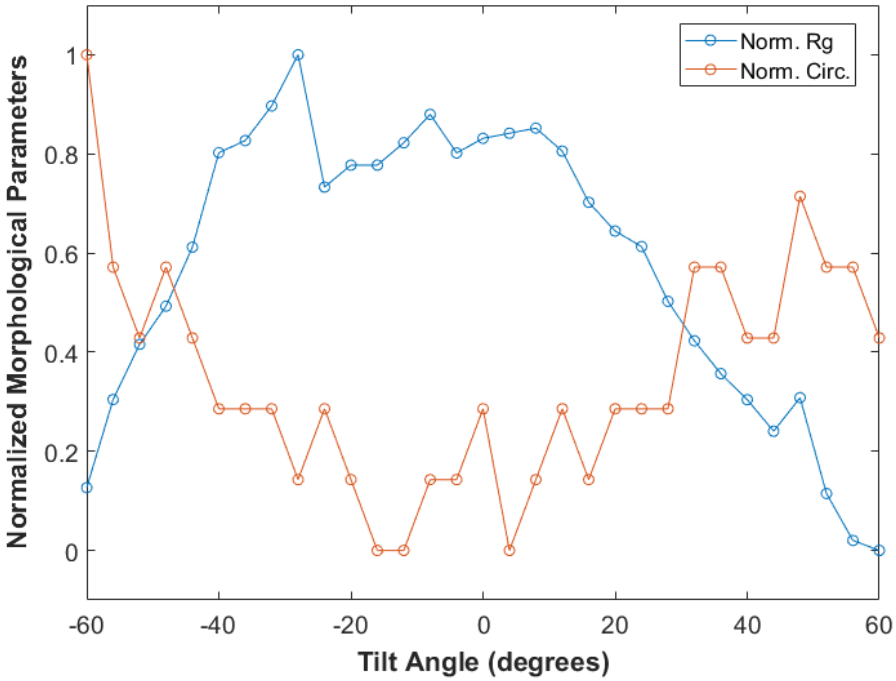


Figure-4.12: A plot comparing the normalised variation of radius of gyration and circularity measurements as a function of tilt-angle.

4.4 – Conclusion

This chapter details the first uses of ET and TEM for soot study in this project, using a case study of a flame-generated soot nanoparticle. The tomographic reconstruction of soot using Etomo was useful for understanding the opportunities for optimisation within

the process. As accuracy in 3D-derived results is the primary reason for attempting to develop ET for soot, the use of potentially more accurate reconstruction algorithms is an obvious point of interest. Similarly, variable tilt-ranges in prior ET studies of both soot and non-soot species, and the knowledge that oil can be a significant contaminant in TEM, marks the size of the tilt-series as another area for potential optimisation. Finally, the segmentation of the tomogram in this work was particularly lengthy at over 2 hours for a single nanoparticle, and so this process is clearly another area primed for improvements.

The results detailed in this chapter describe the comparative morphological analysis of an individual FG soot nanoparticle in 3D *via* ET, and in 2D accounting for multiple TEM projection angles. As in previous works by other authors, it has been observed that for several commonly measured morphological parameters a single soot nanoparticle can produce a wide range of results when accounting for different orientations. Also, significant differences were measured between 2D-derived and 3D-derived morphology for many of the parameters considered. These results can be summarised as follows:

- Area-based measurements (Vol, SA, N_p) varied strongly with projection angle (40-45%)
- D_f *via* box-counting was highly insensitive to projection angle (only 3% variation), in agreement with Lottin [156], and in contrast to Wentzel [83].
- D_f *via* Lapuerta's iterative method was moderately variable with respect to projection angle (16%) and showed expected approx. inverse relation to radius of gyration
- Radius of gyration was moderately variable (18%) and on average reasonably accurate from 2D-methods (8% deviation from 3D-R_g)
- Circularity was highly variable with respect to projection angle (69%), and was quite closely inverse to R_g
- On average, Volume was significantly underestimated by 2D (36%)
- On average, surface was moderately larger than 3D (13%), but possessed strong 2D variability and clear deficiencies of the method are noted
- D_f was significantly underestimated by box-counting (26%) and the iterative method (21%), roughly in-line with findings of other authors (Rogak [74], and Tence [213])
- Average 2D-circularity was 18% < the 3D equivalent, and was the most susceptible to variation with orientation

5 - Optimisation of Electron Tomography for Soot

The work in this chapter details the optimisation of 3 major facets of the tomographic reconstruction process in Etomo: the tilt-series composition, the computational reconstruction step, and tomogram segmentation. Using the flame-generated soot nanoparticle from the previous chapter, two common methods for tomographic reconstruction were compared: the simple and quick WBP algorithm, and the slower but theoretically superior SIRT algorithm. Through qualitative and quantitative comparison of the resulting tomograms and particle models, it was determined that WBP was of similar quality to SIRT, but completed significantly quicker (30 seconds *vs.* 1.5 hours). Next, the effects of maximum tilt-angle and tilt-increment on the quality of reconstruction were compared. While reduction in overall tilt-range from ±60° to ±50° and ±40° resulted in significant decreases in quality, increase in tilt-increment up to 3° still produced tomograms of high quality. The optimum tilt-series was a ±60° tilt-range with 3° increments, cutting potential beam exposure to the sample by two thirds. For the final stage of optimisation, nanoparticles extracted from the oil of GTDI engine were included in the testing. General TEM observation of the sample revealed abundance of localised amorphous carbon structures and crystalline material in addition to typical soot nanoparticles. A small sample of 6 GTDI nanoparticles were reconstructed in 3D using the WBP algorithm and a ±60° tilt-series with 3° increments. The effect on reconstruction quality by utilising linear interpolation in segmentation to varying degrees was assessed. While increased use of interpolation drastically reduced the time required for segmentation, significant information losses also occurred. Only by using interpolation between every 5^{th} slice of the tomogram was acceptable quality of reconstruction retained, resulting in a 44% decreased in time required for segmentation. For the FG soot nanoparticle, the overall optimised process was associated with a 67% decrease in time required compared with a procedure based on examples in the literature (1.3 hours *vs.* 4 hours).

The work included in this chapter is adapted from a publication in the Journal of Microscopy:

Haffner-Staton E., La Rocca A., Fay M.W. Progress towards a methodology for high throughput 3D reconstruction of soot nanoparticles via electron tomography. Journal of microscopy. **2018**;270(3):272-89.

5.1 - Introduction

The work of the previous chapter demonstrates the development of expertise with electron tomography for soot. As was known prior to the project, a basic 3D-TEM methodology for soot study is far too slow to ever offer a viable alternative to the current state-of-the-art methods. This was confirmed when we applied ET to soot for the first time in the previous chapter. The main topic of this research project was the development of a high-throughput 3D characterisation technique that could challenge traditional 2D-TEM. This would require increasing the throughput of the technique whilst also ensuring that quality remains high enough that a significant improvement over 2D-TEM is realised. The first step was to consider the optimisation of the 3D reconstruction process. Various methodologies for the different stages of 3D reconstruction were to be compared in order to find the optimal conditions for both high quality and high speed. This chapter considers the optimal choice of tilt-series arrangement (*i.e.* tilt-range and increment size), reconstruction algorithm (back-projection *vs.* iterative), and segmentation protocol (use of interpolation with manual segmentation). Optimisation of image acquisition is considered separately in chapter 6.

The outcome of the previous chapter was the application of ET to an FG soot nanoparticle. This would act as the primary data set with which to begin optimisation of the ET process for soot. In addition to this, samples were prepared for GTDI soot-in-oil from a real passenger vehicle. The FG soot nanoparticle was used effectively as a standard because it represents an *extreme* case study in many senses. The FG soot nanoparticle is very large and complex in comparison to most soot-in-oil nanoparticles that are observed in this thesis, and were observed in previous work by the group [40, 41, 70, 198]. The tilt-series images are also relatively low resolution. Because of this the FG soot nanoparticle should be particularly difficult to reconstruct and segment accurately, so is useful for benchmarking a worst case scenario. GTDI soot-in-oil nanoparticles have generally been observed to possess distinctly different morphologies to typical FG soot, being generally smaller, less complex, and more 2-dimensional [40]. As study of GTDI was the goal for the work performed in this thesis, 6 example GTDI soot-in-oil nanoparticles were included to represent a more typical level of difficulty.

In order to efficiently assess the reconstruction algorithm, tilt-series conformation, and segmentation method, the investigation was carried out in a cascade arrangement (see figure-5.1 for a graphical representation). That is to say, a particular set of variables was isolated and the optimal result incorporated into the following tests. The initial optimisation tests were conducted only with the FG soot nanoparticle for the reasons

given in the previous paragraph. As the computational reconstruction step possesses the most scope for long durations, it was the first step the be considered. Two of the most commonly used algorithms were tested; WBP and SIRT. Following the comparison of the two methods, the optimal algorithm would be used in all following reconstructions. Next, the maximum tilt-range of the tilt-series (±60°, ±50°, and ±40°) and the size of the increment between images (1°, 2°, 3°, 5°, and 10°) was investigated. Finally, the effect incorporating varying degrees of interpolation into a manual segmentation process was considered. Manual segmentation was performed every *n* images in the tomogram, where *n = 5, 10, 15, 20*. Linear interpolation was used to automatically generate the intermediate ROIs in the tomogram. Increased contribution from linear interpolation reduces the time required for manual segmentation, but results in inaccurate ROIs. While only the FG soot nanoparticle was considered for the first 4 levels of the cascade, the 6 GDI soot-in-oil nanoparticles were also used in the final level.

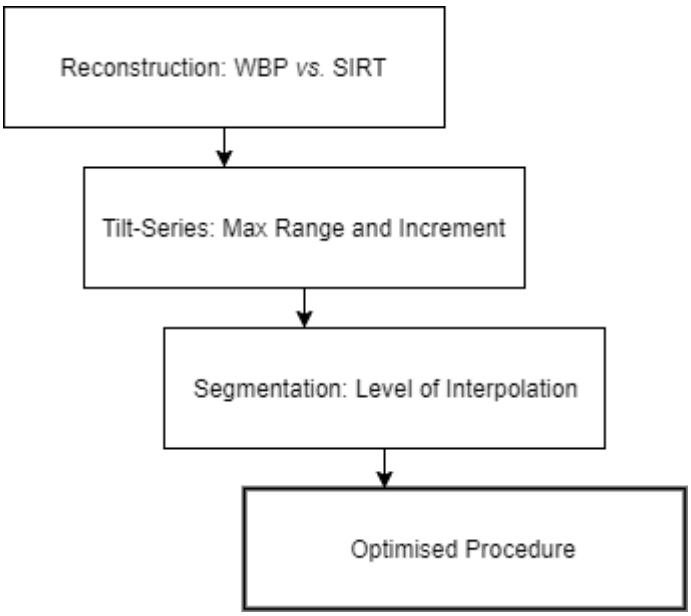


Figure-5.1: The cascade design of the optimisation investigation

5.2 - TEM Study of GTDI Soot-in-Oil

Details on the sample preparation of GTDI soot-in-oil for TEM imaging are provided in section-3.4.2. As mentioned, preparation of high-quality samples of the GTDI soot-in-oil required some degree of trial and error due to the low soot concentration, and difficulty of removing oil contamination. Once a suitable grid had been created, the sample was studied in a primarily qualitative sense by standard 2-dimensional TEM,

HR-TEM, and EDX. Overall, concentration of solid carbonaceous material on the grid was adequate but perhaps a little lower than ideal. However, the proportion of that matter that was in the form of typical soot nanoparticles was low. In terms of study nanoparticle morphology, this would make it difficult to quickly identify structures of interest. This was particularly prominent in the case of tilt-series acquisition with its additional constraints on particle location. A significant amount of time was required for the operator to identify structures of interest for tomography. The small scale of soot in relation to the size of the grid makes manually searching the grid inefficient, and would be a significant bottleneck in a full-scale 3D soot study. Figure-5.2 shows a low-resolution (x10,000 magnification) image of the TEM grid, showing typical concentration and population. The structures identified in this image are discussed shortly.

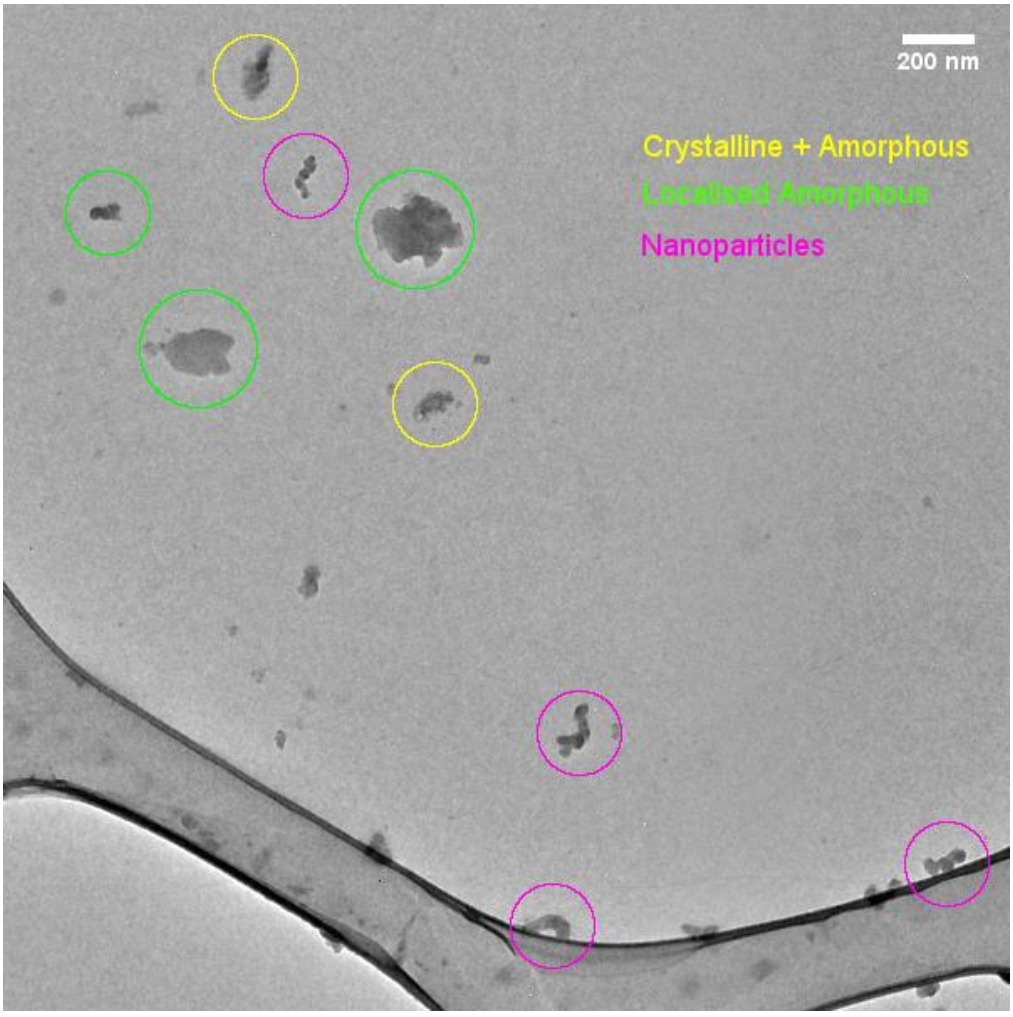


Figure-5.2: TEM image of GTDI soot-in-oil acquired at x10,000 magnification. Annotations show examples of commonly observed structures

Large areas of the TEM grid were considered to understand the nature of the particulate matter that had been extracted from the lubricant oil. A comprehensive analysis of the nanostructure of this sample in comparison to diesel soot-in-oil, carbon black, and an additional GTDI soot-in-oil sample was performed by my colleague, and fellow PhD student, Sebastian Pfau [108]. Some of the observations included in this section are also included in that work.

In general, 3 types of structure were most prominent on the grid. Firstly, the typical soot nanoparticle formed from primary particles (figure-5.3). These structures tended to be fairly small overall, displaying only a moderate degree of branching. They were also highly robust, displaying no appreciable signs of damage or restructuring under the electron beam, even at high resolution. Previously, study of diesel soot-in-oil nanoparticles also found more modest sizes in comparison to what typically is observed for flame-generated soots, with average length of around 120 nm [41, 141].

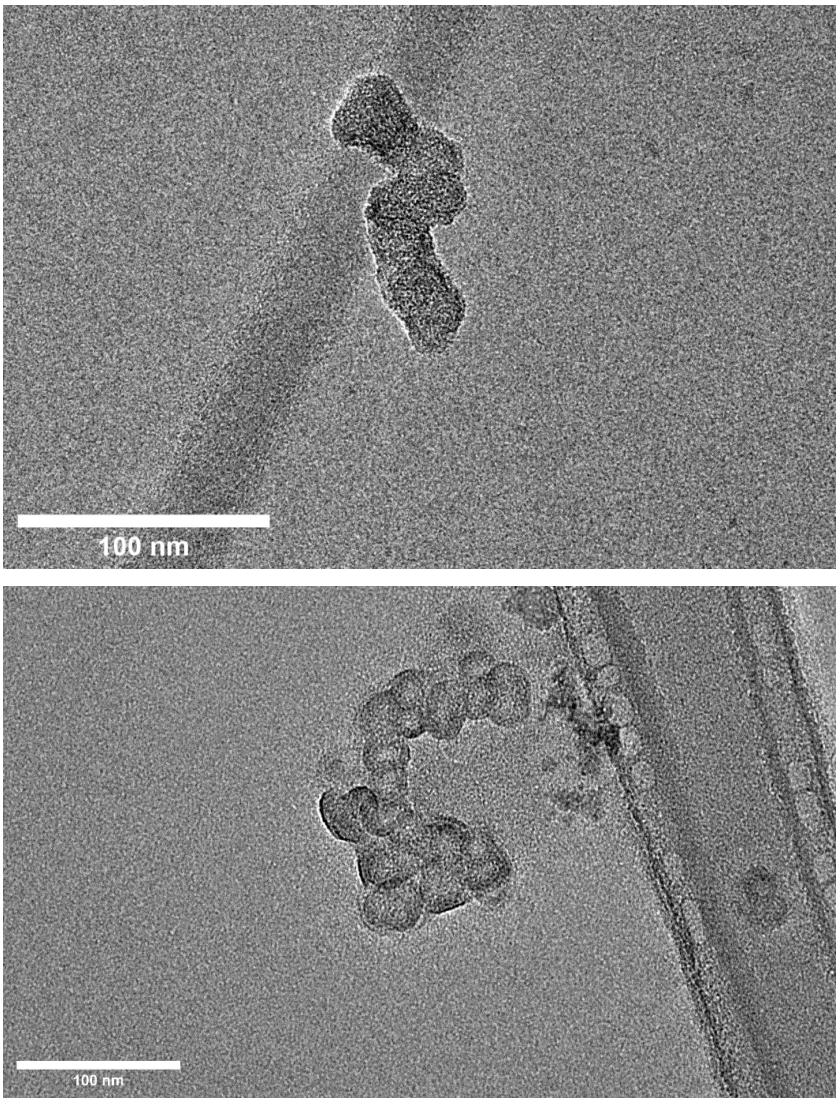


Figure-5.3: TEM images of GTDI soot-in-oil nanoparticles

An interesting observation was that soot nanoparticles seemingly had a slight preference for adhering to the lacey carbon support rather than the graphene oxide. In fact, this can be observed in both figure-5.2 and figure-5.3. In some cases this is due to breakage of the GO film; there is only lacey carbon for the soot to be attached to. In areas where there was ample GO however, soot was still often found at the edges of the lacey carbon. A possible cause for this observation may be differences in polarity of the two support materials; while GO is more polar due to its higher oxygen content, the amorphous lacey carbon should be more apolar. This may indicate that these GTDI soot-in-oil nanoparticles tend to have low surface polarity. In future, if detailed surface analysis of this sample were carried out it could be expected to observe low surface reactivity and concentration of oxygen functional groups.

High-resolution TEM imaging of the primary particles was employed to understand the nanostructure of the aggregates. A typical core-shell structure, with nuclei consisting of several fullerenic centres and turbostratic carbon, and a shell of concentric graphitic micro-crystallites, was observed for most nanoparticles (figure-5.4).

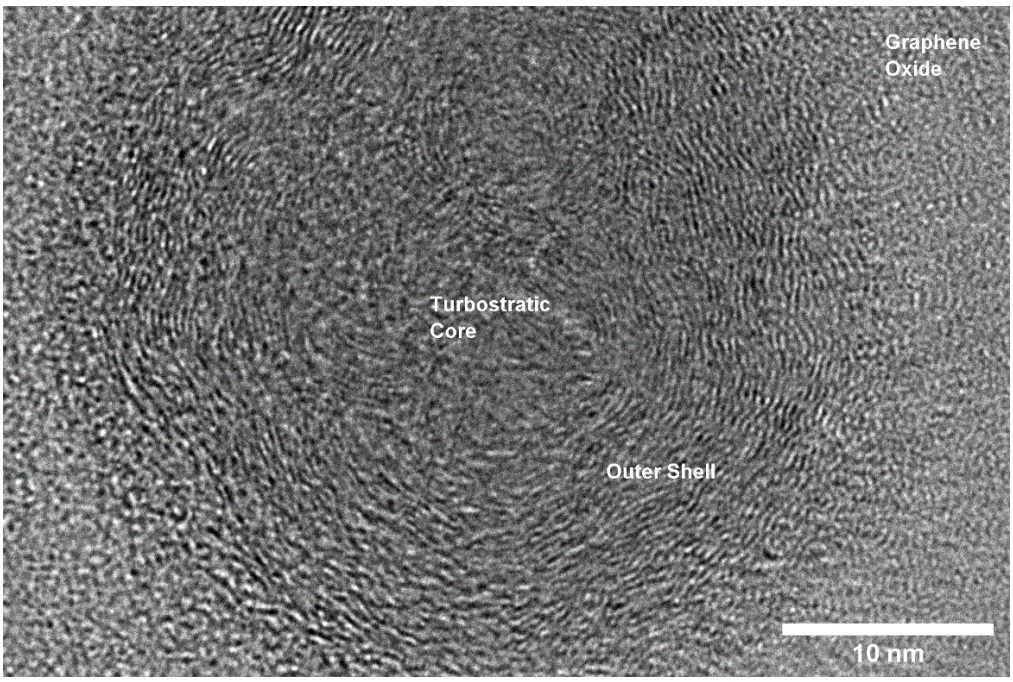
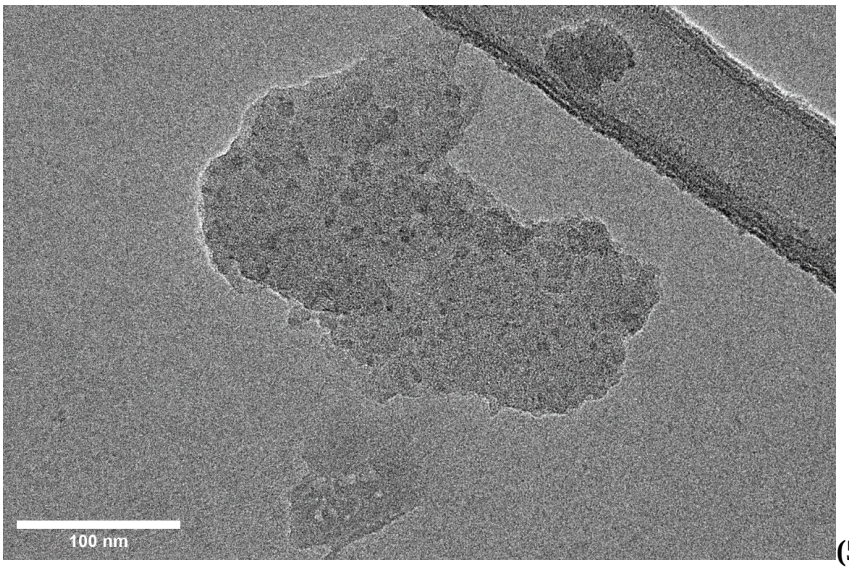


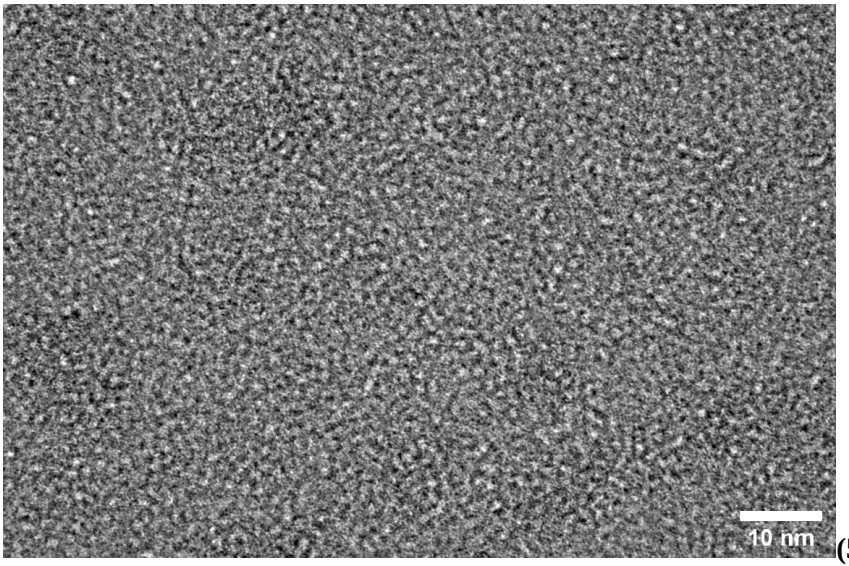
Figure-5.4: HR-TEM image of primary particle, with annotations showing location of amorphous graphene oxide film, concentric fringes of the outer shell, and disordered fringes of the core.

In addition to nanoparticles, a common observation was presence of localised amorphous carbon (figure-5.5). EDX analysis was used to confirm this material was predominantly carbon in structure, though no clear long-range ordering of atoms (*i.e.* crystallinity) could be observed in the nanostructure (figure-5.6). The amorphous

carbon structures were present in isolation, as well as in combination with typical nanoparticles. Previously, study of GDI soot-in-oil by Uy *et al*. had observed similar structures which they described as "soot-like" [21]. While in that study such structures were noted to be prone to beam contamination, in this study such effects were not observed, and the amorphous carbon appeared highly resistant to the electron beam.



(5.5a)



(5.5b)

Figure-5.5: (a) TEM image showing localised amorphous structure. Note inclusion of small darker patches, relating to crystalline material. (b) HR-TEM of amorphous carbon (a different particle to above) showing minimal ordering.

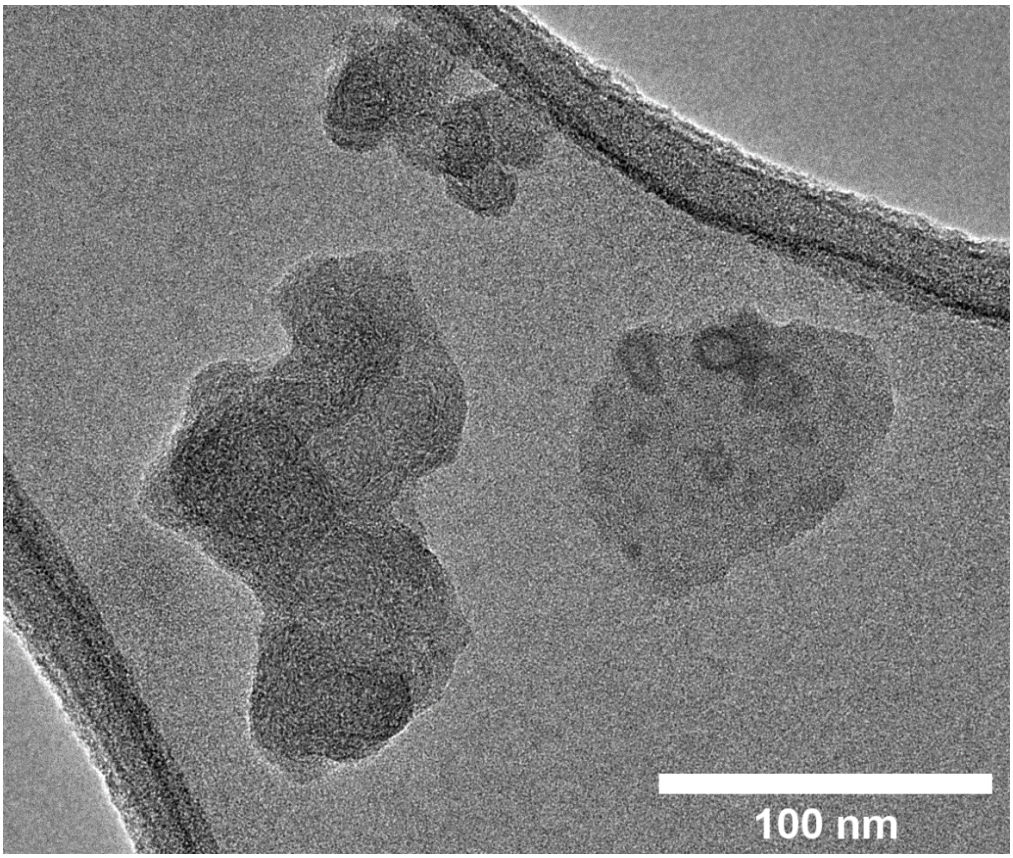


Figure-5.6: TEM image at x50,000 magnification suggesting presence of graphitic order in a nanoparticle (left and upper), and lack of order in amorphous section (right). Note primary particle-like structures inside amorphous carbon

Finally, this sample also contained significant quantities of apparently crystalline material (figure-5.7). Dark, grainy patches were observed both in localised patches, and in combination with amorphous carbon structures (*e.g.* figure-5.5). HR-TEM analysis observed presence of crystal lattice structures, and such areas were prone to restructuring and damage under the electron beam (figure-5.8) .

Previous study of diesel soot-in-oil by Sharma *et al.* had observed presence of crystalline structures within nanoparticles [214]. EDX results were suggestive of lubricant additives as their origin. In this work, EDX was performed to a qualitative level on typical crystalline patches. The determination of background spectra and repeat results were quantitatively carried out, due to the exploratory nature of the work at that stage. In comparison with empty areas of the graphene oxide film, these structures displayed increased levels of Ca, S, and P, which are associated with common lubricant oil additives [21, 108, 214-216].

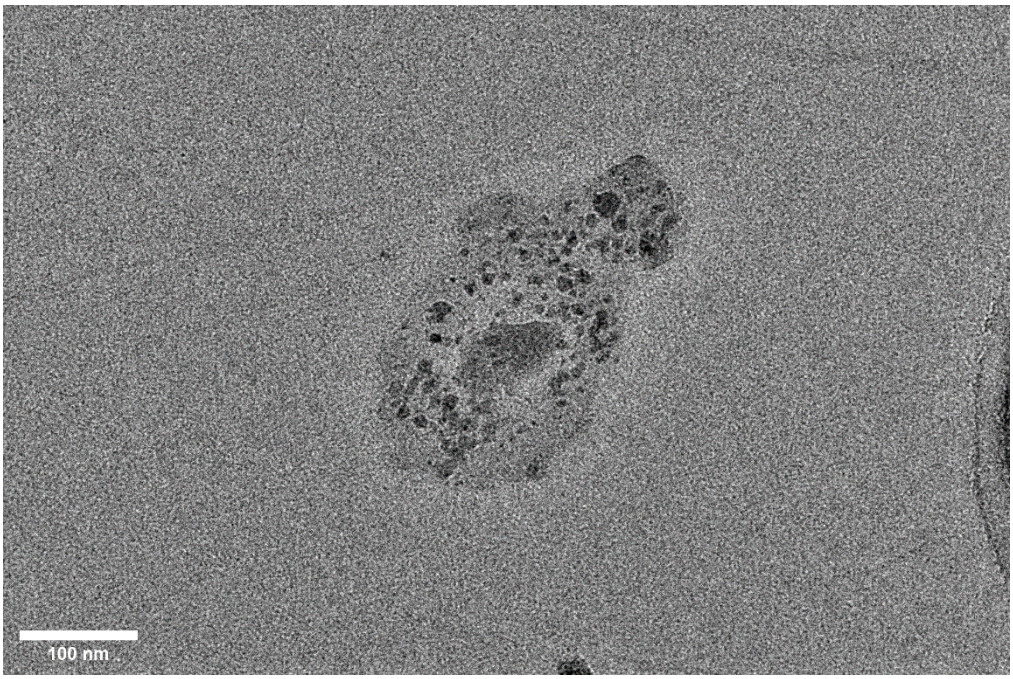


Figure-5.7: Standard TEM image showing patch of grainy crystalline material.

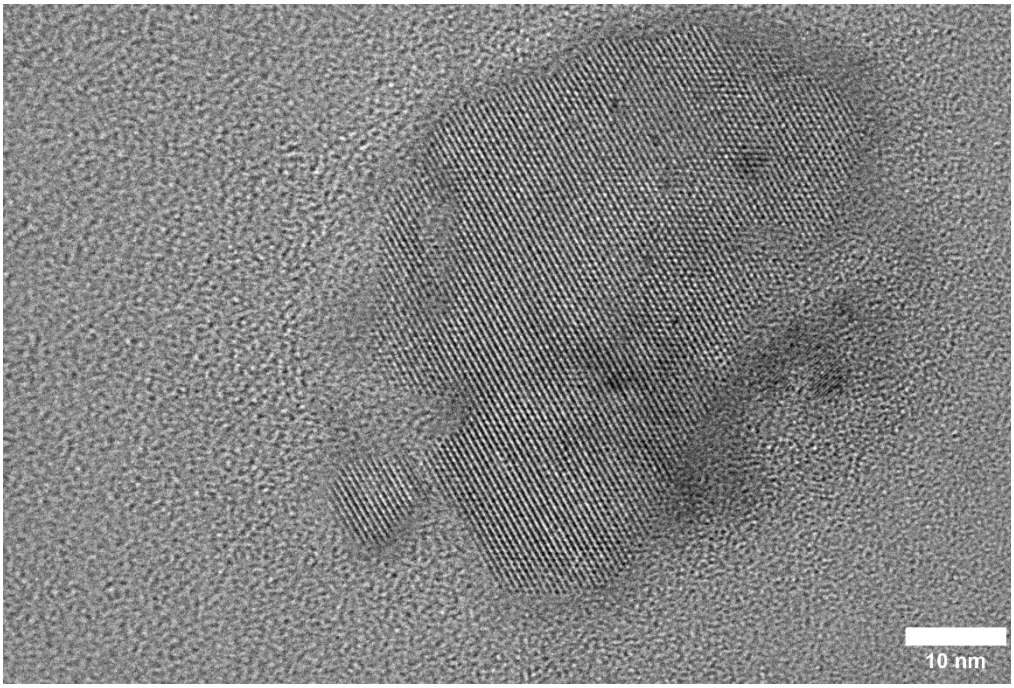


Figure-5.8: HR-TEM image showing presence of crystalline material *via* regularly spaced fringes

In general, the literature contains very few examples of the study of gasoline soot-in-oil. Those studies that have been carried out have tended to observe particular differences in characteristics *vs.* exhaust soot and even diesel soot-in-oil [21, 108, 217]. The observations here are no exception. The study of gasoline soot-in-oil is a promising and exciting area of research, and of particular importance given the increasing

popularity of new GDI engine technology in recent years. In particular, presence of the non-soot carbonaceous and inorganic materials seen in this sample may have important consequences for the study of the soot-oil relation.

5.3 - Tomographic Reconstruction: WBP vs. SIRT

Two of the most commonly used tomographic reconstruction algorithms were tested; WBP and SIRT. These two methods are both incorporated directly into Etomo, and applicable to soot. While there exist a number of advanced algorithms, such as those mentioned in the experimental and literature review sections [191-194], these are not generally available in open source software such as Etomo. Development of advanced methods is generally performed in-house by research groups according to their specific needs, and while described in publications are not available to use in general. It was also not the scope of this project to develop our own in-house method; the scope was very much to use established methods to create an optimized technique. In any case, many advanced techniques require prior knowledge, such as that of expected grey-levels in DART [191, 192]; such information does not exist for soot. Also, it is implicit that advanced techniques take significant longer than even basic SIRT reconstruction. Regardless of accuracy it is highly unlikely such methods would ever be viable in an optimized technique, as too many individual particles are required to be reconstructed for reliable soot sample characterisation.

Using Etomo, both the standard WBP reconstruction process and SIRT with 50 iterations were applied to the FG soot nanoparticle. For this first stage of optimisation all images within the ±60° tilt-range were included in the computation. As mentioned, the tilt series consisted of 121 individual 16-bit images, 1000 x 668 pixels in size. The tomograms and models produced by the two algorithms will referred to as *FG-WBP* and *FG-SIRT*. For distinction of the two different levels of iterations of the SIRT algorithm used, the names $FG\text{-}SIRT_{50}$ and $FG\text{-}SIRT_{30}$ will be used where appropriate.

5.3.1 - SIRT: Choice of Iterations

The quality of SIRT reconstruction is known to improve with increasing number of iterations. However, as each iteration contains the equivalent of 2 back-projections it can be many times slower than WBP [166]. Commonly, SIRT is performed with between 30 and 50 iterations [166], though in some cases as many as 100 are used [37,

194]. The choice was made to perform SIRT with a fairly high number of iterations in the first instance (50), rather than working from lower iterations upwards. In theory, this should ensure that first time a tomogram is produced it is towards the upper limits of SIRT accuracy. If the accuracy was not significantly better than WBP, then it would mean we would have avoided a time-consuming process in which we might have moved stepwise through increasing numbers of iterations. With that in mind we did also perform a reconstruction with 30 iterations for comparison. This number is more similar to that which has been used to study soot by other authors [34, 36, 218]. While not subjected to the same complete testing that is described in the following sections, the resulting tomogram was used to contextualise the effect of increased iterations.

5.3.2 - Reconstruction Details

In Etomo, the same choice of fiducial markers was made to align the tilt-series for both algorithms. Alignment for the FG soot nanoparticle required around 5 minutes to complete, needing only a small degree of operator correction. Both reconstructions were performed using default settings (other than number of iterations for SIRT), and set to produce a tomogram 300 slices thick in the Z-direction. Resulting tomograms were handled in Fiji for segmentation, and were trimmed in the Z-direction to the upper and lower limits of the particle structure. The FG-WBP tomogram measured 203 nm in the Z-direction, while the FG-SIRT tomogram measured 202 nm. In the previous chapter it was noted that the FG-WBP tomogram erroneously included a small, adjacent soot structure that was observed in the tilt-series to be unattached. While it was easy to remove the small section from the tomogram, for consistency between the multiple segmentations used in this work this structure remained attached for all measurements. Hence, the values of morphological parameters reported in this chapter will be slightly different compared to those in the previous chapter.

For both particles, manual segmentation was performed on all slices contained within the tomogram. Morphological characterisation was performed according to the methods described in the experimental section. The nanoparticle was measured in terms of volume, surface area, radius of gyration, 3D-circularity, and fractal dimension. In reference to the use of BoneJ for the surface area measurement, a resampling factor of 2 was used as in the previous chapter. The cube-set used in the Df calculation was again based on Lottin's 2013 study [156], where maximum cube-size is set to approx. equal to the mean primary particle diameter, and minimum cube-size was in the region of 10-20% of this size.

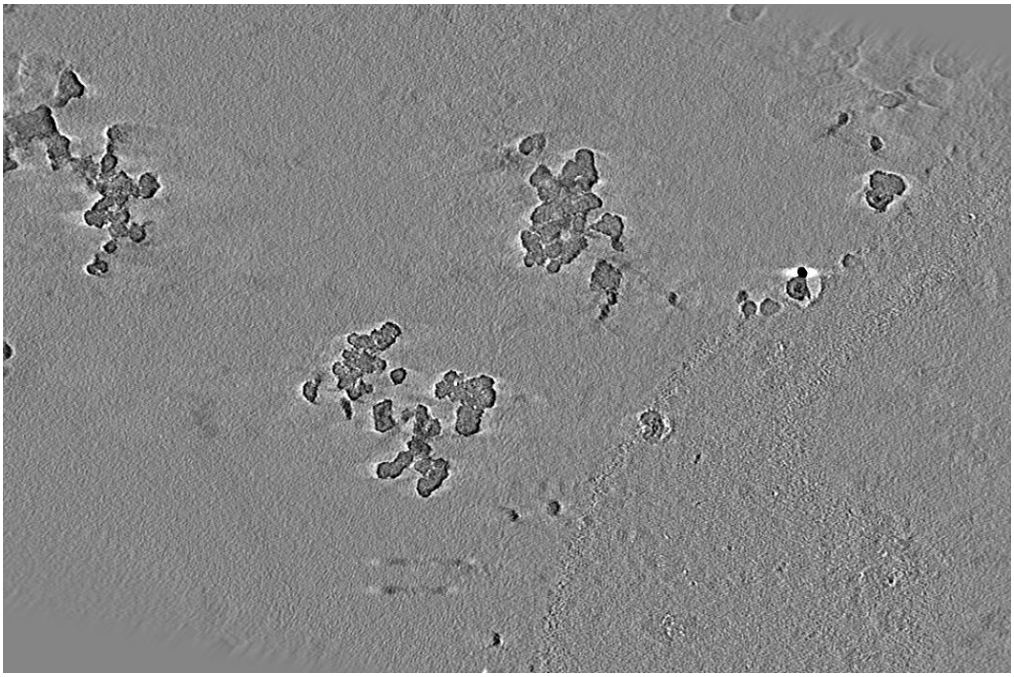
As expected, the weighted back-projection algorithm completed much more quickly than the iterative technique, taking only around 30 seconds. For SIRT reconstruction with 50 iterations the computational step took 135 minutes to complete. By comparison, SIRT with 30 iterations completed in 94 minutes. With a view towards high throughput characterisation of soot nanoparticles, even at this early stage it appeared that the SIRT method could be too slow regardless of the quality of reconstruction. Our overall aim is to develop a method to characterise soot samples to a higher level of detail than current methods allow, but within a similar time frame. Characterisation of the average morphology of a soot sample requires the consideration of upwards of 100 particles [70], and at this speed would take around 1 month simply for the production of the tomograms, and therefore even longer for the full characterisation. Given the time required for the computation, SIRT must present pronounced improvements in reconstruction accuracy in comparison to the WBP method to even be considered.

The quality of reconstruction was assessed both quantitatively and qualitatively. In a qualitative sense, the tomograms were compared by considering their visual appearance (noise, contrast, *etc.*) and the ordering of particle matter within the slices. Quantitative analysis was performed by comparing the values of volume, surface area, fractal dimension, 3D-circularity, and radius of gyration measured from each of the 3D particle models. Ideally, quantitative comparison of the two methods would be carried out in terms of absolute accuracy *vs.* the exact values for the nanoparticle. For future reference, such data (exact morphology results for a nanoparticle) is known as *ground truth*, and this term will be used frequently in chapter-7. Of course, for real soot nanoparticles ground truth morphology does not exist. In the chapter-7, artificial ground truth data in the form of simulated soot nanoparticle models is created, and used to assess overall accuracy of soot reconstructions. It was not required for the FG soot particle as direct comparison of WBP-derived and SIRT-derived morphology revealed the two methods to be extremely similar. So while absolute accuracy could not be confirmed at this stage, we were at least able to consider *relative* accuracy of WBP and SIRT. Morphological results for both the FG-WBP, and FG-SIRT reconstructions are given in table-5.1 later in the text.

5.3.3 - Qualitative Analysis: FG-WBP vs. FG-SIRT

Firstly, a direct visual comparison of the tomograms was performed. As mentioned, both the FG-WBP and FG-SIRT tomograms had been trimmed in the Z-direction to the edges of the particle matter. This resulted in only 1 slice difference in tomogram Z-

depth for the two methods. Figure-5.9 shows examples of comparative slices from the two tomograms.



(5.9a)



(5.9b)

Figure-5.9: Comparative slices from FG-WBP tomogram (a) and FG-$SIRT_{50}$ tomogram (b)

Equivalent slices from the tomograms were viewed side-by-side from the default XY-plane view used in Fiji segmentation. Overall, the definition of the particle from the background due to the differences in contrast was of very similar quality. In terms of

the *character* of the image quality, there were some differences. The FG-SIRT tomogram possessed a smoother, and more photographic quality. By contrast, the FG-WBP slices were slightly more noisy, with grainy patterns more easily visible. However, blurring from fanning effects appeared more prominently in the background in the FG-SIRT tomogram. Though visibile, this did not significantly obscure the particle matter. Despite these differences, the overall image quality was very similar and lead to a similar degree of subjectivity during manual segmentation.

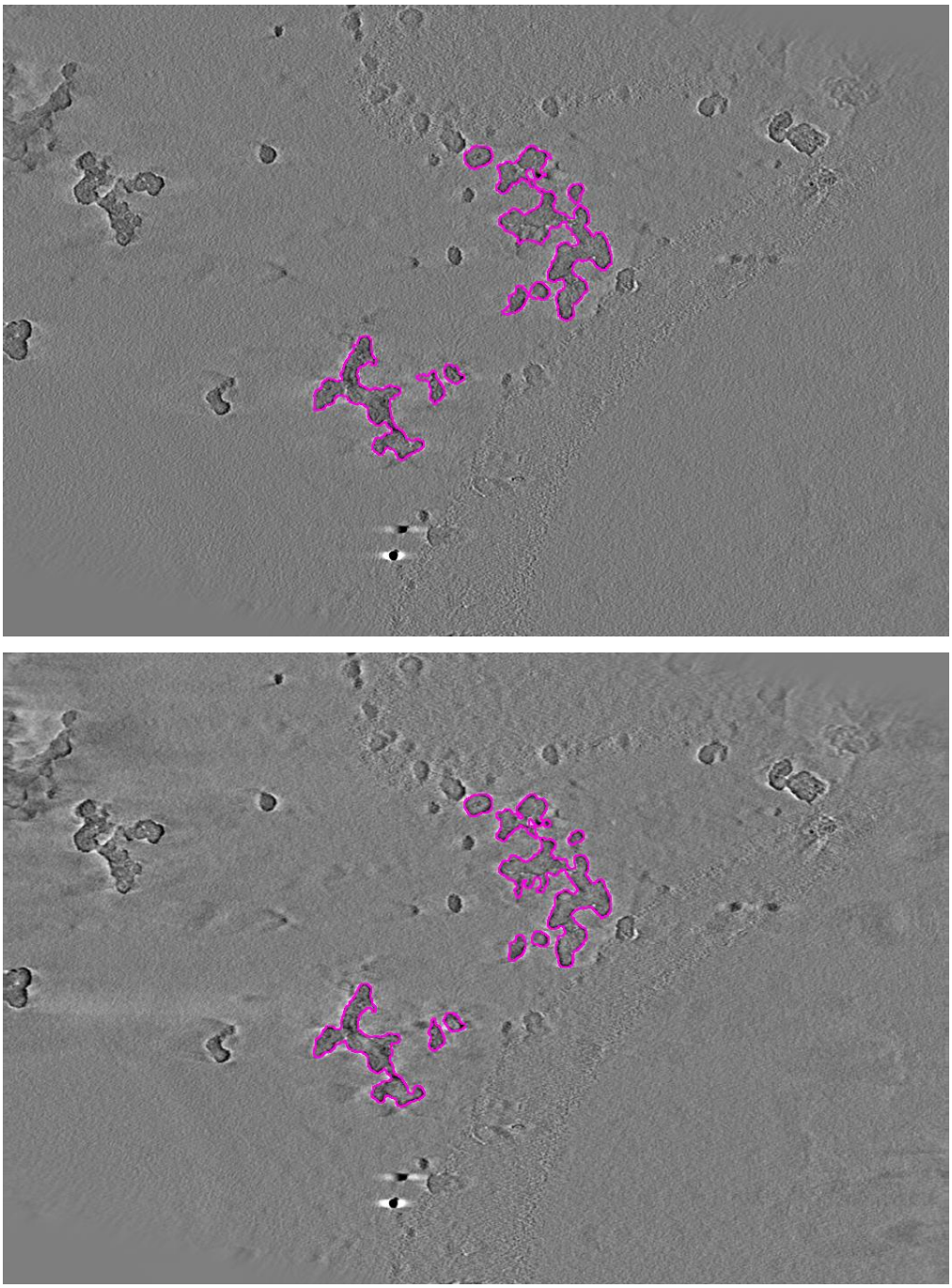


Figure-5.10: Comparative slices from FG-WBP and FG-SIRT tomograms, superimposed with ROI selection of the other tomogram. (Above) FG-WBP with SIRT ROI, (below) FG-SIRT with WBP ROI

After segmentation the content of each of the tomograms were compared by superimposing the ROI set for FG-WBP onto the FG-SIRT tomogram, and *vice versa*. As has already been mentioned, the tomograms were very similar in size after trimming in the Z-direction. The superposition of the ROI sets (shown in-5.10) showed that the ordering of particle matter within the tomogram slices was essentially identical. When the FG-WBP ROI set was viewed with the FG-SIRT tomogram, the selections appeared to be almost exactly correct. The same result occurred when overlaying the FG-SIRT ROI set onto the FG-WBP tomogram. By these qualitative standards, the result is that SIRT and WBP reconstruction appear to have produced tomograms of near identical content and quality.

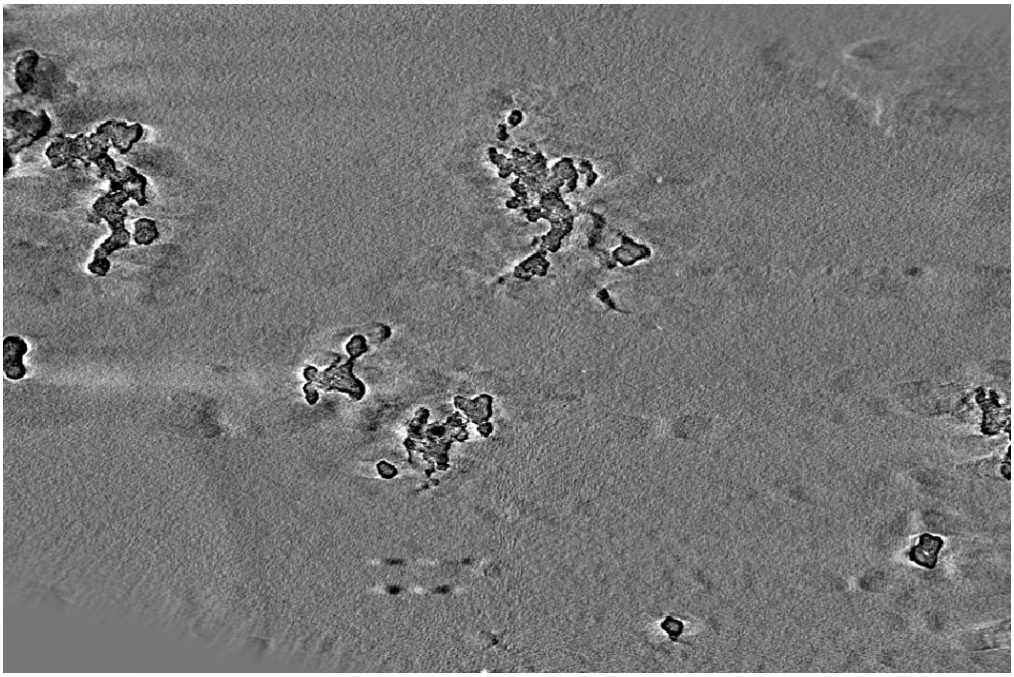


Figure-5.11: Slice from the $SIRT_{30}$ tomogram. This image was taken from exact same tomogram depth as those in figure-5.9. Note greater prevalence of fanning effects, and difference in the shape of the particle matter visible.

5.3.3.1 - SIRT with 30 iterations

For comparison, a tomogram was produced *via* SIRT with 30 iterations. Viewing the tomogram slice-by-slice it was easy to notice quite distinct differences in image quality *vs.* both FG-WBP and $FG\text{-}SIRT_{50}$ (see figure-5.11). Though the contrast between particle matter and background was good like for $FG\text{-}SIRT_{50}$ and FG-WBP, both noise and fanning effects were more prominent. In particular, the 'shadow' of fanning effects around particular features continued through numerous slices both before and after the structure itself was visible in the tomogram. While also visible in both the FG-WBP and

FG-SIRT$_{50}$ tomograms, the presence of light-coloured rings around particle matter was much stronger for FG-SIRT$_{30}$.

By viewing comparative slices side-by-side it was observed that the FG-SIRT$_{30}$ tomogram was *not* identical in content to the FG-WBP and FG-SIRT$_{50}$ tomograms. In fact, superimposing of the other ROI sets showed distinct differences in ordering of the particle matter in the FG-SIRT$_{30}$ tomogram (see figure-5.12). It is known that increased iterations of SIRT improve the accuracy of reconstruction, and also that WBP arrives closer to the true result than SIRT does when performed with a low number of iterations. Bearing in mind the close agreement between the FG-WBP and FG-SIRT$_{50}$ tomograms, it is therefore logical to assume that SIRT with 30 iterations is producing an inaccurate tomogram to some degree. As such, it reinforces the choice of extended number of iterations as the default, and means that we will not consider lower numbers of iterations in this work any further.

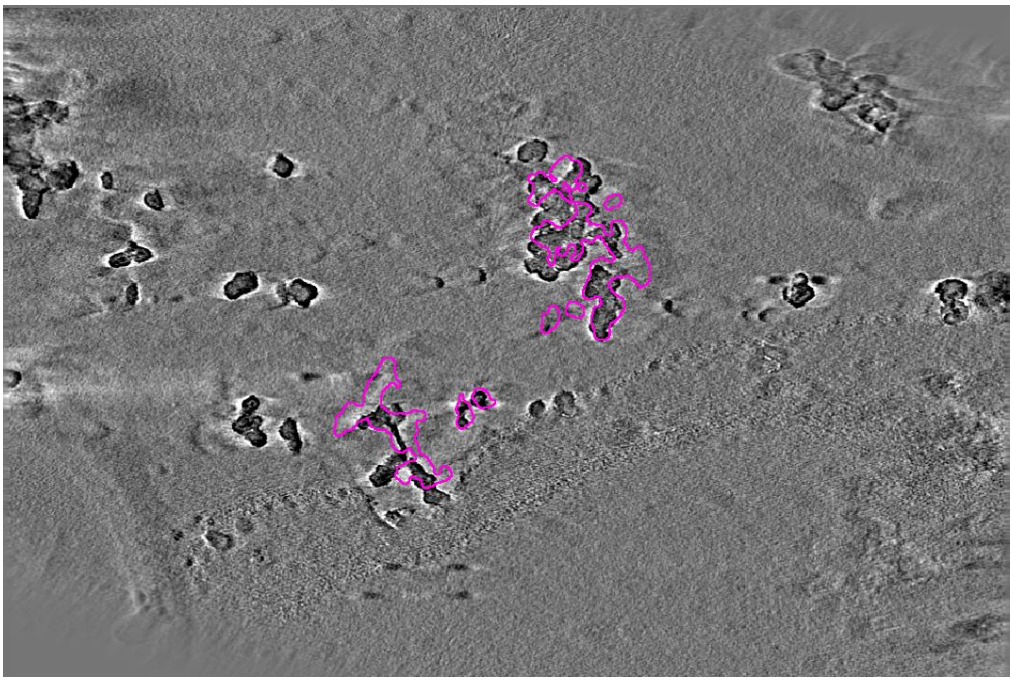


Figure-5.12: Slice from FG-SIRT$_{30}$ tomogram with equivalent slice ROI from FG-WBP tomogram superimposed

5.3.4 - Quantitative Analysis: FG-WBP vs. FG-SIRT

In the absence of ground truth data for the FG soot nanoparticle, quantitative analysis could only be performed relatively between the two methods. As qualitative observations had already shown, there was strong similarity between the contents of each tomogram. As such it was expected that measured morphology of the particle models would be similar. Values for the morphological parameters measured are given

in table-5.1. The difference percentage values shown are the absolute difference in measured values between the two methods represented as a percentage of the average measurement for the two methods. *For the time entry, the difference percentage shown is as a percentage of the FG-SIRT$_{50}$ value only.

Tomogram	Time (mins)	Volume (nm^3)	Surface Area (nm^2)	Radius of Gyration (nm)	3D-Circularity	Fractal Dimension
FG-WBP-1	0.5	1,819,400	309,100	148.59	0.113	2.49
FG-SIRT-1	135	1,920,000	319,500	148.50	0.113	2.50
Difference %	*-99.6%**	*5.4%*	*3.3%*	*0.1%*	*0.4%*	*0.4%*

Table-5.1: Showing measured morphological parameters for the two versions of the FG soot nanoparticle created from the FG-WBP and FG-SIRT$_{50}$ tomograms. The 'difference %' row refers to the difference between the measured values from the two methods, presented as a percentage of the average value of the two methods. In the case of the 'time' column, the value shown is the difference between the methods as a percentage of the FG-SIRT$_{50}$ value.

Generally, these results show close agreement between the two methodologies. In terms of overall particle bulk, the FG-SIRT tomogram produced a larger particle, as shown by the higher volume and surface area values. This is possibly due to the increased prominence of blurring and fanning effects in the FG-SIRT tomogram, as was mentioned earlier and illustrated in figure-5.9. Blurring can act to broaden the edges of the particle matter in the tomogram, which could affect the selection made manually by the operator. The differences for the remaining parameters were even smaller. The factors that describe the complexity of the particle shape (R_g, 3D-circularity, D_f) show extremely small differences, indicating that despite differences in bulk the shape of the particles is very similar. Surface area has been observed on several occasions to have a strong impact factors such as on oil viscosity [32], human health [29], and biological process in marine environments [103, 219], and is therefore perhaps one of the most important morphological parameters that can be measured. As such, it is promising to observe that simple WBP can produce SA values in such close proximity to those produced by SIRT with a high number of iterations, a theoretically higher quality method. Similarly, fractal dimension has been shown to be a key factor in determining the effects of soot such as depth of inhalation of soot by humans [99], lifetime and radiative potential in the atmosphere [101, 102], and coagulation as an aerosol [31]. In

terms of this parameter, the measured values from the two tomograms were almost identical.

Overall, high levels of similarity were observed between WBP and SIRT reconstruction in terms of both qualitative and quantitative analysis. Given the lack of ground truth data with which the truly establish overall accuracy, at this stage it could only be concluded that WBP and SIRT with 50 iterations appear to produce tomograms of approximately equal quality. Given how much quicker WBP reconstruction computations are, at this stage it could only be concluded that WBP is the optimal choice in terms of speed and quality.

5.4 - Tilt-Series Optimisation: Range vs. Increment

The investigation into optimisation continued by considering how the number of images contained within a tilt series would affect the speed and quality of 3D reconstruction. In particular, consideration was given to a reduction in total tilt-range and increases in the size of the tilt-increment. Depending on the type of structures being considered and the type of reconstruction algorithm being employed, tomographers use tilt-series of varying levels of total tilt-ranges and sizes of increments between images [36, 37]. Some more advanced algorithms are able to produce high quality reconstructions from as few as 10 images [37].

It is expected from the underlying Fourier Slice Theorem that a larger tilt-range and smaller tilt increment should result in more accurate reconstruction, as the 3D-FT of the object is more completely sampled [220]. However, if a reduced tilt-range could produce a tomogram of acceptable quality then it may potentially be of some benefit. A reduction in the number of images could save time during acquisition, but perhaps more importantly can help protect more sensitive specimens from damage caused by excessive beam exposure. While the soot-in-oil extraction method from the earlier sections demonstrated that our soot samples did not suffer significant beam contamination [88], this could be important for more problematic oil samples or if the technique were ever extended to non-soot samples that are beam-sensitive. From the full ±60° tilt-series, it was easy to reduce the maximum tilt-range or increase the tilt-increment by simply excluding certain images from the reconstruction in Etomo. This meant it was a particularly convenient way in which to test the limits of our methodology. In this section, 6 models of the FG soot particle were produced from tilt series that varied in the size of increments between images, and the total tilt range. The

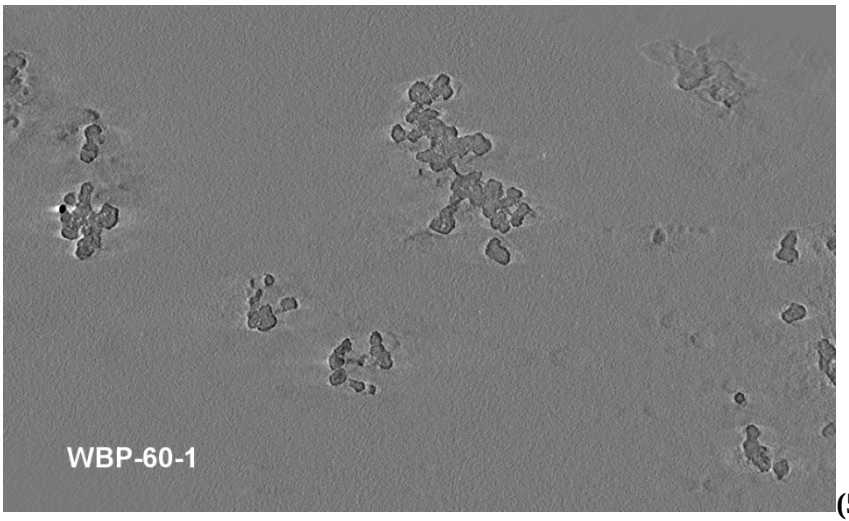
conformations of these different tilt-series, their respective names, and the morphological parameters measured from their resulting particle models are listed in table-5.2. The different reconstruction are named according to: reconstruction algorithm, tilt-series range, and increment size. For example, WBP reconstruction of a ±60 tilt-series with images acquired every 2° is referred to as "WBP-60-2". Reconstructions were performed using the WBP algorithm in Etomo, as per the results of the previous section, and no appreciable difference was noted in the time required to complete the computational step (approx. 30 seconds).

Name	Tilt range	Tilt Increment	No. images	Vol (nm^3)	SA (nm^2)	R_g (nm)	3D-Circ.	D_f
WBP-60-1	±60°	1°	121	1,819,400	309,100	148.6	0.113	2.46
				Values Reported as % difference vs. FG-WBP				
WBP-60-2	±60°	2°	61	4.8 %	2.8 %	0.1 %	0.6 %	0.4 %
WBP-60-3	±60°	3°	41	1.5 %	0.3 %	-0.2 %	1.1 %	-0.4 %
WBP-60-5	±60°	5°	25	-2.5 %	-2.6 %	0.0 %	1.5 %	-0.8 %
WBP-50-1	±50°	1°	101	-4.5 %	-4.3 %	-0.8 %	2.1 %	-1.2 %
WBP-40-1	±40°	1°	81	7.5 %	8.5 %	-0.6 %	-4.8 %	-0.4 %
$SIRT_{50}$-60-1	±60°	1°	121	5.5 %	3.4 %	0.1 %	0.4 %	0.4 %

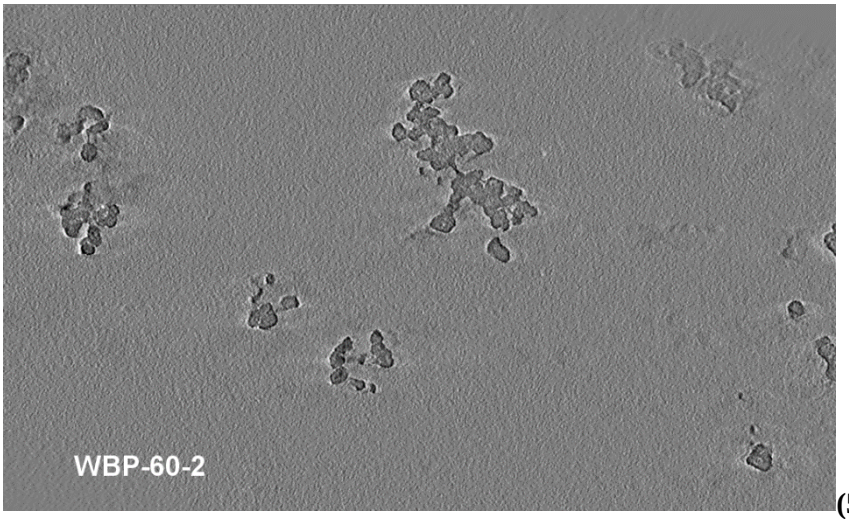
Table-5.2: Different tilt-series conformations used to produce FG soot nanoparticle models. Absolute values of morphological parameters are reported for the FG soot WBP reconstruction. Values for other methods are reported as: difference vs. FG-WBP values, as a percentage of the FG-WBP values. The results of the FG-$SIRT_{50}$ method are also included for comparison

5.4.1 - Tilt-Series Optimisation: Qualitative Analysis

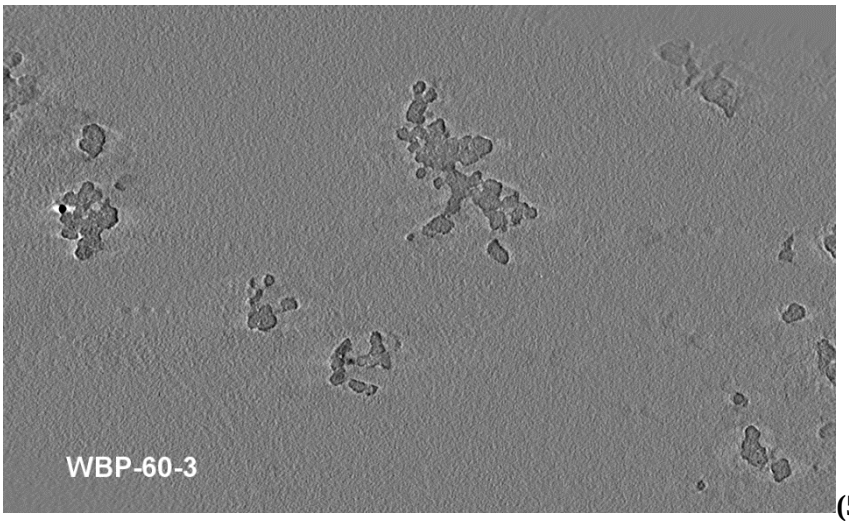
Figure-5.13 shows comparative slices from each of the 6 tomograms. In terms of visual quality, only minor degradation was observed for the WBP-60-2, WBP-60-3, WBP-50-1 tomograms. Graininess and blurring were both slightly more prevalent, but there were no major increases in subjectivity in terms of which pixels determined the edges of the particle matter. For the WBP-60-5 and WBP-40-1 tomograms, these issues were more strongly pronounced.



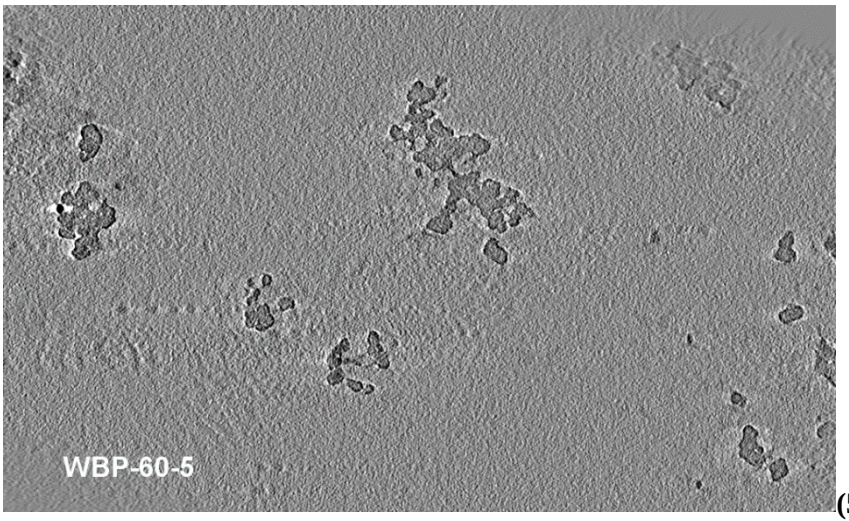
(5.13a)



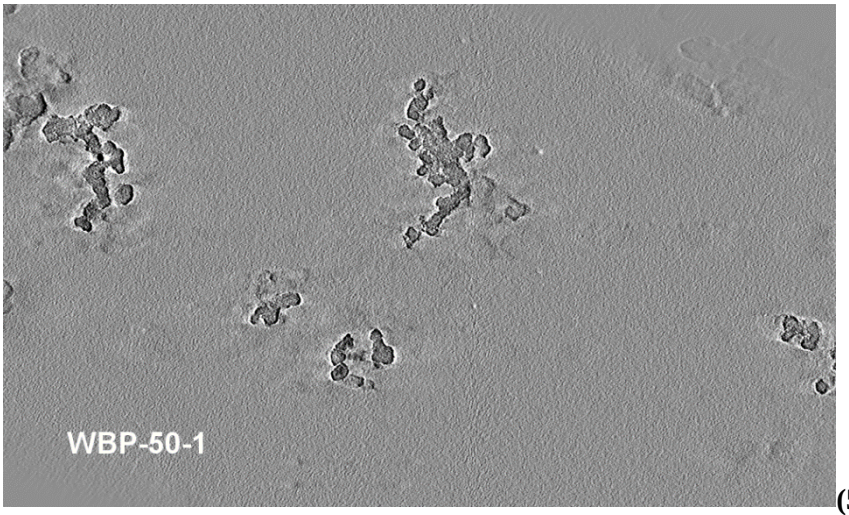
(5.13b)



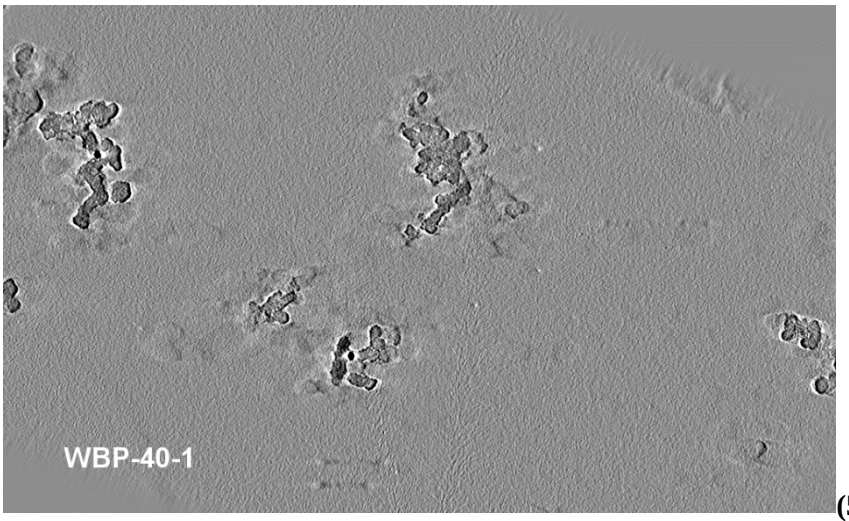
(5.13c)



(5.13d)



(5.13e)



(5.13f)

Figure-5.13: Comparing the central tomogram slices for the different methods of reconstruction involving reduced tilt-series: (a) WBP-60-1, (b) WBP-60-2, (c) WBP-60-3, (d) WBP-60-5, (e) WBP-50-1, (f) WBP-40-1

The reduction in tilt-range (WBP-50-1, WBP-40-1) lead to more prominent blurring effects that were particularly noticeable around the edges of particle matter. This is not unexpected, as blurring relates to the missing wedge, which has increased in size. These effects made it difficult to discern which pixels were truly particle matter and which were related to artefacts. By comparison, the increase in tilt-increment (WBP-60-2,3,5) was observed to more significantly increase graininess and noise than blurring, and decrease the contrast between particle and background. The difference in the propagation of the reconstruction artefacts is again not unexpected as though both included fewer images than the original WBP-60-1 computation, information was effectively removed from different areas of the 3D-FT of the nanoparticle. While the size of the missing wedge was not increased for WBP-60-5, less information was present in the other areas (predominantly XY) causing decreased contrast and resolution. These effects also increased the difficulty of determining where the edges of particle matter began and ended. In a qualitative sense, these three methods were considered to have degraded image quality to the point that the ease of segmentation was significantly affected. While the content of the tomograms is not necessarily affected significantly (see next section for quantitative analysis), the time required for segmentation increased, and confidence in the repeatability diminished significantly.

Initially, it had been planned to also include an WBP-60-10 reconstruction (±60° tilt-series, 10° increments). A tomogram was produced *via* this method, but the quality was extremely poor, and segmentation was not attempted. An example of the tomogram quality is given in figure-5.14.

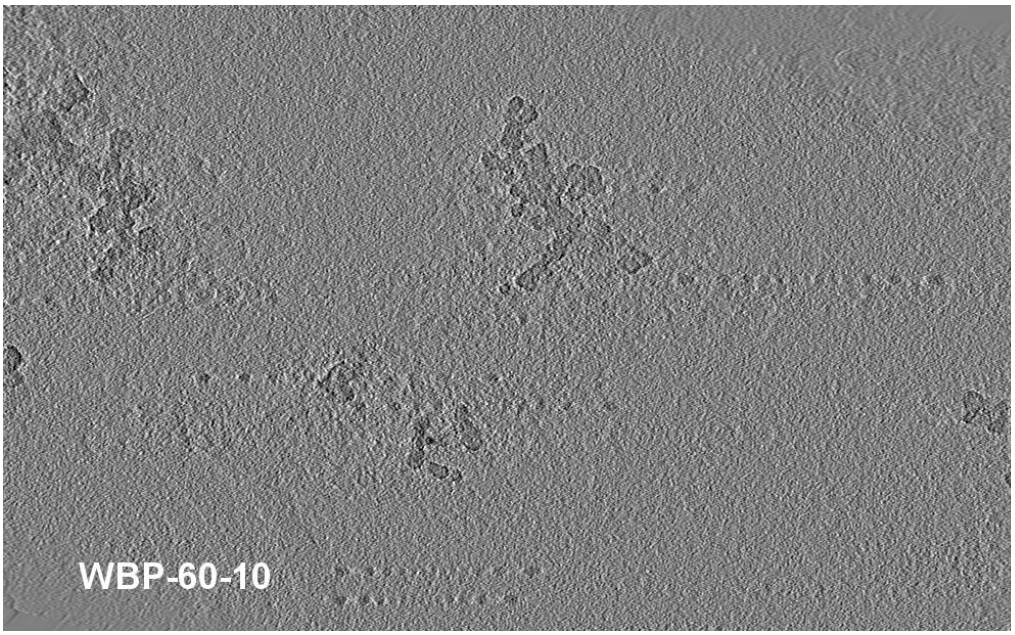


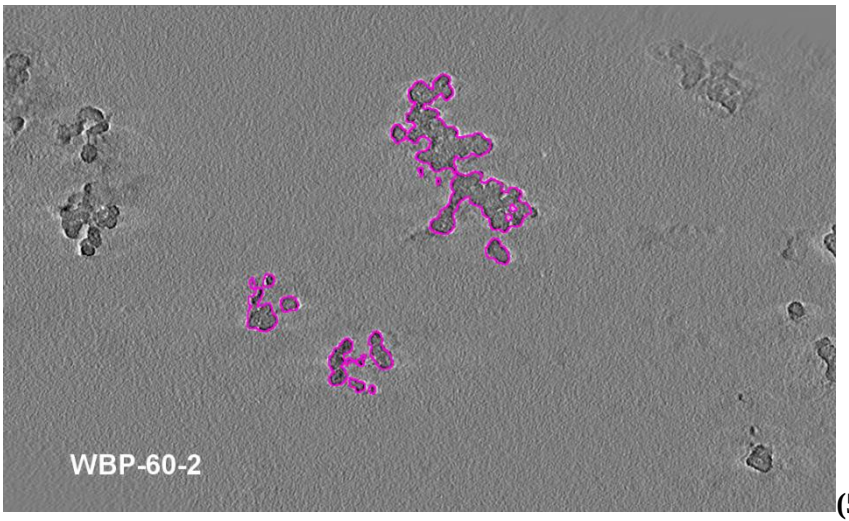
Figure-5.14: Central slice from the WBP-60-10 tomogram

In a similar fashion to that performed during the comparison of the WBP and SIRT methods, the original WBP-60-1 ROI set was superimposed onto all tomograms produced from reduced tilt-series. Given that WBP-60-1 was produced from the most complete tilt-series, this method should provide the most accurate tomogram and as such was used as the standard to which all other tomograms were compared. It was observed that the content of the WBP-60-2 tomogram was essentially identical to WBP-60-1, as in every single slice the ROI selection appeared completely acceptable (as was seen earlier for $SIRT_{50}$-60-1).

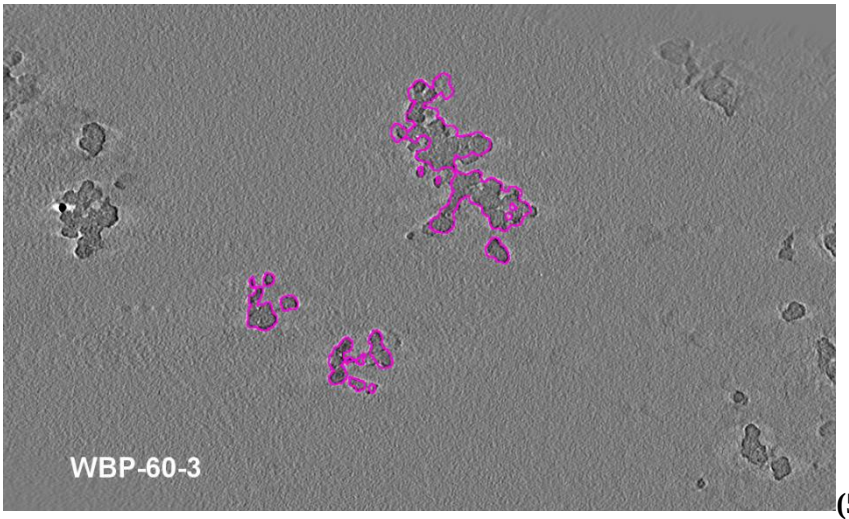
The WBP-60-3 tomogram showed some small differences in comparison to the WBP-60-1 tomogram. While some areas of the tomogram (lower-left area of the nanoparticle) were closely matched throughout the image stack, there was some degree of different ordering of material in other areas (upper right – see figure-5.15). It was not so much that differences were completely erroneous, it appeared more like the same material was present but was simply displaced slightly in space. If the WBP-60-1 ROI set was shifted by a few slices in the Z-direction, then the previously mismatched areas aligned well the ROI selections.

Despite the significant reduction in image quality in the WBP-60-5 tomogram, the content of particle matter was not greatly different to that of WBP-60-1. Rather than a asymmetric mismatching like was described in the previous paragraph, the propagation of difference versus WBP-60-1 was more even over the whole tomogram area. A small degree of relatively stochastic difference was seen in most areas, but there were no regions that were hugely different.

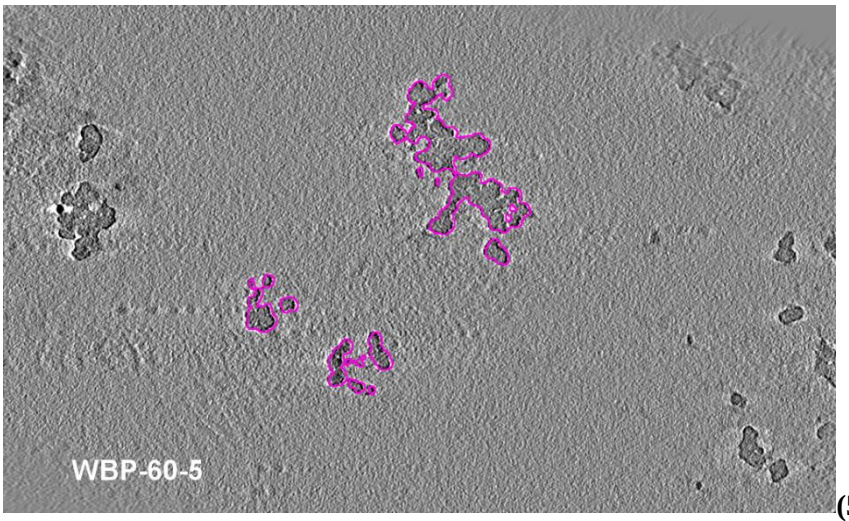
The WBP-50-1 tomogram showed the strongest differences in tomogram content *vs.* the WBP-60-1 tomogram. Not only was the ordering of particle matter in the tomogram largely different, but it was also spatially displaced in most regions. The WBP-40-1 tomogram showed differences versus WBP-60-1 that were most similar to WBP-60-5. Error in comparison to WBP-60-1 was not strongly located to particular regions of the tomogram, but was more significant than was seen for WBP-60-5.



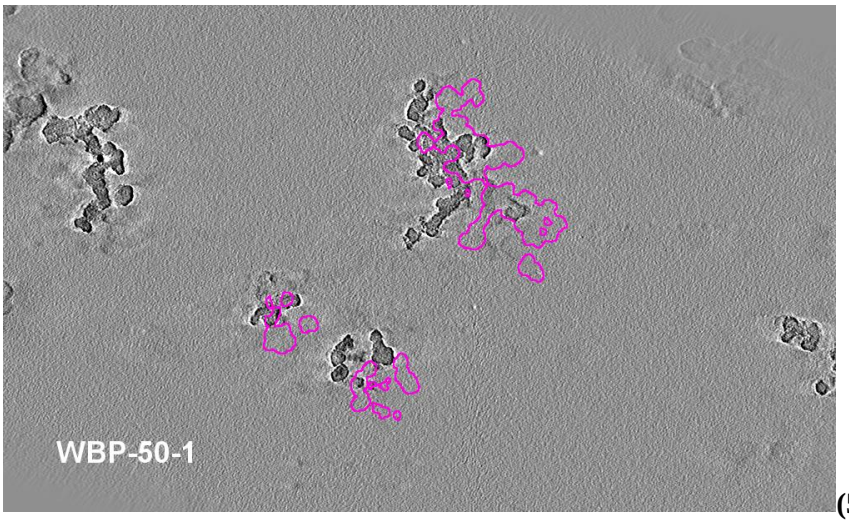
(5.15a)



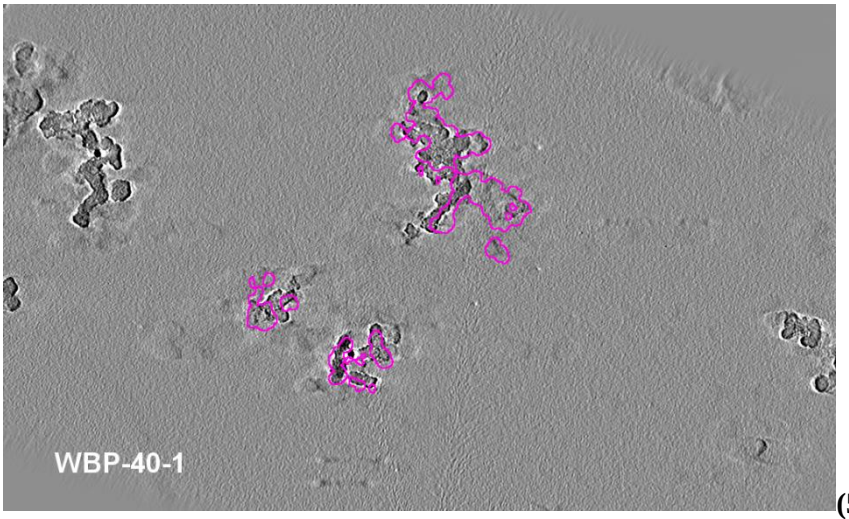
(5.15b)



(5.15c)



(5.15d)



(5.15e)

Figure-5.15: Central slices from tomograms produced from reduced tilt-series, with equivalent ROI from FG-WBP tomogram superimposed.

In the previous sub-section, differences in the content of the $SIRT_{30}$-60-1 tomogram was related to inaccuracies of the SIRT method when performed with insufficient iterations. In this section, they are related to the differences between the content of the full and the reduced tilt-series. The tomogram is a direct product of the back-projection of the input tilt-series. Different compositions of the tilt-series results in a different pattern of interference of the back-projection rays during reconstruction. Although the reduced tilt-series only contain images that are also found in the full tilt-series, the removal of the high-angle images alters the overall contributions from the remaining projections. As such, the areas of strong back-projection interference can change position within the tomogram and result in a different arrangement of the particle matter.

Overall, the results of the qualitative analysis are as follows. The WBP-60-2 and WBP-60-3 methods produced the tomograms with the least degree of image quality

degradation, though both display a small degree of additional of noise, blurring, etc. Both the WBP-60-5 and WBP-40-1 methods saw significant degradation of image quality that significantly hampered manual segmentation, though propagation of reconstruction artefacts was different for the two methods. The image quality of the WBP-50-1 tomogram was fairly good, though significant differences were observed in the ordering of particle matter in the tomogram. Only the WBP-60-2 method produced a highly similar tomogram to the standard WBP-60-1 method, but differences were generally quite small for WBP-60-3 too. Given these results, the optimal protocol for reducing number of tilt-series images appears to be either WBP-60-2 or WBP-60-3. While fewer images are required in the WBP-60-3 tomogram, differences in the ordering of particle matter in the tomogram was observed, and would require quantitative analysis to consider whether this effect is significant or not. The reduction in tilt-range resulted in greater degradation of image quality and differences in tomogram content, while reducing the number of images less significantly. Clearly, reduction of tilt-increment offered a superior route to reducing number of images in the tilt-series.

5.4.2 - Tilt-Series Optimisation: Quantitative Analysis

Again, the lack of ground truth data for the FG soot nanoparticle meant that the morphology of the 3D models could only be compared relative to one another. Given that Fourier Slice theory dictates that the ±60° tilt-series should result in a more accurate reconstruction, and the tomogram slices were of the highest quality, this model was used as the standard to which the results of the reduced tilt-series were compared. The morphological data is presented in table-5.2, also included for comparison is that data for the $SIRT_{50}$-60-1 method. The values reported in the data table show the difference between the particles produced by reduced tilt-series and that produced by the original WBP-60-1 method. These differences are presented as a percentage of the WBP-60-1 values, as this method acted as the standard.

Firstly, from the volume and surface area measurements it can be seen that the reduced tilt-series methods produced particles both bulkier (WBP-60-2, WBP-60-3, and WBP-40-1), and less bulky than the WBP-60-1 particle (WBP-60-5, WBP-50-1). In terms of Vol and SA, only the WBP-40-1 method produced a particle with greater differences than were observed between WBP-60-1 and $SIRT_{50}$-60-1. Given the strong similarity observed between the WBP-60-1 and $SIRT_{50}$-60-1 tomograms, this suggests that the

particle matter contained within the tomograms from reduced tilt-series tends to be highly accurate, despite the differences in spatial arrangement of the particle matter.

Despite the strong degradation of image quality observed for WBP-60-5, and the differences in tomogram ordering observed for some of the other tomograms, overall there was relatively little impact on the morphology of the segmented particles. Radius of gyration and fractal dimension in particular were highly accurate for all of the different methods. Only the circularity parameter seemed to observe some degree of a pattern in the deviation versus WBP-60-1. For the altered tilt-increment methods, circularity deviation increased slightly as number of tilt-series images decreases, and similarly so for the two altered tilt-range methods.

In summary, all methods except WBP-40-1 produced particle models as similar to WBP-60-1 as the $SIRT_{50}$-60-1 method, which in theory should be highly accurate given the high number of iterations. Even the highly noisy and low-contrast WBP-60-5 tomogram was within this consideration. But, considering also the qualitative observations and increased difficulties associated with manual segmentation, this particular method could not be suggested as optimal. As the WBP-60-3 method observed no strong deterioration of image quality, produced a very similar particle to WBP-60-1, and contained the fewest images of the remaining viable methods, it was considered to be the optimal tilt-series configuration.

5.5 - Tomogram Segmentation: Effect of Interpolation

The previous sections have so far revealed WBP as a more efficient algorithm than SIRT, and that high quality tomograms can still be produced when the increment between tilt-series images is as high as 3°. WBP reduced the time required for reconstruction by a huge margin; 30 seconds for WBP *vs.* 135 minutes for SIRT. Tilt-increments of 3° permits reduction of tilt-series images by two thirds, requiring only 41 images over the ±60° range.

The final area assessed for optimisation in this chapter is the use of interpolation in manual segmentation of tomograms. As has been described, manual image processing is the prevailing method for tomogram segmentation as strong variability in appearance, as well as implicit high noise and low contrast, impede development of a generally applicable automated alternative [221]. Use of interpolation is expected to reduce the time required, but lead to inaccuracies in the size and shape of the produced particle as

the interpolation does not make any knowledgeable prediction of the intermediate particle matter.

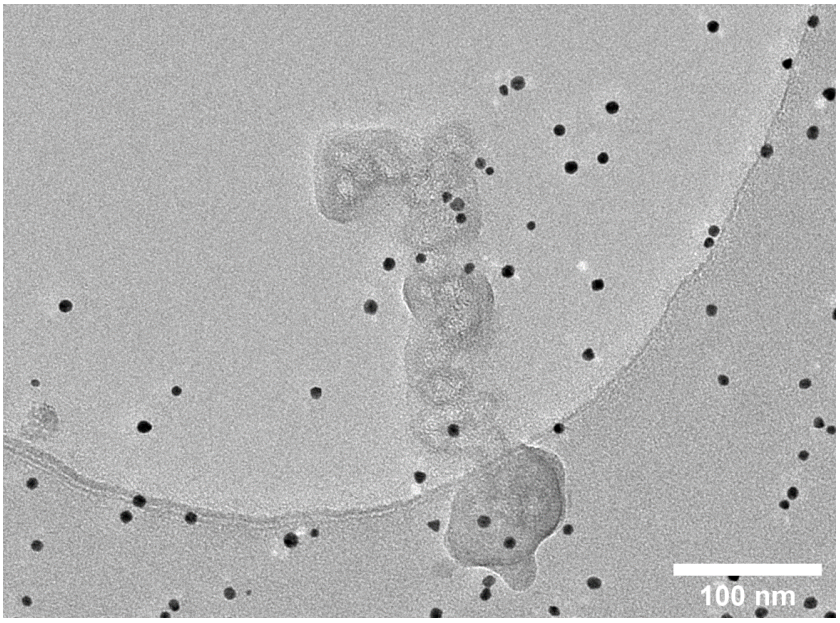
In this section, 6 GTDI soot-in-oil nanoparticles were included alongside the FG soot nanoparticle. Early observation of the GTDI sample, as well as prior study of soot-in-oil species [21, 40, 41, 70, 214], has predicted significant differences in morphology in comparison to flame-generated soot. While FG tends to be highly complex and 3-dimensional, soot-in-oil tend to be smaller and more modest in terms of branching. As study of GTDI soot was chosen as the focus of this work, these nanoparticles were included to account for any differences in accuracy of interpolated segmentation that may arise due to particle morphology. In the previous steps it was considered sufficient to only include the FG soot nanoparticle. The high complexity of shape and relatively low resolution of the tilt-series meant that we could consider this nanoparticle as a 'worst case scenario'. Artefacts from reconstruction and difficulty in segmentation were likely to be strong for this nanoparticle.

The 6 GTDI soot-in-oil nanoparticles had tilt-series acquired with 3° increments between images, as per the results of the previous section. The scale of pixels in the images ranged from 0.2688 nm px^{-1} to 0.6698 nm px^{-1} depending on the size of the nanoparticle. Images were un-binnned and 2004 x 1336 pixels in size, resulting in tilt-series file size of around 200 MB. Reconstruction was performed using the WBP in Etomo. Due to similar file size, the computational step completed in around 30 seconds as it had done for FG soot. Representative TEM images of each of the nanoparticles is shown in figure-5.16.

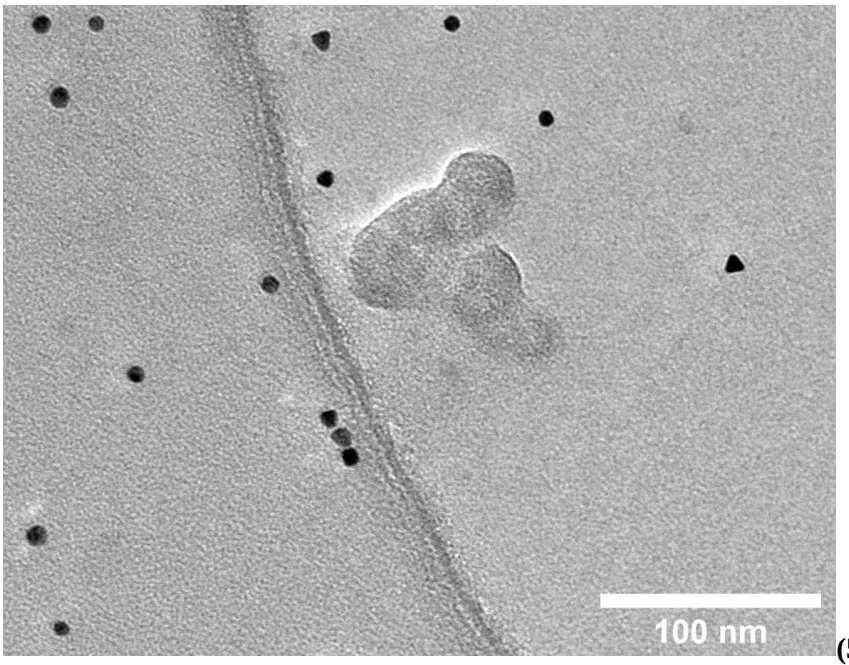
Multiple versions of each particle were produced by segmentation utilizing 5 different levels of interpolation. For each tomogram, manual selection of the appropriate particle matter was performed only every 20^{th}, 15^{th}, 10^{th}, or 5^{th} slice. The intermediate ROI selections were produced *via* linear interpolation using Fiji. Additionally, particles were produced by manually considering the particle matter in every slice, with no interpolated results (termed "full" manual segmentation). The time required to complete each segmentation scheme for each particle was recorded.

For each version of each nanoparticle, the reconstructed model was measured in terms of Vol, SA, R_g, 3D-circularity, and D_f as in the previous sections. Again, the set of cube sizes used in the Df calculations has been guided by the work of Lottin [156]. For the GTDI soot nanoparticles, the resampling factor used in the surface area calculations was guided by the work included in appendix section-A.2. Given the typical size of the

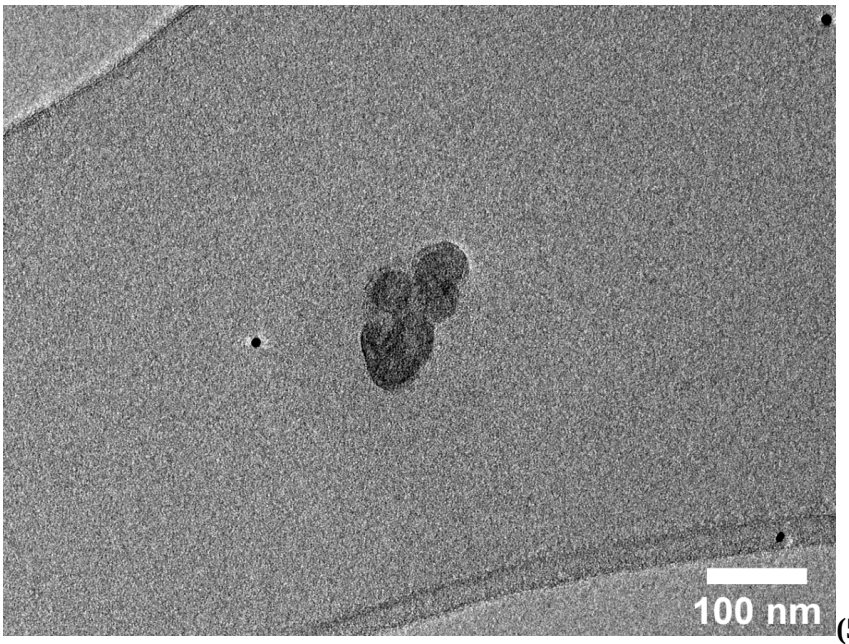
primary particles (30-40 nm in diameter), and the scales of the images, a resampling factor of 6 was deemed appropriate.



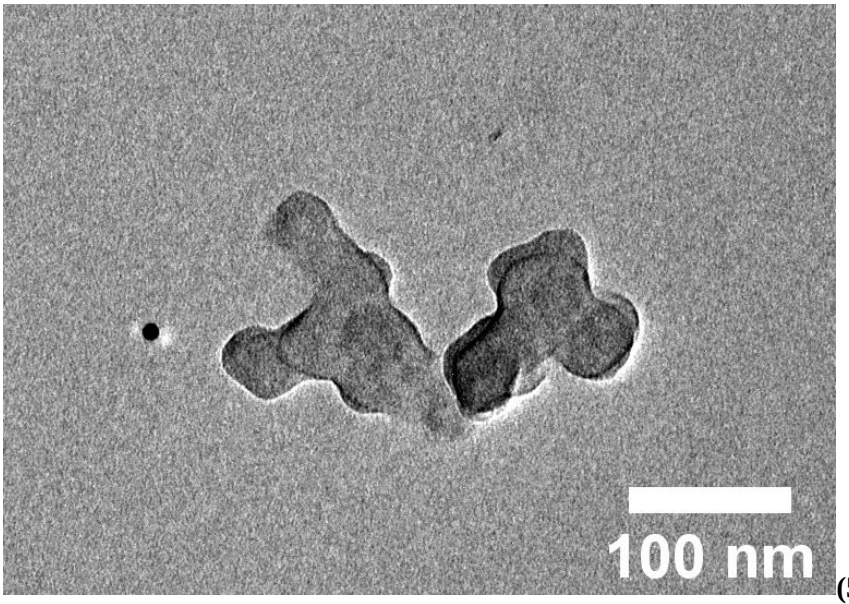
(5.16a)



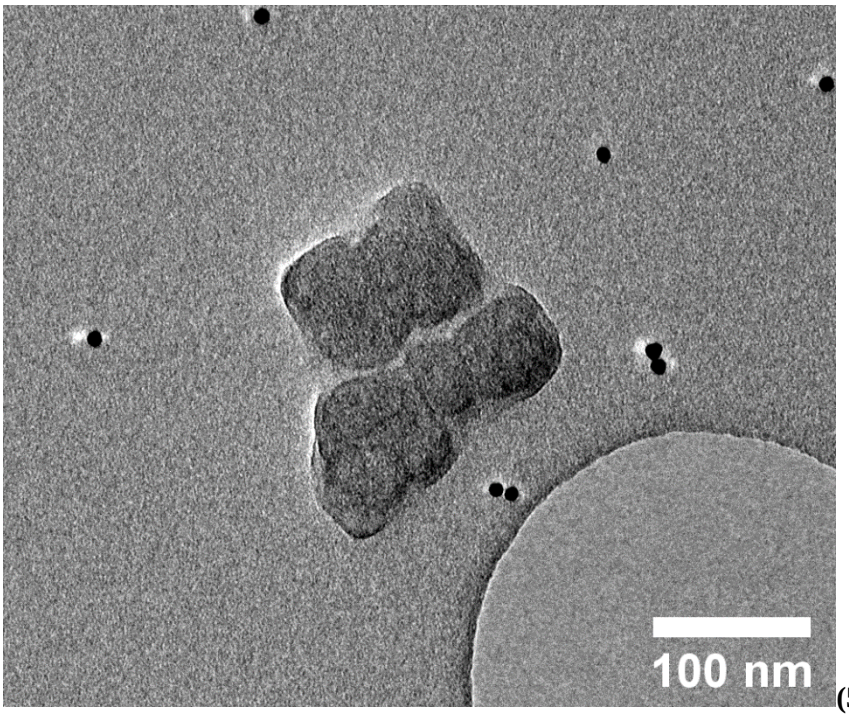
(5.16b)



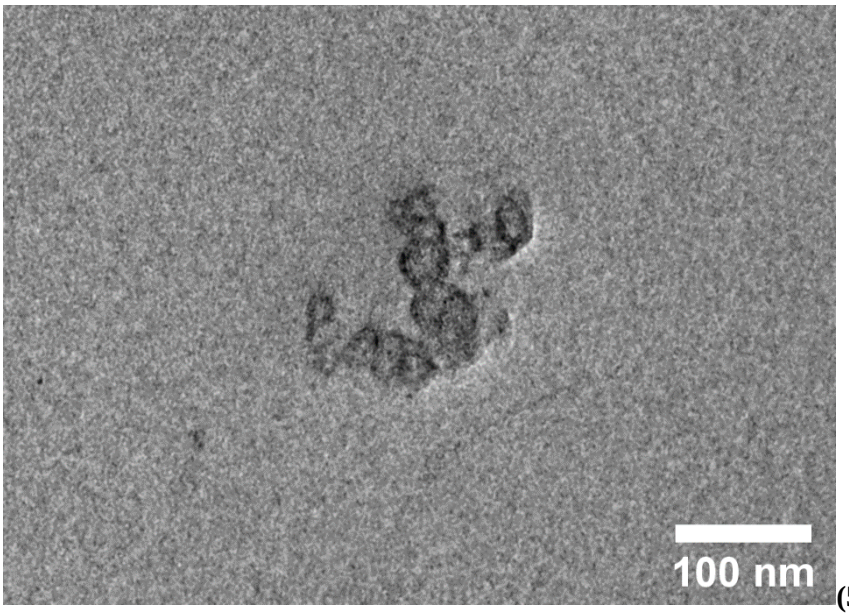
(5.16c)



(5.16d)



(5.16e)



(5.16f)

Figure-5.16: TEM images of the 6 GTDI soot-in-oil nanoparticles used in this work

5.5.1 – Effect of Interpolation: Results

Firstly, the time saved by using interpolated segmentation was linearly proportional to percentage of images manually segmented in each tomogram, as would be expected (figure-5.17). The amount of time saved even at the 5^{th} slice level of interpolation was significant, at around 40-50% of the time taken for full manual segmentation. The amount of time saved increased to a maximum of around 80-85% when manual segmentation was performed only every 20^{th} slice in the tomogram. There was no

apparent correlation between the amount of time saved and any morphological features of the different nanoparticles, or the scale of the tilt-series images.

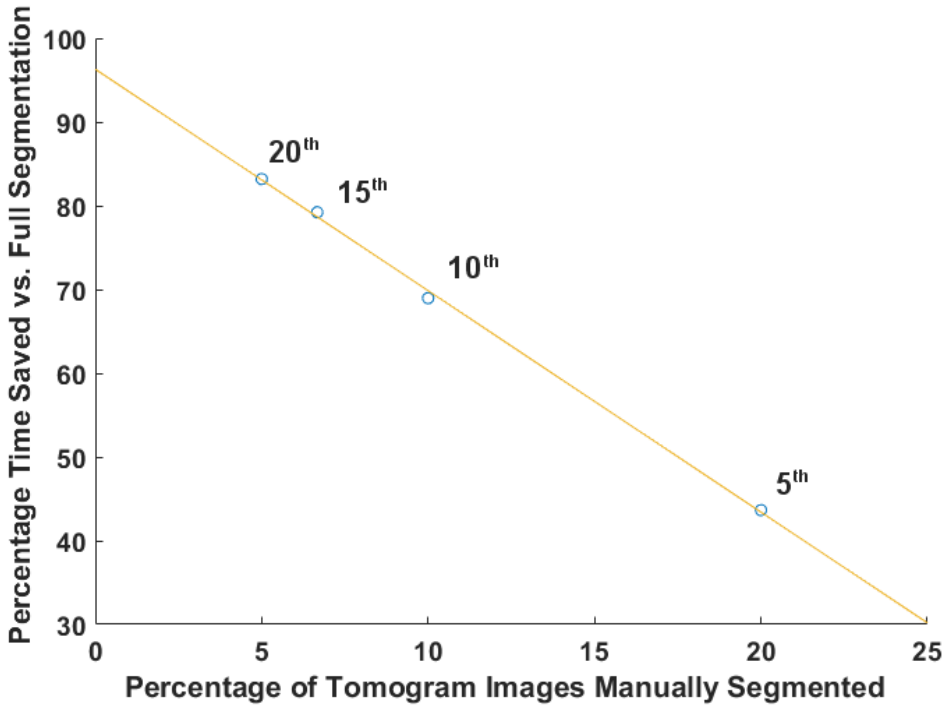


Figure-5.17: Time saved using interpolated segmentation (as percentage of time required for full segmentation) as a function of the number of images manually segmented (as a percentage of the total images in the tomogram)

Of course, improvements to the speed of segmentation are meaningless unless the effects upon the quality of the characterisation are also considered. For each of the agglomerates reconstructed, the morphological parameters of the 'interpolated particles' were compared to those of the fully segmented particle. The changes in the values of the parameters were quantified as a percentage of the 'full' values. Results averaged over all 7 nanoparticles used are presented in table-5.3.

Interp. level	Time saved (%)	Percentage deviations in measured morphology in comparison to 'full' manual tomogram segmentation (Standard Dev.)									
		Volume		Surface Area		Radius of Gyration		3D-Circularity		Fractal Dimension	
5th	44	-3.6	(1.6)	-4.3	(1.4)	-1.3	(1.1)	3.1	(1.8)	-0.9	(0.4)
10th	69	-7.9	(3.8)	-10.3	(3.6)	-3.0	(2.7)	8.5	(3.7)	-1.6	(1.6)
15th	79	-9.8	(5.3)	-14.9	(4.8)	-4.6	(4.1)	15.1	(5.8)	-2.7	(1.8)
20th	83	-20.8	(12.5)	-23.0	(3.5)	-6.5	(5.8)	16.8	(14.1)	-3.3	(2.8)

Table-5.3: Presenting morphological results of the different interpolated segmentation schemes. For each nanoparticle, the deviation between the morphology of the interpolated particles and fully segmented particle was calculated as a percentage deviation vs. the full-manual result. The values were then averaged over the 7 nanoparticles (FG soot + 6 GTDI soot-in-oil). Standard deviations are shown in brackets

An initial and important observation was the direction of the deviations that occurred between morphology of interpolated particles and those from full manual segmentation. For all parameters other than 3D-circularity, use of interpolation caused a decrease in the values measured. Reductions in volume and surface area are indicative that interpolation has reduced the bulk of the particles. Though not directly related to volume of particles only, reduced radius of gyration with interpolation does suggest that on average the particle mass is closer to the centre of mass. The slight reduction in fractal dimension that occurs suggests that particles have become less clustered to some degree, which is in-line with observations of decreased bulk.

The only parameter to increase with interpolation was 3D-circularity. This parameter describes the ratio of volume to surface area in terms of reference values for a perfect sphere. While this parameter can indicate particle shape complexity as it will change depending on the degree of branching, the dependence upon the surface area means it also reflects the ruggedness of the surface. That is to say, if there were two particles largely similar in branching shape but one had a more rugged surface, the more rugged particle would have a lower circularity value (see figure-5.18). In this regard, since overall particle complexity is similar due to relatively small deviations in R_g and D_f, the increased circularity indicates that the surfaces of the particles are smoother when interpolation is used.

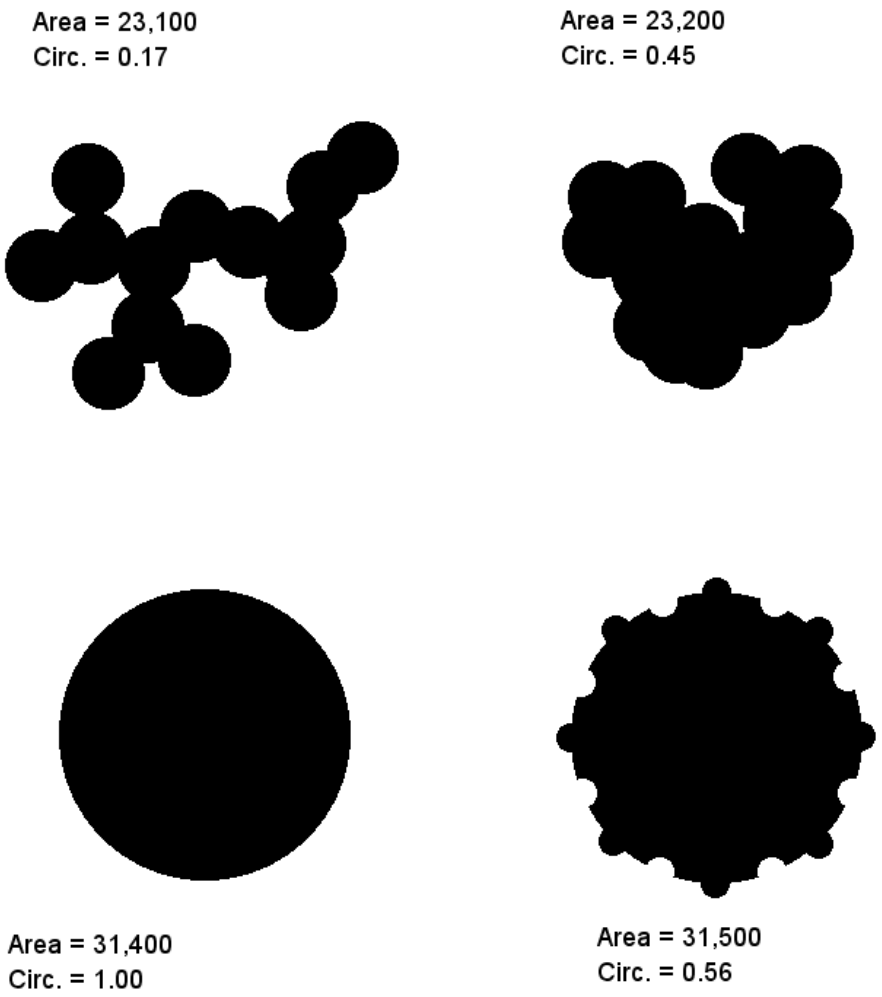


Figure-5.18: Example of the effect of branching and of surface ruggedness on the circularity parameter in 2D. Despite largely similar areas for the two scenarios (top and bottom separately), increased branching decreases circularity (above) and increased surface ruggedness increasing circularity (below).

The changes in these parameters can be rationalised by understanding that linear interpolation in Fiji has the tendency to underestimate the extent of particle matter in the tomogram. Linear interpolation effectively draws a straight line between manual segmentations in the Z-direction. This in particular is the reason why circularity increases and surface area decreases, as the particle edges become smoother. The type of error that is caused by interpolated is illustrated in an exaggerated fashion in figure-5.19.

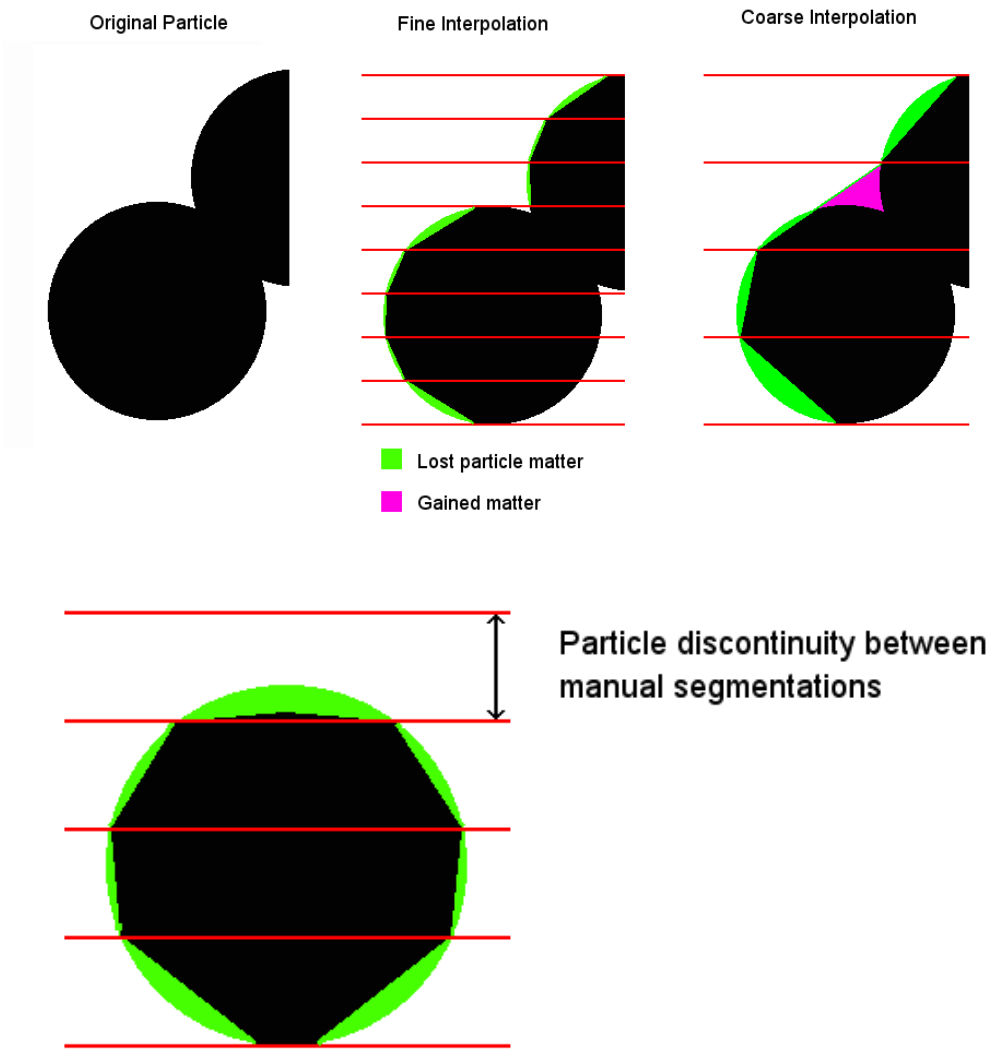


Figure-5.19: Examples of error that arises due to use of interpolation. In the above example it can be observed that frequent manual selections lead to small error between true and interpolated results. At larger increments between manual selections, significant amounts of particle matter are erroneously lost or gained, altering particle morphology significantly. In the below example, the top of the circle (*cf.* a primary particle) terminates between manual segmentations. In this section, the effect on particle morphology is significant.

Where the level of interpolation is lower, *e.g.* 5th level, the distance between manual segmentations are small. This means that the area of the particle over which interpolation occurs is small compared to the irregularities of the particles (*i.e.* the primary particles). As such, the error between the real particle and the interpolated ROIs is smaller. Also, areas in which particle discontinuities occur between manual segmentations are less significant. As such the overall particle morphology is less significantly affected. At coarser levels of segmentation, *e.g.* 20th slice, more significant

portions of the particles are subject to estimation by linear interpolation, so errors are more significant.

For the interpolated particles, acceptable bounds for the size of deviations from the morphology of the fully manually segmentation nanoparticles needed to be established. A first rough boundary was considered by reference to the high similarity between the original FG-WBP and FG-SIRT tomograms, which had been observed *via* the superposition of the FG-WBP ROI set on the FG-SIRT tomogram, and *vice versa*. In a sense, the differences in morphology measured from full manual segmentation of both of these tomograms could be considered to represent the scale of deviation that can result simply from errors in manual segmentation. That is to say, due to their strong similarity, the differences in Vol, SA, Rg, 3D-circ., and D_f observed are the level of variation that can be expected to arise simply from the natural uncertainty in manual selections. These results were presented earlier in table-5.1. Of course, despite the high similarity it cannot be denied that the characteristics of the FG-WBP and FG-SIRT images are different; while the former is more grainy, the latter showed greater blurring. These factors will surely have an effect on the choices made in manual segmentation.

In order to eliminate the effect of the differences in image quality between FG-SIRT and FG-WBP, full manual segmentation was performed on the FG-WBP tomogram on two more separate occasions. This resulted in there being 3 separate segmentations of the exact same tomogram. The differences in the various morphological parameters between these 3 models can be considered to derive only from the susceptibility of manual segmentation to variation. This is related both to inconsistency in selections of areas, and the natural lack of resolution of the edges of particle matter in the tomogram. The size of the variation in morphology by this method is given below in table-5.4. In short, these values show high repeatability of manual segmentation even over extremely large data sets (tomograms) comprising over 100 million voxels, producing particle models containing almost 2 million voxels.

	Volume (nm^3)	**Surface Area (nm^2)**	**Radius of Gyration (nm)**	**3D-Circularity**	**Fractal Dimension**
FG-WBP original	1,819,400	309,100	148.6	0.113	2.49
FG-WBP repeat 1	1,836,400	303,300	148.8	0.117	2.50
FG-WBP repeat 2	1,807,700	301,300	148.6	0.116	2.49
Max. Range	28,600	7,800	0.224	0.004	0.01
Variation %	*1.6 %*	*2.6 %*	*0.2 %*	*3.8 %*	*0.4 %*

Table-5.4: Morphological parameters measured from 3 particles created from the same FG-WBP tomogram on 3 separate occasions.

In comparison to these bounds for acceptable levels of variation, only interpolation at the 5th slice level was close. In terms of volume, interpolation at the 5th slice level caused an average decrease of 3.9% in comparison to the fully segmented particle (2.8-5.0% 95%CI), slightly in excess of the variation observed for manual segmentation alone. Decreases in volume at the 10th and 15th slice were fairly linear, but at the 20th slice interpolation level significantly greater decreases were observed. The size of the standard deviation also increased from 5th to 20th slice interpolation levels. In one single instance, interpolation at the 20th slice level actually caused an increase in volume in comparison to the fully segmented particle. This is not entirely unexpected, as depending on the positioning of the manually segmented slices within the tomogram, interpolation can act to add excess matter to the particle. For example, consider the pink pixels shown in figure-5.19, where the effects of interpolation on particle morphology are illustrated.

In terms of surface area, the 5th slice level of interpolation saw average decreases of 4.6%, with 95% confidence intervals falling between 3.7% and 5.5%. Again, the 20th slice level of interpolation saw a marked drop-off in quality, underestimating surface area by 24% on average.

For radius of gyration and fractal dimension, overall accuracy of the interpolated particles was higher. All levels of interpolation for these parameters resulted in decreases *vs.* full segmentation of < 6%, though this is still in excess of the very small variation observed due to manual segmentation alone. The form of these decreases with interpolation level was the same as seen for volume and surface area, *i.e.* showing a sharper decrease from 15th to 20th slice level.

In contrast to the other morphological parameters, the 3D-circularity parameter observed an inverse relationship with interpolation level, as coarser interpolation caused increases in its value. For this parameter in particular, use of interpolation at the 5th slice level actually resulted in more accurate retention of the original 3D-circularity value than was observed for the repeated full segmentations of FG-WBP. This behaviour did not hold for higher levels of interpolation, however.

In table-5.3, it can be observed that the size of the standard deviations tend to increase significantly at coarser interpolation levels. This increase in their size is related to the size of the increment between manual selections in relation to the size of the particle. The larger the increment becomes, the greater the likelihood that significant areas of irregularity in the particle structure will occur between manual selections. This results in the greatest degree of variation *vs.* full manual segmentations, and as such large

variability is seen at the coarser levels of interpolation (*e.g.* the 20th slice level). At this point, variation depends strongly on the complexity of the particle, and how the manual segmentations happen to coincide with the morphology. At the finer levels of interpolation, losses in bulk due to interpolation are fairly consistent as they occur well below the scale at which significant irregularities occur (*i.e.* towards primary particle diameter).

Overall, for Vol, SA, R_g, and D_f the average levels of variation from the 'fully' segmented particles (table-5.3) were only slightly greater than those resulting solely from manual segmentation errors. In terms of 3D-circularity, particles interpolated at the 5th slice level actually retained original morphology to a greater degree that the repeated segmentations of the FG-WBP tomogram. In reference to the variation between FG-WBP and FG-SIRT, interpolation at the 5th slice level was even closer, and volume deviations were actually smaller.

Overall, our data on these 7 agglomerates suggested that interpolated segmentation between every 5th slice would provide particles that could be characterised to a level of accuracy similar to that of full manual segmentation. At this level of interpolation, segmentation could be expected to take around 44% less time than a fully manual inspection of the tomogram, concurrent with decreases of around 4-5 % in volume and surface area, around 1 % in fractal dimension and radius of gyration, and increases of around 3% in 3D-circularity.

The strongly directional nature of variations due to interpolation (*i.e.* systematic decreases in V, SA, R_g, and D_f, and increases in 3D-circ), it is possible that these may be able to corrected for quite simply. However, given that the data set in this section consists of only 7 particles, we do not have to confidence to suggest that, for example, volume decrease at the 5th slice interpolation level is *always* in the range of 3-5%.

5.6 - Conclusions

In this chapter, various schemes for tomographic reconstruction, tilt-series conformation, and tomogram segmentation were assessed in terms of speed and quality, in order to suggest an optimised methodology. Initial test were carried out using the FG soot nanoparticle considered in the previous chapter. Qualitative comparison of WBP and SIRT reconstruction showed similar quality, but much quicker speed for WBP (30 seconds *vs.* 135 minutes). Tilt-series with reduced number of images were considered for potential gains in time required for image acquisition and reduced beam damage to

samples. In this regard, reduction in tilt-increment was more effective than reduction in total tilt-range. Reconstruction of tilt-series over a ±60° range with 3° increments produces high quality tomograms while reducing potential beam exposure by two thirds.

Soot was extracted from the oil of a GTDI passenger vehicle and studied with TEM. Interesting observations were made on the structures present, which included high concentrations of localised amorphous carbon and crystalline patches in addition to typical soot nanoparticles. From this sample, 6 nanoparticles were reconstructed in 3D and included in the final assessments of optimisation. The effect of interpolation during manual tomogram segmentation was assessed, as it was expected to increase speed but most likely decrease quality of reconstructions. Interpolation between manual segmentations in every 5^{th} slice of the tomogram reduced the time required by 44%, while retaining acceptable quality of reconstruction. The conclusion of our investigations into the optimisation of 3D reconstruction is to suggest the following conditions: ±60° tilt series with an image every 3° (41 images total), WBP reconstruction, and interpolated segmentation between every 5^{th} slice.

By comparison, a typical reconstruction procedure for the study of soot nanoparticles, based on the conditions in the work of van Poppel [34], Adachi [36, 222], Okyay [37], and Cabie [218], could be: ±60° tilt series with an image every 1° (121 images total), single-axis SIRT with 30 iterations, and full manual segmentation. Our optimised method was compared to this averaged protocol for reconstruction of the FG soot particle for the time required. In terms of the number of images used, potential beam dosage experienced by the sample is cut by two thirds. This is particularly advantageous for soot-in-oil samples, where contamination causing obscuring is a major problem. The time required for SIRT reconstruction (computational step only) of the tilt series was 94 minutes, compared to <1 minute for WBP reconstruction. The time required for alignment etc. pre-reconstruction was identical. Full manual segmentation of the SIRT tomogram required 144 minutes, compared to 79 minutes for segmentation in every 5^{th} slice. Overall, our optimised method reduced the time required by 67%, or over 2.5 hours. Due to the combination of high morphological complexity, low image resolution and contrast, and presence of adjacent soot-like material, the FG soot particle represents a ‘worst case’ scenario in terms of difficulty of segmentation, and as such the time required for manual segmentation was much greater than for the 6 GDI nanoparticles studied. However, in the extent of a full-scale characterisation of a soot sample, consisting of potential hundreds of nanoparticles, these improvements are significant.

6 - Development of Semi-Automated TEM Imaging for High-Throughput ET

This chapter describes the development of a methodology to permit automated TEM imaging of soot samples to facilitate high-throughput ET. The procedure consists of automated screening of large areas of TEM grids, and the creation of maps through which to control TEM operation. A logging system permits storing of locations of nanoparticles for study over subsequent sessions. Automated image processing is used to identify structures of interest, with a manual review process used to remove false-negative selections and permit rapid 2D-TEM analysis. The semi-automated methodology significantly reduces manual labour in TEM imaging of soot, helping to increase throughput *via* off-peak operation and decrease bias in selections of nanoparticles. The technique was developed for the study of the GTDI soot-in-oil sample also studied in chapter-5. Finally, 2D-TEM characterisation was carried out on the sample by utilising the optional process for improving automated selections and identifying non-selected structures. In total, 524 soot nanoparticles were studied in 2D (271 fully automated selection, and 253 fully manual selections). Typical 2D morphology was determined for this sample and compared to prior study of GTDI soot-in-oil nanoparticles by La Rocca *et al*. [41]. In this work, mean primary particle diameter = 33 nm, mean aggregate Feret diameter (maximum length) = 118 nm, mean R_g = 35 nm, and fractal dimension = 1.73. Convergence in the mean radius of gyration of nanoparticles occurred after around 150 individual measurements. Based on these results, this sample of nanoparticles appears to be slightly larger in their overall aggregate size, but less open and branched in their morphology.

The work in this chapter is adapted from a recent SAE technical paper that was presented at the SAE Naples 14th International Conference on Engines and Vehicles:

Haffner-Staton E., La Rocca A., Cairns A., Fay M. Morphological characterisation of gasoline soot-in-oil: development of semi-automated 2D-TEM and comparison with novel high-throughput 3D-TEM. SAE Technical Paper; **2019**. Report No.: 0148-7191.

6.1 – Introduction

The previous 2 chapters have detailed progress towards the development of a high-throughput 3D-TEM methodology for morphological characterisation of soot nanoparticles. So far this has considered a case-study of flame-generated soot with

which to practice and identify targets for optimisation, and then the optimisation of reconstruction, segmentation, and tilt-series conformation. Sample preparation was optimised for a GTDI soot-in-oil sample, and initial observations of that sample were detailed.

As was mentioned in the chapter-5, a less quantifiable but no less important cause of lost time in the 3D-TEM process is the identification of suitable structures. As the TEM grid must be tilted, structures of interest cannot be located too close to adjacent structures (the copper grid bars, and other nanoparticles/structures). While an overlapping grid bar will obscure the structure completely (as it is completely opaque under the TEM beam; see figure-3.8), adjacent carbonaceous structures can appear to be part of the nanoparticle of interest. Also, structures must be surrounded by a suitable number of gold fiducial markers to permit accurate tracking of images and alignment of the tilt-series. However, high concentration of Au-NPs can also obscure the structure of interest due to their opaque nature. A final consideration is the concentration of soot on the grid. Too high concentration results in a greater likelihood of particle overlap like that just mentioned, but too low concentration can mean long durations to locate suitable structures. The latter is a more prominent issue for soot-in-oil samples as soot fraction in oil can be very low, and the degree of solvent dilution and washing can make it difficult to adequately load a TEM grid. The former is probably a more prominent issue for exhaust or FG soot, where deposition is still uncontrolled at the nanoscopic level but overall concentrations can be much greater.

Overall, the additional constraints placed on soot for suitability for 3D-TEM means that a significant bottleneck occurs at the image acquisition stage. The time required to locate appropriate nanoparticles is significant, especially given the number of individual nanoparticles required to characterise an entire sample. However, it is probably the extent of manual effort that is the most prominent issue. Time on TEM equipment is at a premium, especially when also requiring the time of a trained operator on shared equipment. Any advances that could facilitate automated operation of the TEM can take advantage of lower costs and greater availability during non-peak times, and with minimal operator involvement. The necessity of the TEM operator manually searching the grid for suitable structures may also be an important source of selection bias, which could affect validity of results.

This chapter details the efforts made towards improving the throughput of TEM imaging of soot for ET. An ideal solution to the issues mentioned was envisaged as an automated process in which the TEM grid is screened for potential structures of interest. These

structures could then be reviewed in terms of suitability for 3D-TEM, guiding subsequent tilt-series acquisition. Such a process would make the image acquisition stage more efficient, particularly in terms of operator time and effort (and subsequent cost). Scanning of large of areas of the TEM grid could also facilitate rapid 2D-TEM morphological characterisation of soot, and a registration process enabling logging of particles of interest for study over numerous sessions of microscopy.

To achieve this goal, the main developments necessary were:

- A method by which to acquire images over a large area in TEM
- Automated 2D-TEM image segmentation to locate potential structures
- Review process in which false-positive selections (non-soot strucutres) are rejected
- Communication with TEM to facilitate the automated location of chosen structures for subsequent imaging

Finally, the developed technique was used to facilitate high-throughput 2D-TEM characterisation of the sample, involving the measurements of 524 individual nanoparticles.

6.2 – Automated Electron Microscopy in the Literature

Inspiration and guidance for the development of an automated procedure was taken from numerous examples in the literature. Due to the wide-spread usage of TEM for study of nanoscopic structures across a range of disciplines, the literature contains many examples of processes that have been automated to some degree. Given that the size, shape, structure, and appearance of specimens under TEM can vary so significantly, it was apparent that the most applicable studies would be those relating to soot, or soot-like materials.

Given that typical soot characterisations by TEM would require imaging of potentially hundreds of individual nanoparticles, it is unsurprising that numerous automated procedures for 2D image segmentation have been developed for soot. Most examples of automation in TEM study of soot focus on the retrieval of primary particle size and number from TEM projections [150, 160, 207, 208, 223, 224]. Primary particle characteristics are strongly dependent upon the soot formation conditions, and as such contain a wealth of information on this process. Primary particle size and number are also a key factor in inferring fractal morphology of soot nanoparticles [73, 75].

Several of these methods seek to identify circular patches in the projected images of soot, which are assumed to represent primary particles. This is often achieved using an image processing algorithm known as the circular Hough transform [207, 208, 223]. Alternatively, the edge contour of the aggregates may be used to infer primary particle sizes instead. For example, the work of Bescond *et al.* utilised Euclidean distance mapping to determine the smallest distances to the edges of the nanoparticle, and related it to primary particle diameter [150]. Dastanpour *et al.* used a novel method that considered the probability of nanoparticle matter being found at a certain distance from its centre [160], and primary particle size was then determined by the rate of decay of this probability.

While certainly interesting, these primary particle specific methods are not directly of use in this work, as the project had no specific primary particle focus. Instead, the focus of this work lay in the automatic segmentation of entire soot nanoparticles. The goal for this type of process was to rapidly identify soot structures that are potentially sparsely located over large areas of the TEM grid. Several examples of such methods are actually contained within those mentioned above. In the works of Grishin [208], Wang [207], and Dastanpour [160], the determination of aggregate ROIs is a pre-requisite for those methods used to determine primary particle sizes.

In their 2012 study, Grishin *et al.* performed automated segmentation of soot aggregates in TEM by first performing thresholding *via* the Otsu method, followed by removal of background features using a rolling-ball filter [208]. The Otsu method binarizes an image by dividing the pixel intensity histogram into two classes, and minimizing the variance between those classes. As such, darker particle matter is separated from lighter background material. The rolling-ball filter removes noise features by subtracting a background value from the image, which is guided by the average intensity surrounding each pixel. A similar combination of the Otsu method and rolling-ball filter was also employed by Dastanpour *et al.* [160].

In 2016, Wang *et al.* employed a different technique for TEM image segmentation [207]. It should be noted that the images included in their work are not BF-TEM images, but rather appear to be acquired using dark-field TEM since the contrast is inversed. However, no specific details of the TEM imaging processing are given in that work. Their method involved median filtering as the first step. This process alters the colour-value of a pixel by replacing it with the average value of those pixels directly surrounding it. The ‘level’ of the filter can be changed to include a larger or smaller number of surrounding pixels. Median filtering helps to remove spurious noise from the

image. Following median filtering, the image was inversed in colour. The inverse image was then subtracted from the original in a process which acts to remove background pixels, and enhance the contrast of features. Finally, the Canny edge detecting algorithm was applied to produce a map of nanoparticle outlines. This algorithm contains a series of filters to enhance features where the contrast gradient is strongest in the image, eventually resulting in only the outline of the object being visible.

In the literature there are also numerous examples of automated TEM segmentation methods for non-soot samples. However, given the strong dependence of appearance in TEM on the structure of material under study, these methods are not generally applicable. For example, the 2011 study of Gontard *et al*. developed a strategy for automatic segmentation of platinum nanoparticles deposited on a carbon support material [225]. This method involved creation of a multi-scale thresholding algorithm to rapidly and successfully identify the structures of interest. In comparison to soot, however, these features are much smaller, higher contrast, and are spherical in shape, so the technique cannot directly apply to samples such as GTDI soot-in-oil. Instead, such works would act as a rough guide, useful for identifying potential filters and operations.

Of course, TEM image segmentation is only a part of the process that is envisioned. Also required is the architecture with which to screen large areas of the TEM grid, and communicate the chosen positions to the TEM computer for automated acquisition. In the literature there are multiple examples of established procedures for high-throughput EM that are automated to at least some degree. This includes automation of SEM study of aerosols [226], TEM study of biological samples [227] and protein crystals [228] among others. These methodologies include use of auto-sampling of specimens, as well as automated microscope control directed by on-line image processing.

There even exists an excellent example of a soot-specific, on-line automated image acquisition system for TEM, as described by Toth *et al.* in their 2013 study [209]. The emphasis for this work was in part deficiencies of available methods for automated TEM control [228], which cannot operate at a fine enough scale for soot nanoparticle study. This work incorporates automated image processing at different scales to eventually facilitate HR-TEM imaging of the nanostructure of soot aggregates. A matlab script running on an ‘adjacent’ PC is used to autonomously control the TEM acquisition PC. Online image processing during live imaging is used to ‘drive’ the microscope view in a desired path between the 3 scales. The coarsest scale is that of the squares of the TEM grid. Simple image thresholding is used to automatically locate the contours of the lacey

carbon support. In Toth's work, the TEM grids did not possess the additional graphene oxide support used in our work, so soot nanoparticles are imaged only when they cling to the edges of the lacey carbon, and appear in contrast to the vacuum of the microscope. The nanoparticles themselves were located using unspecified methods described as 'morphological operations, the intensity gradient or local identity statistics'. These locations were used to 'drive' the microscope focus on nanoparticles at higher resolution. Finally, the highest magnification images are achieved using HR-TEM, and various filters are used to define the graphitic fringes.

The lack of a graphene oxide film on the TEM grid in that study means that the positioning of soot is fundamentally different to that in ours, and also given the lack of details on the image processing technique the same methods cannot be applied here. The same applies to most examples in the literature too; distinct differences in sample types and lack of specific image processing mean direct application is not possible. Additionally, many include hardware such as auto-samplers that we do not have access to. Nonetheless, the overall processes provide an excellent example of the desired type of methodology. Given the scope of this project, development of a fully integrated and on-line procedure was not possible. However, a methodology was successfully developed for the automated identification of soot-in-oil in TEM, despite the difficulties associated with image processing of graphene oxide coated TEM grids, and the presence of significant quantities of non-soot materials in the sample. In this work the foundations were laid for what will soon become a fully integrated technique, and can still provide significant improvements to throughput in the meantime.

6.3 – A Semi-Automated Procedure for Image Acquisition of Soot in TEM

The following sub-sections detail the steps of the semi-automated procedure by which large areas of the TEM grid are imaged and screened for suitable particles. Chosen particles are then registered and assigned locations, and subsequently imaged for 3D-TEM. The automated procedure was developed using the TEM grids prepared with the GTDI soot-in-oil sample described in the experimental chapter (section-3.5.2) and in chapter-5.

6.3.1 - Low-Magnification Imaging and Grid Registration with SerialEM

The process begins once the soot sample has been suitably prepared, and the grid placed inside the TEM. In this work, the open-source software SerialEM was used to achieve automated microscope control [173]. The initial step is to acquire a low-magnification (x50) image of the centre of the TEM grid, which is manufactured so that the corners of the copper mesh around the centre are distinguishable (see figure-6.1). This helps the operator to orient themselves with respect to the grid, as orientation depends on how the grid was placed into the TEM specimen holder and will change, to some small degree at least, each time the grid is loaded.

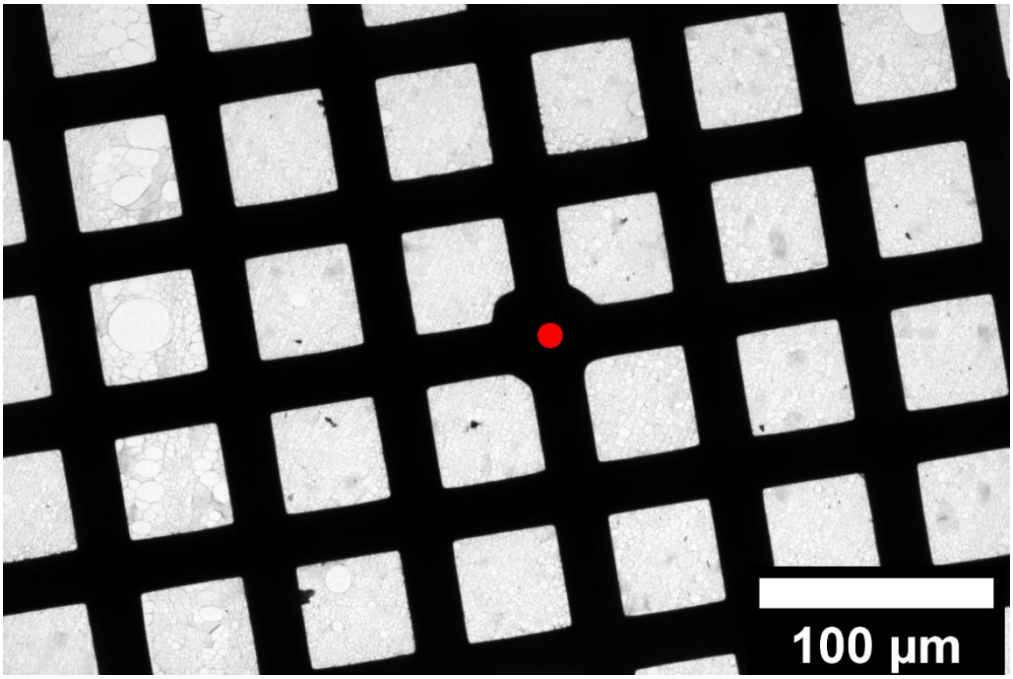


Figure-6.1: Low-magnification (x50) image showing the central area of the TEM grid (red-dot designates centre)

This low-magnification image is then designated as a *navigator map* in SerialEM. A navigator map is a previously acquired *static* image (as opposed to the *live* feed of the TEM camera) that can be used to direct the position of the live TEM feed. This allows the operator to simply select a location on the navigator map and the position of the live camera will automatically locate to that point. For a navigator map to function, several (*e.g.* 5-6) easily identified and evenly dispersed positions must be chosen in the static image to align the map with the live position of the microscope. An example of such selections is given in figure-6.2. These locations are centred in the live image feed, and their physical stage coordinates (*i.e.* the absolute position of the specimen stage within the microscope column) are recorded and registered to the positions on the navigator

map. When a desired position in the navigator map is chosen, the software can calculate the exact stage position to which the TEM live feed must reposition.

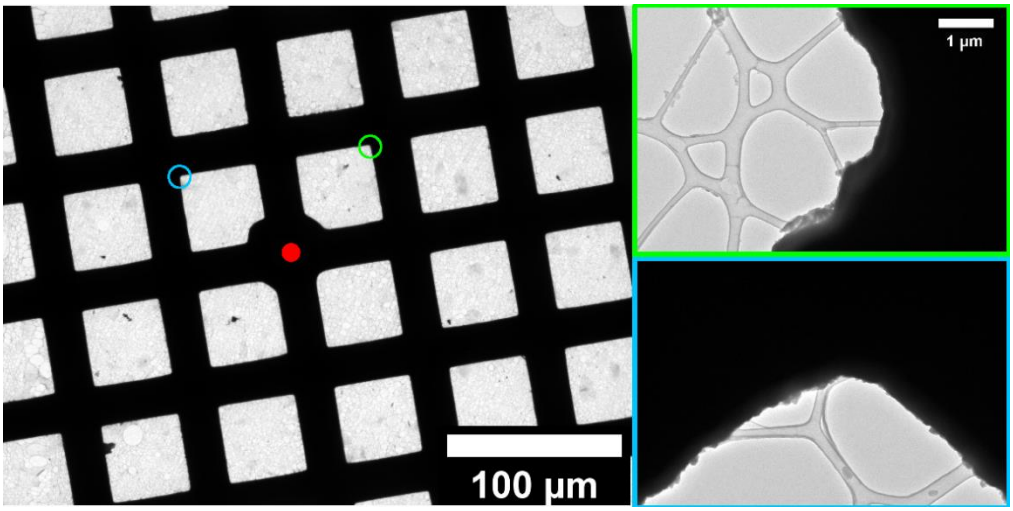


Figure-6.2: Example of registered points for low-mag montage. Images on the right show examples of live stage positioning at higher magnification (x4000)

A consideration of the registration step is the magnification used when recording stage positions in the live image feed. Errors in positioning occur between different levels of magnification in TEM (*e.g.* due to imperfect correction of the rotation that occurs with changing magnification). A navigator map registered at x50 magnification will not be able to accurately locate a structure at x10,000 magnification in the live image feed. As such, the registration must be performed at the magnification at wish you desire to view the sample. In this work, registration of the low-mag navigator map is performed at x10,000 magnification (the choice of this magnification is discussed in the next sub-section).

This low-resolution map is extremely useful for setting up a registry of the grid so that locations of interest can be easily found and imaged on numerous occasions. Given the extremely small size of soot nanoparticles in comparison to the TEM grid, it would be almost impossible to relocate structures of interest without some type of registration system. Once the low-mag navigator map has been created and registered to the position of the TEM camera, it can be used to easily direct *montage* acquisition of large areas within the grid squares (see next sub-section).

6.3.2 - Medium-Magnification Montaging in SerialEM

In order to efficiently screen large areas of the grid for suitable soot structures, *montaging* is performed. Montaging refers to the acquisition of a series of individual images in a grid-pattern over a desired area. These images have a degree of overlap between them which can be altered as desired. The individual images of a montage can then be 'stitched' together to produce a single, large image covering the entire area.

In this work, the aim is to scan the grid for structures suitable for tilt-series acquisition, *i.e.* with no adjacent structures and sufficient Au-NPs. A key pre-requisite is that particles cannot be located too close to the copper grid bars, as it will obscure them at high tilt-angles. As such, our default choice for montage area is a polygon covering the central section of a grid square. The entire grid square area is approximately 40 x 40 µm, and the chosen montage area is around half of those dimensions (see figure-6.3 for an illustration).

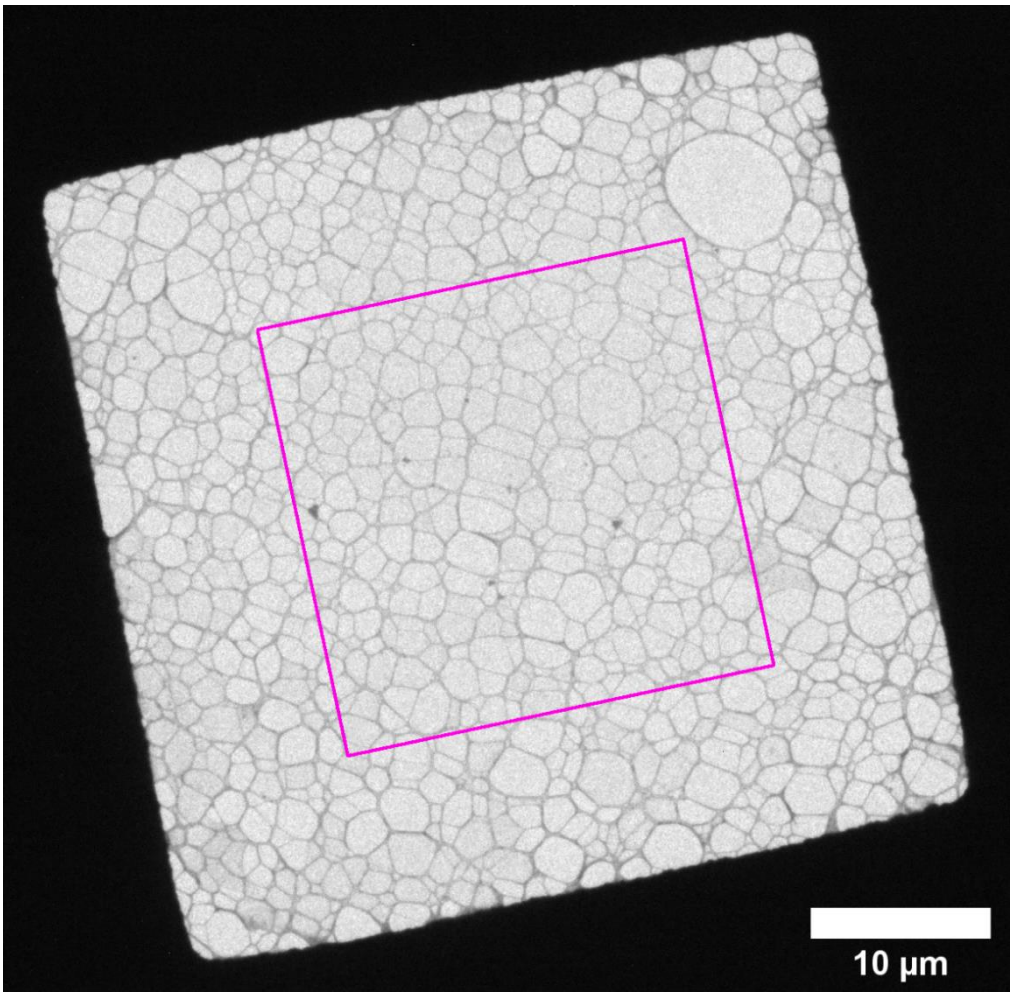
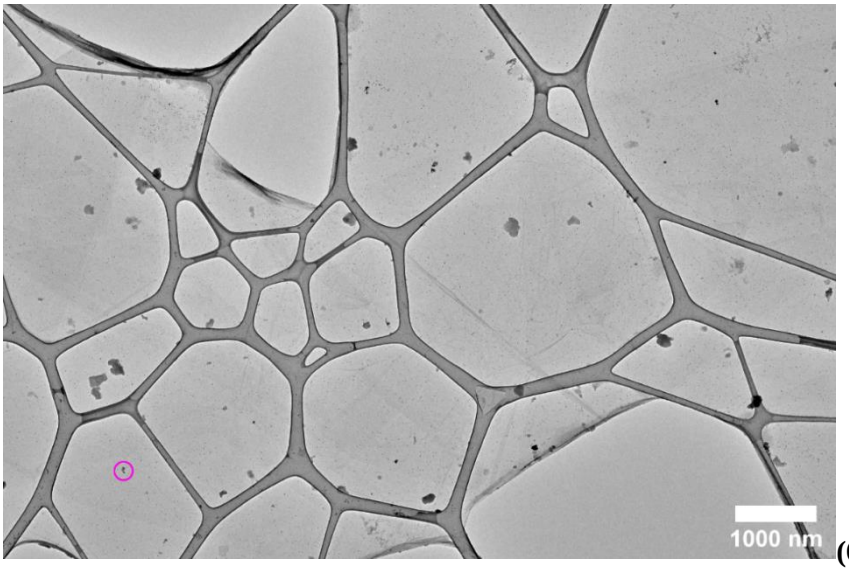
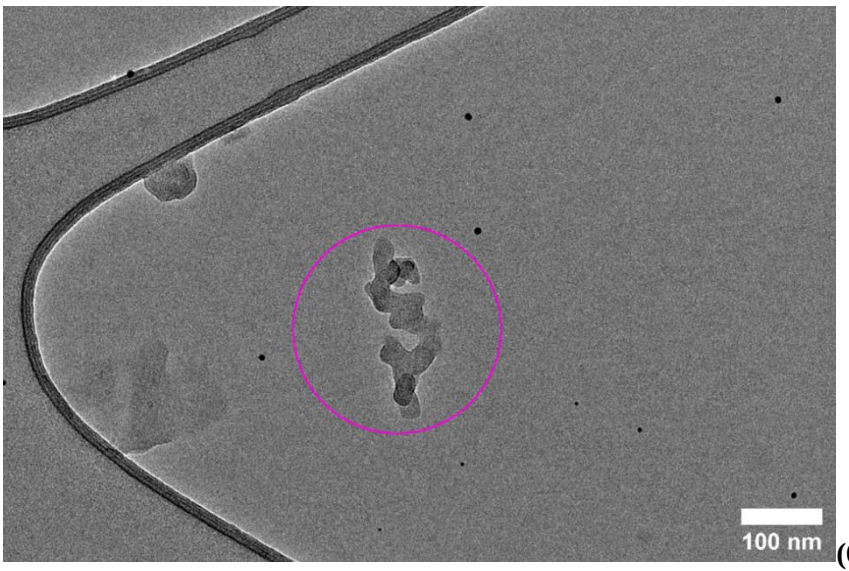


Figure-6.3: Typical area covered by montage imaging at x10,000 magnification.

The choice of magnification that montage images are acquired at is a compromise between efficiently screening the grid (lower magnification = fewer images, therefore quicker) and being able to clearly identify soot structures (high magnification = better resolution). A low magnification image at x2,000 measures approx. 11 x 7.5 μm in dimension, so only around 12 images are required to cover a typical montage area (20 x 20 μm). However, at this scale a 100 nm aggregate is only around 16 pixels in length and so extremely hard to verify suitability for further imaging. At x25,000 magnification, a 100 nm particle measures around 200 pixels in length, but would require around 1,200 images to cover the same area. This would be expected to take as long as 6-7 hours to complete. A comparison of TEM images at these scales is provided in figure-6.4.



(6.4a)



(6.4b)

Figure-6.4: Comparison of scale of TEM images at x2,000 magnification (a) and x25,000 magnification (b). Circled nanoparticles are approximately the same size.

With this in mind, a standard montage magnification of x10,000 was used in this work. Each individual image of the montage is 2004 x 1336 pixels (2.64 x 1.76 μm). A 9 x 14 image grid is used (126 images in total) with ~20% image overlap, producing a montage over an approx. 20 μm^2 area. At x10,000 magnification, each pixel measures 1.32 nm in length. At this scale, a soot primary particle is around 15-30 pixels in diameter, and a 200 nm nanoparticle would be 152 pixels in length, allowing acceptable identification of suitable nanoparticle. An example TEM image at this scale is provided in figure-6.5.

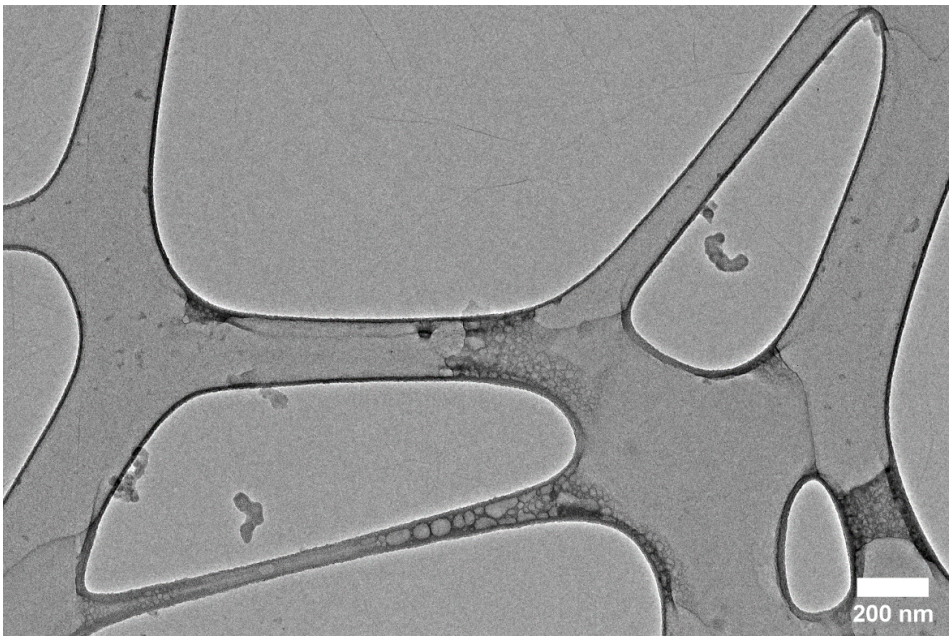


Figure-6.5: TEM image acquired at x10,000 magnification, with soot nanoparticles visible. Scale bar shows 200 nm.

The area to be imaged during montage acquisition can be defined in several ways using SerialEM. The TEM operator can manually measure stage coordinates from the live images and define the edges of the montage, or can even draw a polygon shape in the low-mag navigator map (similar to that seen in figure-6.3). The positions of montages can be logged in the low-mag navigator map so that the operator can track which squares have been imaged. Acquisition of a montage containing 126 images typically takes around 20-40 minutes to complete, similar to a tilt-series of 121 images. All montage acquisitions were performed using the relatively large value of -12 μm for the microscope operating parameter known as *defocus*. Defocus of the microscope is controlled by shifting the focus of the objective lens, and can be used to alter the appearance of the images that are acquired. A large defocus of -12 μm results in lower resolution but greater contrast, and was useful for improving accuracy of montage stitching (see following paragraphs). In theory, SerialEM montage acquisition can be

performed without operator supervision. As such, the somewhat lengthy process of montage acquisition could be performed in off-peak times (evenings, weekends, *etc.*), increasing throughput and potentially significantly reducing cost. Unfortunately, the operation of SerialEM was prone to small errors that required operator corrections. While a single montage could complete fully automatically, a series of several montages would likely need operator presence at some point during the process. At this time, the full benefits of automation to throughput could not be realised, but it is still highly beneficial to throughput to have even partially automated montage acquisition.

Once the individual images of the montage have been acquired, they must be stitched together to create a single image. SerialEM will automatically produce a roughly stitched image that has been binned to reduce its size significantly. Although this can be a useful visual aid, the resolution and accuracy is not high enough to perform the automated image segmentation and to direct locating of particles of interest. High-quality montage stitching is performed using the Fiji *Stitching* plugin [229]. This plugin compares images that are expected to occur adjacent to one another based on the pattern of image acquisition, and uses cross-correlation (similar to that used in tilt-series alignment) to find the correct overlap between them. The positions of the two images with respect to one another is altered until the minimum difference between them (in terms of the cross-correlation value) is reached. As mentioned, a relatively large defocus was used during montage acquisition. Initially, more typical values of defocus were used (around 6 μm) but in many cases the stitching plugin could not correctly compute the image overlaps. At the relatively coarse scale of x10,000, many features of the grid are relatively small. Particularly in barren areas of the grid, where large holes in the lacey carbon support can span across several images, there are few feature points with which to cross-correlate images in the montage. By employing a high defocus, we were able to increase the ease with which the plugin could match features, resulting in much more reliable results.

The stitched montage images that result are approximately 15,000 x 15,000 pixels in size, depending on the degree of image overlap and how much was successfully stitched. A highly-binned version is provided as an example in figure-6.6. The high-quality stitched montage can then be loaded into SerialEM, where it can be designated as a new *navigator map*. For clarity, this will be referred to as the *montage map*. Like for the low-mag navigator map discussed earlier, the stitched montage can then be used to control the position of the live image feed. Again, easily identified features of the montage map must be matched to the physical stage positions of the microscope by centring those features in the live image feed. If desired, the registration can be performed at a higher

level of magnification (in fact, several magnifications can be registered at the same time).

The next step of the process is to automatically locate structures of interest on the montage map, and feed these positions directly into the SerialEM software to enable automated imaging.

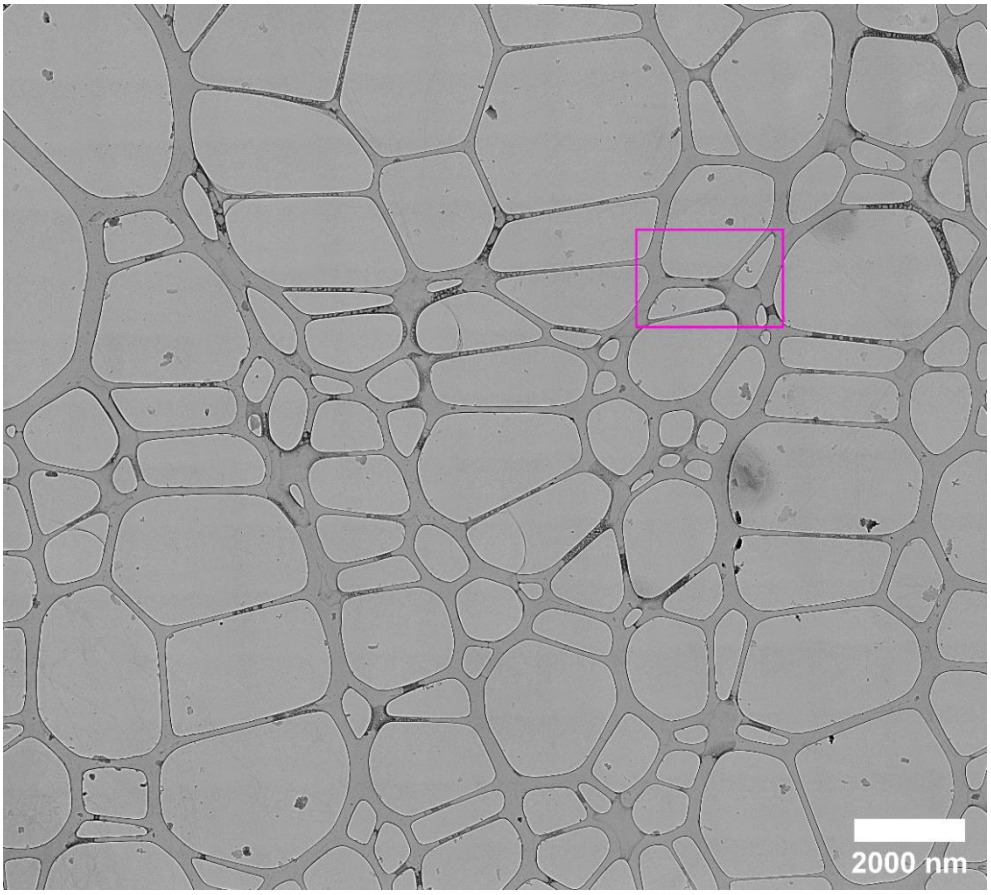


Figure-6.6: Example of a stitched montage. Area is approx. 18 x 16 μm, and has been binned by a factor of 4. Pink box highlights the area shown in figure-6.5.

6.3.3 - Image Processing of the Montage Map

Unlike in the work of Toth *et al.* [209], it was not possible to develop on-line image processing of the montage map. For security, the PC controlling the microscope was disconnected from the main University network, and was not permitted to be connected to the image processing PC. However, the process of automatically locating structures of interest functioned very similarly off-line to how it would have been on-line, and could easily be integrated if the opportunity arose.

In bright-field TEM operation, denser objects result in darker pixels in the TEM images. In an ideal scenario, soot particles would be significantly denser than the grid support

material and therefore easily separated from the background film by a simple threshold (where pixels below a certain grey-level are considered to be particle, and those more-than are ignored). However, the soot nanoparticles and the graphene oxide and lacey carbon support films are almost entirely carbon in their elemental composition and similar in their thickness. This results in relatively similar appearance of soot and the background film in TEM images. As such, in order to accurately separate soot particles from the background with a threshold, image filters must first be applied to enhance the contrast between them.

Some examples of image filtering in previous publications were provided in the earlier section, though specific details on their exact application were hard to come by. In any case, the appearance of soot nanoparticles in TEM is strongly dependent upon factors such as the soot source, preparation method, TEM grid composition, TEM operating voltage and imaging parameters (such as defocus), and the quality of the camera. As such, even if a specific *recipe* were detailed, it may not apply directly to our specific sample. There would likely be a degree of fine-tuning through trial-and-error in any case.

The use of Fiji for image processing meant that it was very easy to test a wide variety of different image filters and algorithms, as they are already built into the software. Typical images of the sample at x10,000 magnification were used to develop a reliable strategy for automated segmentation of our samples.

In this procedure, a median filter and then a Gaussian filter are first applied to the montage image. Both of these filters consider each pixel of the image separately. They will replace a pixels colour value with the one based on that measured in the neighbourhood pixels. The size of the 'neighbourhood' is determined by the level of the filter (*e.g.* level 1 = 1 pixel in all directions). While median filtering simply uses the average grey-level of the neighbourhood, Gaussian filtering weights the values of surrounding pixels according to a Gaussian distribution. These filters are useful for removing small areas of noise, smoothing the image so that particle matter appears in greater contrast. For our montages, it was generally acceptable to perform median filtering at level 1, and Gaussian filtering at level 2 or 3. The values of these filters could easily be altered, which may be necessary if conditions affecting TEM imaging were changed. The effect of these filters on a small sub-section of a montage map is shown in figure-6.7.

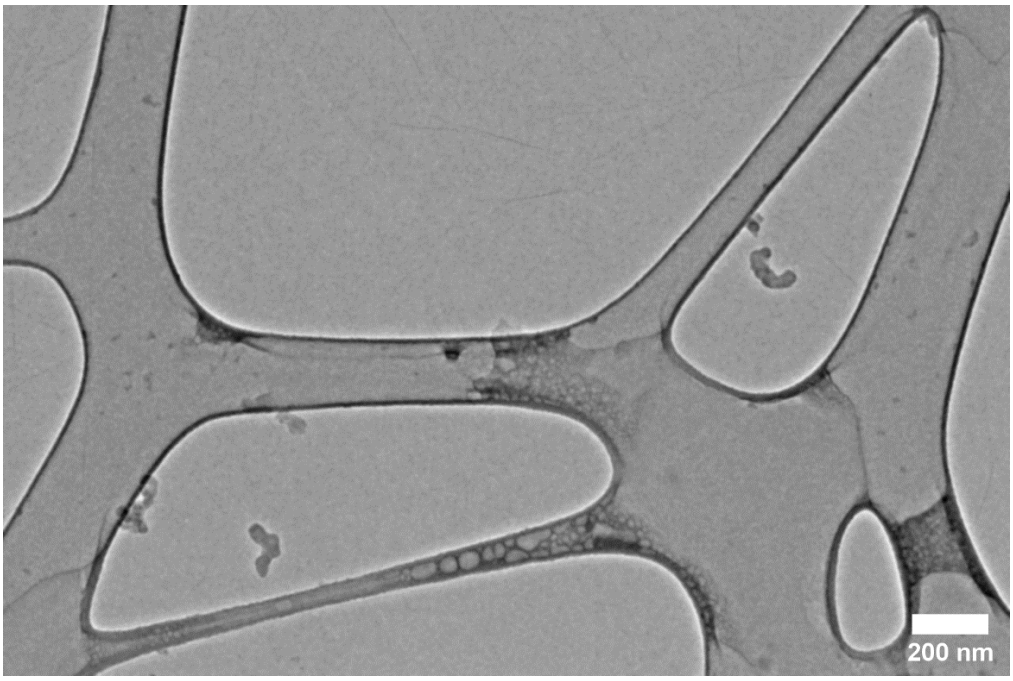


Figure-6.7: Showing same x10,000 magnification image as in figure-6.5, after application of median and Gaussian filters.

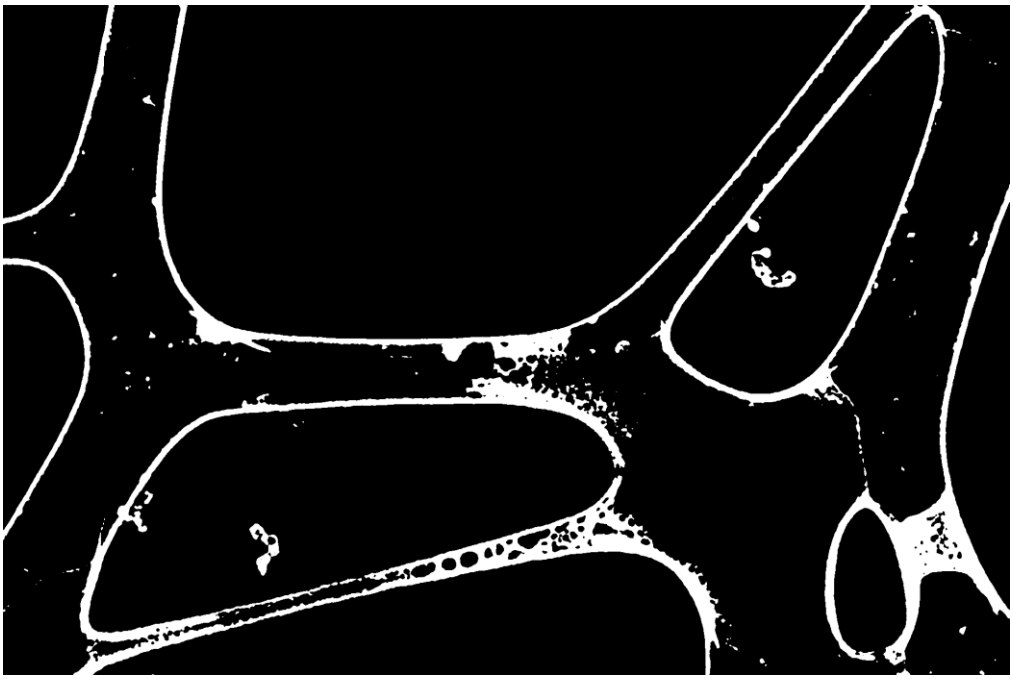


Figure-6.8: Result of Otsu thresholding of the same image shown in figure-6.7.

The montage map image is then binarized by using automated thresholding with the Otsu method (as described earlier in section-6.2). A binarized sub-section of the montage map is shown in figure-6.8. In the resulting binary image (where all white pixels correspond to particle matter, and all background is black), patches of connected

white pixels are separated and identified using Fijis *Analyze Particles* plugin. Despite the best efforts of the smoothing filters, some areas of high contrast resulting from noise are still selected by Otsu thresholding. Also selected may be non-soot structures on the grid, which as discussed in chapter-5 (section-5.3) were common for the GTDI soot-in-oil. This can include small pieces of crystalline debris, or larger amorphous areas that are primarily carbon but lack typical soot nanostructure. Additionally, it is unavoidable that the lacey carbon edges will also be included in the binarization, as they are high contrast under the electron beam (due to their thickness).

In order to remove as many of these non-soot structures as possible, the areas selected by *Analyze Particles* are then constrained in several different regards. Firstly, all areas overlapping the edges of the images are deselected. This step is able remove many of the lacey carbon edges. Next, a maximum size constraint is applied to remove any remaining selections of lacey carbon. As the lacey carbon holes are much larger than even the largest soot nanoparticles, their high area makes them easy to distinguish from structures of interest. The maximum area chosen in this size-filtering process is the equivalent to that occupied by 250 individual primary particles, of the assumed or measured mean diameter. This value was chosen as it is significantly greater than the maximum size of engine soot aggregate typically observed; Martos *et al.* observed that that approx. 95% of diesel soot aggregates consist of <200 primary particles [230]. Figure-6.9 shows the result of the maximum size filter.



Figure-6.9: Removal of lacey carbon with maximum size and edge constraint

Due to the transparency of soot under the electron beam, projection of 3D structures can result in variable contrast within a particle. Where particle material overlaps in the vertical direction, darker colour values are observed. This variation can cause problems with Otsu thresholding, and nanoparticles selections can appear fractured (figure-6.10).

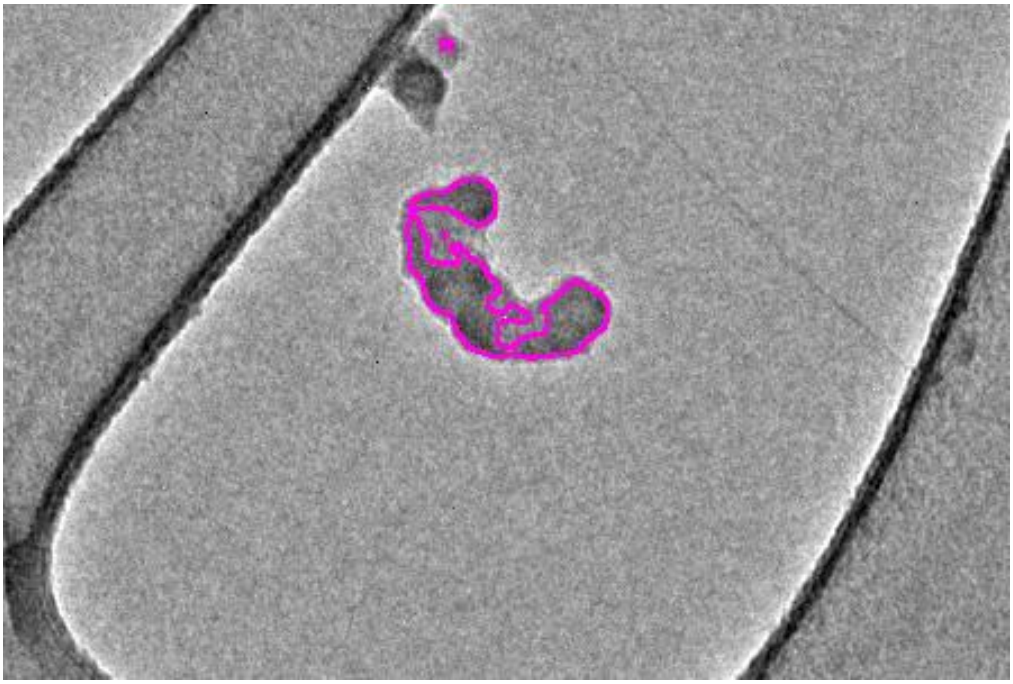
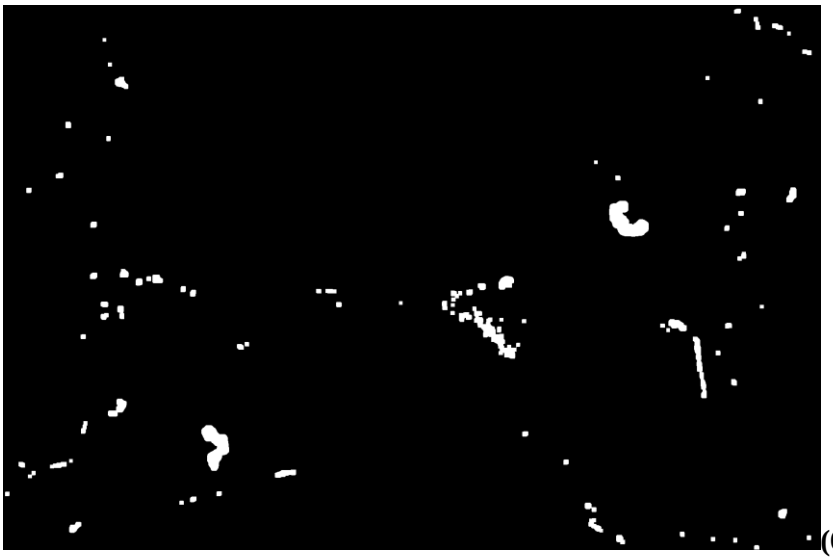


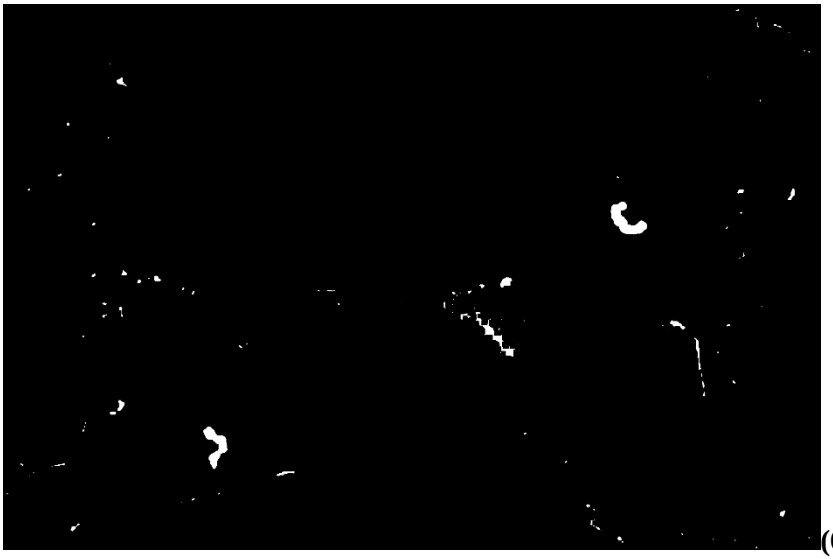
Figure-6.10: Fractured segmentation of a nanoparticle, due to uneven contrast within the particle.

In order to reduce the number of fractured selections, a dilation operation is applied to enlarge areas of white pixels. A filling operation is then applied to close the gaps of closely related structures. The inverse of dilation, an erosion operation, then reduces selections of white pixels back towards their original size. This is important, as otherwise patches of noise appear large in size and may be misinterpreted as particle matter. The different stages of this part of the process are illustrated in figure-6.11.

Minimum size constraints are then used to remove noise, gold nanoparticles, and other small non-nanoparticle carbon features. The minimum acceptable size is defined by the area equivalent to 3 primary particles of the measured or assumed average diameter, as Kondo *et al.* had previously considered this as the minimum size of soot aggregates [39]. This value is generally lower than what most authors in the field consider as a minimum size. The purpose of this filter is to remove small incorrect selections, but should also not be so large as to remove selections of real, but modestly sized, soot nanoparticles. As such, a relevant but somewhat low value was chosen from the literature as a compromise. See figure-6.12 for an example of the result of this minimum size filter.



(6.11a)



(6.11b)

Figure-6.11: Showing the result of dilation of figure-6.8 (a), followed by erosion (b)

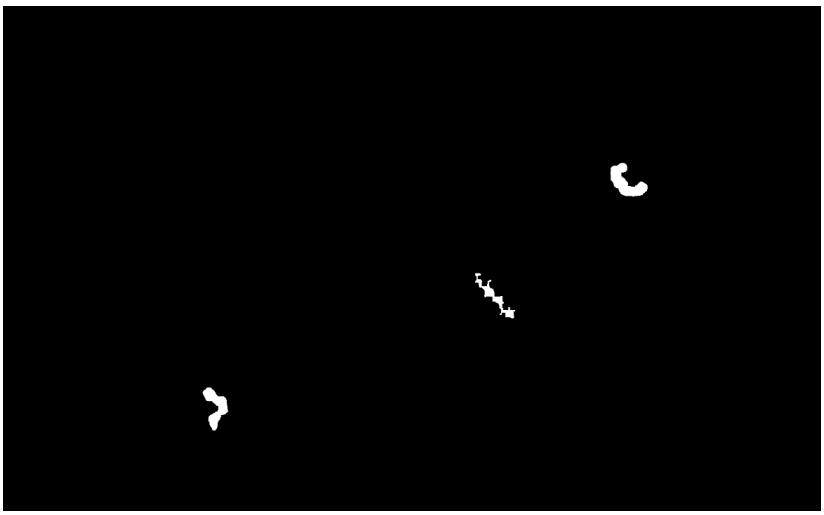


Figure-6.12: Result of application of minimum size constraint (area ≥ 3 x average primary particles). Two nanoparticle selections, and 1 noise selection

Patches of white pixels that remain are subjected to further constraints in terms of circularity. As described in chapter-3, this parameter describes a shape in terms of its similarity to a perfect circle. High values (towards the maximum of 1.0) indicate highly circular selections, which given the typically fractal nature of soot nanoparticles are more likely to correspond to false positive selections. This includes non-soot features such as large patches of amorphous carbon, or small areas of the lacey carbon film not ruled out by the maximum size constraint. Low values of circularity (close to 0.0) indicate highly branched and irregular structures that often correspond to spurious patches of noise, or features such as folds in the graphene oxide film. In the montage, false-positive selections were identified in order to establish upper and lower bounds for circularity that would exclude them. Approximate upper and lower bounds of circularity were determined as 0.8 and 0.2 respectively. An example is given in figure-6.13.

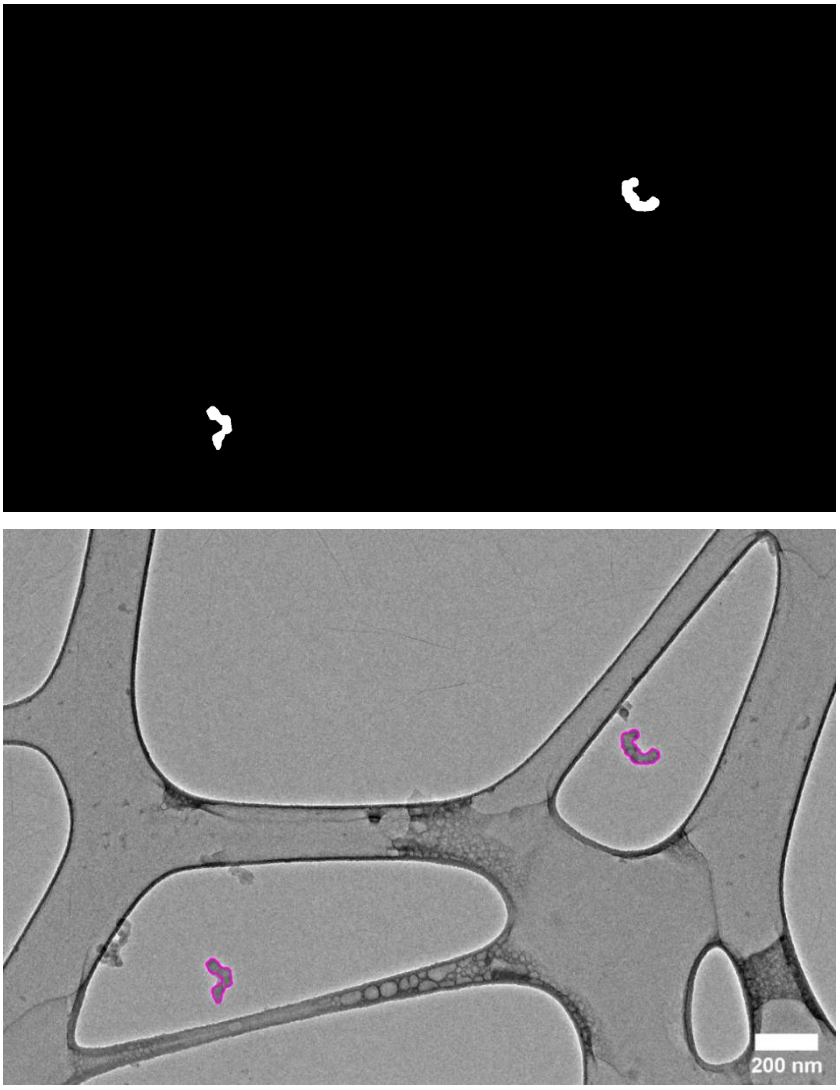


Figure-6.13: Final result of automated selection process, after application of circularity constraint (0.2 < circ. < 0.8) to remove noise selection.

All patches of white pixels in the binarized version of the montage map now correspond to areas in the original montage image that are most likely to correspond to soot nanoparticles. Given the predisposition of the GTDI soot-in-oil samples towards possessing high levels of non-soot structures (both carbonaceous and inorganic in nature), the issue of false positive selections has been particularly prominent. The example image used so far in figures-6.7 to 6.13 represent a relatively 'easy' area for automated segmentation, as the only large structures are the two nanoparticles. In areas such as this, the automated segmentation process works well. Another example of an easy automated segmentation is shown in figure-6.14, which includes carbon black nanoparticles. Figure-6.15 shows an example of a more typical area of the grid, with selections of non-nanoparticle carbon material that made it through all the constraints.

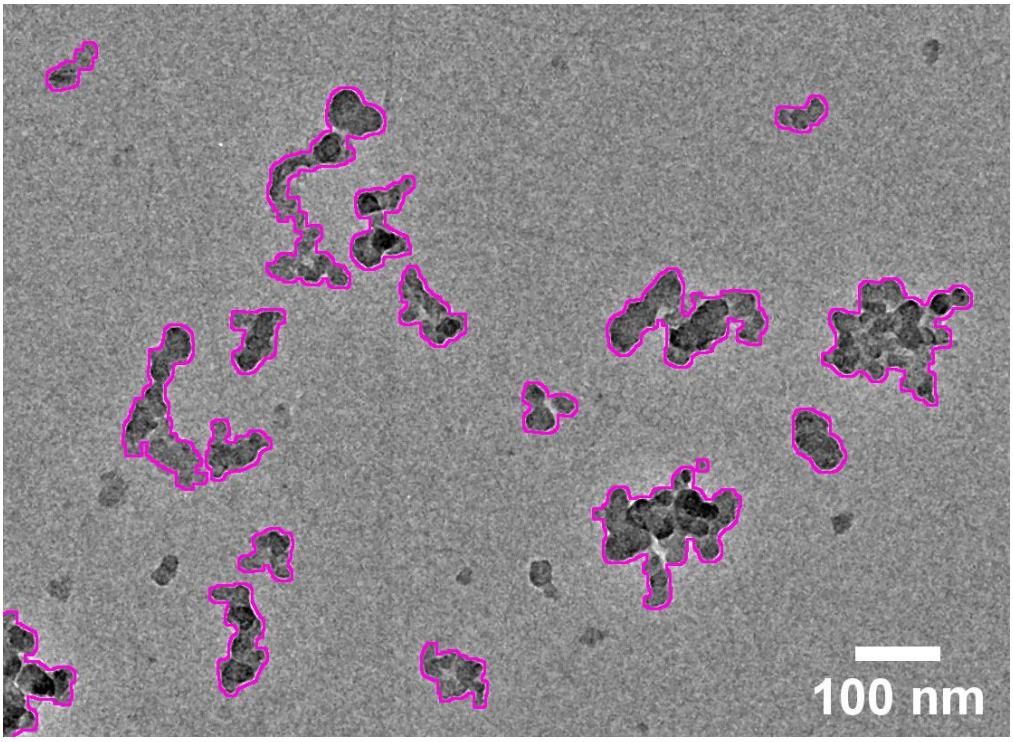
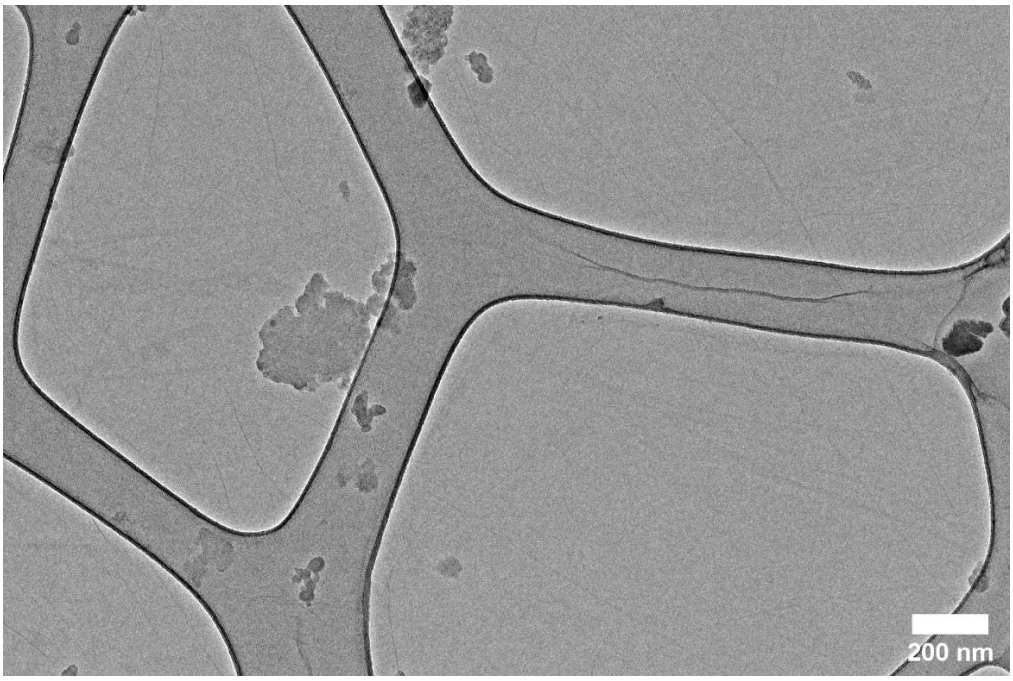
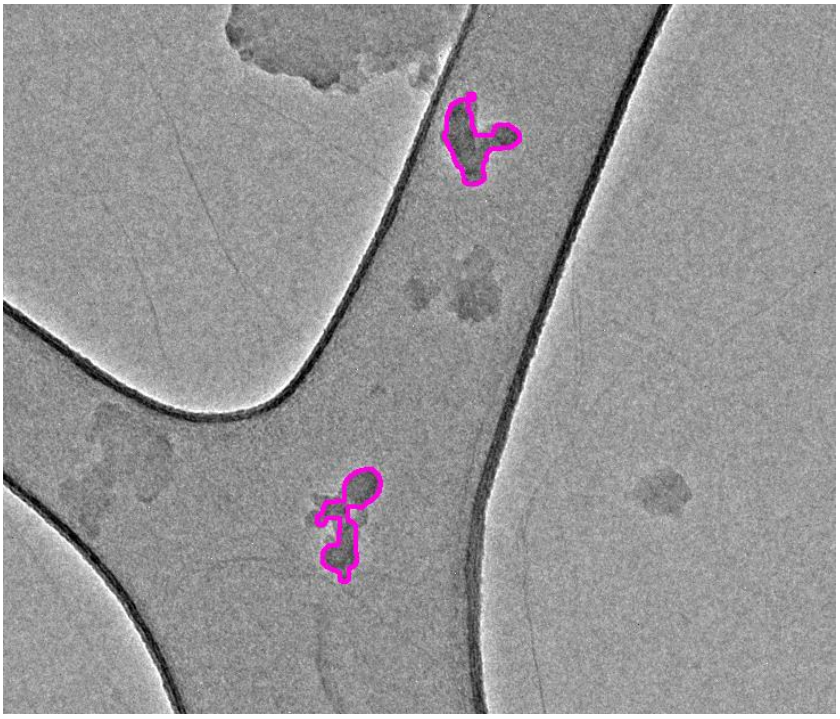


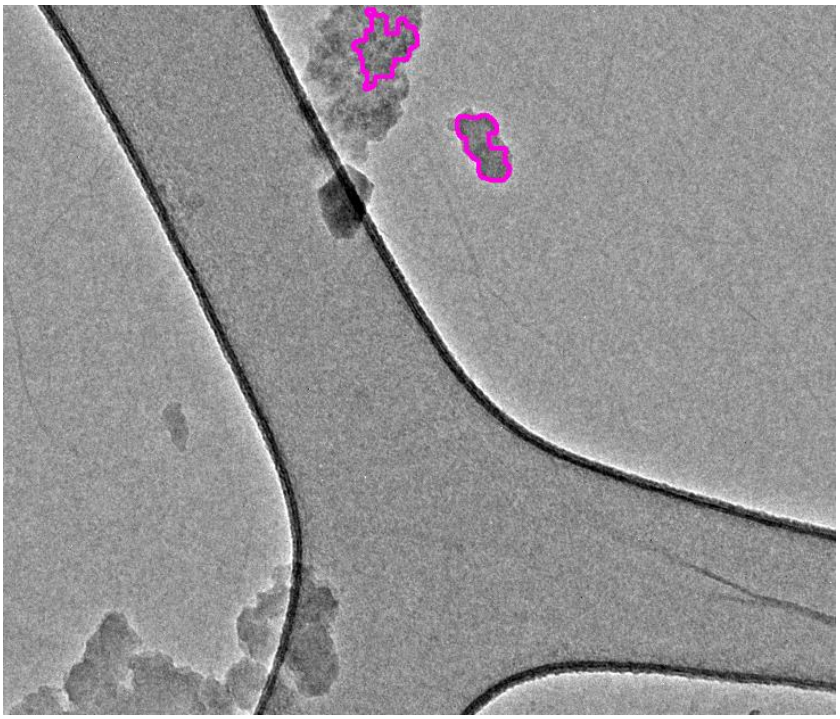
Figure-6.14: Showing accurate automated selections of carbon black nanoparticles



(6.15a)



(6.15b)



(6.15c)

Figure-6.15: Typical area of GTDI soot-in-oil montage containing both localised amorphous carbon and typical soot nanoparticles. (b) automated segmentation of nanoparticles. (c) automated segmentation of areas of localised amorphous carbon

The most simplistic solution to the problem of false positive selections was to implement a manual review process. Through development of a macro for Fiji, each ROI is rapidly presented to the operator at an appropriate level of zoom, who is able to quickly accept or reject the selection. Typically this required around 1 second per selection. This review process not only gives the user the opportunity to differentiate soot nanoparticles from false positives, but also to consider whether the accurate selections are placed adequately for tilt-series acquisition in terms of proximity to other large structures (potential for overlap/obscuring at high tilt) and gold nanoparticles (for alignment).

6.3.4 - Rapid 2D-TEM Characterisation

As the primary aim of this automated process is simply to locate structures suitable for tilt-series acquisition, the automated selections are not required to perfectly encapsulate particles of interest. Indeed, as long as the majority of a selection overlaps with the majority of a particle it is sufficient to generate an accurate coordinate. An example is provided in figure-6.16, highlighting both accurate and inaccurate true positive selections (of nanoparticles) and accurate selections of non-nanoparticles (false positive).

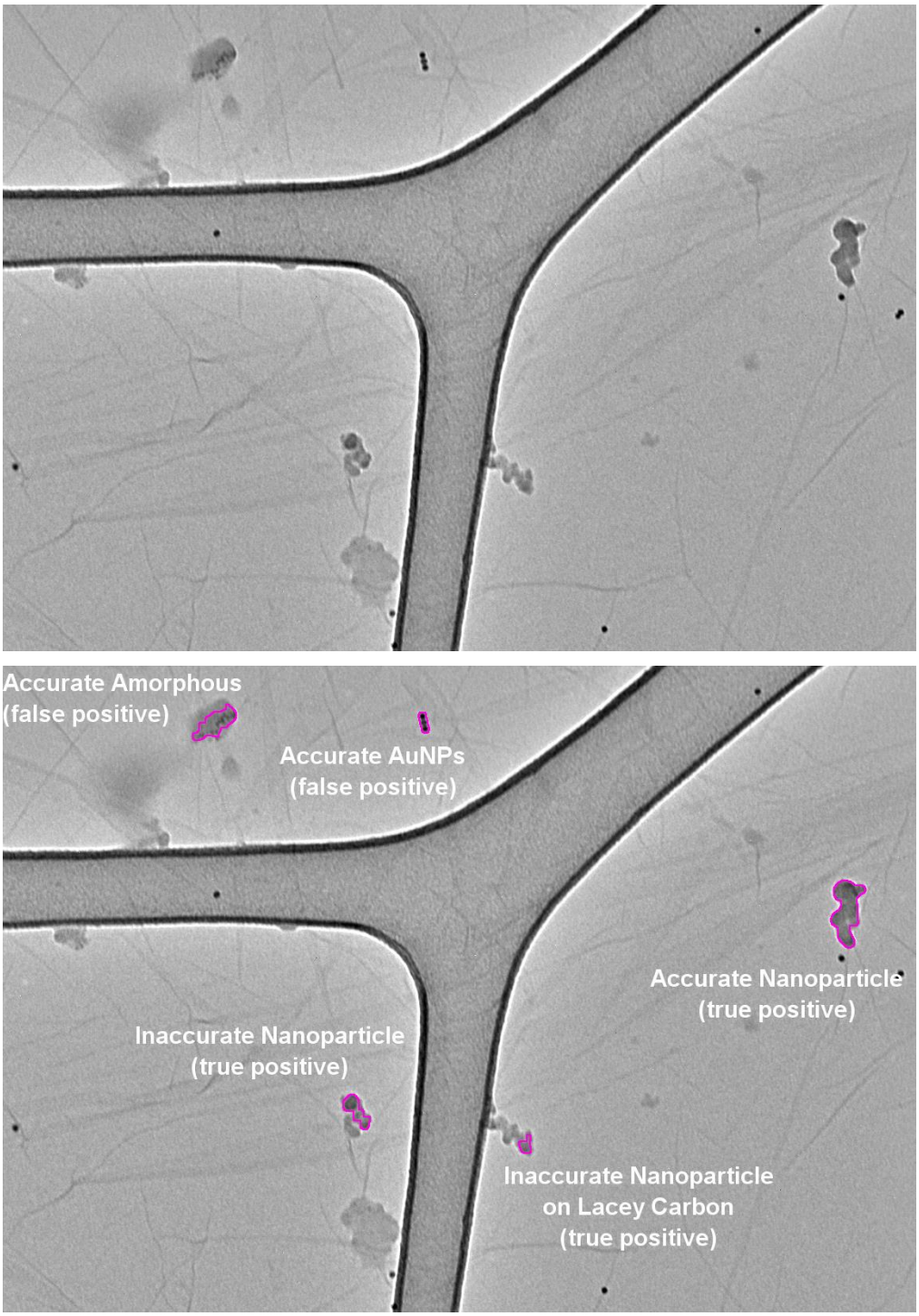


Figure-6.16: Showing the selections resulting from automated image processing of an area of a montage. Highlighted are 3 selections of nanoparticles (true positives), for which 1 is accurate and 2 are inaccurate. Inaccurate selections still result in usable coordinates, but can be improved manually to facilitate rapid 2D characterisation. Also highlighted are two false positive selections, which despite relatively accurate identification are not soot nanoparticles.

In theory though, if automated selections were of high enough quality they could be used to achieve rapid 2D-TEM characterisation of soot nanoparticles. While highly accurate for the most well-defined nanoparticles, in general the automatic segmentations were not sufficient for typical 2D characterisation. Though development of an automated segmentation protocol that is *always* highly accurate was not feasible within the scope of the project, a useful stop-gap approach was developed. In the manual review process, a stage was implemented that allowed the operator to manually correct the automated selections if desired. Depending on the accuracies, these corrections could be major or minor. Though significantly lowering the throughput (and slightly undermining the purpose of an automated segmentation method), it offers a useful '2-for-1' opportunity to permit both particle identification *and* rapid 2D-TEM characterisation of soot in a 'semi-automated' process. For example, the two 'inaccurately' segmented nanoparticles in figure-6.16 could be improved in the manual process, while the accurate selection needs no update.

This procedure also permitted the fully manual identification of unselected soot nanoparticles that were visible in the montage adjacent to automated selections that were being reviewed. As described in section-5.3, GTDI soot-in-oil nanoparticles showed a preference towards positioning on the lacey carbon rather than the graphene oxide. This can be due to breakages in the GO film, but may also be related to differences in polarity of the GO (more polar) and lacey carbon (less polar). The removal of the lacey carbon edges from the automated selections (by the maximum area constraint) will remove many of the soot nanoparticles that appear in such locations. However, soot aggregates that are positioned on the edges of the lacey carbon support are generally not ideal for tomography. Being viewed on a thicker support reduces resolution as fewer electrons are transmitted through both particle and support. Also, nanoparticles positioned right on the edges are can potentially become obscured at higher angles of tilt, which can introduce errors in reconstruction. While less suitable for tomography and therefore acceptable to be removed from the automated selection process, many of these structures are still suitable for typical 2D characterisation. When implementing the optional method for segmentation correction, an additional option was made to allow the user to create fully manual selections of any particles entirely missed by the automated segmentation. This was predominantly useful for identifying those particles on the lacey carbon edges, though in some cases true false-negatives (*e.g.* soot nanoparticles on clear sections of GO) were corrected. An example of such a particle that could be selected in this regard is given in figure-6.17. In that example, an area of the montage sees one nanoparticle close to the lacey carbon accurately selected, while

an adjacent nanoparticle is not. This unselected nanoparticle could easily be identified manually in this optional step.

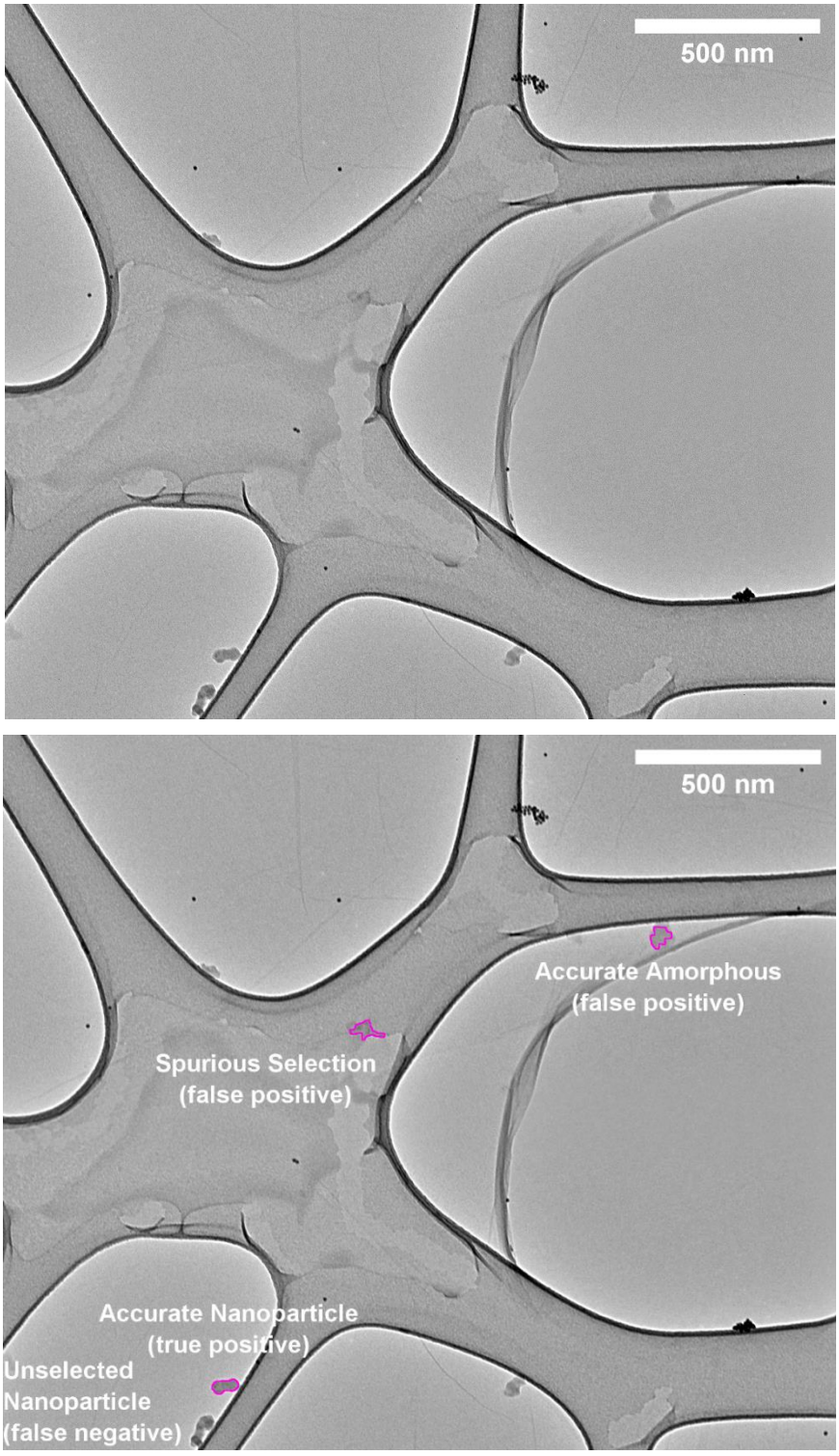


Figure-6.17: Showing the selections resulting from automated image processing of an area of a montage. Highlighted are 3 selections of nanoparticles (true positives), for which 1 is accurate and 2 are inaccurate. Inaccurate selections still result in usable coordinates, but can be improved manually to facilitate rapid 2D characterisation. Also highlighted are two false positive selections, which despite relatively accurate identification are not soot nanoparticles.

6.3.5 - Communication with SerialEM for Automated Operation

Following the manual review process, a final list of suitable structures is associated with a list of locations on the montage map. In Fiji these locations are in terms of pixel coordinates, where the (0,0) position is defined as the upper-left corner of the montage map. These coordinates must be converted to match the orientation, scale, and absolute position of the TEM specimen stage. This was performed using a self-made Matlab script, the main steps of which are detailed in the following paragraphs. The Matlab script requires only the positions of the reference and registered points to be entered as both pixel and stage coordinates.

Firstly, the rotation between the montage map and the live microscope feed is calculated. If montage map image processing occurs within the same session (*i.e.* the TEM grid has not been removed from the microscope), then this step will not be necessary as there will be no rotation. However, if the work occurs across multiple days, as is likely to be the case for shared faculty equipment such as our own, rotation is likely to occur. This is because it is essentially impossible to place the TEM grid into the specimen holder in the exact same orientation each time.

The rotation between the Fiji pixel coordinate system and the microscopes physical stage position is calculated by comparing the two sets of coordinates for the *registered points* of the montage map (see figure-6.18). One of the registered points (it can be any) is designated as a 'reference point', and the displacements in X & Y between the reference point and all of the other registered points is calculated. An angle (θ) made between the reference point, the registered point, and a vector running horizontally through the reference point is calculated *via* equation-6.1:

$$\theta = tan^{-1}\left(\left|\Delta y\right| \Big/ \left|\Delta x\right|\right) \qquad \textbf{(6.1)}$$

Where ΔX and ΔY are the horizontal and vertical displacements from the registered points to the reference point.

In both the pixel and stage systems, the vector running through the reference point remains in an equivalent position, but all of the other registered points are rotated with respect to it. As such, between each reference-registered point pair there will be a systematic difference in the angle measured in the two systems; this is the angle of rotation between them.

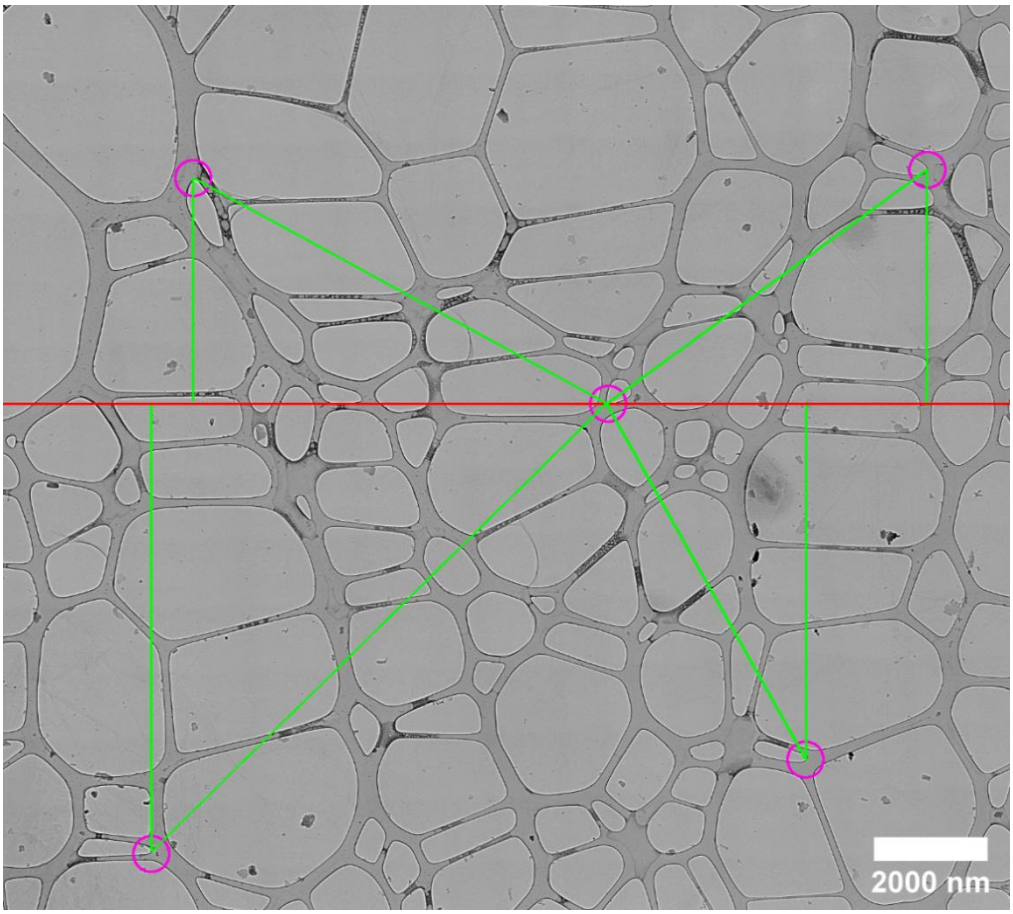


Figure-6.18: Example of calculations of angles between the vector running horizontally through the reference point (central) and the other registered points.

The rotation is then applied in reverse to the pixel coordinates, so that the spatial arrangement matches the stage system. Next, the scale factor that exists between the stage system (in µm) and the Fiji system (in pixels) is determined by comparing the calculated distance between each reference-registered point pair in each of the two coordinate systems. The distances in pixels are then divided by the distance in microns to calculate the scale factor. An average for all point pairs is taken to account for any small deviations that may exist across the map.

The positions of the (rotated) registered points in the Fiji system are then scaled to match the stage system simply by dividing their pixel values by the scale factor. However, these positions are still displaced in X & Y from their locations in the stage system, and these 'offsets' in X & Y must be calculated. This is because the origin in the Fiji system is the top-left of the montage map, while in the stage system the origin is a physical location that changes depending on how the TEM grid is loaded.

For each of the registered points, the rotated & scaled Fiji coordinates are simply subtracted from the stage coordinates, resulting in the offsets in both the X and Y

directions. If these are applied in reverse to the rotated and scaled Fiji coordinates, they will closely match the stage positions as measured in the live TEM imaging session.

The Matlab script is then able to write entries directly into the SerialEM file that is associated with the navigator montage map. Entries are written for each of the automatically segmented structures that were approved in the manual review process. Once this file is loaded into SerialEM, markers will appear on the montage map at the locations of the chosen particles. The user can then simply select one of the tagged locations on the montage map to centre the live camera on the feature of interest. The magnification can then be increased to one appropriate for tilt-series acquisition (*e.g.* x25,000-50,000). At this stage a final check for suitability is unavoidable, and relates to the orientation of the grid in the TEM specimen holder. Depending on the orientation of the TEM grid in the specimen holder, the position of the tilt-axis during tilt-series acquisition will change. This may cause adjacent features to overlap with, and obscure the feature of interest. However, given the manual review process it is likely that most accepted locations will not be affected by this as they will be spatially removed from any large structures.

6.4 – 2D-TEM Characterisation of GTDI Soot-in-Oil

Following the development of this semi-automated procedure for TEM imaging, the GTDI soot-in-oil sample described in chapters-3 and 5 was screened for structures of interest for 3D study. The results of 3D morphological characterisation are presented in chapter-8, but here results are also presented for large-scale 2D morphological characterisation. By utilising the options for manual selection of nanoparticles during the review process, 524 individual soot nanoparticles were characterised in 2D. The preparation of TEM grids with this sample had already been carried out according to the method described in section-3.5.2.

6.4.1 – Application of the Automated TEM Procedure to GTDI Soot-in-Oil

Montage maps were produced for 9 squares of the TEM grid, covering approximately 4000 μm^2 in total. Typical duration for montage acquisition was around 20-40 minutes, similar to the time required for acquisition of a 121 image tilt-series. Though ideally this process is fully automated, occasional errors occurred in SerialEM relating to the positioning of the microscope camera. Essentially, the microscope was not positioned where it predicted it ought to be based on the grid-pattern of the montage sequence. This

was likely due to difficulties tracking barren areas of the TEM grid, for example large holes in the lacey carbon support that can span several microns (see figure-6.19).

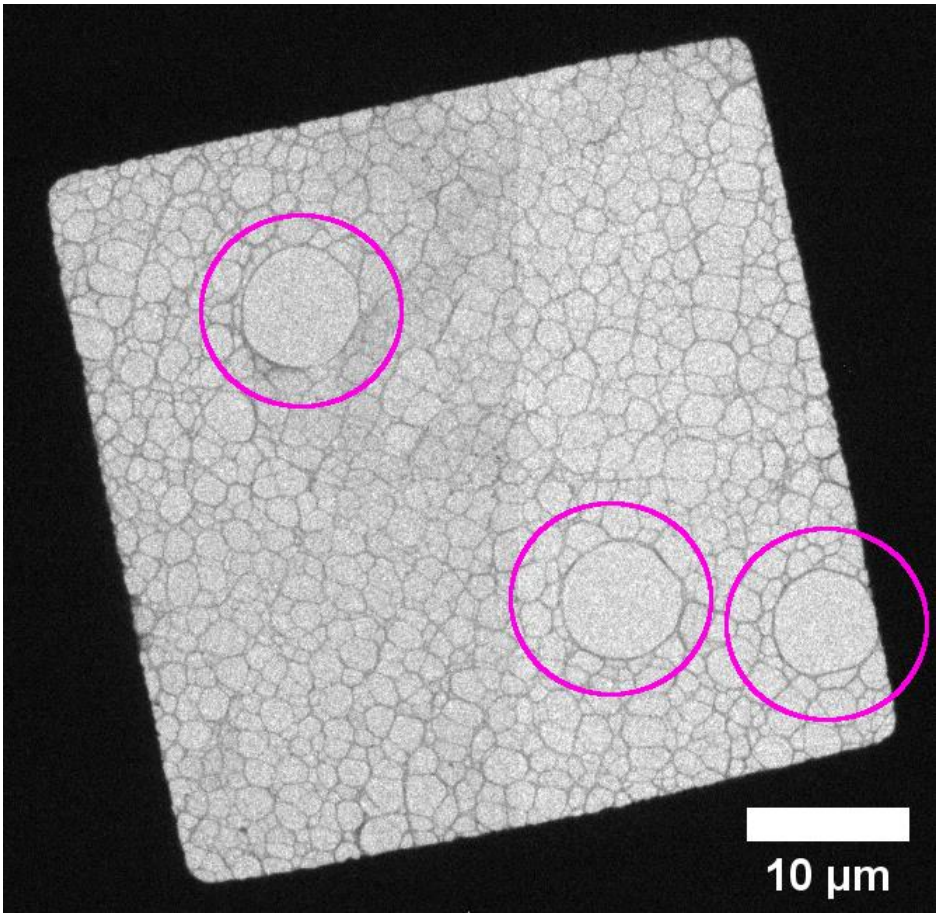
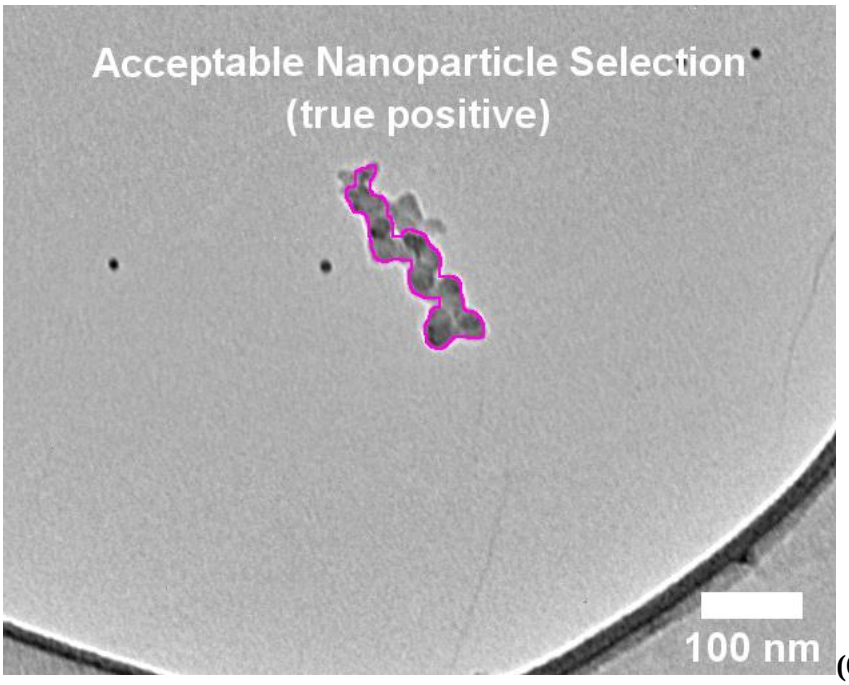


Figure-6.19: Low-magnification image (x250) image of entire grid square. Highlighted are large holes in the lacey carbon support, measuring approx. 7-8 µm in diameter. It is easy for the GO film to break over these large holes, leading to complete lack of structures and therefore difficulty tracking during montage acquisition and stitching.

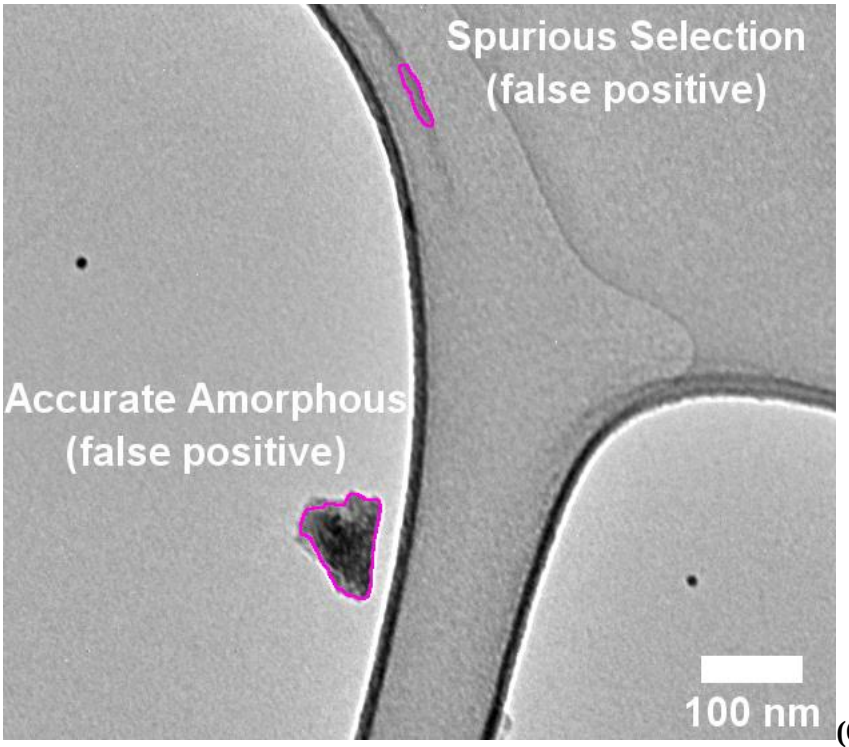
Stitching of montage maps required only a few minutes per montage (< 5 minutes), provided the higher level of defocus (-12 µm) was used. Automated image processing completed in around 1 minute for a stitched montage comprised of approx. 225 million pixels (~15,000 by 15,000 px). The manual review of automatically chosen locations required around 1-2 seconds per selection, and so up to several minutes per montage map (average of around 150 selections per map).

From these 9 montage maps, 271 soot nanoparticles were automatically identified. However, due to the prevalence of non-soot structures on the grid, this accounted for only around 20% of all automated selections (1373 total). However, approx. 60% of all automated selections were actually considered acceptable identification of the *non-soot* structures that were visible (*e.g.* localised amorphous carbon). As such only around 20% of the automated selections were genuine *false positives*, which includes features such

as small holes in the lacey carbon support, folds in the graphene oxide film, spurious noise, and poor selections of actual deposited material. Examples of true positive and false positive selections can be found in figure-6.20, as well as figures 6.16 and 6.17.



(6.20a)



(6.20b)

Figure-6.20: Showing an example of a true-positive selection of a soot nanoparticle (above), a positive selection of a non-nanoparticle structure (below – lower), and a false-positive selection of a wrinkle in the lacey carbon (below – upper)

During the manual review process, the option was taken to improve any inaccurate nanoparticle selections, and to identify any nanoparticles that had been completely missed by automated segmentation. This lead to the additional selection of 253 nanoparticles, the vast majority of which were located on the edges of the lacey carbon support. Only a very small number were genuine false negatives, in that they were located in open sections of graphene oxide and should realistically have been selected.

6.4.2 – Morphological Measurements

Once nanoparticles selections had been created or updated to acceptable standards they were all characterised in terms of their morphology using Fiji. This step is extremely efficient and measurements of even hundreds of nanoparticles completes within a couple of minutes.

For this section, nanoparticles were characterised in terms of Feret diameter, radius of gyration, and fractal dimension. The radius of gyration was determined using the pixel-based method according to equation-3.8. The Feret diameter (maximum length of the nanoparticle) was determined directly using Fiji. The fractal dimension (D_f) was determined according to the method described by Koylu *et al*. [75]. First, the number of primary particles (N_p) was determined according to equation-3.2, while fractal dimension of the sample as a whole was determined according to equation-6.2 below:

$$N_p = k_f \left({}^{D_g}\!/_{d_{pp}} \right)^{D_f} \qquad \textbf{(6.2)}$$

Where D_g is the diameter of gyration, and d_{pp} is the average primary particle diameter. The D_f is determined from the slope of a log-log plot of Np *vs.* (D_g/d_{pp}).

General features of the structures present in the GTDI oil sample have already been summarised in chapter-5, section-5.3. As reiterated in this chapter, typical nanoparticles were present alongside large quantities of localised amorphous carbon and patches of crystalline material. The images obtained during those initial explorations of the sample were used to determine primary particle diameter. Though the scale of the montage images (x10,000 magnification) is sufficient for whole aggregate sizing, individual primary particles are too small for accurate measurements.

6.4.3 – Primary Particle Diameter

The initial step in the 2D characterisation method is the determination of N_p according to equation-3.2. A mean diameter of 33 nm was determined based on 236 individual measurements from 64 images of soot nanoparticles. The primary particle size distribution is shown in figure-6.21, with number of bins (= 9) chosen based on Freedman-Diaconis criteria [210]. The plot shows a log-normal distribution, with a modal interval at 25-30 nm. The minimum diameter measured was 17 nm, while the maximum was 58 nm. A wide range in primary particle size has been observed before for GDI exhaust soot [86, 87].

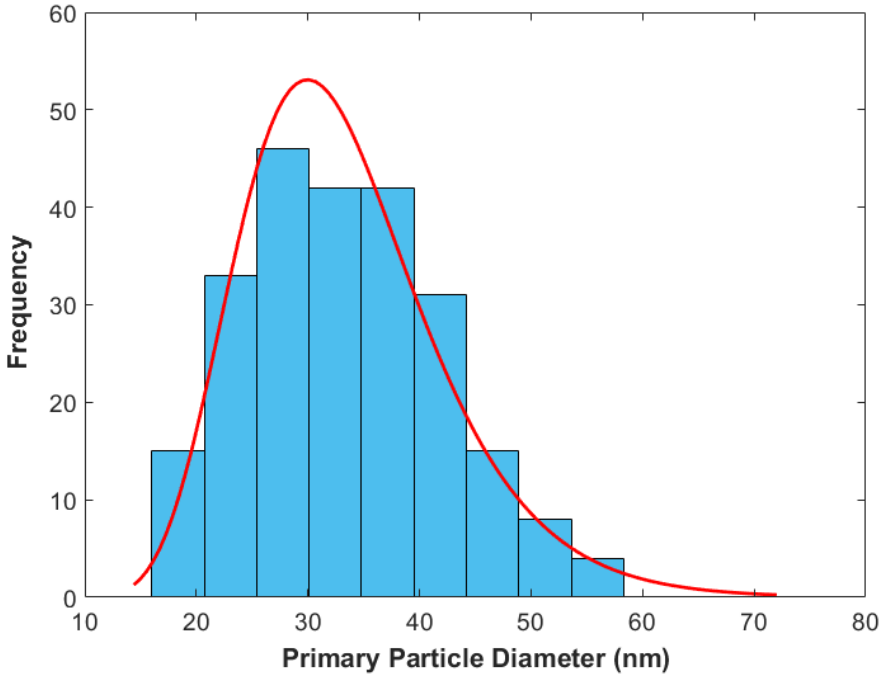


Figure-6.21: Size distribution of primary particle diameters. Modal diameter is between 25-30 nm, and mean diameter is 33 nm.

Previously, TEM study of soot-in-oil from a 1.6 L GTDI test engine had been performed by members of the Powertrain research group at Nottingham in collaboration with researchers from Oxford Brookes University [41]. In that work, soot-in-oil samples were collected after 30 hours of testing using a drive cycle to mimic typical urban driving environments. Mean primary particle diameter in that study was slightly larger at 36 nm, and the range of diameters was also larger at 20-90 nm. Though in that previous study primary particle nanostructure included an additional outer-most layer comprising around 5 nm of amorphous carbon, this was not typically observed for the sample in this work.

Differences between the two soot samples may relate to the differences in engine operation. For example, the real-world driving that generated the soot in this current work will have included cold-starts while the prior study was fully-warm at all times. Additionally, while the 1.4 L GTDI engine utilised spray/air-guided fuel injection, the 1.6 L GTDI engine in the previous work used wall-guided fuel injection, thus leading to different charge mixture preparations.

6.4.4 – Aggregate Morphology

The first consideration was convergence in the mean radius of gyration measurement, as the study of over 500 individual nanoparticles represents a relatively large 2D-TEM characterisation study. Previous work by Kondo *et al*. studying soot from diesel flames had suggested that up to 1000 individual aggregates needed to be studied in order to have acceptable mean convergence in this parameter (within ±2 nm). Following the method used in that work, figure-6.22 shows the mean R_g for the GTDI soot-in-oil sample convergences within around 150 individual measurements.

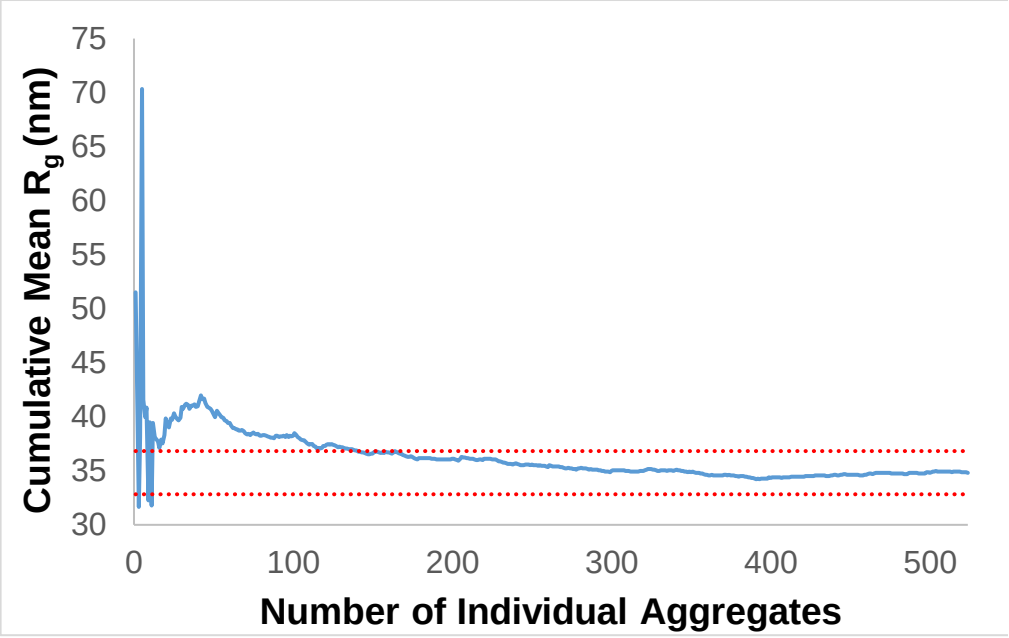


Figure-6.22: Convergence of mean radius of gyration. Dashed lines represents ±2 nm from the final mean value.

Though this value is clearly far smaller than the 1000 suggested in the previous study, the data plot used in that work to derive the number ("figure-16" in [39]), actually shows relatively strong convergence from around 150 measurements. They note that incorporation of measurements from a particular area of the TEM grid act to skew the

mean towards a larger value. Without inclusion of those results, the number of measurements required for convergence seems likely to be much more similar to our value.

Next, comparisons are made to the morphology measured for the GTDI soot-in-oil sample studied in the work of La Rocca *et al.* [41]. The first consideration is the overall size of the nanoparticles. In that previous study, around 100 nanoparticles were characterised in terms of *skeleton length*. This is effectively the longest distance that can be measured through the branched morphology of a nanoparticle, staying roughly equidistant to the edges of the structure. As such, the skeleton length should be expected to almost always be greater than the Feret diameter, which only measures a straight line between the furthest points of the structure. How much greater depends on how complicated the fractal-like morphology of the nanoparticles is. An example can be observed in "figure-3" of La Rocca's earlier work on diesel soot-in-oil nanoparticles [70], where skeleton length is over 50% larger than a simple length measurement.

The Feret diameter distribution for the GTDI soot-in-oil sample in this work is shown in figure-6.23. This plot shows an approximately log-normal distribution, with a modal interval at 107-124 nm, and a mean Feret diameter of 118 nm. The minimum Feret diameter was 53 nm, while the largest was 342 nm. In the study of La Rocca *et al.*, mean skeleton length was 153 nm, while the modal interval was around 120 nm. The maximum skeleton length was 405 nm, while the minimum was 53 nm.

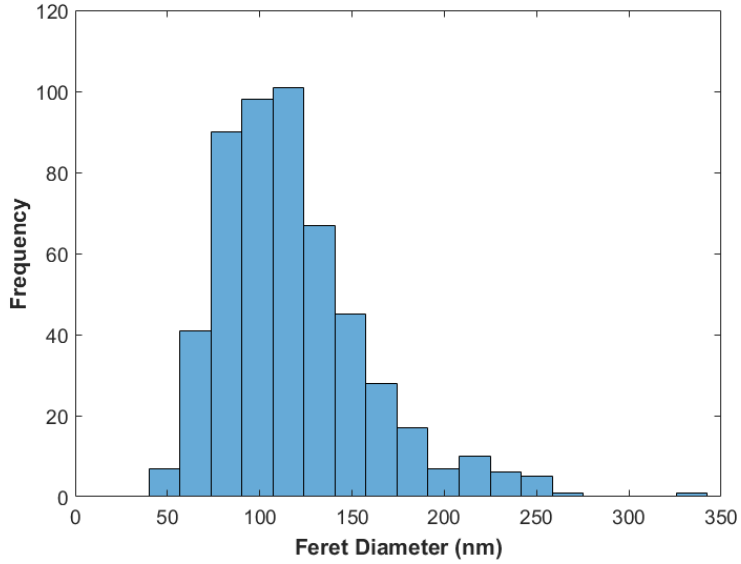


Figure-6.23: Distribution of Feret diameter measured in the GTDI soot-in-oil sample. The modal interval is at 107-124 nm.

Despite the fact that skeleton length measurements of aggregates are inherently larger than Feret diameter measurements, the modal values in both this study and that of La Rocca *et al.* are very similar at around 120 nm. In contrast, the mean value of skeleton length is significantly larger than the Feret diameter. This reflects that overall larger measurements were observed in the previous study (405 nm *vs.* 342 nm in this work), causing a right-skew to that data. Though the relationship between Feret diameter and skeleton length strongly depends on the fractal nature of each nanoparticle, the fact that modal values are overall fairly similar is perhaps indicative that aggregates in this work tend to be at least slightly larger on average.

The final comparison was in terms of fractal dimension. In this work a commonly used 'ensemble' style method was used, rather than a composite of individual measurements. As described the fractal dimension was determined from the slope of a log-log plot of N_p *vs.* (D_g/d_{pp}) shown in figure-6.24, and provided a value of 1.73. By comparison, the GTDI soot-in-oil nanoparticles studied by La Rocca *et al.* were associated with an average fractal dimension of 1.44. This suggested that the nanoparticles in that study tended to be more branched and open in their structure, while those in this study are relatively more clustered.

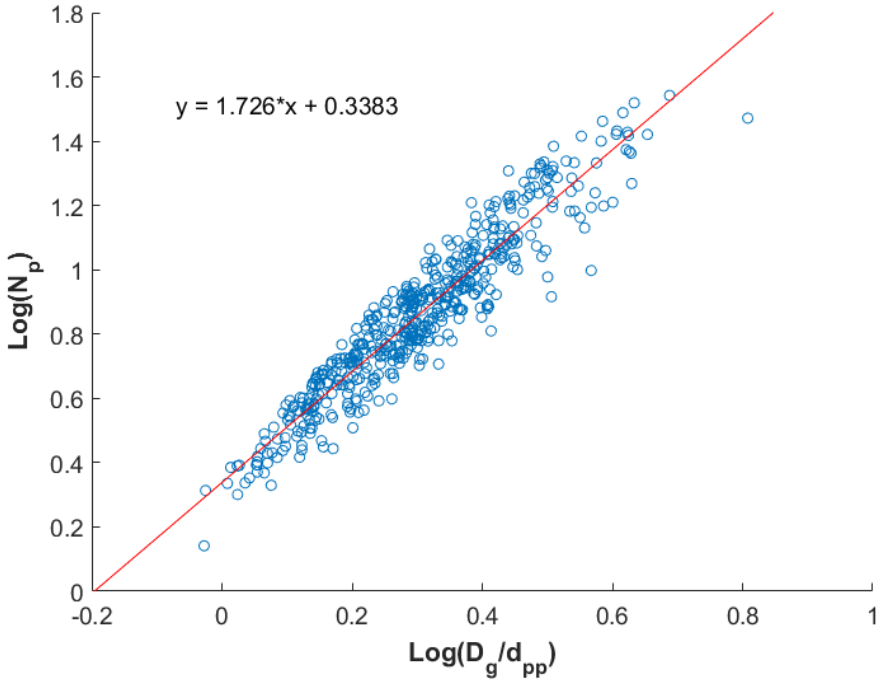


Figure-6.24: Log-log plot for calculation of fractal dimension *via* the slope. R-square = 0.8921.

6.5 – Conclusions

The work included in this chapter was performed in order to improve throughput of ET for 3D soot morphology characterisation. In the early work using ET to study a flame-generated soot nanoparticle (chapter-4), stages of the reconstruction process were identified for optimisation. When the ET technique was applied to study a GTDI soot-in-oil sample in chapter-5, it became apparent that significant improvements could also be made during the TEM image acquisition stage. Constraints on suitability for particles arise due to the necessity of tilting the TEM grid, and needing to align the tilt-series using gold nanoparticles. Populating TEM grids with ideal concentrations of soot can be difficult for GTDI soot-in-oil; mineral oil is a strong contaminant in TEM and must be removed with solvent dilution, but soot concentration can be very low (*e.g.* 0.6%). High dilution leaves very little soot in the suspension, but lower dilution results in oil contamination. The result is fairly sparsely populated TEM grids and, since soot is so small compared to the size of the grids, long durations searching for particles suitable for 3D study.

A plan was devised to use automation *via* SerialEM to improve efficiency of TEM imaging. Large areas of the TEM grid can be screened with minimal manual involvement. Large scale maps are produced of the grid, and automated image processing is used to identify structures on the grid. Constraints in size and shape are used to remove selections of most non-soot structures, but is somewhat unavoidable for GTDI soot-in-oil due to their high abundance (*e.g.* amorphous carbon, crystalline material, and general debris). A manual 'review' process was included to ensure removal of any false positives, and suitability for tilt-series acquisition. Options were also included to manually improve inaccurate automated selections, and identify nanoparticles that were completely unselected. These optional steps could be used to facilitate rapid 2D characterisation of nanoparticles.

By utilising these options, a total of 524 individual nanoparticles were characterised in 2D. The number of individual nanoparticle measurements required for mean convergence in radius of gyration was around 150, compared with 1000 in a prior study of diesel flame-soot [39]. Primary particle measurements showed an average diameter of 33 nm, and log-normal distribution. Compared with prior study of GTDI soot-in-oil nanoparticles by La Rocca *et al.* [41], this sample showed slightly smaller average diameter (*cf.* 36 nm) and a smaller range of values. The modal value of overall particle length (Feret diameter) was around 115 nm, compared with around 120 nm in the prior study. However, differences in measurement technique indicate that nanoparticles in the

sample are likely to be at least slightly larger on average. Average fractal dimension of nanoparticles in this sample was determined as 1.73, compared with 1.44 in the previous work. This suggests that while nanoparticles in this study tend to be larger, they also tend to be more clustered in their structure.

7 - Assessing the Accuracy of Electron Tomography for Soot

The work included in this chapter describes assessment of the accuracy of 3D volume reconstruction *via* ET in Etomo. For this assessment, computational voxel-based models of soot-like aggregates were developed to act as ground truth, *i.e.* their 3D morphology is known exactly. A simple sphere model is also used as ground truth for consideration of the effect of shape on the propagation of reconstruction errors. From 13 total soot-like aggregate models, TEM-style tilt-series are produced and subjected to the full ET procedure developed in chapter-5. The morphology of post-reconstruction models are then compared to the originals to determine absolute accuracy of different ET procedures. Efforts are made to reflect typical soot-in-oil morphology and appearance in TEM images, so that propagation of reconstruction errors and artefacts are as realistic as possible. The results of this work indicated that tilt-series created over a ±80° tilt-range observed practically no elongation (<1%) due to the missing wedge. By comparison, ±60° tilt-series observed only minor elongation (3-4%), with practically no differences between tilt-series with 1° increments and 3° increments between images. A simple sphere model was elongated by around 10% when reconstructed from a +60° tilt-series. While reconstructions from ±80° tilt-series lead to a slight underestimation of the true particle bulk, reconstruction from ±60° tilt-series lead to a slight overestimation; overall accuracy for the two methods was similar. Reconstruction from ±60° tilt-series with 3° increments (referred to as ±60_3°) was overall highly accurate for soot-like aggregates, resulting in deviations from ground truth values for volume, surface area, radius of gyration, 3D-circularity, and fractal dimension of <3%. Analysis of the effect of interpolation in manual segmentation was inconclusive due to inherent differences between appearance of real aggregates and simulated aggregates.

The work included in this chapter is adapted from a recently published SAE Technical Paper, which was also presented at the 2019 SAE World Congress in Detroit:

Haffner-Staton E., La Rocca A., Cairns A., Mcghee M., Fay M. *Assessing the Accuracy of Soot Nanoparticle Morphology Measurements Using Three-Dimensional Electron Tomography*. SAE Technical Paper; **2019**. Report No.: 0148-7191.

7.1 - Introduction

Chapter-4 tested a basic methodology of ET for soot, and explored a possible important source of error in typical 2D soot characterisation relating to the orientations of nanoparticles in TEM. The chapters that followed started a process of optimisation of TEM imaging ET reconstruction for soot, in order to begin close the gap in usability to the current state-of-the-art method, 2D-TEM. In chapter-5, the choice of reconstruction algorithm, conformation of the tilt-series, and use of linear interpolation in manual segmentation was refined, resulting in an almost 70% reduction in time required in comparison to a typical ET procedure from the literature. In that chapter, optimisation was considered in terms of speed and quality of the reconstruction. While speed was straightforward to assess, the quality of tomographic reconstruction was only established on a relative basis. That is to say, accuracy of different ET procedures was determined by considering whether their results were similar or dissimilar. Guidance in terms of overall accuracy came only from knowledge that certain methods are fundamentally more accurate than others, for example SIRT with high iterations > SIRT with low iterations, and more complete tilt-series > reduced tilt-series. Absolute accuracy could not be confirmed as so-called ground truth morphological data for *real* soot nanoparticles does not exist.

The major source of error in ET is the missing wedge, which results from limitations of the equipment used for high-tilt imaging. Though in theory typical equipment can tilt specimens over a ±80° range, in practice slight mechanical imperfections limit the accessible range to ±60° (see section-3.3.2 of chapter 3 for more details).

The missing wedge error originates from the violation of the underlying Fourier Slice Theorem, that states that tomographic reconstruction requires *all possible* 2D projections to recreate the 3D object [166]. Obviously, a ±60° tilt-series does not represent a full set of projections. This means that there is a lack of projection data of the particle taken from directions predominantly perpendicular to the TEM support film on which the particle is deposited (designated as the Z-direction). Missing information in the reconstruction causes blurring of the particle matter, which occurs in the direct of the missing wedge. This can cause elongation of the reconstructed object, and a deviation from the true morphology. The extent of this elongation in single-axis tomographic reconstruction is in theory described by Radermacher's equation-7.1 [231], which provides a value of 1.55 for a single-axis ±60° tilt (55% stretch). However, other authors have established that the morphology of the structure (and its appearance in the TEM images) also influences the extent of the missing wedge artefacts [232].

With this well-known source of error in mind, and given that the fundamental purpose of this project is to improve characterisation accuracy *vs.* 2D-TEM, determination of the accuracy of ET is of great importance.

$$e_{xz} = \sqrt{\frac{\alpha + \sin(\alpha)\cos(\alpha)}{\alpha - \sin(\alpha)\cos(\alpha)}} \qquad \textbf{(7.1)}$$

The established practice for determining accuracy of a tomographic method is to create a *ground truth* (GT) data set [233, 234]. In tomography, GT is an object for which 3D morphology is exactly known. The object is then subjected to the tomographic method and the morphology of the resulting model is compared to that of the original.

Of course, tomography is widely used in many fields and ET is not the only variation. Tomographic reconstructions can be carried out using many different forms of electromagnetic radiation and particles as the transmitting medium. As such, it can be applied to samples made of many different materials, and of different shapes and sizes. For example, X-ray micro-CT (*computerized tomography*) has been used to study root structures of plants *in vivo* [235, 236], whilst positron emission tomography is used in oncology for the imaging of tumours [237, 238]. In the study of soot we employ electrons because of the need for extremely high resolution, and the fact that soot is semi-transparent to electrons. Depending on the field of study ground-truth data can take various forms, though ideally should always closely represent the structures typically measured. This is to ensure that reconstruction artefacts propagate as realistically as possible given that they depend upon the structure studied [232].

In some areas, the size and nature of the structures studied mean that physical objects can be used as ground truth data. For example in their study of periodontal conditions *via* X-ray CT, Mol *et al.* used the locations of physical sites on dry skulls as ground-truth [239]. In the study of plant root structures, different authors have used real root systems removed from soil as GT, by physically measuring their morphology with tools such as high-precision callipers [235, 240]. In that same field of research, ground truth has been created in the form of physical 'phantoms', which are structures of known morphology and appearance in X-ray CT created by the user. Perret *et al.* created a phantom consisting of plastic tubing filled with soil, sand, and various objects such as blocks of wood and plastic tubing [241].

In many situations, such as our own, this is clearly not possible and GT tends to be created computationally [37, 195, 235, 242, 243]. It is common for simplified structures

to be used as model systems due to difficulties associated with the creation of synthetic data-sets. For example, Okyay's SEM tomography study of soot used a simple sphere model, and observed no elongation for a ±80° reconstruction [37]. However, it is also accepted that the shape of the structure to be reconstructed has a defining effect on the extent of elongation observed [232], so the relevance may be limited. As such, some authors choose to create more realistic structures, to better represent the errors that will occur with real data sets. For example, in their study on the evaluation of root segmentation procedures for X-ray CT data, Mairhofer *et al.* opted for GT in the form of models with conical shapes, as they were considered the most basic structural unit of real roots [235]. In their study of positron emission tomography, Hatt *et al.* developed ground truth data based on real segmentation of patient data, re-applying artificial reconstruction to a segmented volume model [238]. Hamarneh *et al.* developed a method for producing ground truth in the form of artificial vascular networks, in order to facilitate easier segmentation validation and training in real medical applications [244]. This serves as only a small sample of the various schemes for validation and development of GT in some diverse fields. The concepts discussed are generally applicable to our own area despite the significant fundamental differences. Based on these examples it was decided that a simple aggregation model would be used to create soot-like 3D models to act as ground truth for validation of our ET methodology.

7.2 – Soot-like Aggregate Models: Ground Truth

Using the image processing software Fiji [180], 13 models were created to represent small soot nanoparticles similar to those seen in the GTDI soot-in-oil sample described earlier. The models were made from attaching between 10 and 30 spheres (representing primary particles) that were 100 pixels in diameter. If real primary particles are usually around 30 nm in diameter, the size of these spheres represents a scale of roughly 0.30 nm pixel-1, which is towards the highest resolution of real tilt-series we have acquired experimentally (approx. x40,000 magnification). The aggregation algorithm was not intended to mimic real GTDI soot-in-oil formation to a quantitative degree. Detailed information on this process does not yet exist in the literature for the specific case of GTDI soot-in-oil, and its implementation would be non-trivial and beyond the scope of this work even if it did. Instead, the aim of the simple aggregation model was merely to produce structures that qualitatively represented soot-in-oil nanoparticle morphology. In order to establish any differences in propagation of missing-wedge errors for objects

of different morphology, a simple sphere model was also created (similar to that in Okyay's study [37]) to act as ground truth.

The procedure for aggregate simulation is summarized as follows:

- A single sphere is positioned at the centre of an empty 3D volume
- A second sphere is attached to the first in a random position in XYZ, with the size of the intersection between them within predefined limits of overlap (set as 10-20%)
- One of the existing spheres in the structure is randomly chosen to act as the seed for an additional sphere attachment
- The incoming sphere is attached to seed sphere, again in a random XYZ orientation within the overlap limits
- This process is repeated until the desired number of spheres comprise the aggregate model
    - If the same spheres are chosen as a seed multiple times it results in a more clustered structure. Branched structures resulted from attachment away from the central spheres.

This procedure created models in the form of a binary 8-bit *.tiff image stack. All white pixels correspond to the model, while black pixels represent background only. The true values of all morphological parameters (surface area, volume, *etc.*) can easily be measured in Fiji as described in section-3.6.2. These measurements are henceforth referred to as 'ground truth' or 'true' values. Figure-7.1 provides an example of 5 of the simulated soot models, rendered using UCSF Chimera [211]. Also created was a simple model of a single sphere, similar to that used in other tomography studies [37].

Original models are then subjected to a realistic tomographic reconstruction procedure in order to evaluate the extent and propagation of errors in 3D-TEM. Firstly, a TEM-style tilt-series of 2D projections must be created to mimic the real reconstruction process. Not only must the set of 2D projections be created, but the images of this pseudo-tilt-series must also fulfil the projection requirement (see experimental chapter section 3.3.1 for more details). The density of the simulated aggregates in the 2D projections must be directly related to their grey-levels/colour values. This was achieved using the 'Volume Viewer' plugin for Fiji. This plugin allows the user to represent a 3D volume in 2-dimensions from a chosen viewing angle, and also allows for alteration of the contrast and transparency of the projections to replicate real TEM images and adhere to the projection requirement for tomography. Tilt-series were created over a ±80° tilt range in 1° increments, with the particles in random orientations. The raw-output of this

process is shown in figure-7.2. Next, images are inverted and contrast is altered so that grey-levels in these simulated tilt-series match those seen in real TEM images of soot. Average values for the graphene oxide (GO) film, and single/layered primary particles on GO were measured in real TEM images of a variety of soot samples. An example of grey-levels in an 8-bit TEM image of soot on graphene oxide is given in figure-7.3.

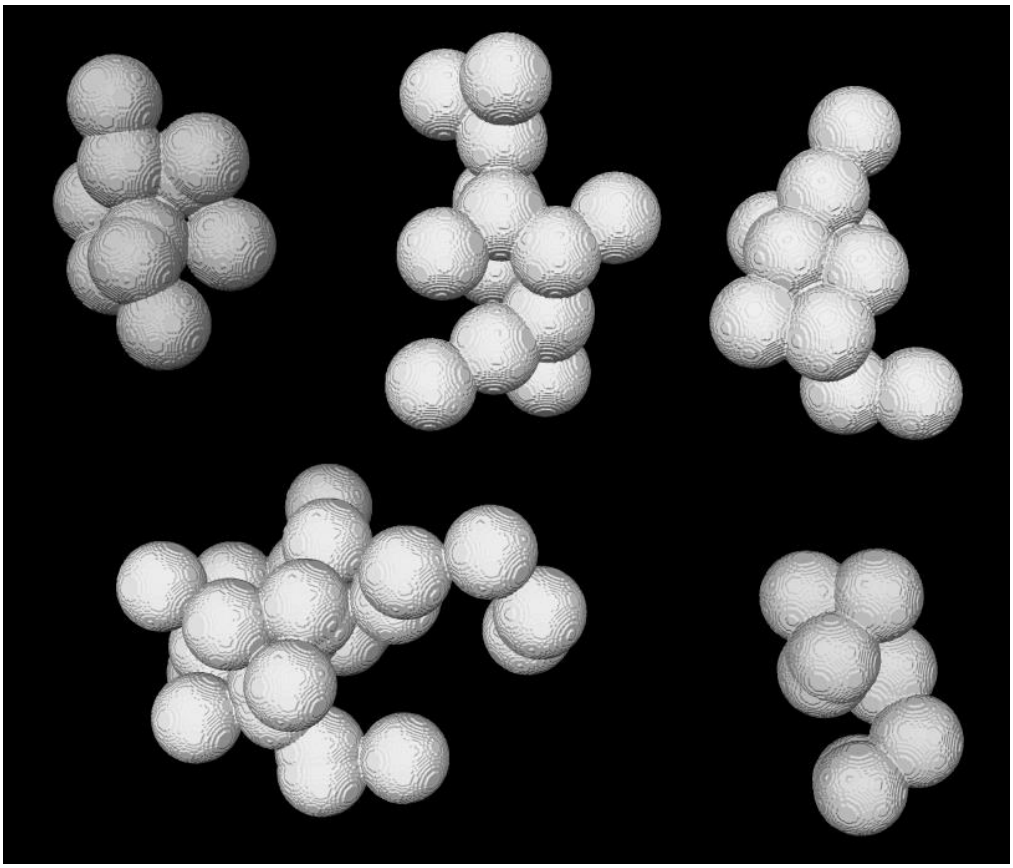


Figure-7.1: Example 3D renders of simulated soot-like aggregates, produced using UCSF Chimera

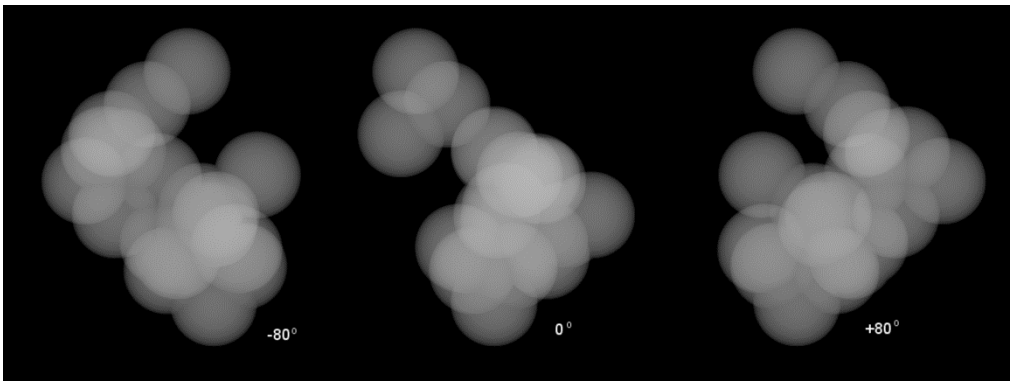


Figure-7.2: Raw output of *Volume Viewer* plugin for Fiji. Showing simulated 2D projections of aggregate model at -80°, 0°, +80° (left to right)

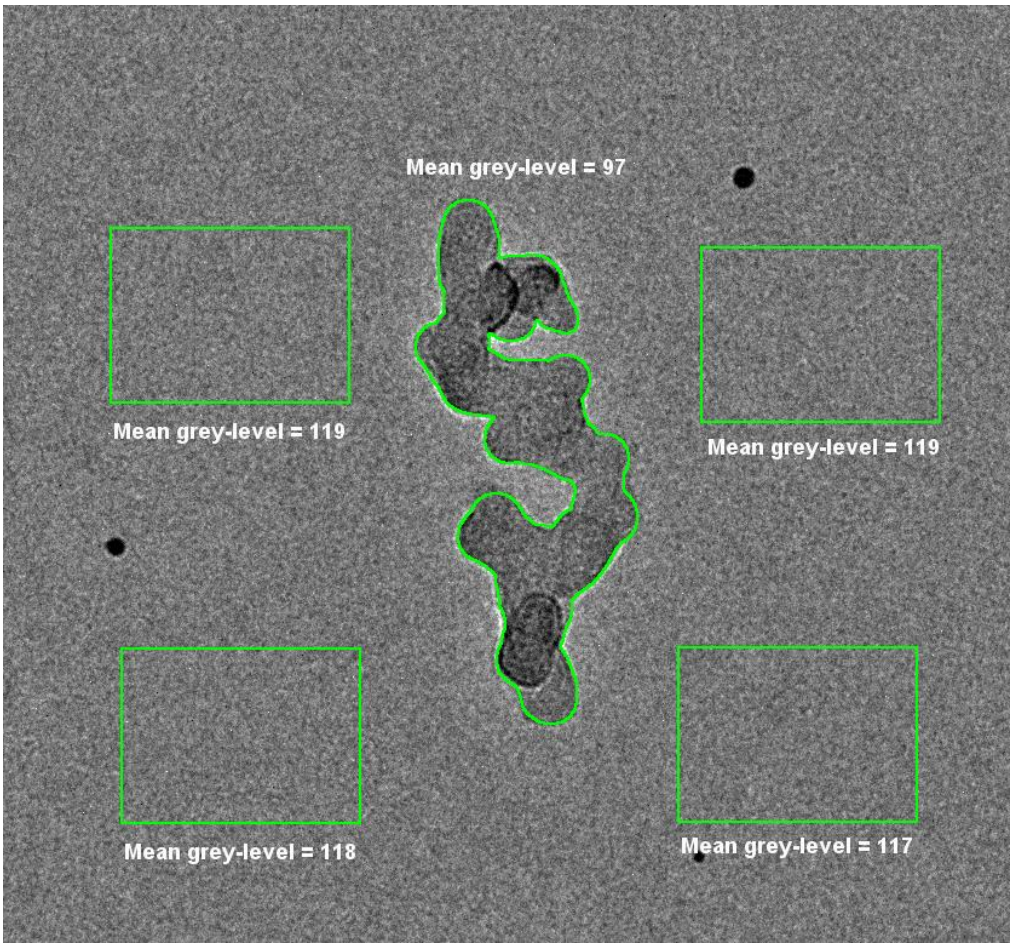


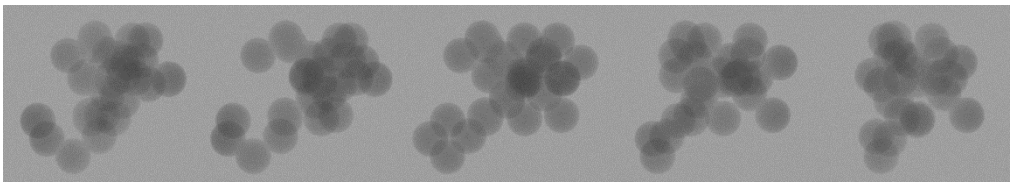
Figure-7.3: Example of average grey-level values of pixels in ROI selections of soot nanoparticle and graphene oxide support film in standard TEM image (8-bit image).

Next, TEM stylings were applied to the tilt-series to appear similar to the quality present in real TEM images. This is an important factor for accurately representing real reconstruction errors. An example of a methodology for the simulation of real TEM image appearance on a synthetic tilt-series is found in the work of Friedrich *et al.* [195]. In that work, the authors considered the aberrations of BF-TEM imaging to estimate the point-spread function (*i.e.* blurring) they should apply to their models of spheres in the form of a Gaussian blur.

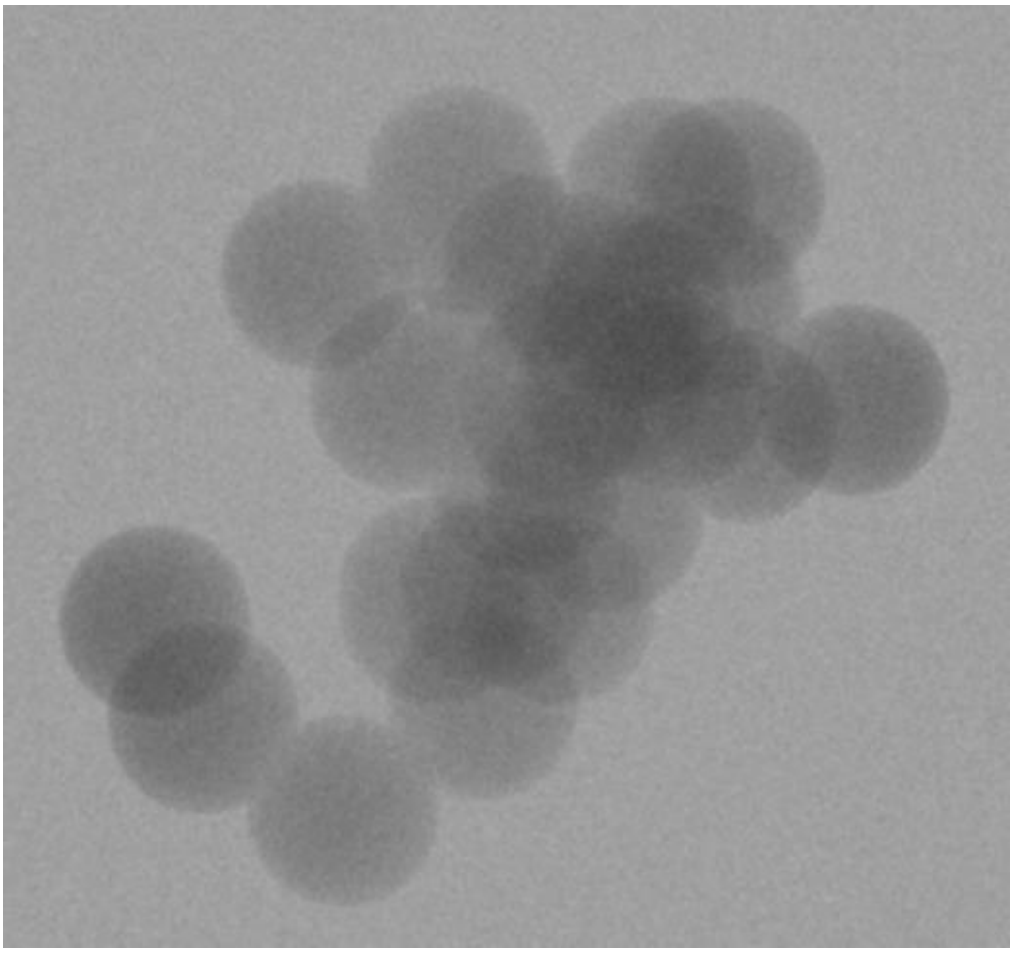
In this work, the *specified noise* plugin in Fiji was used to add random noise according to a Gaussian distribution. The application of noise is highly qualitative as *perfect* resolution images of soot do not exist, so it is impossible to quantify the true signal to noise ratio (SNR). The level of random noise added was a trial-and-error process to qualitatively match that seen in real images.

A degree of blurring was added to simulate the decreased resolution seen in real TEM images of soot due to the PSF, similar to that performed by Friedrich [195]. This was

achieved using a Gaussian blur operation, which replaces the grey-level of each pixel with a value determined from the surrounding pixels in a 3x3 grid. The effect of this process is perhaps underwhelming visually, but this relates to the fact that the structures are aggregates of perfect spheres so even with application of blurring still appear quite precisely defined. Examples of tilt-series style images are shown in figure-7.4.



(7.4a)



(7.4b)

Figure-7.4: (a) Showing 5 images from a simulated tilt-series, after processing to match appearance of real soot TEM images (addition of noise and blurring). (b) A single projection is shown in greater resolution.

At this point, three variations of each tilt-series were made for each model: the full ±80° tilt-series (161 images), a ±60° tilt-series (121 images), and a ±60° tilt-series with 3° increments (41 images; henceforth referred to as ±*60_3*°). Respectively, these represent

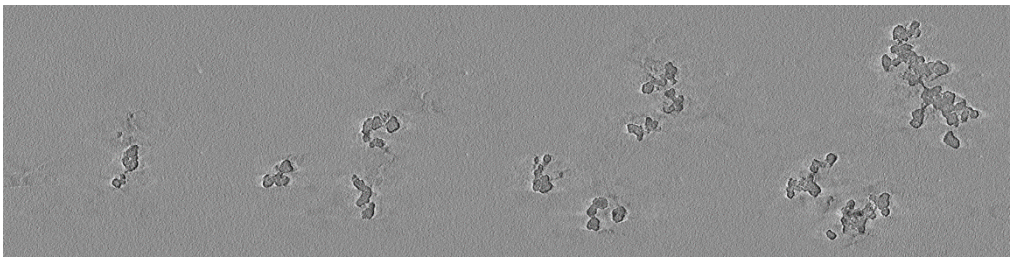
the maximum tilt-series that can be reconstructed with the Etomo (±80°), the largest tilt range that can routinely be recorded experimentally with TEM (±60°), and a reduced tilt-series as per the results of optimisation in chapter-5 (±60_3°).

For each of the 13 aggregate models, the 3 different tilt-series were reconstructed to produce a total of 39 tomograms. Reconstructions were performed using Etomo [176], utilizing the weighted back-projection (WBP) algorithm. Reconstruction of the full ±80° tilt-series took around 1 minute to complete (30-50 MB tilt-series file), ±60° tilt-series around 30 seconds (20-40 MB), and ±60_3° around 10 seconds (5-15 MB). Reconstructions were all performed on a Lenovo PC with a 3.50 GHz Intel Xeon E5-1620v3 processor (8 CPUs) and 32 GB RAM, using a 64-bit version of Windows 10.

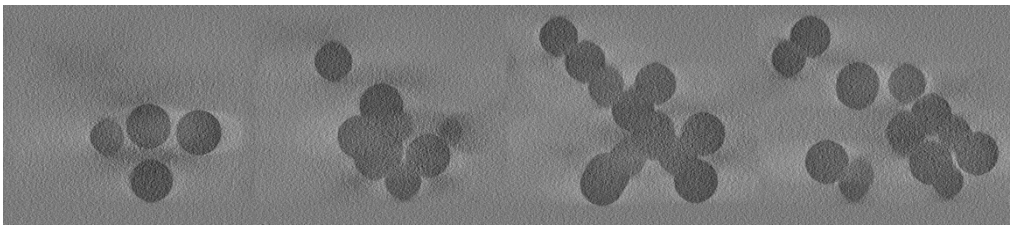
7.2.1 – Methodology for Accuracy Analysis

In each of the 39 tomograms, the maximum length of the particle in the Z-direction was determined. In theory this would reveal the extent of any elongation that is caused by the missing wedge and should increase in the order ±80° < ±60° ≤ ±60_3°. The Z-length can be measured without fully segmenting the tomogram, simply by scrolling through the XY-plane slices and determining where the particle starts and ends. Care was taken so that this measurement was performed without any prior referral to true value in the original models, so as to reduce risk of biased selections.

For the 13 aggregate models, only the ±60_3° tomograms were fully segmented so as to produce particle models. Segmentation was performed *via* a process that employed use of manual selections and linear interpolation to varying degrees, similar to that used in chapter-5 (only not including the 15th slice level). For each aggregate model, 4 reconstructed particles resulted from the use of interpolation at the 20th slice, 10th slice, and 5th slice level, as well as a full manual segmentation. Example images from simulated soot tomograms, and images from a real soot tomogram are shown in figure-7.5.



(7.5a)



(7.5b)

Figure-7.5: (a) Several slices from the real FG soot tomogram (arranged side-by-side). (b) Several slices from the tomogram for a simulated soot nanoparticle.

For 2 models only, the ±80° tomograms were fully segmented (all others were used only to determine maximum Z-length of the particles). This represents the most complete tilt-series reconstruction that could be performed with Etomo, and is a larger tilt-range than is likely to be possible experimentally. The tomogram is created from the greatest amount of 2D data, and should therefore be the highest quality of the three reconstructions produced for each aggregate model.

Morphological characterisation of all the original and reconstructed particle models was carried out using Fiji and the BoneJ plugin [201], as in the earlier chapters. The parameters measured were volume, surface area, radius of gyration, fractal dimension, and 3D-circularity. For the surface area measurement, a resampling factor of 6 was deemed suitable based on the 'primary particle' diameter of 100 pixels (as per the calibration performed in the appendix section-A.2). Again, Lottin's methodology was used to determine the minimum and maximum box-sizes for calculating Df *via* the Minkowski-Bouligand method [156].

For the model of a single sphere, the same 3 tilt-series were created and for each the Z-elongation only was determined.

7.3 – Accuracy Assessment of ET: Results

In this work, 13 simulated soot-like aggregate models were created to act as ground truth for assessing the accuracy of an optimized 3D-TEM procedure. The 3D morphology is known exactly for the original models, and is compared to results produced after simulated 2D-projections of the models are subjected to a realistic tomographic reconstruction procedure. The efforts taken to reflect genuine soot morphology and real tomographic reconstruction were made given that it is known, but not robustly described, that deviation from the true structure occurs during reconstruction and that it depends upon the morphology of the structure in question. For comparison, a simple sphere model was also created and reconstructed.

7.3.1 - Missing Wedge Z-elongation

The 13 aggregates models (and the simple sphere model) were reconstructed using three different tilt-series: ±80°, ±60°, and ±60° with 3° tilt-increment. In theory, larger tilt-range and greater number of images should result in a less elongated, more accurate tomogram. The tilt-series were positioned so that Z-depth in the tomogram matched that in the original models. As such, it was possible to quickly measure total Z-length of the particle in the tomogram by simply finding the first and last slices where particle matter appears. See figure-7.5 for examples of tomogram images. All selections were made manually, and without prior referral to the ground truth value to limit biased selections. Average results for the aggregate models are shown in table-7.1.

	Tilt-Series	**Z-elongation %**	**Z-elongation No. slices**	**Standard Deviation**
Aggregate Models	**±80°**	0.4 %	1.3	0.5 %
	±60°	4.0 %	12.8	1 %
	±60_3°	3.5 %	11.5	0.8 %
Sphere Model	**±80°**	0.0 %	0	N/A
	±60°	10.6 %	16	
	±60_3°	9.9 %	15	

Table-7.1: Length in Z-direction of post-reconstructed soot-like aggregates in comparison to original models. Average over 13 models is presented alongside results for sphere model.

For the ±80° tilt-series, the largest tilt-range than can be reconstructed with Etomo, elongation was marginal. Only 2 of the models showed elongation by more than a single slice (equivalent to ~0.3nm in the simulated scale), and on average elongation was 0.4% of the original ground truth Z-length. For ±60° tilt-series reconstruction, elongation was more pronounced at an average of 4.0% longer in Z than the original model. For the ±60_3° tilt-series, average elongation was marginally less than was seen for ±60° reconstructions, at 3.5% longer *vs* ground truth. Though this was consistent for most of the models (7 out of the 13) the difference *vs* the ±60° method is small in absolute terms, and the standard deviations overlap significantly. For the sphere model, the ±80° sphere reconstruction showed no elongation at all in agreement with the work done by Okyay [37]. The ±60° and ±60_3° methods saw greater elongation of the sphere than for the aggregate models. Again, the ±60_3° method observed marginally less elongation. Propagation of missing wedge elongation due to particle shape is discussed detail in appendix section-A.1

These results show that elongation of soot tomograms due to the missing wedge is small, and much less than predicted by Radermacher's equation [231]. When converted to approximated *real* size using 1 pixel = 0.3 nm, typical elongation for reconstructions of ±60° or ±60_3° tilt-series is around 3-4 nm for a soot aggregate. The comparison of the aggregate model and the simple sphere appears to demonstrate the effect of the shape of the object on the extent of elongation. The appendix section-A.1 considering the FFTs of 2D objects also observed the effect of shape, particularly in respect to the missing wedge direction, on the extent of missing wedge elongation. The sphere model presents a larger, smoother, and less complex surface in the direction of the missing wedge, and as such the blurring and associated elongation is more significant. This elongation is visualised in figure-7.6.

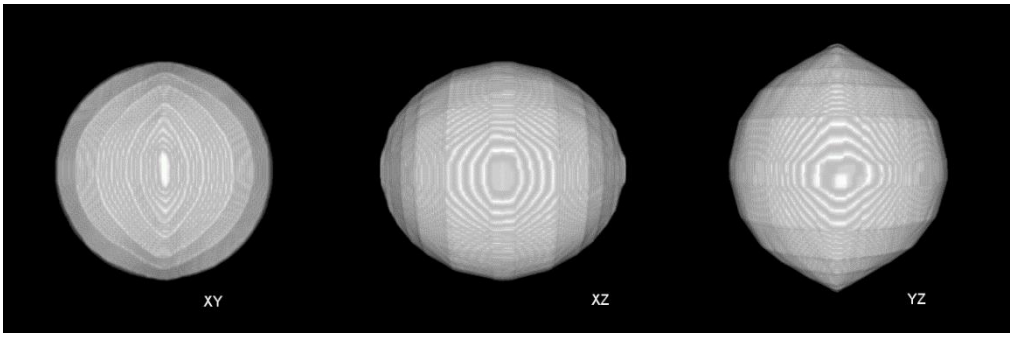


Figure-7.6: Result of ±60_3° reconstruction of sphere model, rendered using Fiji 3D viewer plugin. Missing wedge elongation propagates in the Z direction, resulting in alterations of morphology. Ridges in the model structure show locations of manual segmentations, as interpolation was used. From left to right, showing the XY, XZ, and YZ planes.

7.3.2 - Comparison of the ±80° and ±60_3° methods

For 2 of the soot-like models (named Random6 & Random9), the ±80° tomograms were fully segmented. Previously, only the Z-lengths of the particles were measured from these tomograms. Following full manual segmentation, the morphology of the reconstructed models was compared to that of the originals. The deviations between reconstructed and original morphologies are presented in table-7.2, as percentages of the original morphological values.

		% Deviations vs. Ground Truth					
		Volume	**Surface Area**	**Radius of Gyration**	**Fractal Dimension**	**3D-Circulairty**	**Z-depth**
Random6	±80°	-0.9 %	-1.2 %	-0.3 %	-0.5 %	0.9 %	0.4 %
	±60_3°	2.0 %	0.8 %	0.2 %	-1.0 %	0.9 %	4.5 %
Random9	±80°	-1.1 %	-2.0%	-0.3 %	0.0 %	2.1 %	0.3 %
	±60_3°	2.3 %	-0.4 %	0.1 %	-1.0 %	2.9 %	4.6 %

Table-7.2: Comparison of the accuracy of the ±80° and ±60_3° reconstructions of two aggregate models in comparison to GT (morphology of original models)

For both ±80° reconstructions, the measurements of volume, surface area, and radius of gyration are marginally underestimated in comparison to the ground-truth values. This underestimation is more pronounced in surface area, leading to slight increases in 3D-circularity values for both models *vs* GT, indicating that the shape of the model differs slightly. In comparison to ±80° reconstruction, the ±60_3° method results in an increase in the absolute values of volume and surface area by area 2-3%, and in radius of gyration by around 0.5%. Despite causing a relative increase in the measured bulk of the particles (volume and surface area), the fact that the magnitude of the increase is small and that ±80° results are inherently underestimated means that ±60_3° reconstruction is similarly (and highly) accurate in comparison to GT. The magnitude of the difference between the ground truth morphology and ±60_3° reconstructed morphology is very similar to that resulting from multiple manual segmentations of the FG soot tomogram. For the simulated aggregates at least, the effect of reducing tilt-series from 161 images over ±80° to 41 images over ±60° appears to be no greater than variability arising from manual segmentation of the tomograms.

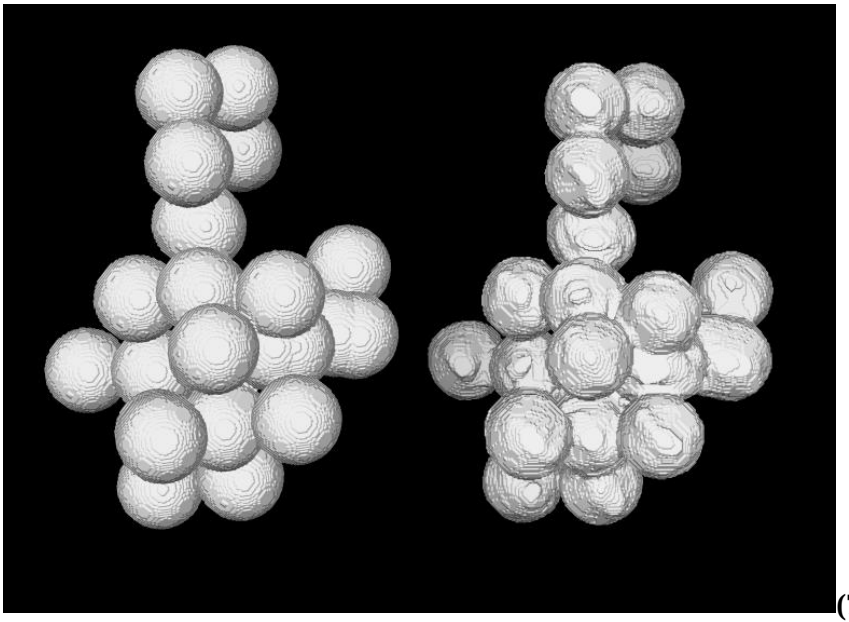
7.3.3 - ±60_3° Reconstruction: Full Morphological Analysis

In chapter-5, the ±60_3° tilt-series configuration was found to be the optimum choice in terms of speed and quality. In terms of accuracy it had been found that overall tilt-range was more important than total number of images, and that 3° increments significantly reduced potential beam exposure whilst having no significant negative effect on tomogram quality. However, 'acceptable' quality in that work was defined as providing results similar to those of ±60° reconstruction, which in theory should be more accurate. In the current work, we are able to compare results of ±60_3° reconstruction directly to the ground-truth values, and can provide a definitive answer on the quality of this protocol. This section focuses on morphology resulting from full manual segmentation of the tomograms (effect of interpolation is assessed in the following section). Results are shown in table-7.3, and figure-7.7 shows a visual comparison of an original simulated soot model, and the same model after ±60_3° reconstruction has been performed.

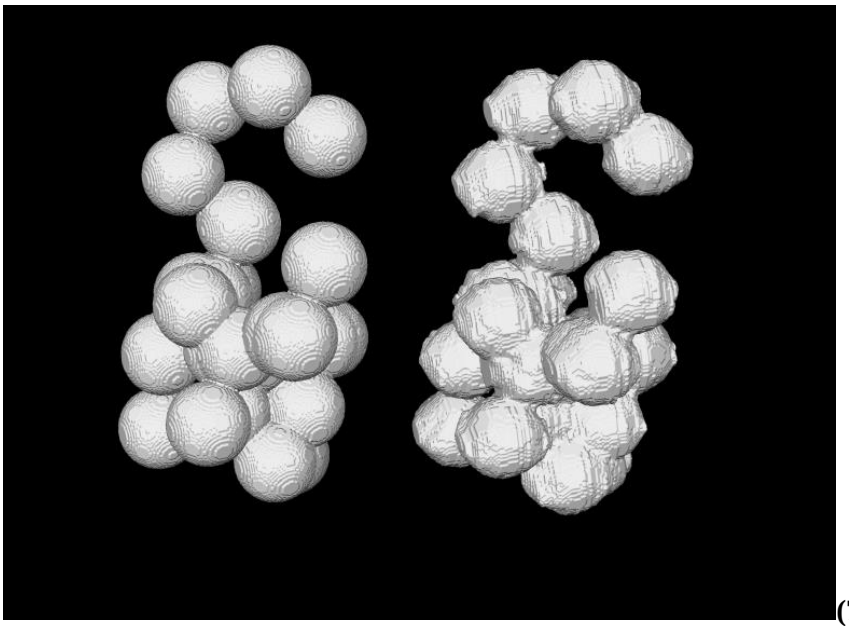
These results show that the reconstruction of the simulated soot-like models created for this investigation *via* the ±60_3° methodology is generally excellent. Important and descriptive morphological parameters show only minor deviations from ground-truth values on average, and even maximum deviations are well within 10%. All values of volume were seen to be overestimated in comparison to ground truth, whereas surface area was split almost evenly between under- and over-estimation. Deviation in radius of gyration were generally marginal at most. 3D-circularity is used to describe the shape of the particles, as it involves a ratio of volume to surface area. Deviations in 3D-circularity were predominantly increases in comparison to ground truth values. As 3D-circularity moves towards a value of 1 for more spherical/clustered objects, this indicates a change in the shape of reconstructed particles such that they are slightly bulkier and/or possess less rugged edges (increased volume, decreased surface area). There were no clear trends that linked the magnitude of deviations in 3D-circularity with any other morphological parameter (*e.g.* volume, surface area, radius of gyration, Z-length, absolute 3D-circularity, size, *etc.*). On average, deviations in fractal dimension *vs* ground truth were marginal. As has already been described, the ±60_3° reconstruction resulted in an average Z-elongation of 3.5%. As this effect only propagates over the very tips of the particle structure in the Z-direction (see appendix section-A.1) rather than over the whole structure evenly, this parameter showed the largest deviation *vs* GT values.

	Volume	Surface Area	Radius of Gyration	Fractal Dimension	3D-Circularity	Z-depth
Mean % Deviation from GT	2.0 %	-0.1 %	0.2 %	-0.7 %	2.3 %	3.5 %
Standard Dev.	1.7 %	1.7 %	0.2 %	1.4 %	2.4 %	0.8 %

Table-7.3: Accuracy of ±60_3° reconstructions averaged over all 13 models, in comparison to GT morphology



(7.7a)



(7.7b)

Figure-7.7: A comparison of the original (left) and post-reconstructed (right) model of a soot-like aggregate. (a) shows the XY plane, (b) shows the XZ plane.

If it can be accepted that the simulated soot nanoparticle reconstruction demonstrated in this work is a realistic representation of both genuine soot structures and reconstruction artefacts and errors, then this data shows that our optimised 3D-TEM procedure can produce highly accurate morphological measurements. This is potentially a very important point of emphasis for 3D-TEM, as there can now be confidence in saying that deviations between 2D and 3D soot characterisations is due to inaccuracies of 2D-TEM alone, rather than artefacts of 3D reconstruction.

7.3.4 - Effect of Interpolation on Segmentation

It was seen in chapter-5 that the use of interpolation in segmentation could greatly improve the speed of 3D-TEM characterisation, though can result in significant decreases in particle volume and surface area that greatly affect the accuracy of the model. The optimal method was 5th slice interpolation, which on average required 40% less time than full manual segmentation, but was associated with average decreases in volume and surface area of 3.4 and 3.9% respectively. In the current work, the accuracy of interpolated results can be quantified in comparison to the ground truth values. The average deviations for the different levels of interpolation in comparison to GT values are shown below in table-7.4.

Overall, these results suggest that all levels of interpolation resulted in accurate morphology in comparison to the original models. The 3D-circularity parameter is the useful for highlighting changes in shape, as it amplifies situations where, for example, volume is accurate but surface area is not. With this in mind, even the 20th slice interpolation is only slightly outside the size of deviation that was observed for repeated manual segmentation of the FG-WBP tomogram (3.8%) (chapter-5, section-5.6.1).

		Average deviation % vs Ground Truth			
Interpolation level	**Volume**	**Surface Area**	**Radius of Gyration**	**Fractal Dimension**	**3D-Circularity**
None (full manual)	2.0	-0.1	0.2	-0.7	2.3
5th Slice	2.3	0.2	0.2	-0.8	-2.0
10th Slice	2.5	-0.3	0.1	-0.6	2.9
20th Slice	1.5	-2.5	-0.3	-0.2	5.5

Table-7.4: Accuracy of reconstructions of aggregate models performed using various level of interpolation in tomogram segmentation. Results are presented as percentage deviation *vs.* GT morphology, and are averaged over the 13 models.

These results stand in stark contrast to the study of real soot tomograms in chapter-5, where above the 5th slice interpolation level significant deviations were observed. As was discussed in chapter-5, the errors that result from interpolation are due to simplification of the irregularities of the soot structure. When there is a greater degree of manual input, interpolation only occurs across relatively small distances and the surface irregularities are less likely to be simplified or missed. When interpolation is used to a greater extent, important features of the surface may be missed by manual segmentation, and there not accounted for by interpolation. In this regard, the much higher accuracy of the 10th and 20th slice interpolation levels may be due to the lack of surface irregularities on the simulated aggregate models.

Real soot nanoparticles are formed from primary particles that are *not* perfectly spherical, and are poly-disperse in size. Additionally, real soot does not always appear to be formed explicitly from discrete primary particles. By contrast, the simulated aggregates are formed from perfectly smooth spheres, and surface irregularities only occur at the junction of these spheres. In real soot aggregates, irregularities can also occur below the size of primary particle due to non-spherical shape and irregular attachments between primary particles. The higher levels of interpolation perform better for the aggregate models because, simply put, there are fewer irregularities to be missed by between the manual segmentations.

As such, despite the efforts made to accurately reflect real soot structure, lack of irregularities on the sub-primary particle scale mean that this is not a complete test of the accuracy of interpolated segmentation. In future, simulation of aggregates could include some factors to introduce poly-dispersity of primary particle size and other sources of surface irregularity into their morphology.

As we have observed the effects of the missing wedge to be more prominent for smoother surfaces, it is not expected that the lack of irregularity in the simulated nanoparticles to affect the validity of the results in the previous sections. If anything, the smooth surfaces of the simulated aggregates may expose the reconstructions to a stronger degree of missing wedge artefacts.

7.4 - Conclusions

This work highlights that 3D-TEM is a new high-fidelity tool for soot nanoparticle characterisation, which is able to overcome the limitations of more traditional 2D-TEM methods. It permits direct measurement of morphological parameters such as volume, surface area, and radius of gyration of 3-dimensional soot structures, without the significant errors associated with orientation uncertainty and empirical correction factors of 2D-TEM. The optimized reconstruction procedure described in this and a previous paper [245] greatly improves the speed of 3D-TEM, allowing for its use for high-throughput soot characterisation, and has now been shown to produce highly accurate 3D volume reconstructions. In particular, the work carried out on the simulated soot nanoparticles has led to the following conclusions:

- Propagation of missing wedge elongation in simple sphere models is not equivalent to that in soot-like models
- ±80° reconstruction results in marginal elongation only (<1%)
- ±60° and ±60_3° reconstruction result in minor elongation only (3-4%)
- In comparison to ±80° reconstruction, ±60_3° method causes increase to bulk of the particle (surface area and volume) though inherent underestimation at ±80° means both methods are similarly accurate
- ±60_3° reconstruction (full manual segmentation) in general is highly accurate, with average values of volume, surface area, radius of gyration, fractal dimension and 3D-circularity all within 3% of ground truth values
- Use of interpolation at 5^{th}, 10^{th}, and 20^{th} slice levels is similarly accurate to full manual segmentation, in contrast to results in chapter-5
    - Likely due to lack of sub-primary particle irregularities in the aggregate models. This should be corrected if it is to be assessed again in the future.

8 – 2D and 3D Morphological Characterisation of GTDI Soot-in-Oil

In this chapter, the automated TEM imaging method developed in chapter-6 is utilised to facilitate the 3D reconstruction of 34 nanoparticles from the GTDI oil sample – the most extensive 3D study of a soot-in-oil sample to date. Over a TEM grid, approx. 4000 μm^2 was screened for particles, equivalent to around 9 grid squares. From a pool of 271 possible locations, 28 nanoparticles were chosen for 3D study (in addition to the 6 studied in chapter-5). Due to the limited number studied (due to time and cost constraints), they were chosen to represent the extremes of morphology observed in the sample so as to highlight benefits of the 3D method. A comparison was made between the 2D- and 3D-derived morphology measurements for a range of parameters. The mean 2D-3D discrepancy is significant for volume, surface area, and circularity measurements (~20-35%), and subject to significant variation across the 34 nanoparticles (up to 84% in surface area). No obvious correlations are observed between morphology of nanoparticles and relative accuracy of the 2D method, though smaller nanoparticles showed slight tendency towards more accurate 2D-volume measurements. Measurements of fractal dimension showed moderate 2D-3D discrepancy (14%) and relatively little variability of the 34 nanoparticles. Finally, radius of gyration as calculated *via* a pixel/voxel based method was on average highly similar when calculated in 2D, with only 1.2% difference *vs.* 3D-derived results.

In terms of qualitative analysis, the 3D models were also useful for observation of morphological features that could not be made using 2D TEM alone. Distinctly 3-dimensional structures and features such as cavities and arches were observed, and discussion was made over their potential implications for nanofluid research.

The work in this chapter is adapted from a recent SAE technical paper that was presented at the SAE Naples 14th International Conference on Engines and Vehicles:

Haffner-Staton E., La Rocca A., Cairns A., Fay M. Morphological characterisation of gasoline soot-in-oil: development of semi-automated 2D-TEM and comparison with novel high-throughput 3D-TEM. SAE Technical Paper; **2019**. Report No.: 0148-7191.

8.1 – Introduction

As described in section-6.4.1 of chapter-6, the semi-automated methodology for TEM imaging was applied to the GTDI soot-in-oil sample. SerialEM was used to produce large-scale maps of 9 grid squares in a heavily automated process. Over an approx. 4000 μm^2 combined area of the TEM grid, 271 locations were identified as containing soot nanoparticles.

Due to constraints on time and resources, only a limited number of these nanoparticles could feasibly be studied in 3D using ET; 28 nanoparticles were chosen from the pool of 271. These particles were in addition to the 6 studied in chapter-5, bringing the total studied in 3D to 34. It did not make sense to perform a fully randomized sampling of the selected particles since the number was too low for a meaningful representation of the sample anyway. Of course, this *would* be the case if the aim was a full-scale characterisation of the sample. Instead, it was decided that the most information-dense method of sampling was to pick nanoparticles that represented towards the most extreme morphologies present in the sample. This included both highly 3-dimensional and highly 2-dimensional particles, as well as those both very small and very large in size. It was hoped that this type of sampling could be useful for understanding whether 2D-derived measurements may be more accurate for certain kinds of morphology. The choice of particularly large particles was also useful for the observation of interesting morphological features that cannot be fully appreciated with 2D-TEM study alone. TEM images and 3D renderings showing a sample of some of the 28 nanoparticles studied in this chapter are provided in figure-8.1. Images showing the 6 nanoparticles previously studied can be found in chapter-5 (figure-5.16). Despite the limitations on the number of nanoparticles studied, this still represents the most extensive 3-dimensional study of a soot-in-oil sample to date, and possibly any sample of soot nanoparticle as well.

As per the results of optimisation in chapter-5, all tilt-series were acquired over a ±60° tilt-range with an average increment size of 3° between images. Tomographic reconstruction was carried out using the weighted back-projection (WBP) algorithm in Etomo [176], and segmentation of tomogram data was performed using a combination of manual segmentations with interpolation at the 5^{th} slice level.

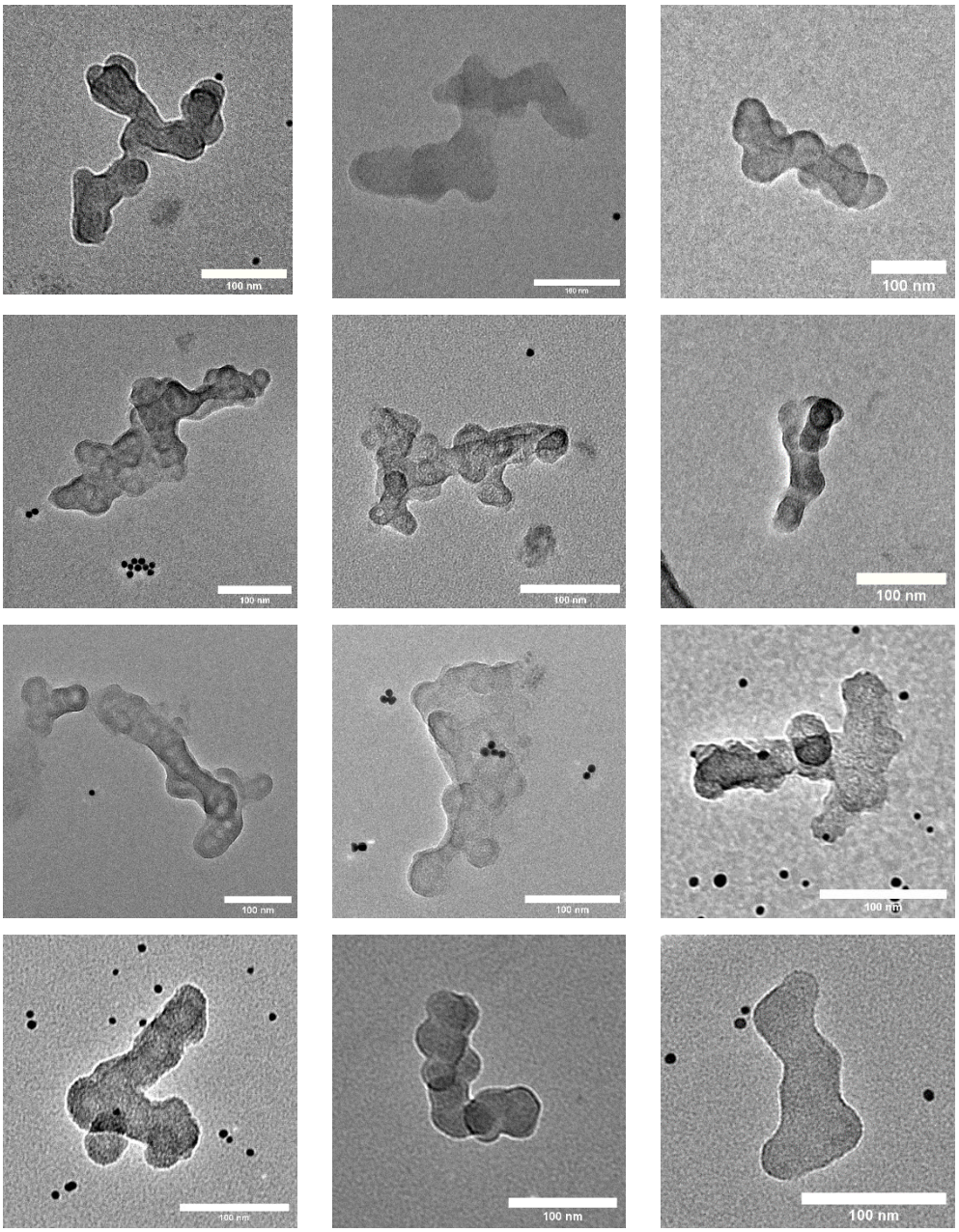


Figure-8.1a: A selection of TEM images showing nanoparticles studied in this chapter. All scale bars measure 100 nm in length.

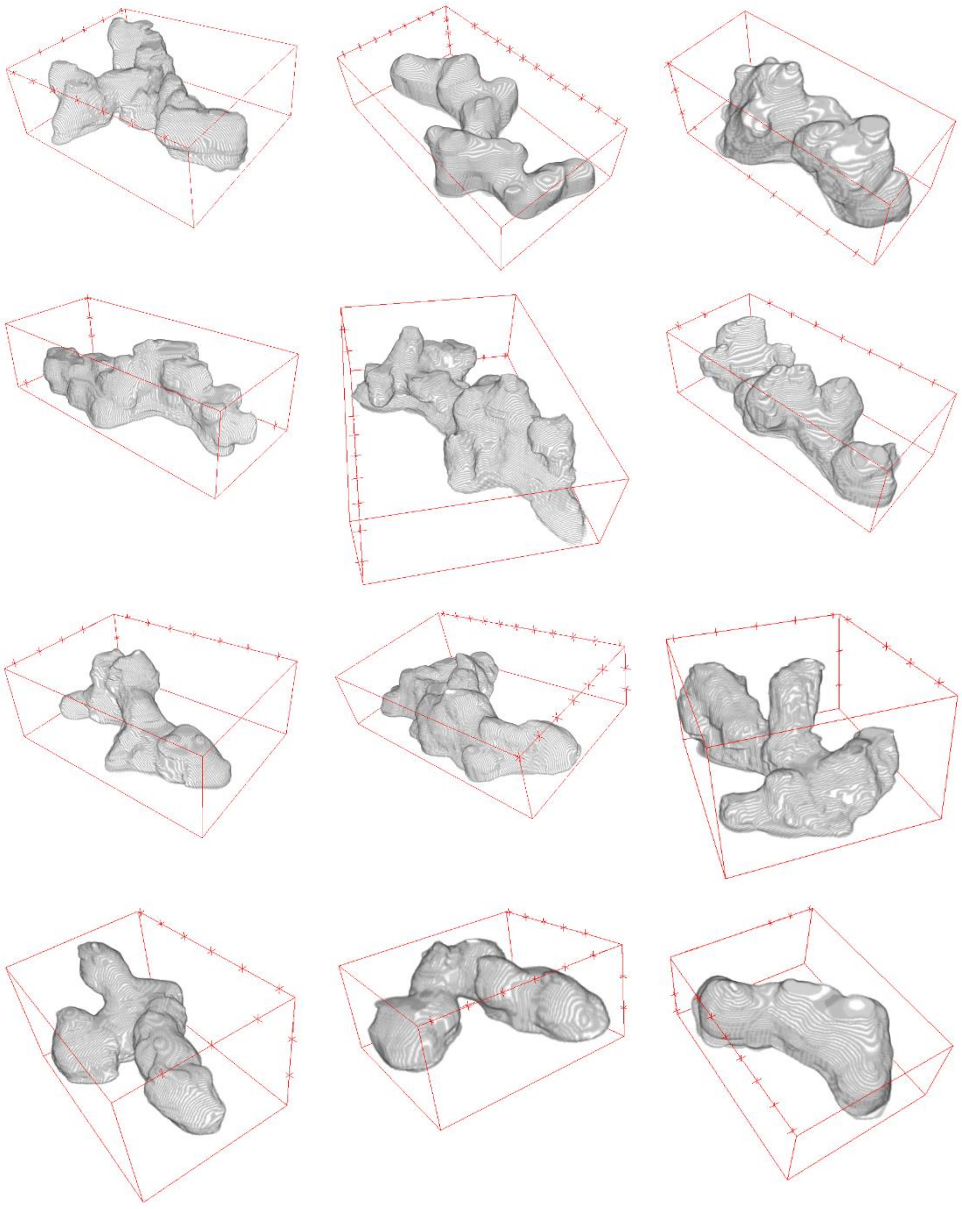


Figure-8.1b: 3D renders corresponding to the TEM images shown in figure-8.1a.

8.2 – Morphological Characterisation in 2D and 3D

All 34 nanoparticles were characterised in both 2D and 3D to enable comparison of the relative accuracy of the two methods. Based on the results of chapter-7, it is assumed that 3D reconstruction is sufficiently accurate so that the results essentially act as 'ground truth' for which 2D measurements can be compared to.

8.2.1 – 3D Morphology Measurements

Once reconstructed, the morphology of the 34 nanoparticle models were characterised in terms of volume, surface area, radius of gyration, 3D-circularity, fractal dimension, and aspect ratio (AR).

As before the 3D volume, surface area, and fractal dimension were determined using the BoneJ plugin for ImageJ. Again, the suggestions in Lottin's work were used to guide the choice of box-set in the calculation of fractal dimension [156]. Radius of gyration was determined using a self-produced macro for Fiji according to equation-3.8, and 3D-circularity was calculated according to equation-3.10. For the 3D particle models, aspect ratio was determined *via* the creation of minimum bounding boxes in Fiji. Aspect ratio was calculated as the mean of the maximum length in the X and Y directions, divided by the maximum length in the Z-direction.

8.2.2 – 2D Morphology Measurements

In order to compare relative accuracy of 2D- and 3D-derived morphology measurements, each of the 34 nanoparticles was also characterised using traditional 2D methods. This was performed on the un-tilted (0°) image of each tilt-series, and the same properties were measured as in 3D.

As described in section-6.4.3 in chapter 6, mean primary particle diameter was determined to be 33 nm. This parameter is required for the calculation of N_p according to equation-3.2, and subsequent calculations of 2D-derived volume and surface area according to equations 3.3 and 3.4 respectively.

Previously for the FG soot nanoparticle, a calculation of surface area accounting for primary particle overlap could not be performed. The resolution of the 2D TEM projections was too low to clearly define primary particle overlap. For the GTDI soot-in-oil sample, the resolution of the images was generally higher and this could be performed. As described in the chapter-3, the Brasil [154] and Bau [155] methods for 2D-derived surface area require determination of a primary particle overlap coefficient. The coefficient ($C_{ov,P}$) is measured for the overlap of primary particles in 2D-TEM projections (equation-3.5), where d_p is the average primary particle diameter, and d_{ij} is the distance between the centres of pairs of overlapping primary particles. Example measurements are provided in figure-8.2. From 60 measurements of our sample, the average d_{ij} was determined as 27 nm. An additional overlap coefficient, C_{ov}, is calculated *via* equation-3.6, where ζ_1 and ζ_2 are equal to 1.1 and 0.2 respectively. Finally,

an estimate of 3D surface area is calculated using equation-3.7, where ϕ is an empirically determined constant equal to 1.3. For our sample, equation-3.6 revealed C_{ov} as a small negative value, and was adjusted to 0 to cooperate with equation-3.7 for surface area (as surface area should not be greater than the no-overlap value, SA_1). A value of 0 for C_{ov} results in this method being equivalent to the simple, non-overlap calculation (equation-3.4).

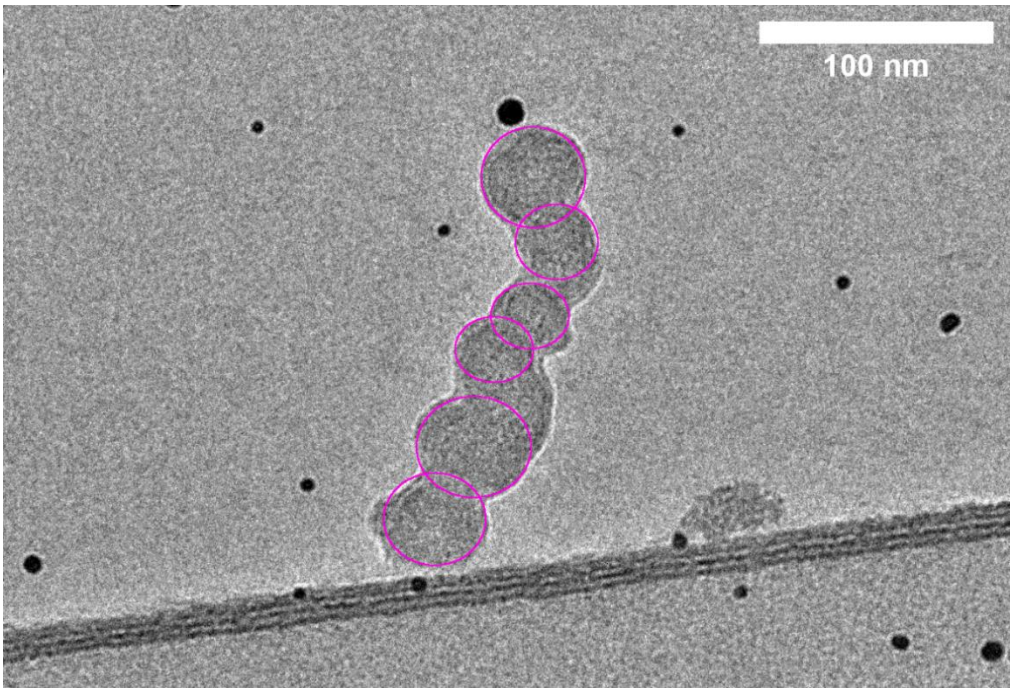


Figure-8.2: Example of measurements of primary particles in a soot nanoparticle

Radius of gyration was calculated using a self-produced macro for Fiji, according to equation-3.8. Fractal dimension was calculated using the *Fractal Box-count* plugin for Fiji, with a box-set chosen based on the suggestions of Lottin [156]. Finally, circularity and aspect ratio can be calculated directly in Fiji.

8.3 – 3D Morphology of GTDI Soot-in-Oil

Given that only 34 nanoparticles are considered in the 3D study, it is accepted that the measured morphologies cannot be used to reliably represent the true morphology of the sample. However, the selection criteria used to sample towards the extremes of nanoparticle structures means it is still interesting to look at the general magnitude of some morphological parameters. The values of a selection of morphological parameters are summarised in table-8.1 below.

Given that 3D morphological characterisation of soot is not commonplace, some of the values measured in this work have fairly little context as there is little with which to compare them. As such, it is hard to have a meaningful discussion about all of these measured values at this stage.

		Volume (nm^3)	N_p equiv.	Surface Area (nm^2)	Radius of Gyration (nm)	3D-Circularity	Fractal Dimension	Aspect Ratio
3D	mean	837,300	45	73,800	69.1	0.448	2.06	2.22
	min	72,800	4	11,600	26.3	0.260	1.90	1.26
	max	3,158,900	168	256,700	116	0.659	2.14	3.78
2D	mean	578,200	31	105,100	69.5	0.360	1.76	2.48
	min	79,100	4	14,400	26.2	0.16	1.68	1.26
	max	2,059,900	109	374,500	117.6	0.697	1.83	4.69

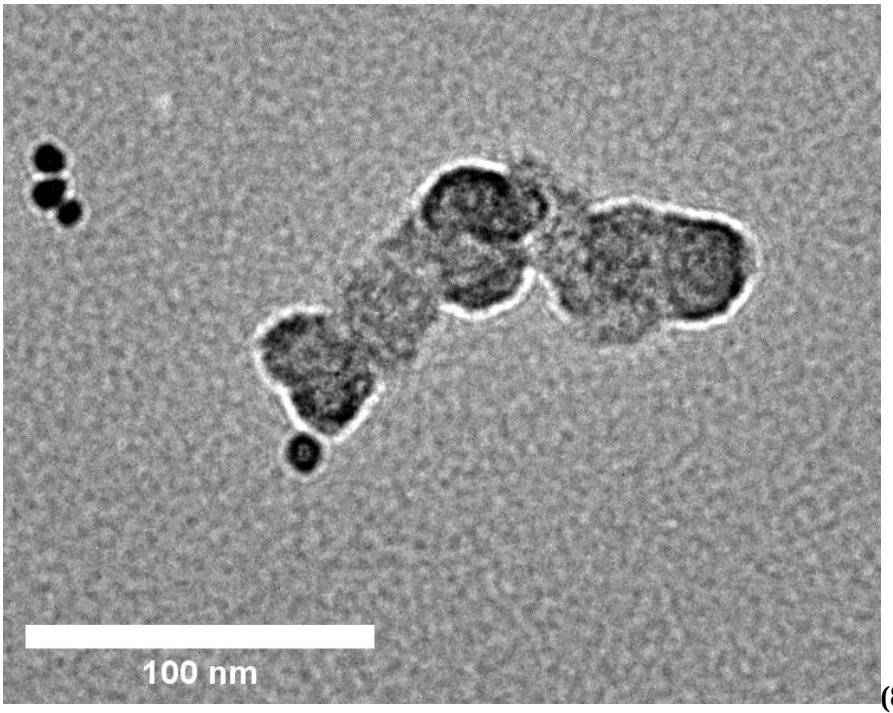
Table-8.1: Mean, minimum, and maximum values of morphological parameters measured from 34 GTDI soot-in-oil nanoparticles in 2D and 3D.

With this in mind, a useful way in which to consider the measured volume is in terms of equivalent primary particles. This is calculated simply by dividing the measured 3D volume by the equivalent volume of a perfectly spherical particle with the average primary particle diameter (= 33nm). Figure-8.3 shows TEM images showing the particles corresponding to the largest and smallest values of this 3D-derived N_p value.

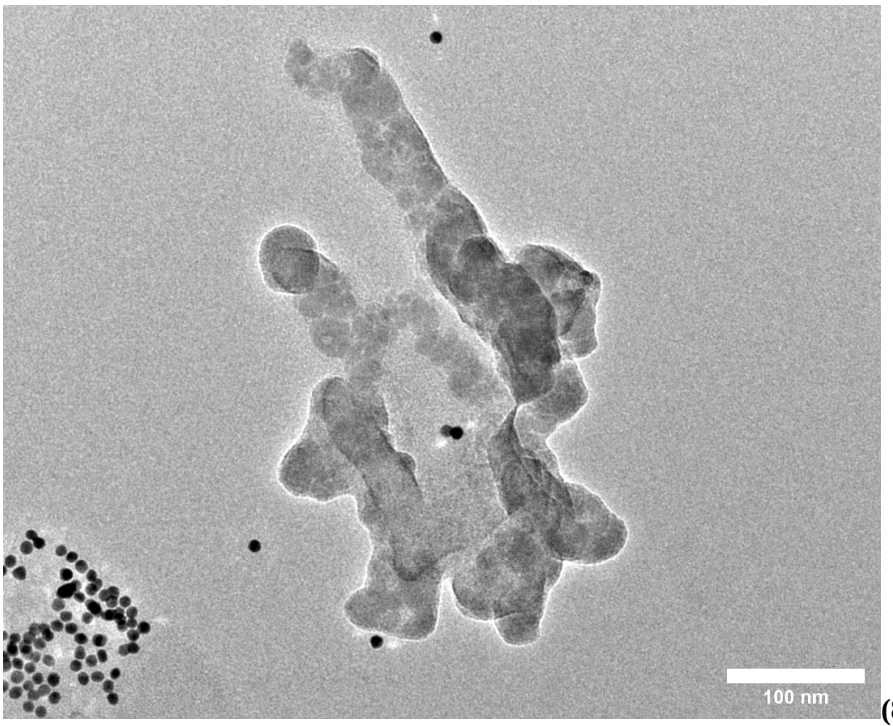
Though number of primary particles is commonly calculated for soot when studied *via* TEM, it is primarily to facilitate calculation of fractal dimension rather than to be reported as parameter in its own right. However, prior work by Martos *et al.* lead to the conclusion that <5% of diesel exhaust soot nanoparticles were comprised of >200 primary particles [230]. In contrast, Neer *et al.* studied diesel exhaust soot morphology as a function of engine speed and load, and their calculation of D_f included contributions from nanoparticles with well over 1000 primary particles [75]. A rare publication including quoted values of average N_p per aggregate is that of Mikhailov *et al.*, in which average N_p = 195-221 for soot from acetylene flames [246].

Even the largest particle studied in this work is only equivalent to 168 primary particles, which in comparison to those values indicates that the GTDI soot-in-oil nanoparticles tend to be fairly small in size overall. Similar conclusions were drawn based on calculations of Feret diameters using 2D-TEM in chapter-6, where nanoparticle lengths

were similar to other soot-in-oil samples but generally significantly smaller than exhaust and flame soots (see section-6.4.4).



(8.3a)



(8.3b)

Figure-8.3: (a) One of the smallest nanoparticles (in terms of 3D-volume) studied in this work, consisting of only a small number of primary particles. (b) The largest nanoparticle, possessing the equivalent volume of 168 nanoparticles.

Another parameter which can be useful for indicating the general state of the GTDI soot-in-oil nanoparticles is the aspect ratio. Nanoparticles with strong 3D character will

possess values towards 1, whereas more 2-dimensional particles will possess higher values. This is an interesting parameter to inspect, as previous study of diesel soot-in-oil had observed that nanoparticles tended to be very flat, and no more than 2 primary particles thick on average [40]. In this work, the average aspect ratio over the 34 nanoparticles was around 2.2, *i.e.* the average length in the XY plane is 2.5 times larger than the Z-depth of the particles. Again this indicates that on average GTDI soot-in-oil nanoparticles tend to be developed primarily in 2-dimensions, rather than in 3-dimensions. This kind of structure was particularly pronounced for some nanoparticles, which possessed very long and 2-dimensional morphologies (an example is provided in figure-8.4). This sample was not totally devoid of 3-dimensionality however, and some nanoparticles clearly possessed distinct 3D structures (see figure-8.5 for examples). A more significant 3D study of diesel soot-in-oil would be required for an in-depth comparison with GTDI soot-in-oil, though these results indicate they are somewhat similar.

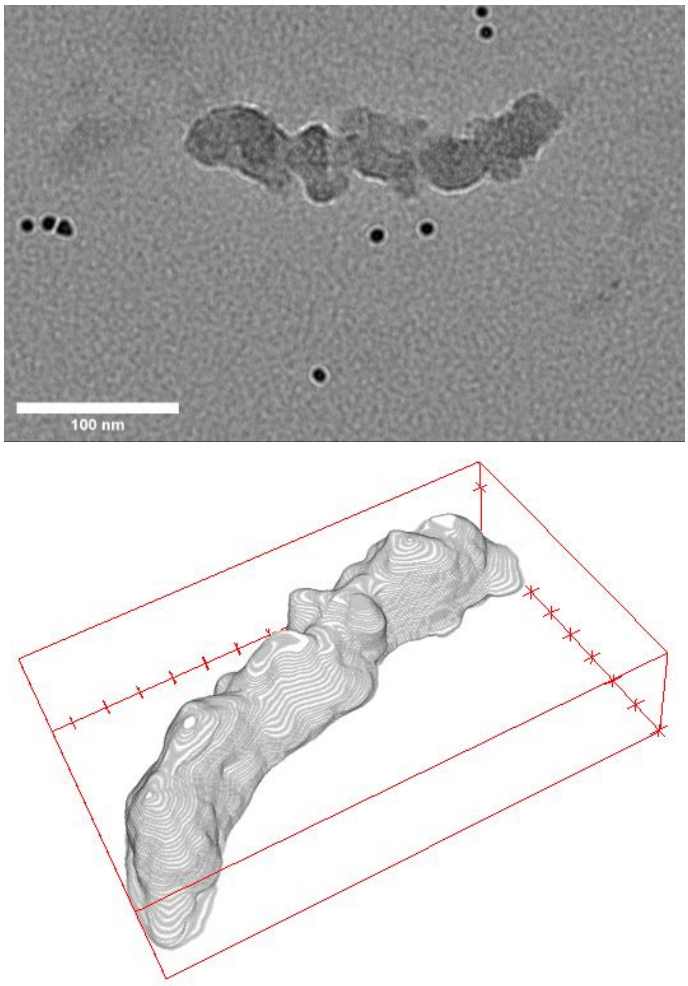


Figure-8.4: The above image shows a standard BF-TEM image of a very 2-dimensional nanoparticle. The below image shows the corresponding 3D render with minimum bounding box highlighting the very flat shape.

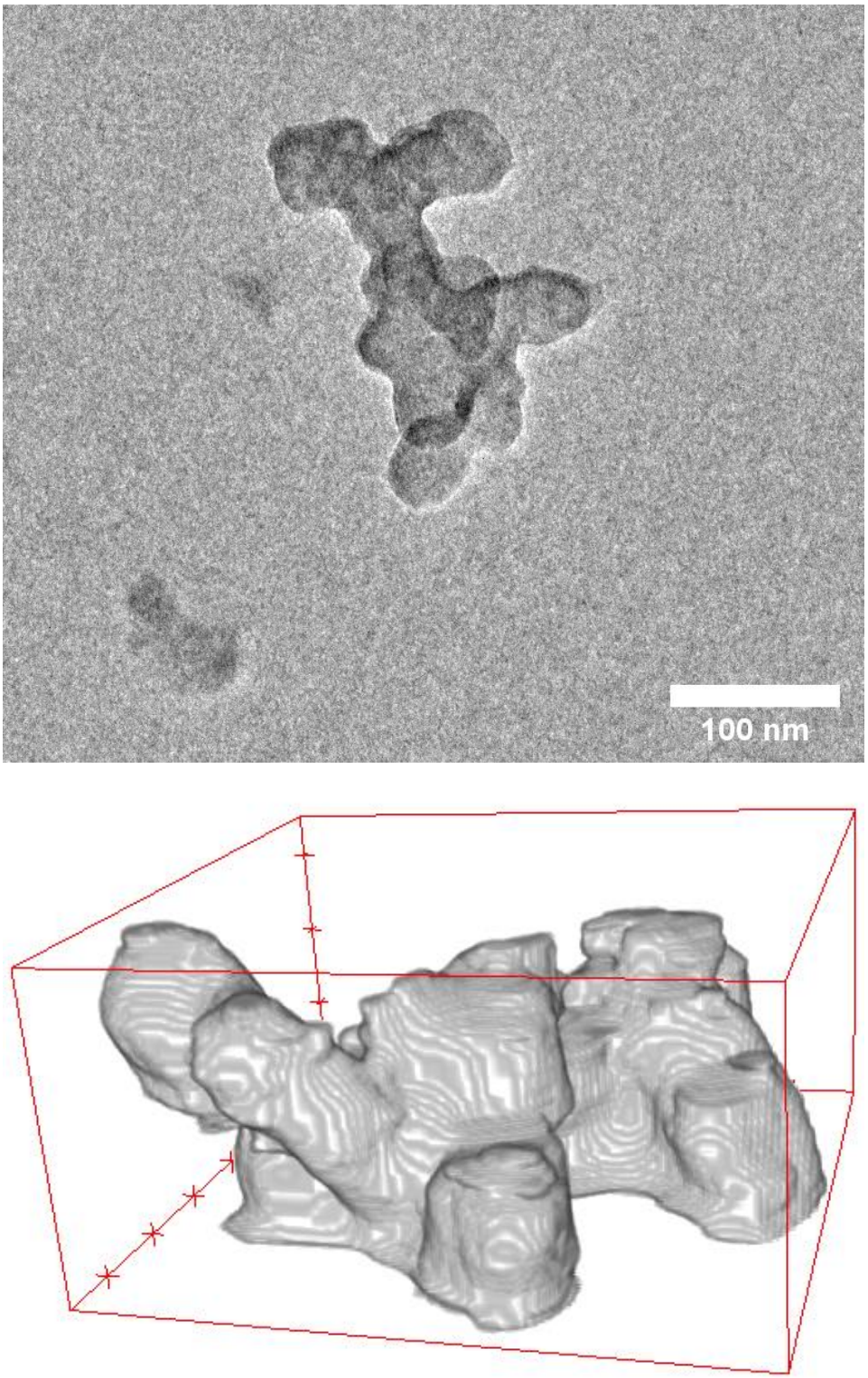


Figure-8.5: A TEM image and corresponding 3D render of a particle with particularly low 3D aspect ratio (AR = 1.3). Minimum bounding box highlights presence of distinct 3D character.

8.4 – Comparison of 2D- and 3D-derived Morphology

For each particle, 2D- and 3D-derived morphological parameters (volume, surface area, circularity/3D-circularity, radius of gyration, fractal dimension, and aspect ratio) were directly compared. The average discrepancies over all 34 nanoparticles are presented in table-8.2, showing the size of the under/over-estimation by 2D methods in comparison to the 3D-derived result for the same particle.

	Volume	**Surface Area**	**Radius of Gyration**	**Circularity**	**Fractal Dimension**	**Aspect Ratio**
Mean 2D discrepancy	-23 %	35 %	-1.2 %	-18 %	-14 %	14 %
Max. over-estimate	17 %	84 %	9 %	22 %	**N/A** (-8 %)	119 %
Max. under-estimate	-52 %	**N/A** (5 %)	-13 %	-46 %	-19%	-40 %
Standard Deviation	17 %	17 %	5 %	16 %	3%	36 %

Table-8.2: Comparison of 2D- and 3D-derived morphology measurements, averaged over 34 GTDI soot-in-oil nanoparticles.

It should be noted that the values provided in table-8.2 above are calculated as follows:

- For each individual nanoparticle, the 2D-derived value is calculated in terms of an over- or under-estimation *vs.* the respective 3D-derived value.
- For each parameter these values are then averaged over the 34 nanoparticles; these are the values reported above

As such, the values presented in table-8.1 do not directly correspond with a comparison of the mean 2D- and 3D-derived values presented earlier in table-8.2.

8.4.1 - Volume

For the 34 particles studied, 2D-TEM derived volume results on average underestimated the 3D volume results by 23%. The range of discrepancies was large and is reflected in the size of the standard deviation. The size of the average discrepancy is smaller than previous results seen for the larger, more branched and complex FG soot nanoparticle studied in chapter-4 (36% underestimation). In general, the results in table-8.2 suggest that for this sample, 2D-TEM has tended to underestimate the number of primary particles that comprise the aggregates (*via* equation-3.2). In turn, this means the

correction factors (k_a and α) may have over-compensated for the extent of primary particle overlap, and/or underestimated the 3D-extent of the particles.

A small minority of the particles observed an overestimate by 2D methods (4 particles out of 34). These nanoparticles shared similar morphological traits that include small primary particles *vs.* the average 33 nm diameter (~20-25 nm), shallow Z-depth perpendicular to the TEM grid (predominantly just a single primary particle thick), and more linear/string-like morphology (see the example in figure-8.6, and the uppermost images in figures-8.3 and 8.4). These somewhat unusual features are possibly what leads to the 2D-TEM method overestimating the 3D nature of the particles, as they are less complex than expected.

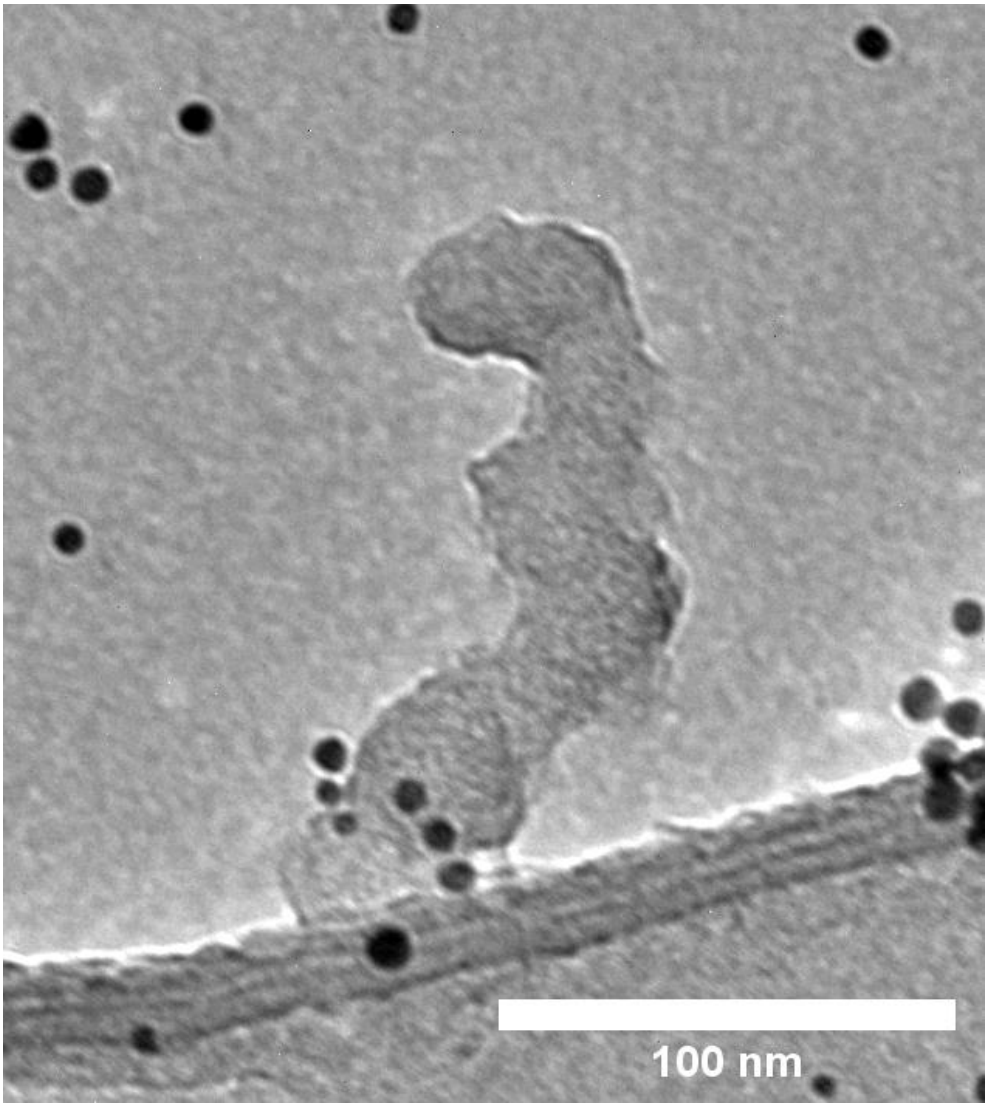


Figure-8.6: Example TEM image showing a nanoparticle for which 2D-methods over-estimated volume. Note the very linear appearance with minimal branching. Similar structures are also observed in figures-8.3a and 8.4, for which 2D-derived volume measurements were also small-overestimates *vs*. 3D-volume.

Scatter plots were produced to check for any correlations that may link 2D-TEM accuracy with any particular traits of 3D-morphology. A plot of 3D-derived volume *vs.* accuracy of 2D-derived volume is shown in figure-8.7. Accuracy of 2D-derived volume showed some minor signs of correlation with overall particle bulk, though considering sample size and strength of the correlations the results are at best merely suggestive of a relationship. The 2D-TEM method tended to produce more accurate volume results when particles possessed smaller 3D volume, surface area, radius of gyration, and Z-depth (length perpendicular to the TEM grid). These parameters can be considered indicative of overall particle size, thus suggesting that smaller particles may be more accurately characterized. However, the very smallest particles resulted in an over-estimation by 2D-TEM, indicating there was possibly an optimum size for particles that resulted in highest 2D-accuracy. There was no clear evidence of a link between particle complexity (in terms of 3D-circularity, Rg, or Df) with accuracy of 2D-derived volume results.

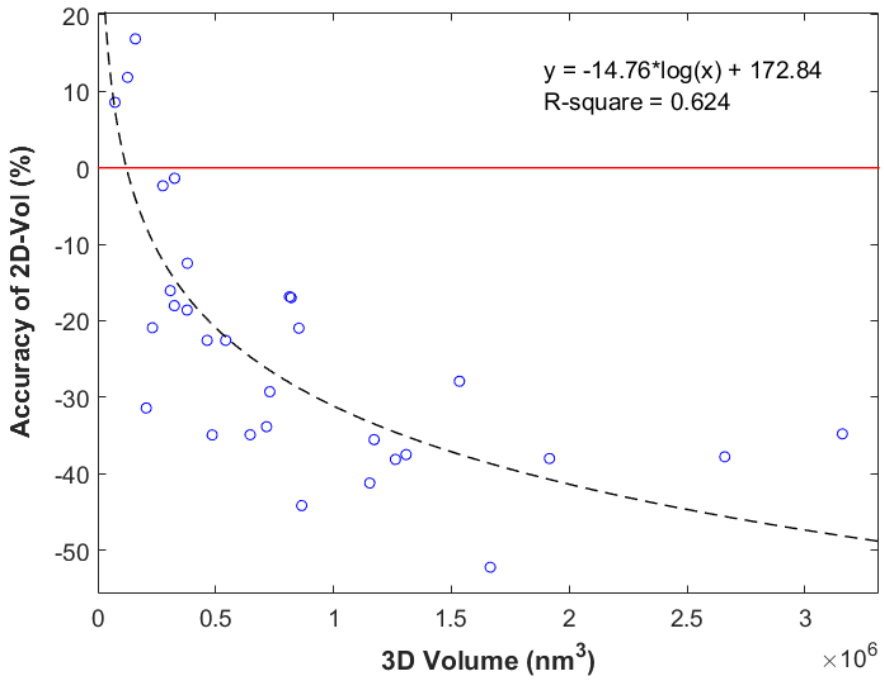


Figure-8.7: A scatter plot showing 3D-derived nanoparticle volume as a function of the accuracy of 2D-derived volume measurements. Logarithmic fitting has been applied according to the inset equation.

8.4.2 - Surface Area

In contrast to the 2D-derived volume measurements, on average 2D-derived surface area resulted in an *overestimation* of the 3D-SA for all 34 nanoparticles. In the first working chapter, 2D-SA was also seen to overestimated 3D-SA for the flame-generated soot nanoparticle. In that chapter, the 2D surface area measurements ignore primary

particle overlap and thus are fully expected to produce overestimations (due to inability to calculate primary particle overlap factors). The 2D method of Brasil *et al.* includes a correction for primary particle overlap [154], but in the case of our sample this became equivalent to the basic, no-overlap method. The average size of the overestimation by 2D-TEM was 35%, though the range was again large (5% to 84% larger than 3D-SA). In terms of any links between accuracy of 2D-derived SA and morphological features of the nanoparticles, evidence was less clear than for 2D-volume. While there was limited indication of a link between smaller particles (lower 3D-volume, 3D-SA, and 3D-R_g) and more accurate 2D-SA, the effect of outlying data-points was significant (see figure-8.8). There was no observable relationship between the accuracy of 2D-SA and the Z-depth of nanoparticles.

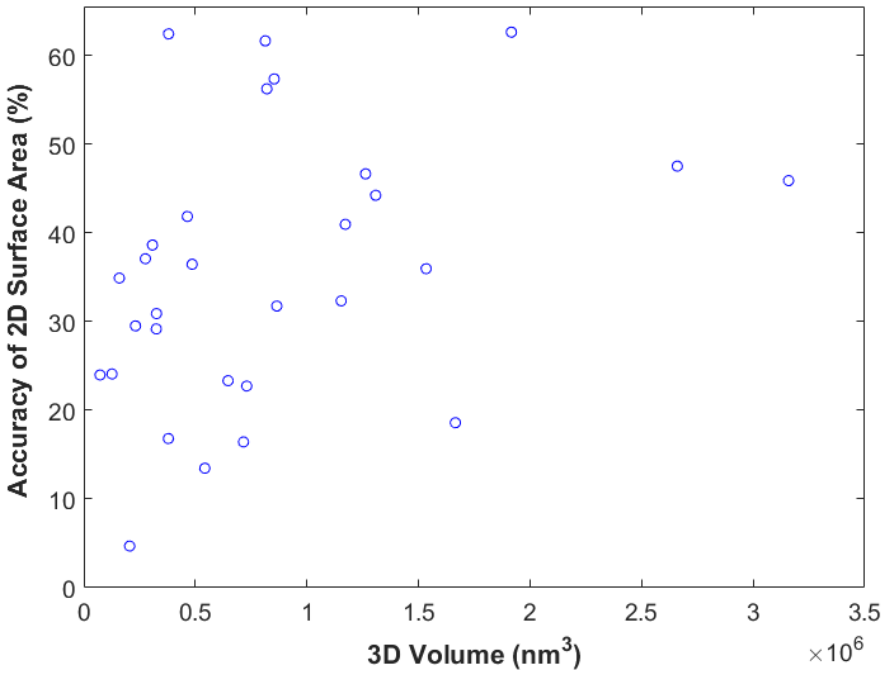


Figure-8.8: A scatter plot showing 3D-derived nanoparticle volume as a function of the accuracy of 2D-derived surface area measurements. No clear or obvious relation between the two parameters can be observed over the whole data range.

8.4.3 - Radius of Gyration

The measurement of radius of gyration in 2D- and 3D-TEM is carried out *via* a near identical methodology, the only difference being distances from each pixel to the centre of mass (r_i) being calculated in 3-dimensions *vs.* in 2-dimensions. While the similarity between the two methodologies is clear, it should be noted that the 2D-R_g method does not involve any terms or factors to estimate the 3D extent of the particle and as such is a purely 2-dimensional parameter. Typically, 2D-R_g measurements were much more

accurate in comparison to 2D-Volume and 2D-Surface area, on average only a 1.2% underestimate of the 3D-R_g value with a standard deviation of 5%. The split of under-/over-estimates by the 2D method was much more even (12 overestimates, 18 underestimates). A scatter plot showing the accuracy of 2D-derived R_g against absolute 3D-R_g is provided in figure-8.9. Accuracy of the 2D method for radius of gyration may reflect the typically more 2-dimensional nature of soot-in-oil nanoparticles that was observed in previous studies by our group [40], and suggested by the 3D aspect ratio values reported in section-8.3. Given that the greatest extent of the particles is parallel to the grid (X- and Y-axes), the inclusion of the Z-depth of the particle does not significantly affect the measured R_g. As such, it is not unexpected that the underestimation of the 3D-R_g value by the 2D-TEM method is not particularly significant.

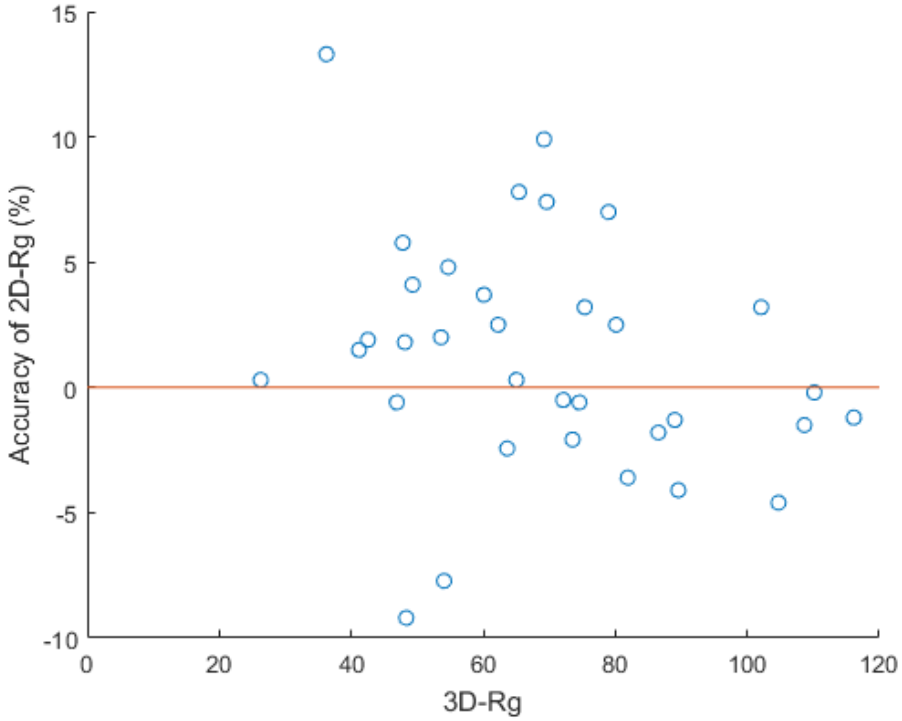


Figure-8.9: A scatter plot showing 3D-derived radius of gyration as a function of the accuracy of 2D-derived radius of gyration measurements. No clear or obvious relation between the two parameters can be observed over the whole data range.

8.4.4 - Circularity

As for 2D-derived radius of gyration, 2D-circularity is a purely 2-dimensional parameter in the sense that it contains no factors to account for expected 3D extent of the nanoparticles. Additionally, only for the comparison of a circle *vs* a sphere is there a 1:1 relationship between the 2D- and 3D-circularity of an object (a perfect sphere can

only project in 2D as a perfect circle, regardless of orientation). This is because of how the appearance of a non-spherical 3D object can change when projected in 2-dimensions. However, given the similarity of the derivation of the parameters and their usefulness in describing complexity of the particles they will be directly compared here. In comparison to 3D-ciruclarity values, on average 2D-circularity resulted in an underestimation of 18%, with a large range similar to that for 2D-volume and 2D-surface area. Only in terms of 3D-circularity was there evidence of a relationship with accuracy of 2D-circularity, for which accuracy increased alongside 3D-circularity (see figure-8.10). This suggests that the more spherical, clustered particles are more accurately characterized by 2D methods in terms of circularity.

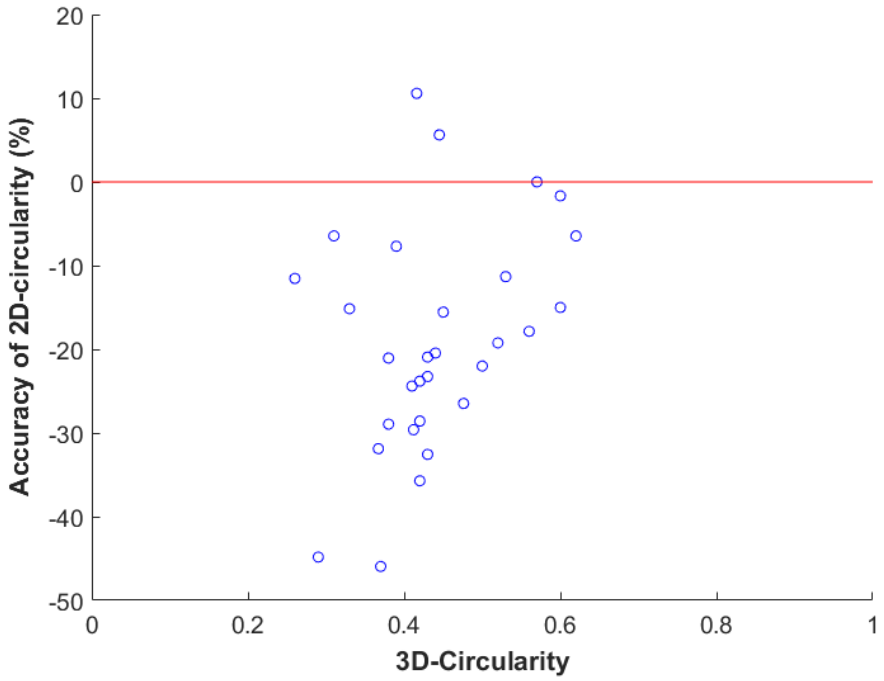


Figure-8.10: A scatter plot showing 3D-derived nanoparticle circularity as a function of the accuracy of 2D-derived circularity measurements. Horizontal red line indicates point at which 2D-derived value is exactly equivalent to the 3D-derived values (*i.e.* completely accurate).

8.4.5 - Fractal Dimension

The final parameter considered was the fractal dimension. Fractal dimension calculations for individual aggregates are most commonly carried out using the Minkowski-Bouligand method, also known as the box-counting method. As before in this work, the choice of box-set was guided by the work of Lottin [156], and the same box-sets used for 3D-D_f were also used for 2D-D_f calculations. This method, similarly to 2D-RG and circularity, is a purely 2-dimensional parameter. The value calculated is

fundamentally limited to ≤2, and this shortcoming, which has been acknowledged in the literature [36, 74], means an underestimation of the 3D-D_f is expected. On average the 2D-D_f values from the 0° images of the tilt-series underestimated the 3D-D_f values by 14%. All measured values were underestimated in comparison to the 3D result, as expected. The range of results saw the maximum underestimation at 19%, and the minimum (most accurate 2D-D_f value) underestimation at 6%. The standard deviation over the 34 particles was small at only 3%, showing reasonable consistency in the deviation *vs.* 3D-D_f.

These results are closely in-line with the predictions of Rogak [74] and Tence [213], who expected deviations between 2D- and 3D-D_f of 10-20% and ≤30% respectively. It is also reasonably smaller than the average underestimation that was observed over the FG soot tilt-series, which was a 26% underestimation. The FG soot nanoparticle possessed a 3D-D_f value of 2.47, which is significantly larger than those measured for the GTDI soot-in-oil sample (for which the range of 3D-D_f = 1.90-2.12). Given the fundamental limitation of the 2D-D_f method, it is expected that nanoparticles with lower 3D-D_f values will be more accurately measured by the 2D method, particularly those with 3D-D_f ≤ 2. A scatter plot showing accuracy of the 2D-D_f values as a function of the absolute 3D-D_f (see figure-8.11) offers no suggestion that this relation exists.

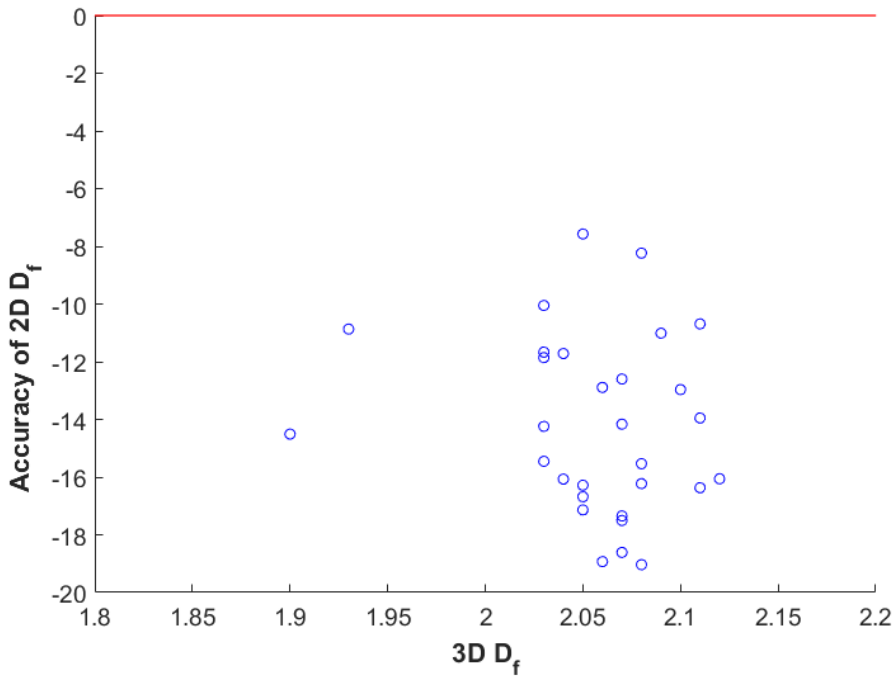


Figure-8.11: A scatter plot showing 3D-derived fractal dimension as a function of the accuracy of 2D-derived fractal dimension measurements. Horizontal red line indicates point at which 2D-derived value is exactly equivalent to the 3D-derived values (*i.e.* completely accurate).

8.4.6 – Aspect Ratio

On average, 2D-derived aspect ratio was 14% larger than the 3D-derived equivalent. This average over-estimation by 2D methods is not entirely unexpected, as it has already been shown earlier (section-8.3) that typical GTDI soot-in-oil nanoparticles tend to be about twice as large in the XY-plane than in the Z-direction. As such, incorporation of a smaller dimension into the aspect ratio calculation would be expected on average to decrease the value. A scatter plot comparing 2D- and 3D-derived values of aspect ratio is given in figure-8.12.

Despite the modest 2D-3D discrepancy on average, this parameter was associated with very strong variability across the 34 nanoparticles. Depending on the particle under study, deviations between 2D- and 3D-derived aspect ratios were measured from between -40% and +119%. There were no obvious correlations between particle morphology and the accuracy of 2D-derived aspect ratio, though the largest deviation was observed for a very long and thin nanoparticle (see figure-8.13). In 2D, this particle possessed a very high aspect ratio (= 4.1), but incorporation of the 3rd dimension drastically reduced this value (= 1.9) due to significant 3D character.

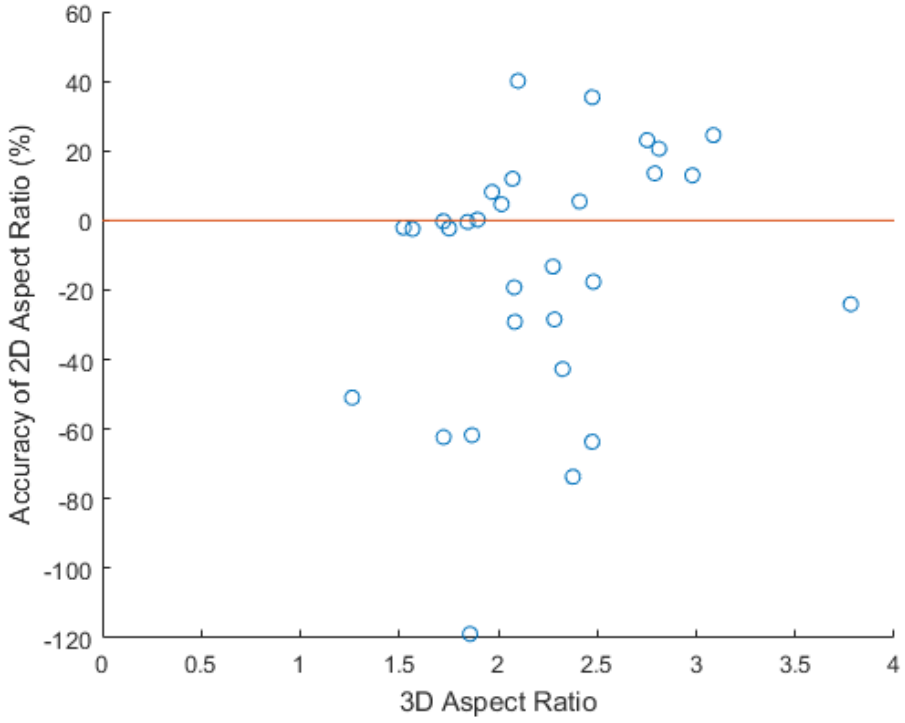


Figure-8.12: A scatter plot showing 3D-derived aspect ratio as a function of the accuracy of 2D-derived aspect ratio. Horizontal red line indicates point at which 2D-derived value is exactly equivalent to the 3D-derived values (*i.e.* completely accurate).

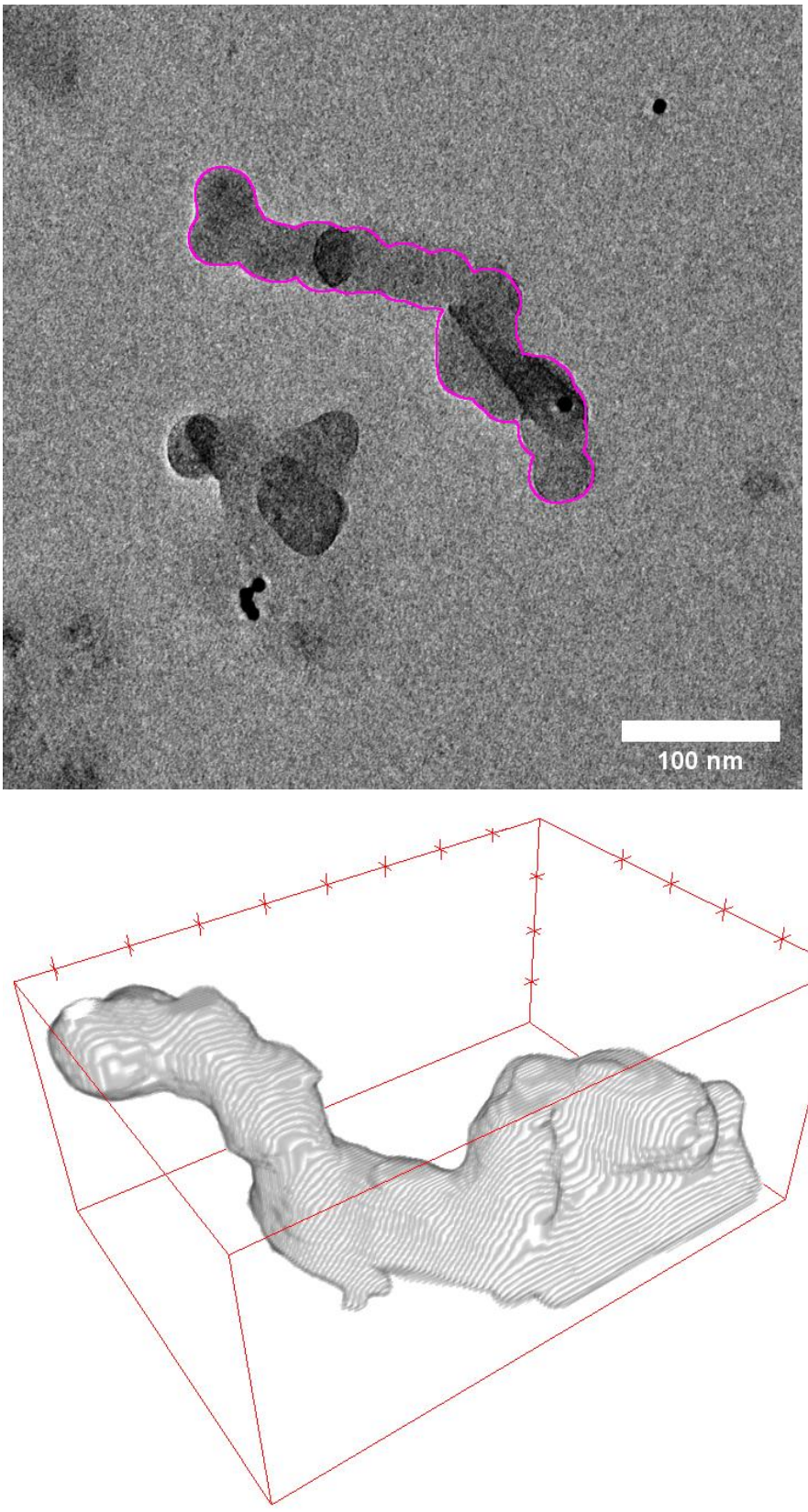


Figure-8.13: The above TEM image shows a 2D representation of a nanoparticle with apparently very high aspect ratio (long and thin). The 3D render of the same nanoparticle below shows distinct 3D character that was not apparent in the 2D projection. The 3D-derived aspect ratio (1.87) is much lower in comparison to the 2D-derived value (4.07).

8.4.7 – Summary: 2D- vs 3D-derived Morphology

For 34 GTDI soot-in-oil nanoparticles, comparisons have been made between commonly measured morphological parameters derived using 2D and 3D methods. The most significant inaccuracies in the 2D method was observed for the surface area measurements. On average 2D methods overestimated 3D surface area by 35%, and results were associated with strong variability reflected in the large standard deviation, equivalent to ±17%. Overestimation was expected given that primary particle overlap was not accounted for in the calculation. Both circularity and volume were on average underestimated by 2D methods to a similar degree; 18% and 23% respectively. Both parameters also saw significant variability in the accuracy the 2D-method, observing both over- and under-estimations of the 3D-derived value. Fractal dimension *via* box-counting was also underestimated by 2D methods, by 14% on average. This was again expected given deficiencies of the 2D method, which makes no attempt to account for the unseen 3D morphology. Results were associated with a small variability, which is not unexpected given previous observation of insensitivity in the parameter (see chapter-4, section-4.3.2.5). Finally, radius of gyration as calculated by 2D methods was extremely close to the 3D-derived value on average. Increased accuracy for GTDI soot-in-oil in comparison to FG soot was assumed to be related to the more 2-dimensional character of the soot-in-oil.

These results show sizeable inaccuracies in 2D morphological characterisation for all parameters considered except radius of gyration. Additionally, most parameters (except Df) were also associated with strong variability, *i.e.* deviations were measured over a large range for the 34 nanoparticles.

8.5 – Unique Outputs of 3D Reconstruction

Not only does 3D reconstruction offer more accurate determination of morphological parameters, it also results in models that can be used to easily visualise the real 3D morphology. Even in 2D-derived measurements were exactly accurate, this type of detail could not be appreciated. This section discusses information on the morphology of GTDI soot-in-oil nanoparticles exclusively available through the use of 3D-TEM study.

8.5.1 – Variation due to Nanoparticle Orientation

In chapter 4, consideration was given to the effect nanoparticle orientation can have on 2D-derived morphology measurements. For the FG soot nanoparticle, measurements of area and N_p varied by up to 45% across at ±60° tilt-series. Previous works in the literature have observed that measurements of a nanoparticles 2D-area across all possible projection angles varied by around 30% [38] and by around 50% [36] (inferred from figures, data not provided in text) for FG soot and aerosol soot respectively.

This variability with nanoparticle orientation is considered almost as an uncertainty associated with 2D-derived methods. The concern is that differences in morphology observed between nanoparticles may due to this variability, rather than actual differences in 3D structure [38]. As such, it may undermine the understanding of the nature of soot samples and their behaviours in certain environments [36].

In this work, the production of 34 nanoparticle models provided an excellent opportunity by which to assess typical variability due to orientation for this sample of GTDI soot-in-oil. Similarly to the methods employed by both Adachi [36] and Baldelli [38], the reconstructed particle models were projected in 2D over a full range of orientations. This was performed using the 3D project plugin for Fiji, and projections were produced every 10° from 0° to 170° in the Y-axis, and from 10° to 170° in the X-axis. The area of the projections was automatically measured using simple thresholding (as particle models are binarized) resulting in 35 measurements per particle.

For each nanoparticle, the variability was calculated as the maximum range of results as a percentage of the mean value. Over all 34 nanoparticles, the average variability was 59%, with a minimum variability of 14% and a maximum of 92%. The standard deviation was 18%. In terms of correlation of variability with any morphological traits of the nanoparticles, the only observation was a weak correlation suggesting particles shorter in the Z-direction showed stronger variability with orientation (figure-8.14). The nanoparticles with the most and least variable 2D-areas appear to hold to this correlation, and are presented in TEM images in figure-8.15. The particle with most variable area is very small and clustered, while the particle with least variable area is large and 3-dimensional.

These results again show the strong variability of morphology with nanoparticle orientation, providing further evidence to support doubts over the efficacy of single-projection analyses. In fact, if soot-in-oil samples tend to be somewhat small and 2-dimensional in nature as prior results have suggested, then the uncertainties in 2D-derived measurements may be even more pronounced than for typical aerosol soots.

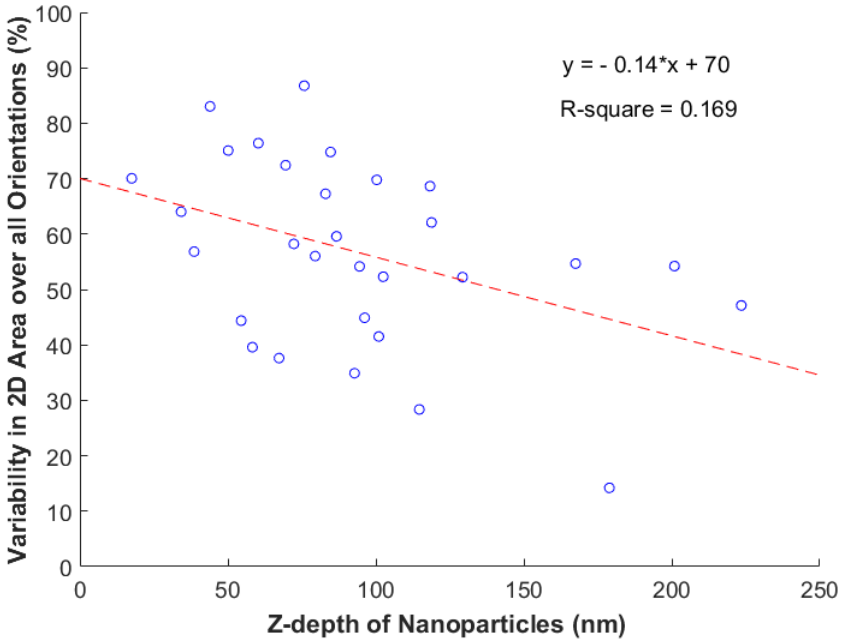


Figure-8.14: A scatter plot showing 3D-derived Z-length of nanoparticles as a function of the variability of nanoparticle 2D-area over full range of projection angles.

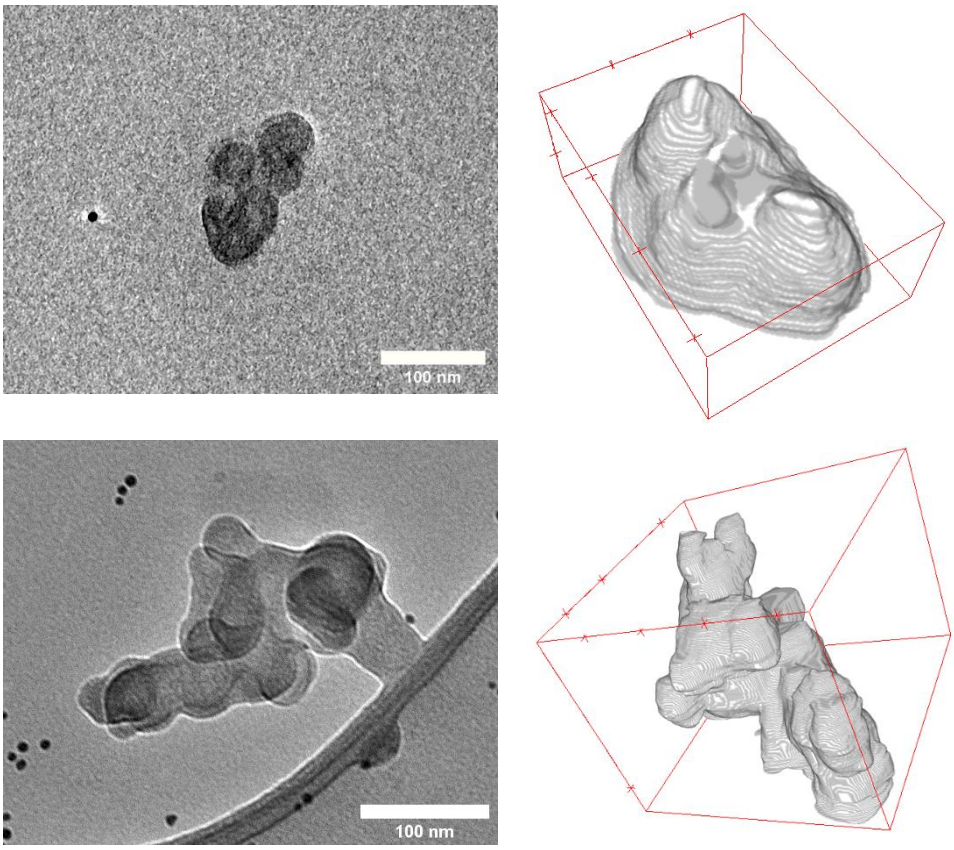


Figure-8.15: The above images show a TEM projection and 3D render of the nanoparticle for which 2D-area was most variable across all projection angles. The below TEM projection and 3D render show the nanoparticle for which 2D-area was least variable across all projections. Note that particle in the lower images is much larger in size and more 3-dimensional in structure.

8.5.2 – Unquantifiable Morphological Observations

As mentioned in the literature review (section 2.3.2), nanoparticle shape has been observed to impact the behaviour of nanofluids [133-137]. Viscosity increases were observed to depend on solid-solid interactions of suspended particles, which in turn depended on their size and shape [133]. More spherical particles experience less friction and lead to smaller viscosity increases [134]. Fractal morphology has also been incorporated into modelling studied in terms of its relation to thermal properties of nanofluids [137].

An exceptionally important area of nanofluid research is in understanding the interaction between soot and oil. As described in the introduction section-1.2.4, oil thickening due to soot is an extremely important concern for modern engines in terms of sustainability. The use of low-viscosity oils is key to meeting increasingly stringent targets for efficiency and emissions, as they reduce friction losses in internal combustion engines [26, 27]. In most cases soot is observed to increase oil viscosity [32, 115, 123], but findings on its influence on wear effects [113, 116], and friction [111, 247] are less unified. On the whole, the complex soot-oil relationship is not well understood. As for other nanofluids, several authors have observed morphological parameters such as surface area [32] and size [130] playing an important role in oil behaviour. However, determination of morphology and shape factors for soot is primarily performed using 2D methods. The work in this thesis so far has discussed limitations of 2D methods for soot characterisation, and has observed strong differences between 2D- and 3D-derived morphology. Given the propensity of morphology to impact nanofluid behaviour, and specific comments in prior soot-oil studies [32], improved morphological characterisation *via* 3D-TEM may be of great use for elucidating the nature of the soot-oil relationship.

Aside from the purely quantitative numerical differences that exist between 2D- and 3D-TEM characterization results, 3D-TEM offers the unique ability to fully appreciate the real morphology of nanoparticles. This permits observation of interesting structural features such as cavities, pits, rings, bridges and other 3-dimensional facets that are common in soot nanoparticles, but not appreciable based on measurements alone. Given the inherent lack of depth perception of 2D-TEM, even if it were otherwise extremely accurate (*i.e.* 2D-derived values exactly equivalent to 3D-derived values) it would still be unable to provide insight into such features. Very recently, exactly these kind of observations have been described by Baldelli *et al.* in their ET study of flame-generated soots [38]. Though not apparent in typical 2D TEM imaging, ring structures were

observed in several nanoparticles when using electron tomography. Interestingly, one of the nanoparticles studied in this work also possessed a ring structure, which is illustrated *via* 2D-TEM images and 3D-renderings in figure-8.16.

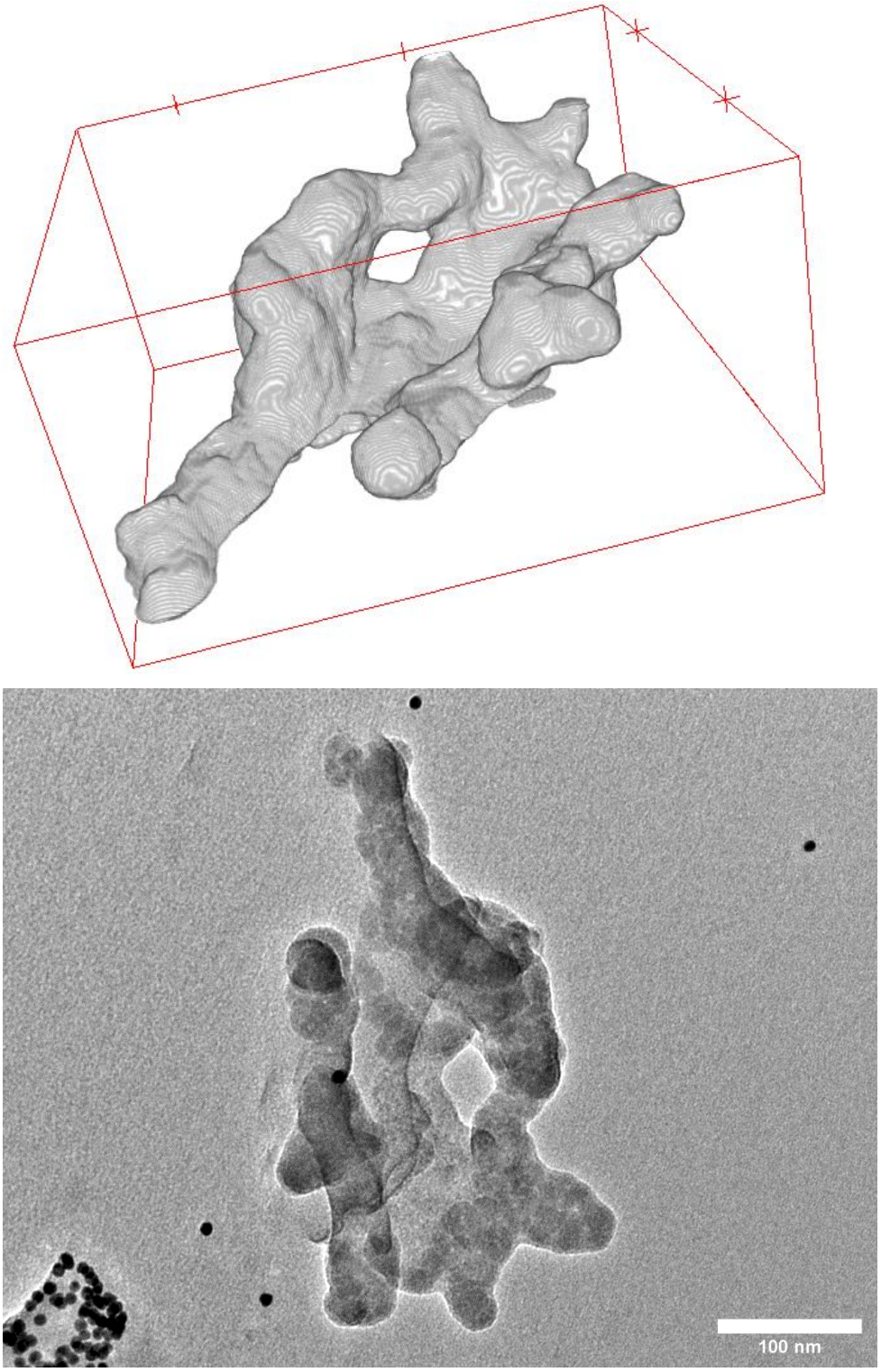
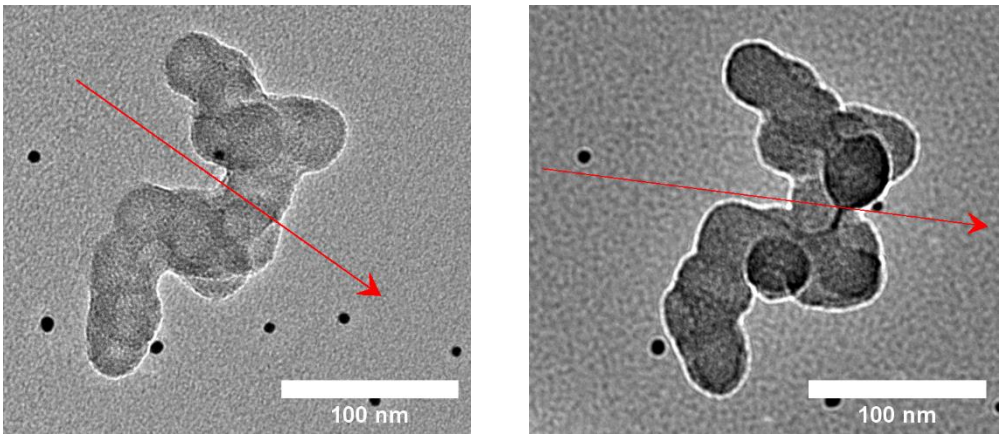


Figure-8.16: (Above) A 3D render of a nanoparticle containing a ring structure. A standard (un-tilted) TEM image of this nanoparticle is shown in figure-8.3b, in which this structure is not visible. (Below) A high-angle TEM image of the nanoparticle in which the ring is revealed to be a real structure, not simply an artefact of 3D reconstruction.

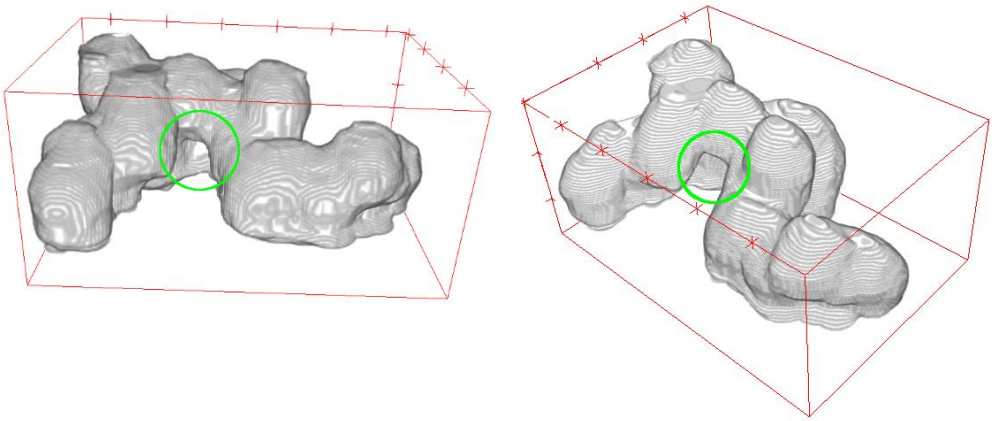
Baldelli related observations of rings structures to the soot formation process, suggesting they could derive from restructuring of bonds between primary particles before significant surface growth occurs. Previously, work by members of my own research group has suggested soot migrates to the oil film of the engine cylinders early during formation [142], thus undergoing highly different oxidation and growth processes compared to exhaust soot. As such, observation of rings and otherwise hard to quantify morphological features may also be important for improving understanding of growth and oxidation processes of soot-in-oil. Further advancement of 3D-TEM permitting full-scale analysis of an entire sample could facilitate this kind of study in the future.

In regards to effect of soot on lubricant oil, it can be envisioned that some morphological features may be more prominent in the promotion of certain interactions. For example, surface irregularities may impact the degree of particle-particle friction, whilst prevalence of elongated arch structures could play a role in particle agglomeration. Internal void spaces or cavities are a feature that could be important for entrainment of lubricant oil within nanoparticles. Pockets of oil decoupled from the bulk fluid-phase may alter the particles effective shape and its Brownian motion. Though such suggestions are the merest speculation at this stage, the outputs of 3D-TEM could provide the necessary data with which to explore such effects in future. Many of the nanoparticles reconstructed in 3D in this work showed presence of interesting 3D morphological features, similar to the ring structure shown above. Two examples of these are shown below in figure-8.17 and figure-8.18.

Figure-8.17 provides an example of what could be considered a cavity feature. A deep, enclosed pit towards the underside of the particle is easily visible in the 3D-reconstruction but is indistinguishable in the 0° TEM image. The existence of the feature (*i.e.* that it is not simply an erroneous *artefact* of reconstruction) is confirmed by viewing the high-tilt images from the tilt-series. Features such as this cavity could potentially entrain fluid, so in the future may be an important consideration for nanofluids study.



(8.17a)

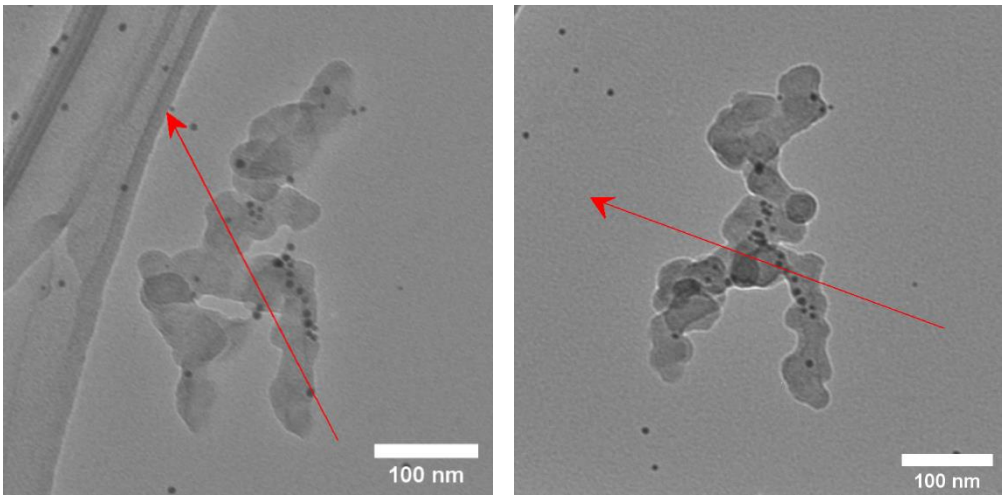


(8.17b) **(8.17c)**

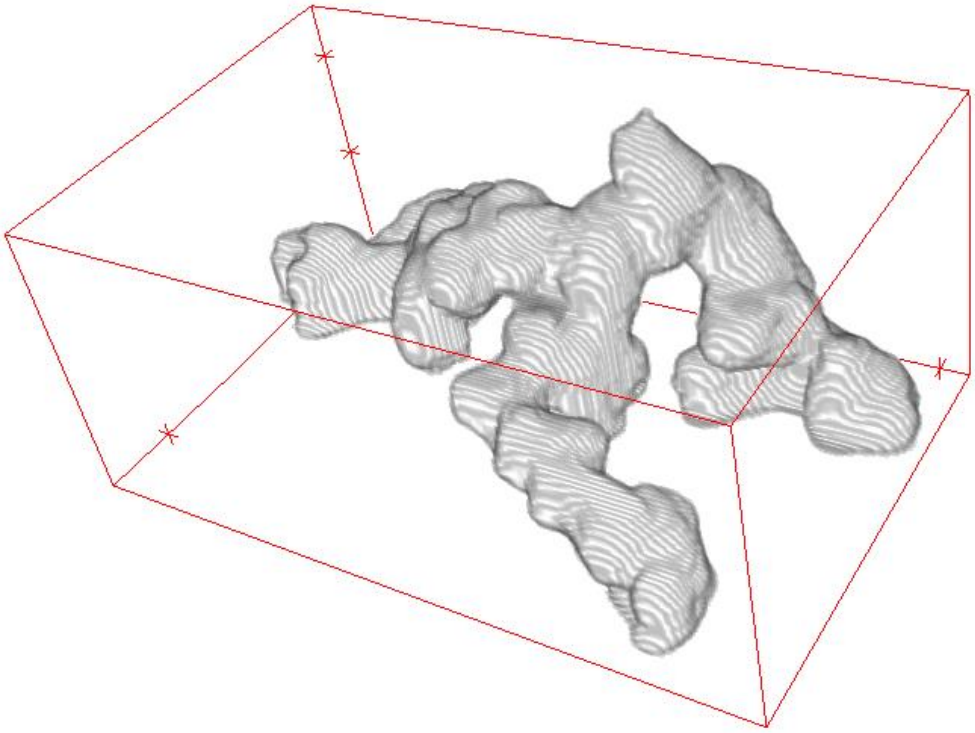
Figure-8.17: A cavity feature in a soot nanoparticle. (a) TEM projections at different angles with arrows running through the cavity. (b & c) 3D render of the same nanoparticle in different orientations, with cavity feature highlighted in green.

Figure-8.18 shows a particularly 3-dimensional soot nanoparticle, possessing 3 distinct arch features in a tripod-like arrangement. Transparency of the soot in the 2D-TEM image suggests 3-dimensionality towards the centre of the particle (see figure-8.18a: darker areas indicate primary particle overlap). However, in the un-tilted TEM image the arch features are not clearly visible as they are predominantly only a single primary particle thick over their length. At high tilt-angle (-50°) the graphene oxide film is visible under the arches and is suggestive of the true 3D structure. The 3D rendering of the particle makes these features clearly visible. This particularly 3-dimensional structure could be conceived to play a role in particle agglomeration, increasing the effective interaction cross-section of the particle and likelihood of collisions resulting in particle aggregation. With 2D-TEM imaging alone these features cannot be quantified, or potentially even recognised.

Due to lack of a high-quality 3D tool to date, it is unknown the extent of control these types of features may have over nanofluid properties. However, due to recent developments in the 3D-TEM methodology we may soon be in a position to research these potential interactions. These observations may also be of relevance for understanding the formation and growth processes of soot-in-oil nanoparticles.



(8.18a)



(8.18b)

Figure-8.18: (a) TEM projections of nanoparticle with prominent 3D arches. Upper-left shows high-angle TEM projection that reveals 3D structure, while the upper-right shows an un-tilted image in which 3D structure is no visible. (b) A 3D render of the same nanoparticle clearly showing prominent 3-dimensional arch structures.

8.6 – Conclusions

The final working chapter of this thesis has detailed the most extensive 3D study of a soot-in-oil sample to date, and possibly of any single soot nanoparticle sample. In total, 34 nanoparticles from a GTDI soot-in-oil nanoparticle were reconstructed in 3D, and their morphology was measured using both 3D and 2D methods. The semi-automated TEM imaging protocol provided a pool of 271 nanoparticles, from which 28 were chosen for study (in addition to 6 nanoparticles already studied in 3D). These nanoparticles were chosen to express the extremes of morphology present in the sample; both large and complex, and small and simple nanoparticles were studied.

In terms of absolute 3D-volume, even the largest nanoparticle considered in this work was only the equivalent of 168 primary particles in size. This result appears rather modest in comparison to some previous studies of exhaust and flame-generated soots, and is consistent with relatively small values of maximum particle length measured in 2D in chapter-6. Previous study of diesel soot-in-oil had observed that nanoparticles tended to be strongly 2-dimensional in structure, and in this GTDI soot-in-oil sample nanoparticles possessed an average 3D aspect ratio of around 2.5. This value again indicates tendency towards 2-dimensionality, significant 3-dimensionality was also observed in this sample.

Comparison between 2D- and 3D-derived morphology observed mean deviations of 23% in volume, 35% in surface area, 18% in circularity, and 14% in both fractal dimension and aspect ratio. For most of these parameters (Vol, SA, circ., AR), the 2D-3D deviations were subject to large variability depending on the particle studied, and could reach as high as 45-120% difference in 2D- and 3D-derived values. Measurements of fractal dimension in 2D and 3D were subject to only small variation, consistent with previous observation of insensitivity in chapter-4. In contrast to these other results, the 2D-method for calculating radius of gyration was on average highly accurate in comparison to the 3D-derived value (only 1.2% difference on average). In general, no strong or obvious correlations were observed between the accuracy of the 2D-derived values and the 3D morphology of a nanoparticle (*e.g.* smaller particles weren't more accurately characterised in 2D than larger particles). A hint of correlation was observed between particle volume and accuracy of 2D-derived volume measurements, and possible reasons for this were discussed in detail.

The 3D nanoparticle models were also used to observe the extent of variability in measured 2D area due to the angle of projection, resulting in an average variation of 59%. This value is larger than had been observed in previous studies of soot in 3D, and

there were indications that smaller particles tended to observe greater variability with orientation. As such, doubts over the efficacy of morphology measured from single 2D projections may be more prominent for samples like soot-in-oil.

The final analysis of the sample was purely quantitative, and observed unusual and interesting morphological features only appreciable *via* 3D study. Features such as rings, cavities, and arches were shown both in 2D and 3D, and purely speculative links towards impact on rheological properties were discussed.

9 – Conclusions

The goal at the start of this PhD project was to develop a tool to permit the morphological characterisation of soot nanoparticles in 3D. Across several disciplines spanning health, environmental, and automotive sectors, the morphology of soot is considered to play a key role in determining the extent and propagation of soot-related phenomena. This includes depth of inhalation in humans and subsequent toxicity, contribution to climate change through radiative forcing and snow-ice melting, and increased oil viscosity and wear leading to decreased efficiency in automotive engines. A path to mitigating soot-related effects is clear: understand morphology and behaviour can be understood, understand how soot behaves and influences environments and solutions can be designed.

Soot nanoparticles possess characteristic fractal morphologies that are complex and highly variable. Typical morphological characterisation with TEM is limited to 2D, leading to doubts over the quality of measurements of 3D structures. In particular, this is related to variability in appearance depending on particle orientation, and derivation of 3D morphology from 2D measurements. In response to these uncertainties, a handful of prior publications had detailed the use of electron tomography for 3D volume reconstruction of soot. In these works, the measurements of real 3D morphology was seen to have strong consequences for models of climatic impact of soot, and enhanced the understanding of the general state of soot-in-oil. Despite impressive benefits *vs.* 2D-derived measurements there had been little in the way of follow-up work. Prior work by the Nottingham Powertrain research group found that a single nanoparticle reconstruction could take up to 1 day to complete. Given that typical soot characterisation studies measure 100+ aggregates per sample, the technique as it stood was not a viable tool. In order to realise the full benefits of 3D morphological characterisation, the 3D reconstruction procedure needed to be optimised. This was to be achieved by evaluating and adapting the available methods for electron tomography and TEM imaging to the challenge of soot, and in particular, soot-in-oil.

Chapter-4 detailed the use of TEM and ET for morphological characterisation of soot in a case-study of a flame-generated soot nanoparticle. In this chapter, the results of 2D- and 3D-derived morphological parameters were compared, and the effect of nanoparticle orientation on 2D-derived measurements was investigated:

- Significant discrepancies were observed between commonly measured 2D- and 3D-derived morphological parameters. 2D-based methods underestimated 3D-

volume by around 36%, while surface area was on average overestimated by 13%. Fractal dimension was underestimated by 2D methods, with a similar scale of deviation (~20-30%) as seen in previous works. Deviations between 2D- and 3D-circularity were 18% on average, while 2D-R_g was reasonably accurate at only 8% difference.

- TEM images acquired at varying angles of projection highlighted significant and asymmetric variation in 2D-derived morphology. Measurements of area, number of primary particles, volume, and surface area varied by 40-45% compared with the mean values, and measurements of circularity varied by up to 69%.

Application of these techniques in the early stages of the project meant areas of the 3D reconstruction process where optimisation would be most beneficial could be targeted. Comparison of 2D- and 3D-derived morphology showed sizeable discrepancies similar to those in prior works by other groups, again highlighting the shortcoming of 2D-TEM and the potential benefits of 3D study. By observing the impact of nanoparticle orientation on 2D-derived measurements it was possible to draw attention to a generally underappreciated, but potentially highly significant source of error in traditional soot characterisations. Large and unpredictable variation in nanoparticle appearance as a function of orientation could result in an uncertainty on 2D-TEM measurements that is in addition to those derived from the fundamental lack of 3D depth perception.

Chapter-5 contained the first steps of the optimisation of the 3D reconstruction process. Different methods for tomographic reconstruction, tilt-series acquisition, and tomogram segmentation were assessed in terms of speed and quality. Also included in this chapter was the study of soot-in-oil from a GTDI engine, a sample chosen due to growing concerns over increased sooting tendencies of modern gasoline engines and the potential ramifications of high soot loading in lubricant oils. A significant lack of study of soot from gasoline oils in the literature meant potential for high impact and novel research outcomes in this work. Those resulting from this chapter are summarised below:

- General TEM observation of the sample revealed abundance of localised amorphous carbon structures and crystalline material in addition to typical soot nanoparticles. This was similar to what had been observed in prior studies of GDI soot-in-oil, and may be an important consideration for effects on oil properties as understanding of such samples continues to grow.
- Reconstruction - WBP *vs.* SIRT: Through qualitative and quantitative comparison of the resulting tomograms and particle models, it was determined

that WBP was of similar quality to SIRT, but completed significantly quicker (30 seconds *vs.* 1.5 hours).

- Reducing tilt-range *vs.* reducing tilt-increment: While reduction in overall tilt-range from ±60° to ±50° and ±40° resulted in significant decreases in quality, increase in tilt-increment up to 3° still produced tomograms of high quality. The optimum tilt-series was a ±60° tilt-range with 3° increments, cutting potential beam exposure to the sample by two thirds.
- Interpolation - speed *vs.* quality: While increased use of interpolation drastically reduced the time required for segmentation, significant information losses also occurred. Only by using interpolation between every 5th slice of the tomogram was acceptable quality of reconstruction retained, resulting in a 44% decreased in time required for segmentation.
- The optimised process was associated with a 67% decrease in time required compared with a procedure based on examples in the literature (1.3 hours *vs.* 4 hours).

The work in this chapter described the first significant steps towards a high-throughput methodology for 3D reconstruction of soot nanoparticles. As far as we are aware, this work presents the first efforts towards optimisation of 3D soot study in the literature to date. The achieved reductions in time and effort (saving >2.5 hours in a case study example) are of significant benefit due to the large number of nanoparticles that would need to be observed in a full-scale study (>100). At this stage a complete 3D study of soot became feasible, though remained highly labour intensive. The combined study of soot-in-oil nanoparticles represents a peak in difficulty for the 3D study of soot due to the presence of lubricant oil – known to be a severe contaminant in TEM imaging. This necessitated the development of a robust and reliable sample preparation technique that can ensure successful study of future soot-in-oil samples. Despite the significant improvements made, at this stage only a small number of particles had been studied so confidence in the results was somewhat limited. Optimisation was carried out based on relative accuracy of 3D reconstructions, while ideally would be based on absolute accuracy. In addition to this, the optimised procedure still required manual involvement in tomogram segmentation, though this was greatly reduced by incorporation of interpolation.

Chapter 6 continued the optimisation process, but focussed instead on improving throughput of TEM imaging through automation. The study of GTDI soot-in-oil in chapter-5 observed low soot concentrations on the TEM grid due to the difficulty of

removing lubricant oil, causing a significant bottle-neck in throughput. To combat this issue, the optimised imaging procedure developed in this chapter consisted of:

- Automated screening of large areas of TEM grids, and the creation of maps through which to control TEM operation
- A logging system to permit storing of locations of nanoparticles for study over subsequent sessions
- Automated image processing is used to identify structures of interest, with a manual review process used to remove incorrect selections and permit rapid 2D-TEM analysis.

The automated procedure also resulted in the unplanned benefit of facilitating high-throughput 2D morphological characterisation. Options were built into the automated imaging process to permit manual updating of automated nanoparticle selections, and were utilised to study the GTDI soot-in-oil sample. Typical 2D morphology was determined for this sample and compared to prior study of GTDI soot-in-oil nanoparticles by members of the Nottingham Powertrain group:

- Automated imaging was performed on 9 squares of the TEM grid, covering approximately 4000 μm^2
- In total, 524 soot nanoparticles were studied in 2D (271 fully automated selection, and 253 fully manual selections).
- The following characteristic morphologies were determined for the sample: mean primary particle diameter = 33 nm, mean aggregate Feret diameter (maximum length) = 118 nm, mean radius of gyration = 35 nm, and fractal dimension = 1.73.
- Compared with prior study of a GTDI soot-in-oil sample, the current sample of nanoparticles appears to be slightly larger in their overall aggregate size, but less open and branched in their morphology.
- Convergence in the mean radius of gyration of nanoparticles occurred after around 150 individual measurements, suggesting a target for future sample sizes

The optimisation of both the reconstruction and TEM imaging procedures resulted in a technique that was now practical for large-scale 3D study of soot nanoparticles. This semi-automated methodology significantly reduces manual labour in TEM imaging of soot, helping to increase efficiency and throughput *via* off-peak operation and decrease bias in selections of nanoparticles *via* the automated identification. In particular, a system to log and store locations of nanoparticles over subsequent imaging sessions is extremely useful, given that it is practically impossible to reliably relocate individual

structures manually. Development of highly automated and rapid 2D characterisation facilitate a multi-faceted approach to morphological characterisation of soot samples, and already showed use for comparison of similar soot-in-oil samples. Though significant progress was achieved in this chapter, the procedure is somewhat limited by an inability to operate fully "on-line", and still retained manual involvement to ensure highly accurate results.

In chapter-7, the accuracy of 3D reconstruction was assessed through the creation of artificial 'ground truth' data, in the form of soot-like 3D aggregate models. From a total of 13 individual models, TEM-style tilt-series were produced and subjected to the full ET procedure developed in chapter-5. The morphology of post-reconstruction models were then compared to the originals to determine absolute accuracy of different ET procedures, resulting in the following observations:

- Tilt-series created over a ±80° tilt-range observed practically no elongation (<1%) due to missing wedge elongation. By comparison, ±60° tilt-series observed only minor elongation (3-4%), with practically no differences between tilt-series with 1° increments and 3° increments between images.
- While reconstructions from ±80° tilt-series lead to a slight underestimation of the true particle bulk, reconstruction from ±60° tilt-series lead to a slight overestimation; overall accuracy for the two methods was similar.
- The propagation of reconstruction artefacts and errors as a function of an objects morphology was assessed using 2D data in an appendix section (A.1). In that mini-investigation, it was observed that missing wedge elongation occurred more prominently on smooth and broad surfaces, but was less significant when applied to intricate soot-like morphologies.
- Reconstruction from ±60° tilt-series with 3° increments (the result of optimisation in chapter-5) was seen to be highly accurate for soot-like aggregates, resulting in deviations from ground truth values for volume, surface area, radius of gyration, 3D-circularity, and fractal dimension of <3%.

An important outcome of this chapter was a greater understanding of the propagation of errors in ET. Previous authors have generally made little effort towards accuracy assessment, often only using simple models of spheres as ground-truth. In this work, efforts were made to reflect typical soot-in-oil morphology and appearance in TEM images so that propagation of reconstruction errors and artefacts are as realistic as possible. Comparison with basic sphere model analysis showed that error propagation is strongly dependent upon the input structure, and missing-wedge elongation acts more

prominently upon smoother surfaces. The work performed in this chapter ultimately confirmed that 3D reconstruction of soot *via* electron tomography is highly accurate, and in-turn that errors of 2D-derived measurements are legitimate deficiencies of that technique. Additionally, the use of artificial ground truth was able to confirm prior observations (chapter-5) that the use of ±60° tilt-series with 3° image increments and the WBP reconstruction algorithm was an acceptable optimised procedure. However, while significant efforts were made to reflect realistic nanoparticle morphology it was apparent that simplified surfaces of the nanoparticles lead to unrealistic accuracies of segmentation interpolation, and should be targeted for improvement in future accuracy assessments.

In chapter-8, the methods developed thus far were employed to facilitate an extended 3D study of a GTDI soot-in-oil sample. From a pool of 271 possible locations identified in chapter-6, 28 nanoparticles were chosen for 3D study - in addition to the 6 studied in chapter-5. Due to the limited number studied, these were chosen to represent the extremes of morphology observed in the sample so as to highlight benefits of the 3D method. Firstly, 3D-derived measurements were used to understand the general state of nanoparticles in this sample:

- In terms of absolute 3D-volume, even the largest nanoparticle considered in this work was only the equivalent of 168 primary particles in size. This result appears modest in comparison to previous studies of exhaust and flame-generated soots, and is consistent with relatively small values of maximum particle length measured in 2D in chapter-6.
- Previous study of diesel soot-in-oil had observed that nanoparticles tended to be strongly 2-dimensional in structure, and in this GTDI soot-in-oil sample nanoparticles possessed an average 3D aspect ratio of around 2.5. Though this value indicates tendency towards 2-dimensionality, significant 3-dimensionality was also observed in this sample.

Next, a direct comparison of 2D- and 3D-derived morphological measurements was carried out for the 34 nanoparticles:

- On average, deviations of 23% in volume, 35% in surface area, 18% in circularity, and 14% in both fractal dimension and aspect ratio were observed.
- For most of these parameters (Vol, SA, Circ., AR), the 2D-3D deviations were subject to large variability depending on the particle studied, and could reach as high as 45-120% difference in 2D- and 3D-derived values.

- Measurements of fractal dimension in 2D and 3D were subject to only small variation, consistent with previous observation of insensitivity in chapter-4.
- In contrast to these other results, the 2D-method for calculating radius of gyration was on average highly accurate in comparison to the 3D-derived value (only 2% difference on average).
- In general, no strong or obvious correlations were observed between the accuracy of the 2D-derived values and the 3D morphology of a nanoparticle (*e.g.* smaller particles weren't more accurately characterised in 2D than larger particles, or vice versa).
- 3D nanoparticle models were used to observe the extent of variability in measured 2D area due to the angle of projection, resulting in an average variation of 59%. This value is larger than had been observed in previous studies of soot in 3D, and there were indications that smaller particles tended to observe greater variability with orientation.

Overall, the work in this chapter represents the largest 3D study of a soot-in-oil sample to date, and possibly the largest study of any single sample of soot nanoparticles (34 nanoparticles in total). Significant deficiencies in the accuracy of 2D-derived measurements and variability due to nanoparticles orientation show that 2D-TEM is fundamentally inferior to accurate 3D study. The final analysis of the sample was carried out based on qualitative observations of 3D morphology that could never be made using typical 2D methods, even if measured values of morphology were highly accurate. Morphological features such as rings, cavities, and arches were observable and quantifiable in 3D, but barely recognizable in 2D. Previous observations of rings in 3D study of soot had been linked to the soot formation process, while features such as cavities and arches may be relevant for nanofluid behaviour. Development of 3D reconstruction for soot presents new opportunities for enhanced understanding of the structure and morphology of soot nanoparticles. Though representing an important landmark in the development of high-throughput 3D study of soot nanoparticles, the work in this chapter is still limited in terms of sample size and the associated reliability of the observations.

In summary, significant progress has been made in relation to the aims of the project. Substantial improvements to speed and throughput of electron tomography and TEM imaging have been achieved through a multi-faceted approach. The project culminated in a extended 3D study of a GTDI soot-in-oil sample, involving a total of 34 individual nanoparticles. Artificial ground truth in the form of soot-like models was established, and used to confirm that the technique was highly accurate, and that the errors of 2D-

TEM characterisations were genuine. The extent of variability in 2D-TEM characterisation due to nanoparticle orientation was observed to be significant, and uncertainties in 2D measurements are potentially most prominent for soot-in-oil samples. In addition to this, comparison of 2D- and 3D-derived morphologies found little in the way of reliable correlations between the techniques, implying that simple corrections factors cannot be applied. These results confirm doubts over the efficacy of 2D-TEM measurements, which are unlikely to diminish even in the extent of extremely large samples sizes. In addition to quantified improvements in characterisation accuracy, uniquely 3-dimensional observations were made regarding the structures of nanoparticles, and may in future provide insight into the formation and behaviours of soot nanoparticles. This work has confirmed the need for advanced 3D reconstruction methodologies to fully appreciate the potential impacts of soot morphology, and this technique now stands poised to permit large scale study of soot in 3D.

9.1 – Future Work

Despite the progress made in the optimisation of 3D-TEM in this PhD project, there are still ample opportunities for further improvement and development.

- General imaging and tilt-series acquisition is somewhat limited by the capabilities of the equipment at the nmRC, in particular the TEM camera. New ‘direct detection’ cameras for TEM permit much more rapid image acquisition and much lower beam exposure to the sample. While tilt-series and montage acquisition currently requires around 30-40 minutes to complete, an improved camera could complete the same actions within a few minutes, or less. This could greatly improve throughput and potentially permit acquisition of larger tilt-ranges, leading to higher quality 3D reconstruction.
- Similar limitations exist in relation to automation of tilt-series and montage acquisition with SerialEM. While in theory full automation is possible, practically this was not the case. Improvement in control of the TEM with SerialEM or other software could facilitate full automation and could take advantage of cheap and efficient operation during non-peak times, and without a TEM operator.
- Automated image processing was hampered by false-positive selections of non-soot material, leading to the necessity of a manual review process. Development of a more accurate and adaptive image processing tool could significantly

decrease non-soot selections and permit fully automated 2D-TEM characterisation.

- Tomogram segmentation is perhaps the most obvious areas for improvement of the methodology. While interpolation significantly improves speed, this step it is still a major bottle-neck. Development of a robust automated segmentation process could possibly be achieved in tandem with improved automated 2D-TEM image processing.
- An obvious opportunity for the employment of the 3D-TEM technique is for the study of typical exhaust or aerosol soot samples. The lack of high concentrations of non-soot material on TEM grid should dramatically improve the quality of automated image processing, and improve the throughput of the entire process. Similarly, an exciting prospect is the adaptation of the 3D-TEM technique for the study of non-soot nanoparticle species, potentially in the fields of materials science and nanotechnology.

10 - References

[1] Aqeg. *Particulate Matter in the United Kingdom: Summary*. London: Defra; **2005**.

[2] Kim K.H., Sekiguchi K., Kudo S., Sakamoto K. *Characteristics of Atmospheric Elemental Carbon(Char and Soot) in Ultrafine and Fine Particles in a Roadside Environment, Japan*. Aerosol and Air Quality Resarch. **2011**;11(1):1-12.

[3] Huang J.C. *Carbon black filled conducting polymers and polymer blends*. Advances in Polymer Technology: Journal of the Polymer Processing Institute. **2002**;21(4):299-313.

[4] Alexander D.T., Crozier P.A., Anderson J.R. *Brown carbon spheres in East Asian outflow and their optical properties*. Science. **2008**;321(5890):833-6.

[5] Bond T.C., Bergstrom R.W. *Light absorption by carbonaceous particles: An investigative review*. Aerosol Sci Tech. **2006**;40(1):27-67.

[6] Adler G., Riziq A.A., Erlick C., Rudich Y. *Effect of intrinsic organic carbon on the optical properties of fresh diesel soot*. Proceedings of the National Academy of Sciences. **2010**;107(15):6699-704.

[7] Vallius M.J., Ruuskanen J., Mirme A., Pekkanen J. *Concentrations and estimated soot content of PM1, PM2. 5, and PM10 in a subarctic urban atmosphere*. Environ Sci Technol. **2000**;34(10):1919-25.

[8] Bond T.C., Streets D.G., Yarber K.F., Nelson S.M., Woo J.H., Klimont Z. *A technology-based global inventory of black and organic carbon emissions from combustion*. Journal of Geophysical Research: Atmospheres. **2004**;109(D14).

[9] Bond T.C., Doherty S.J., Fahey D., Forster P., Berntsen T., Deangelo B., Flanner M., Ghan S., Kärcher B., Koch D. *Bounding the role of black carbon in the climate system: A scientific assessment*. Journal of Geophysical Research: Atmospheres. **2013**;118(11):5380-552.

[10] Klimont Z., Kupiainen K., Heyes C., Purohit P., Cofala J., Rafaj P., Borken-Kleefeld J., Schöpp W. *Global anthropogenic emissions of particulate matter including black carbon*. Atmos Chem Phys. **2017**;17(14):8681-723.

[11] Organization W.H. *Ambient air pollution: A global assessment of exposure and burden of disease*. **2016**.

[12] Jansen K.L., Larson T.V., Koenig J.Q., Mar T.F., Fields C., Stewart J., Lippmann M. *Associations between health effects and particulate matter and black carbon in subjects with respiratory disease*. Environmental health perspectives. **2005**;113(12):1741-6.

[13] Agency U.E.P. Health and Environmental Effects of Particulate Matter (PM). US Environmental Protection Agency [Internet]. 2018 2019.

[14] Hansen J., Nazarenko L. *Soot climate forcing via snow and ice albedos*. Proceedings of the National Academy of Sciences. **2004**;101(2):423-8.

[15] Jacobson M.Z. *Control of fossil-fuel particulate black carbon and organic matter, possibly the most effective method of slowing global warming*. Journal of Geophysical Research: Atmospheres. **2002**;107(D19):ACH 16-1-ACH -22.

[16] Organization W.H. Air Pollution 2019 [Available from: https://www.who.int/airpollution/guidelines/en/.

[17] Organization W.H. Ambient (outdoor) air quality and health 2019 [Available from: https://www.who.int/news-room/fact-sheets/detail/ambient-(outdoor)-air-quality-and-health.

[18] Defra. National Air Quality Objectives and European Directive Limit and Target Values for the Protection of Human Health 2018 [Available from: https://uk-air.defra.gov.uk/assets/documents/Air_Quality_Objectives_Update.pdf.

[19] Eea. Exceedance of air quality standards in urban areas 2019 [Available from: https://www.eea.europa.eu/data-and-maps/indicators/exceedance-of-air-quality-limit-3/assessment-5.

[20] Technologies D. *Worldwide emissions standards: Passenger cars and light duty vehicles 2019-2020*. **2019**.

[21] Uy D., Ford M.A., Jayne D.T., O'neill A.E., Haack L.P., Hangas J., Jagner M.J., Sammut A., Gangopadhyay A.K. *Characterization of gasoline soot and comparison to diesel soot: Morphology, chemistry, and wear*. Tribol Int. **2014**;80:198-209.

[22] Adler J. *Ceramic diesel particulate filters*. International Journal of Applied Ceramic Technology. **2005**;2(6):429-39.

[23] Reijnders J., Boot M., De Goey P. *Impact of aromaticity and cetane number on the soot-NOx trade-off in conventional and low temperature combustion*. Fuel. **2016**;186:24-34.

[24] Esangbedo C., Boehman A.L., Perez J.M. *Characteristics of diesel engine soot that lead to excessive oil thickening*. Tribol Int. **2012**;47:194-203.

[25] Uy D., O'neill A.E., Simko S.J., Gangopadhyay A.K. *Soot-additive interactions in engine oils*. Lubr Sci. **2010**;22(1):19-36.

[26] Macian V., Tormos B., Ruiz S., Miró G. *Low viscosity engine oils: Study of wear effects and oil key parameters in a heavy duty engine fleet test*. Tribol Int. **2016**;94:240-8.

[27] Tormos B., Ramírez L., Johansson J., Björling M., Larsson R. *Fuel consumption and friction benefits of low viscosity engine oils for heavy duty applications*. Tribol Int. **2017**;110:23-34.

[28] Kalghatgi G.T. *The outlook for fuels for internal combustion engines*. Int J Engine Res. **2014**;15(4):383-98.

[29] Oberdörster G., Celein R.M., Ferin J., Weiss B. *Association of particulate air pollution and acute mortality: involvement of ultrafine particles?* Inhalation toxicology. **1995**;7(1):111-24.
[30] Liu L., Mishchenko M.I. *Scattering and radiative properties of complex soot and soot-containing aggregate particles*. Journal of Quantitative Spectroscopy and Radiative Transfer. **2007**;106(1-3):262-73.
[31] Kajino M., Kondo Y. *EMTACS: Development and regional-scale simulation of a size, chemical, mixing type, and soot shape resolved atmospheric particle model*. J Geophys Res-Atmos. **2011**;116.
[32] Bardasz E.A., Cowling S.V., Ebeling V.L., George H.F., Graf M.M., Kornbrekke R.E., Ripple D.E. *Understanding soot mediated oil thickening through designed experimentation-part 1: Mack EM6-287, GM 6.2 L*. SAE transactions. **1995**:1926-40.
[33] Badshah H., Kittelson D., Northrop W. *Particle emissions from light-duty vehicles during cold-cold start*. SAE International Journal of Engines. **2016**;9(3):1775-85.
[34] Van Poppel L.H., Friedrich H., Spinsby J., Chung S.H., Seinfeld J.H., Buseck P.R. *Electron tomography of nanoparticle clusters: Implications for atmospheric lifetimes and radiative forcing of soot*. Geophys Res Lett. **2005**;32(24).
[35] Adachi K., Chung S.H., Buseck P.R. *Shapes of soot aerosol particles and implications for their effects on climate*. J Geophys Res-Atmos. **2010**;115.
[36] Adachi K., Chung S.H., Friedrich H., Buseck P.R. *Fractal parameters of individual soot particles determined using electron tomography: Implications for optical properties*. J Geophys Res-Atmos. **2007**;112(D14).
[37] Okyay G., Heripre E., Reiss T., Haghi-Ashtiani P., Auger T., Enguehard F. *Soot aggregate complex morphology: 3D geometry reconstruction by SEM tomography applied on soot issued from propane combustion*. J Aerosol Sci. **2016**;93:63-79.
[38] Baldelli A., Trivanovic U., Rogak S.N. *Electron tomography of soot for validation of 2D image processing and observation of new structural features*. Aerosol Sci Tech. **2019**;53(5):575-82.
[39] Kondo K., Aizawa T., Kook S., Pickett L. *Uncertainty in sampling and TEM analysis of soot particles in diesel spray flame*. SAE Technical Paper; **2013**. Report No.: 0148-7191.
[40] La Rocca A., Campbell J., Fay M.W., Orhan O. *Soot-in-Oil 3D Volume Reconstruction Through the Use of Electron Tomography: An Introductory Study*. Tribol Lett. **2016**;61(1).
[41] La Rocca A., Bonatesta F., Fay M.W., Campanella F. *Characterisation of soot in oil from a gasoline direct injection engine using Transmission Electron Microscopy*. Tribol Int. **2015**;86:77-84.
[42] Piock W., Hoffmann G., Berndorfer A., Salemi P., Fusshoeller B. *Strategies towards meeting future particulate matter emission requirements in homogeneous gasoline direct injection engines*. SAE International Journal of Engines. **2011**;4(1):1455-68.
[43] Schreiber D., Forss A.-M., Mohr M., Dimopoulos P. *Particle characterisation of modern CNG, gasoline and diesel passenger cars*. SAE Technical Paper; **2007**. Report No.: 0148-7191.
[44] Zhao H. Advanced direct injection combustion engine technologies and development: diesel engines: Elsevier; 2009.
[45] Peckham M.S., Finch A., Campbell B., Price P., Davies M.T. *Study of particle number emissions from a turbocharged gasoline direct injection (GDI) engine including data from a fast-response particle size spectrometer*. SAE Technical Paper; **2011**. Report No.: 0148-7191.
[46] Williams B., Ewart P., Wang X., Stone R., Ma H., Walmsley H., Cracknell R., Stevens R., Richardson D., Fu H. *Quantitative planar laser-induced fluorescence imaging of multi-component fuel/air mixing in a firing gasoline-direct-injection engine: effects of residual exhaust gas on quantitative PLIF*. Combust Flame. **2010**;157(10):1866-78.
[47] Maricq M.M., Podsiadlik D.H., Brehob D.D., Haghgooie M. *Particulate emissions from a direct-injection spark-ignition (DISI) engine*. SAE Technical Paper; **1999**. Report No.: 0148-7191.
[48] Bogarra M., Herreros J.M., Hergueta C., Tsolakis A., York A.P., Millington P.J. *Influence of three-way catalyst on gaseous and particulate matter emissions during gasoline direct injection engine cold-start*. Johnson Matthey Technology Review. **2017**;61(4):329-41.
[49] Ortmann R., Arndt S., Raimann J., Grzeszik R., Würfel G. *Methods and analysis of fuel injection, mixture preparation and charge stratification in different direct injected SI engines*. SAE Technical Paper; **2001**. Report No.: 0148-7191.
[50] Costa M., Sorge U., Allocca L. *Numerical study of the mixture formation process in a four-stroke GDI engine for two-wheel applications*. Simulation Modelling Practice and Theory. **2011**;19(4):1212-26.
[51] Fang T., Chia-Fon F.L. *Low sooting combustion of narrow-angle wall-guided sprays in an HSDI diesel engine with retarded injection timings*. Fuel. **2011**;90(4):1449-56.
[52] Choi K., Kim J., Ko A., Myung C.-L., Park S., Lee Y., Park J., Han S.K. *Evaluation of time-resolved nano-particle and THC emissions of wall-guided GDI engine*. SAE Technical Paper; **2011**. Report No.: 0148-7191.
[53] Lucchini T., D'errico G., Onorati A., Bonandrini G., Venturoli L., Di Gioia R. *Development and application of a computational fluid dynamics methodology to predict fuel–air mixing and sources of soot formation in gasoline direct injection engines*. Int J Engine Res. **2014**;15(5):581-96.
[54] Velji A., Yeom K., Wagner U., Spicher U., Roßbach M., Suntz R., Bockhorn H. *Investigations of the formation and oxidation of soot inside a direct injection spark ignition engine using advanced laser-techniques*. SAE Technical Paper; **2010**. Report No.: 0148-7191.
[55] Henein N.A., Lai M.-C., Singh I., Wang D., Liu L. *Emissions Trade-Off and Combustion Characteristics of a High-Speed Direct Injection Diesel Engine*. SAE Transactions. **2001**:209-24.

[56] Richter H., Howard J.B. *Formation of polycyclic aromatic hydrocarbons and their growth to soot - a review of chemical reaction pathways*. Prog Energ Combust. **2000**;26(4-6):565-608.
[57] Omidvarborna H., Kumar A., Kim D.S. *Recent studies on soot modeling for diesel combustion*. Renew Sust Energ Rev. **2015**;48:635-47.
[58] Kong S.-C., Sun Y., Rietz R.D. *Modeling diesel spray flame liftoff, sooting tendency, and NOx emissions using detailed chemistry with phenomenological soot model*. Journal of Engineering for Gas Turbines and Power. **2007**;129(1):245-51.
[59] Xi J., Zhong B.J. *Soot in diesel combustion systems*. Chemical Engineering & Technology: Industrial Chemistry-Plant Equipment-Process Engineering-Biotechnology. **2006**;29(6):665-73.
[60] Vishwanathan G., Reitz R.D. *Modeling soot formation using reduced polycyclic aromatic hydrocarbon chemistry in n-heptane lifted flames with application to low temperature combustion*. Journal of engineering for gas turbines and power. **2009**;131(3):032801.
[61] Frenklach M., Yuan T., Ramachandra M. *Soot formation in binary hydrocarbon mixtures*. Energ Fuel. **1988**;2(4):462-80.
[62] Haynes B.S., Wagner H.G. *Soot formation*. Prog Energ Combust. **1981**;7(4):229-73.
[63] Totton T.S., Chakrabarti D., Misquitta A.J., Sander M., Wales D.J., Kraft M. *Modelling the internal structure of nascent soot particles*. Combust Flame. **2010**;157(5):909-14.
[64] Johansson K., Head-Gordon M., Schrader P., Wilson K., Michelsen H. *Resonance-stabilized hydrocarbon-radical chain reactions may explain soot inception and growth*. Science. **2018**;361(6406):997-1000.
[65] Frenklach M. *Reaction mechanism of soot formation in flames*. Phys Chem Chem Phys. **2002**;4(11):2028-37.
[66] Tree D.R., Svensson K.I. *Soot processes in compression ignition engines*. Prog Energ Combust. **2007**;33(3):272-309.
[67] Morgan N., Kraft M., Balthasar M., Wong D., Frenklach M., Mitchell P. *Numerical simulations of soot aggregation in premixed laminar flames*. P Combust Inst. **2007**;31(1):693-700.
[68] Clague A.D.H., Donnet J., Wang T.K., Peng J.C.M. *A comparison of diesel engine soot with carbon black*. Carbon. **1999**;37(10):1553-65.
[69] Stanmore B.R., Brilhac J.-F., Gilot P. *The oxidation of soot: a review of experiments, mechanisms and models*. Carbon. **2001**;39(15):2247-68.
[70] La Rocca A., Di Liberto G., Shayler P.J., Fay M.W. *The nanostructure of soot-in-oil particles and agglomerates from an automotive diesel engine*. Tribol Int. **2013**;61:80-7.
[71] Lapuerta M., Martos F.J., Herreros J.M. *Effect of engine operating conditions on the size of primary particles composing diesel soot agglomerates*. J Aerosol Sci. **2007**;38(4):455-66.
[72] Virtanen A.K.K., Ristimaki J.M., Vaaraslahti K.M., Keskinen J. *Effect of engine load on diesel soot particles*. Environ Sci Technol. **2004**;38(9):2551-6.
[73] Koylu U.O., Faeth G.M., Farias T.L., Carvalho M.G. *Fractal and Projected Structure Properties of Soot Aggregates*. Combust Flame. **1995**;100(4):621-33.
[74] Rogak S.N., Flagan R.C. *Characterization of the Structure of Agglomerate Particles*. Part Part Syst Char. **1992**;9(1):19-27.
[75] Neer A., Koylu U.O. *Effect of operating conditions on the size, morphology, and concentration of submicrometer particulates emitted from a diesel engine*. Combust Flame. **2006**;146(1-2):142-54.
[76] Ishiguro T., Takatori Y., Akihama K. *Microstructure of diesel soot particles probed by electron microscopy: First observation of inner core and outer shell*. Combust Flame. **1997**;108(1-2):231-4.
[77] Müller J.-O., Su D.S., Wild U., Schlögl R. *Bulk and surface structural investigations of diesel engine soot and carbon black*. Phys Chem Chem Phys. **2007**;9(30):4018-25.
[78] Devlin C.C., Passut C., Campbell R., Jao T.-C. *Biodiesel fuel effect on diesel engine lubrication*. SAE Technical Paper; **2008**. Report No.: 0148-7191.
[79] Su D.S., Jentoft R.E., Müller J.-O., Rothe D., Jacob E., Simpson C., Tomović Ž., Müllen K., Messerer A., Pöschl U. *Microstructure and oxidation behaviour of Euro IV diesel engine soot: a comparative study with synthetic model soot substances*. Catal Today. **2004**;90(1):127-32.
[80] Lee K.O., Cole R., Sekar R., Choi M.Y., Kang J.S., Bae C.S., Shin H.D. *Morphological investigation of the microstructure, dimensions, and fractal geometry of diesel particulates*. P Combust Inst. **2002**;29(1):647-53.
[81] Lu T., Cheung C., Huang Z. *Effects of engine operating conditions on the size and nanostructure of diesel particles*. J Aerosol Sci. **2012**;47:27-38.
[82] Maricq M.M. *Soot formation in ethanol/gasoline fuel blend diffusion flames*. Combust Flame. **2012**;159(1):170-80.
[83] Wentzel M., Gorzawski H., Naumann K.-H., Saathoff H., Weinbruch S. *Transmission electron microscopical and aerosol dynamical characterization of soot aerosols*. J Aerosol Sci. **2003**;34(10):1347-70.
[84] Park K., Kittelson D.B., Mcmurry P.H. *Structural properties of diesel exhaust particles measured by transmission electron microscopy (TEM): Relationships to particle mass and mobility*. Aerosol Sci Tech. **2004**;38(9):881-9.
[85] Müller J.-O., Su D.S., Jentoft R.E., Wild U., Schlögl R. *Diesel engine exhaust emission: oxidative behavior and microstructure of black smoke soot particulate*. Environ Sci Technol. **2006**;40(4):1231-6.

[86] Liati A., Schreiber D., Eggenschwiler P.D., Dasilva Y.a.R., Spiteri A.C. *Electron microscopic characterization of soot particulate matter emitted by modern direct injection gasoline engines*. Combust Flame. **2016**;166:307-15.
[87] Seong H., Lee K., Choi S. *Effects of engine operating parameters on morphology of particulates from a gasoline direct injection (GDI) engine*. SAE Technical Paper; **2013**. Report No.: 0148-7191.
[88] Shuff P.J., Clarke L.J. *Imaging of Lubricating Oil Insolubles by Electron-Microscopy*. Tribol Int. **1991**;24(6):381-7.
[89] Heywood J.B. Pollutant Formation and Control. In: Heywood JB, editor. Internal Combustion Engine Fundamentals. Singapore: McGraw-Hill; 1988. p. 626-34.
[90] Salvat O., Marez P., Belot G. *Passenger car serial application of a particulate filter system on a common rail direct injection diesel engine*. SAE transactions. **2000**:227-39.
[91] Lanzerath P., Wunsch R., Schön C., editors. The first series-production particulate filter for Mercedes-Benz gasoline engines. 17 Internationales Stuttgarter Symposium; 2017: Springer.
[92] Yang J., Stewart M., Maupin G., Herling D., Zelenyuk A. *Single wall diesel particulate filter (DPF) filtration efficiency studies using laboratory generated particles*. Chemical Engineering Science. **2009**;64(8):1625-34.
[93] Millo F., Vezza D., Vlachos T., Fino D., Russo N., De Filippo A. *Particle number and size distribution from a small displacement automotive diesel engine during DPF regeneration*. SAE International Journal of Fuels and Lubricants. **2010**;3(2):404-13.
[94] Majewski W.A. Gasoline Particulate Filters2019.
[95] Niranjan R., Thakur A.K. *The toxicological mechanisms of environmental soot (black carbon) and carbon black: focus on oxidative stress and inflammatory pathways*. Frontiers in immunology. **2017**;8:763.
[96] Von Klot S., Cyrys J., Hoek G., Kühnel B., Pitz M., Kuhn U., Kuch B., Meisinger C., Hörmann A., Wichmann H.-E. *Estimated personal soot exposure is associated with acute myocardial infarction onset in a case-crossover study*. Progress in cardiovascular diseases. **2011**;53(5):361-8.
[97] Heidari Nejad S., Takechi R., Mullins B.J., Giles C., Larcombe A.N., Bertolatti D., Rumchev K., Dhaliwal S., Mamo J. *The effect of diesel exhaust exposure on blood–brain barrier integrity and function in a murine model*. Journal of Applied Toxicology. **2015**;35(1):41-7.
[98] Barath S., Mills N.L., Lundbäck M., Törnqvist H., Lucking A.J., Langrish J.P., Söderberg S., Boman C., Westerholm R., Löndahl J. *Impaired vascular function after exposure to diesel exhaust generated at urban transient running conditions*. Particle and fibre toxicology. **2010**;7(1):19.
[99] Broday D.M., Rosenzweig R. *Deposition of fractal-like soot aggregates in the human respiratory tract*. J Aerosol Sci. **2011**;42(6):372-86.
[100] LöNdahl J., Massling A., Swietlicki E., BräUner E.V., Ketzel M., Pagels J., Loft S. *Experimentally determined human respiratory tract deposition of airborne particles at a busy street*. Environ Sci Technol. **2009**;43(13):4659-64.
[101] Yon J., Lemaire R., Therssen E., Desgroux P., Coppalle A., Ren K.F. *Examination of wavelength dependent soot optical properties of diesel and diesel/rapeseed methyl ester mixture by extinction spectra analysis and LII measurements*. Appl Phys B-Lasers O. **2011**;104(2):253-71.
[102] Khalizov A.F., Xue H.X., Wang L., Zheng J., Zhang R.Y. *Enhanced Light Absorption and Scattering by Carbon Soot Aerosol Internally Mixed with Sulfuric Acid*. J Phys Chem A. **2009**;113(6):1066-74.
[103] Mari X., Lefevre J., Torreton J.P., Bettarel Y., Pringault O., Rochelle-Newall E., Marchesiello P., Menkes C., Rodier M., Migon C., Motegi C., Weinbauer M.G., Legendre L. *Effects of soot deposition on particle dynamics and microbial processes in marine surface waters*. Global Biogeochem Cy. **2014**;28(7):662-78.
[104] Persson N., Gustafsson Ö., Bucheli T., Ishaq R., Naes K., Broman D. *Soot-carbon influenced distribution of PCDD/Fs in the marine environment of the Grenlandsfjords, Norway*. Environ Sci Technol. **2002**;36(23):4968-74.
[105] Green D.A., Lewis R. *The effects of soot-contaminated engine oil on wear and friction: a review*. P I Mech Eng D-J Aut. **2008**;222(D9):1669-89.
[106] Kittelson D.B., Ambs J.L., Hadjkacem H. *Particulate emissions from diesel engines: influence of in-cylinder surface*. SAE Technical Paper; **1990**. Report No.: 0148-7191.
[107] Suhre B.R., Foster D.E. *In-cylinder soot deposition rates due to thermophoresis in a direct injection diesel engine*. SAE Technical Paper; **1992**. Report No.: 0148-7191.
[108] Pfau S., La Rocca A., Haffner-Staton E., Rance G., Fay M.W., Brough R., Malizia S. *Comparative nanostructure analysis of gasoline turbocharged direct injection and diesel soot-in-oil with carbon black*. Carbon. **2018**;139:342-52.
[109] Liu C.M., Nemoto S., Ogano S. *Effect of soot properties in diesel engine oils on frictional characteristics*. Tribol T. **2003**;46(1):12-8.
[110] Green D.A., Lewis R. *Effect of soot on oil properties and wear of engine components*. J Phys D Appl Phys. **2007**;40(18):5488-501.
[111] Antusch S., Dienwiebel M., Nold E., Albers P., Spicher U., Scherge M. *On the tribochemical action of engine soot*. Wear. **2010**;269(1):1-12.
[112] Hu E.Z., Hu X.G., Liu T.X., Fang L., Dearn K.D., Xu H.M. *The role of soot particles in the tribological behavior of engine lubricating oils*. Wear. **2013**;304(1-2):152-61.
[113] Guo M.F., Cai Z.B., Zhang Z.C., Zhu M.H. *Characterization and lubrication performance of diesel soot nanoparticles as oil lubricant additives*. Rsc Adv. **2015**;5(123):101965-74.

[114] Salehi F.M., Khaemba D.N., Morina A., Neville A. *Corrosive-Abrasive Wear Induced by Soot in Boundary Lubrication Regime*. Tribol Lett. **2016**;63(2).
[115] Bardasz E.A., Carrick V.A., Ebeling V.L., George H.F., Graf M.M., Kornbrekke R.E., Pocinki S.B. *Understanding soot mediated oil thickening through designed experimentation-Part 2: GM 6.5 L*. SAE Technical Paper; **1996**. Report No.: 0148-7191.
[116] Rounds F.G. *Carbon: cause of diesel engine wear?* SAE Transactions. **1977**:2870-81.
[117] Rounds F.G. *Soots from used diesel engine oils-their effects on wear as measured in 4-ball wear tests*. SAE Technical Paper; **1981**. Report No.: 0148-7191.
[118] Bardasz E.A., Carrick V.A., George H.F., Graf M.M., Kornbrekke R.E., Pocinki S.B. *Understanding soot mediated oil thickening through designed experimentation part 4: Mack T-8 test*. SAE Technical Paper; **1997**. Report No.: 0148-7191.
[119] Gautam M., Durbha M., Chitoor K., Jaraiedi M., Mariwalla N., Ripple D. *Contribution of soot contaminated oils to wear*. SAE Technical Paper; **1998**. Report No.: 0148-7191.
[120] Sato H., Tokuoka N., Yamamoto H., Sasaki M. *Study on wear mechanism by soot contaminated in engine oil (first report: relation between characteristics of used oil and wear)*. SAE Technical Paper; **1999**. Report No.: 0148-7191.
[121] Green D.A., Lewis R., Dwyer-Joyce R.S. *Wear effects and mechanisms of soot-contaminated automotive lubricants*. P I Mech Eng J-J Eng. **2006**;220(J3):159-69.
[122] Peng J.-F., Shen M.-X., Cai Z.-B. *Nano Diesel Soot Particles Reduce Wear and Friction Performance Using an Oil Additive on a Laser Textured Surface*. Coatings. **2018**;8(3):89.
[123] George S., Balla S., Gautam V., Gautam M. *Effect of diesel soot on lubricant oil viscosity*. Tribol Int. **2007**;40(5):809-18.
[124] Soejima M., Ejima Y., Uemori K., Kawasaki M. *Studies on friction and wear characteristics of cam and follower: influences of soot contamination in engine oil*. JSAE review. **2002**;23(1):113-9.
[125] Aldajah S., Ajayi O.O., Fenske G.R., Goldblatt I.L. *Effect of exhaust gas recirculation (EGR) contamination of diesel engine oil on wear*. Wear. **2007**;263:93-8.
[126] Salehi F.M., Morina A., Neville A. *The effect of soot and diesel contamination on wear and friction of engine oil pump*. Tribol Int. **2017**;115:285-96.
[127] Chinas-Castillo F., Spikes H.A. *The behavior of diluted sooted oils in lubricated contacts*. Tribol Lett. **2004**;16(4):317-22.
[128] Asango A., La Rocca A., Shayler P. *Investigating the Effect of Carbon Nanoparticles on the Viscosity of Lubricant Oil from Light Duty Automotive Diesel Engines*. SAE Technical Paper; **2014**. Report No.: 0148-7191.
[129] Zeidan M., Jia X., Williams R.A., Wedlock D.J. *Simulation of aggregation with applications to soot laden lubricating fluids*. Particle & Particle Systems Characterization: Measurement and Description of Particle Properties and Behavior in Powders and Other Disperse Systems. **2004**;21(6):473-82.
[130] Covitch M., Humphrey B., Ripple D. *Oil thickening in the Mack T-7 engine test—fuel effects and the influence of lubricant additives on soot aggregation*. SAE Technical Paper; **1985**. Report No.: 0148-7191.
[131] Einstein A. *Eine neue bestimmung der moleküldimensionen*. Annalen der Physik. **1906**;324(2):289-306.
[132] Brinkman H. *A calculation of the viscous force exerted by a flowing fluid on a dense swarm of particles*. Flow, Turbulence and Combustion. **1949**;1(1):27.
[133] Esfe M.H., Afrand M., Gharehkhani S., Rostamian H., Toghraie D., Dahari M. *An experimental study on viscosity of alumina-engine oil: effects of temperature and nanoparticles concentration*. International Communications in Heat and Mass Transfer. **2016**;76:202-8.
[134] An Z., Zhang Y., Li Q., Wang H., Guo Z., Zhu J. *Effect of particle shape on the apparent viscosity of liquid–solid suspensions*. Powder Technol. **2018**;328:199-206.
[135] Hamilton R.L., Crosser O. *Thermal conductivity of heterogeneous two-component systems*. Industrial & Engineering chemistry fundamentals. **1962**;1(3):187-91.
[136] Ghozatloo A., Azimi Maleki S., Shariaty-Niassar M., Morad Rashidi A. *Investigation of nanoparticles morphology on viscosity of nanofluids and new correlation for prediction*. Journal of Nanostructures. **2015**;5(2):161-8.
[137] Wang B.-X., Zhou L.-P., Peng X.-F. *A fractal model for predicting the effective thermal conductivity of liquid with suspension of nanoparticles*. Int J Heat Mass Tran. **2003**;46(14):2665-72.
[138] Van Gulijk C., Marijnissen J., Makkee M., Moulijn J., Schmidt-Ott A. *Measuring diesel soot with a scanning mobility particle sizer and an electrical low-pressure impactor: performance assessment with a model for fractal-like agglomerates*. J Aerosol Sci. **2004**;35(5):633-55.
[139] Symonds J.P., Reavell K.S.J., Olfert J.S., Campbell B.W., Swift S.J. *Diesel soot mass calculation in real-time with a differential mobility spectrometer*. J Aerosol Sci. **2007**;38(1):52-68.
[140] Maricq M. *Size and charge of soot particles in rich premixed ethylene flames*. Combust Flame. **2004**;137(3):340-50.
[141] La Rocca A., Di Liberto G., Shayler P.J., Parmenter C.D.J., Fay M.W. *Application of nanoparticle tracking analysis platform for the measurement of soot-in-oil agglomerates from automotive engines*. Tribol Int. **2014**;70:142-7.

[142] La Rocca A., Di Liberto G., Shayler P., Parmenter C., Fay M. *A novel diagnostics tool for measuring soot agglomerates size distribution in used automotive lubricant oils*. SAE International Journal of Fuels and Lubricants. **2014**;7(2014-01-1479):301-6.
[143] Growney D.J., Mykhaylyk O.O., Middlemiss L., Fielding L.A., Derry M.J., Aragrag N., Lamb G.D., Armes S.P. *Is Carbon Black a Suitable Model Colloidal Substrate for Diesel Soot?* Langmuir. **2015**;31(38):10358-69.
[144] Wei J., Cai M., Zhou F., Liu W. *Candle soot as particular lubricant additives*. Tribol Lett. **2014**;53(3):521-31.
[145] Knoll M., Ruska E. *Das elektronenmikroskop*. Zeitschrift für physik. **1932**;78(5-6):318-39.
[146] Smith W., Wilkes G. *Thermal conductivity of carbon blacks*. Industrial & Engineering Chemistry. **1944**;36(12):1111-2.
[147] Apicella B., Ciajolo A., Tregrossi A., Abrahamson J., Vander Wal R., Russo C. *HRTEM and EELS investigations of flame-formed soot nanostructure*. Fuel. **2018**;225:218-24.
[148] Barone T.L., Storey J.M.E., Youngquist A.D., Szybist J.P. *An analysis of direct-injection spark-ignition (DISI) soot morphology*. Atmos Environ. **2012**;49:268-74.
[149] Bogarra M., Herreros J.M., Tsolakis A., York A., Millington P., Martos F. *Impact of exhaust gas fuel reforming and exhaust gas recirculation on particulate matter morphology in Gasoline Direct Injection Engine*. J Aerosol Sci. **2017**;103:1-14.
[150] Bescond A., Yon J., Ouf F., Ferry D., Delhaye D., Gaffié D., Coppalle A., Rozé C. *Automated determination of aggregate primary particle size distribution by TEM image analysis: application to soot*. Aerosol Sci Tech. **2014**;48(8):831-41.
[151] Ntziachristos L., Saukko E., Lehtoranta K., Rönkkö T., Timonen H., Simonen P., Karjalainen P., Keskinen J. *Particle emissions characterization from a medium-speed marine diesel engine with two fuels at different sampling conditions*. Fuel. **2016**;186:456-65.
[152] Dastanpour R., Rogak S.N. *Observations of a Correlation Between Primary Particle and Aggregate Size for Soot Particles*. Aerosol Sci Tech. **2014**;48(10):1043-9.
[153] Koylu U.O. *Quantitative analysis of in situ optical diagnostics for inferring particle/aggregate parameters in flames: Implications for soot surface growth and total emissivity*. Combust Flame. **1997**;109(3):488-500.
[154] Brasil A., Farias T.L., Carvalho M. *A recipe for image characterization of fractal-like aggregates*. J Aerosol Sci. **1999**;30(10):1379-89.
[155] Bau S., Witschger O., Gensdarmes F., Rastoix O., Thomas D. *A TEM-based method as an alternative to the BET method for measuring off-line the specific surface area of nanoaerosols*. Powder Technol. **2010**;200(3):190-201.
[156] Lottin D., Ferry D., Gay J.-M., Delhaye D., Ouf F.-X. *On methods determining the fractal dimension of combustion aerosols and particleclusters*. J Aerosol Sci. **2013**;58:41-9.
[157] Lapuerta M., Ballesteros R., Martos F.J. *A method to determine the fractal dimension of diesel soot agglomerates*. J Colloid Interf Sci. **2006**;303(1):149-58.
[158] Cai J., Lu N., Sorensen C. *Comparison of size and morphology of soot aggregates as determined by light scattering and electron microscope analysis*. Langmuir. **1993**;9(11):2861-7.
[159] Schenk M., Lieb S., Vieker H., Beyer A., Golzhauser A., Wang H., Kohse-Hoinghaus K. *Morphology of nascent soot in ethylene flames*. P Combust Inst. **2015**;35:1879-86.
[160] Dastanpour R., Boone J.M., Rogak S.N. *Automated primary particle sizing of nanoparticle aggregates by TEM image analysis*. Powder Technol. **2016**;295:218-24.
[161] Vander Wal R.L., Tomasek A.J. *Soot oxidation: dependence upon initial nanostructure*. Combust Flame. **2003**;134(1-2):1-9.
[162] Fernandez-Alos V., Watson J.K., Vander Wal R., Mathews J.P. *Soot and char molecular representations generated directly from HRTEM lattice fringe images using Fringe3D*. Combust Flame. **2011**;158(9):1807-13.
[163] Yehliu K., Vander Wal R.L., Armas O., Boehman A.L. *Impact of fuel formulation on the nanostructure and reactivity of diesel soot*. Combust Flame. **2012**;159(12):3597-606.
[164] De Rosier D., Klug A. *Reconstruction of three dimensional structures from electron micrographs*. Nature. **1968**;217(5124):130.
[165] Frank J. Electron tomography: methods for three-dimensional visualization of structures in the cell: Springer Science & Business Media; 2008.
[166] Fernandez J.J. *Computational methods for electron tomography*. Micron. **2012**;43(10):1010-30.
[167] Kouis P., Yiallouros P.K., Middleton N., Evans J.S., Kyriacou K., Papatheodorou S.I. *Prevalence of primary ciliary dyskinesia in consecutive referrals of suspect cases and the transmission electron microscopy detection rate: a systematic review and meta-analysis*. Pediatric Research. **2017**;81(3):398.
[168] Gillis R.B., Adams G.G., Alzahrani Q., Harding S.E. *A novel analytical ultracentrifugation based approach to the low resolution structure of gum arabic*. Biopolymers. **2016**;105(9):618-25.
[169] Thompson R.F., Walker M., Siebert C.A., Muench S.P., Ranson N.A. *An introduction to sample preparation and imaging by cryo-electron microscopy for structural biology*. Methods. **2016**;100:3-15.
[170] Liu X.H., Huang J.Y. *In situ TEM electrochemistry of anode materials in lithium ion batteries*. Energy & Environmental Science. **2011**;4(10):3844-60.
[171] Chuvilin A., Kaiser U., Bichoutskaia E., Besley N.A., Khlobystov A.N. *Direct transformation of graphene to fullerene*. Nature chemistry. **2010**;2(6):450.

[172] Mcdowell M.T., Lee S.W., Harris J.T., Korgel B.A., Wang C., Nix W.D., Cui Y. *In situ TEM of two-phase lithiation of amorphous silicon nanospheres*. Nano letters. **2013**;13(2):758-64.
[173] Mastronarde D.N. *Automated electron microscope tomography using robust prediction of specimen movements*. J Struct Biol. **2005**;152(1):36-51.
[174] Williams D.B., Carter C.B. Electron Sources. Transmission Electron Microscopy: Diffraction, Imaging, and Spectrometry. New York: Springer; 2016. p. 74.
[175] Carter C.B., Williams D.B. Transmission electron microscopy: Diffraction, imaging, and spectrometry: Springer; 2016.
[176] Kremer J.R., Mastronarde D.N., Mcintosh J.R. *Computer visualization of three-dimensional image data using IMOD*. J Struct Biol. **1996**;116(1):71-6.
[177] Messaoudii C., Boudier T., Sorzano C.O.S., Marco S. *TomoJ: tomography software for three-dimensional reconstruction in transmission electron microscopy*. Bmc Bioinformatics. **2007**;8(1):288.
[178] Agulleiro J.-I., Fernandez J.-J. *Tomo3D 2.0–exploitation of advanced vector extensions (AVX) for 3D reconstruction*. J Struct Biol. **2015**;189(2):147-52.
[179] Schindelin J., Rueden C.T., Hiner M.C., Eliceiri K.W. *The ImageJ ecosystem: An open platform for biomedical image analysis*. Mol Reprod Dev. **2015**;82(7-8):518-29.
[180] Schindelin J., Arganda-Carreras I., Frise E., Kaynig V., Longair M., Pietzsch T., Preibisch S., Rueden C., Saalfeld S., Schmid B., Tinevez J.Y., White D.J., Hartenstein V., Eliceiri K., Tomancak P., Cardona A. *Fiji: an open-source platform for biological-image analysis*. Nat Methods. **2012**;9(7):676-82.
[181] Westenberger P., editor AVIZO-3D visualization framework. Geoinformatics Conference; 2008.
[182] Stalling D., Westerhoff M., Hege H.-C. *Amira: A highly interactive system for visual data analysis*. The visualization handbook. **2005**;38:749-67.
[183] Fernandez J.-J. *Computational methods for materials characterization by electron tomography*. Current Opinion in Solid State and Materials Science. **2013**;17(3):93-106.
[184] Midgley P., Weyland M. *3D electron microscopy in the physical sciences: the development of Z-contrast and EFTEM tomography*. Ultramicroscopy. **2003**;96(3-4):413-31.
[185] Frank J. Introduction: Principles of Electron Tomography. In: Frank J, editor. Electron Tomography Methods for Three-Dimensional Visualization of Structures in the Cell. New York: Springer; 2008. p. 1-16.
[186] Cheng A., Henderson R., Mastronarde D., Ludtke S.J., Schoenmakers R.H., Short J., Marabini R., Dallakyan S., Agard D., Winn M. *MRC2014: Extensions to the MRC format header for electron cryo-microscopy and tomography*. J Struct Biol. **2015**;192(2):146-50.
[187] Brandt S.S. Markerless Alignment in Electron Tomography. In: Frank J, editor. Electron Tomography Methods for Three-Dimensional Visualization of Structures in the Cell. New York: Springer; 2008. p. 187-216.
[188] Van Aarle W., Palenstijn W.J., De Beenhouwer J., Altantzis T., Bals S., Batenburg K.J., Sijbers J. *The ASTRA Toolbox: A platform for advanced algorithm development in electron tomography*. Ultramicroscopy. **2015**;157:35-47.
[189] Van Aarle W., Palenstijn W.J., De Beenhouwer J., Altantzis T., Bals S., Batenburg K.J., Sijbers J. The ASTRA Toolbox 2019 [Available from: https://www.astra-toolbox.com/docs/index.html

https://www.youtube.com/channel/UCcnUlWuFeS9miMR_o8-6v3w/videos.
[190] Gordon R., Bender R., Herman G.T. *Algebraic reconstruction techniques (ART) for three-dimensional electron microscopy and X-ray photography*. Journal of theoretical Biology. **1970**;29(3):471-81.
[191] Batenburg K.J., Sijbers J. *DART: A Practical Reconstruction Algorithm for Discrete Tomography*. Ieee T Image Process. **2011**;20(9):2542-53.
[192] Batenburg K.J., Bals S., Sijbers J., Kubel C., Midgley P.A., Hernandez J.C., Kaiser U., Encina E.R., Coronado E.A., Van Tendeloo G. *3D imaging of nanomaterials by discrete tomography*. Ultramicroscopy. **2009**;109(6):730-40.
[193] Goris B., Roelandts T., Batenburg K.J., Mezerji H.H., Bals S. *Advanced reconstruction algorithms for electron tomography: From comparison to combination*. Ultramicroscopy. **2013**;127:40-7.
[194] Chen D., Goris B., Bleichrodt F., Mezerji H.H., Bals S., Batenburg K.J., De With G., Friedrich H. *The properties of SIRT, TVM, and DART for 3D imaging of tubular domains in nanocomposite thin-films and sections*. Ultramicroscopy. **2014**;147:137-48.
[195] Friedrich H., Guo S., De Jongh P.E., Pan X., Bao X., De Jong K.P. *A quantitative electron tomography study of ruthenium particles on the interior and exterior surfaces of carbon nanotubes*. ChemSusChem. **2011**;4(7):957-63.
[196] Shimizu A., Kimoto T., Kobatake H., Nawano S., Shinozaki K. *Automated pancreas segmentation from three-dimensional contrast-enhanced computed tomography*. International journal of computer assisted radiology and surgery. **2010**;5(1):85.
[197] Iturrondobeitia M., Okariz A., Fernandez-Martinez R., Jimbert P., Guraya T., Ibarretxe J., editors. 3D TEM reconstruction and segmentation process of laminar bio-nanocomposites. AIP Conference proceedings; 2015: AIP Publishing.
[198] Fay M.W., La Rocca A., Shayler P.J. *TEM and HRTEM of Soot-in-oil particles and agglomerates from internal combustion engines*. J Phys Conf Ser. **2014**;522.

[199] Köylü Ü.Ö., Mcenally C.S., Rosner D.E., Pfefferle L.D. *Simultaneous measurements of soot volume fraction and particle size/microstructure in flames using a thermophoretic sampling technique*. Combust Flame. **1997**;110(4):494-507.
[200] Wozniak M., Onofri F., Barbosa S., Yon J., Mroczka J. *Comparison of methods to derive morphological parameters of multi-fractal samples of particle aggregates from TEM images*. J Aerosol Sci. **2012**;47:12-26.
[201] Doube M., Klosowski M.M., Arganda-Carreras I., Cordelieres F.P., Dougherty R.P., Jackson J.S., Schmid B., Hutchinson J.R., Shefelbine S.J. *BoneJ Free and extensible bone image analysis in ImageJ*. Bone. **2010**;47(6):1076-9.
[202] Wadell H. *Sphericity and roundness of rock particles*. The Journal of Geology. **1933**;41(3):310-31.
[203] Gwaze P., Schmid O., Annegarn H.J., Andreae M.O., Huth J., Helas G. *Comparison of three methods of fractal analysis applied to soot aggregates from wood combustion*. J Aerosol Sci. **2006**;37(7):820-38.
[204] Yamaguchi T., Kondo K., Nishigai H., Takano S., Aizawa T. *Direct sampling, TEM analysis and optical measurement of soot particles at different axial locations in a transient spray flame*. SAE International Journal of Fuels and Lubricants. **2012**;5(1):316-28.
[205] Morán J., Cuevas J., Liu F., Yon J., Fuentes A. *Influence of primary particle polydispersity and overlapping on soot morphological parameters derived from numerical TEM images*. Powder Technol. **2018**;330:67-79.
[206] Farias T.L., Carvalho M.G., Koylu U.O., Faeth G.M. *Computational Evaluation of Approximate Rayleigh-Debye-Gans/Fractal-Aggregate Theory for the Absorption and Scattering Properties of Soot*. J Heat Trans-T Asme. **1995**;117(1):152-9.
[207] Wang C., Chan Q.N., Zhang R., Kook S., Hawkes E.R., Yeoh G.H., Medwell P.R. *Automated determination of size and morphology information from soot transmission electron microscope (TEM)-generated images*. J Nanopart Res. **2016**;18(5):127.
[208] Grishin I., Thomson K., Migliorini F., Sloan J.J. *Application of the Hough transform for the automatic determination of soot aggregate morphology*. Appl Optics. **2012**;51(5):610-20.
[209] Toth P., Farrer J., Palotas A., Lighty J., Eddings E. *Automated analysis of heterogeneous carbon nanostructures by high-resolution electron microscopy and on-line image processing*. Ultramicroscopy. **2013**;129:53-62.
[210] Freedman D., Diaconis P. *On the histogram as a density estimator: L 2 theory*. Probability theory and related fields. **1981**;57(4):453-76.
[211] Pettersen E.F., Goddard T.D., Huang C.C., Couch G.S., Greenblatt D.M., Meng E.C., Ferrin T.E. *UCSF Chimera – A Visualization System for Exploratory Research and Analysis*. J Comput Chem. **2004**;25.
[212] Foroutan-Pour K., Dutilleul P., Smith D.L. *Advances in the implementation of the box-counting method of fractal dimension estimation*. Applied mathematics and computation. **1999**;105(2-3):195-210.
[213] Tence M., Chevalier J., Jullien R. *On the measurement of the fractal dimension of aggregated particles by electron microscopy: experimental method, corrections and comparison with numerical models*. Journal de Physique. **1986**;47(11):1989-98.
[214] Sharma V., Uy D., Gangopadhyay A., O'neill A., Paxton W.A., Sammut A., Ford M.A., Aswath P.B. *Structure and chemistry of crankcase and exhaust soot extracted from diesel engines*. Carbon. **2016**;103:327-38.
[215] Patel M., Ricardo C.L.A., Scardi P., Aswath P.B. *Morphology, structure and chemistry of extracted diesel soot-Part I: Transmission electron microscopy, Raman spectroscopy, X-ray photoelectron spectroscopy and synchrotron X-ray diffraction study*. Tribol Int. **2012**;52:29-39.
[216] Patel M., Aswath P.B. *Structure and chemistry of crankcase and cylinder soot and tribofilms on piston rings from a Mack T-12 dynamometer engine test*. Tribol Int. **2014**;77:111-21.
[217] Pfau S.A., La Rocca A., Haffner-Staton E., Rance G.A., Fay M.W., Mcghee M. *Soot in the Lubricating Oil: An Overlooked Concern for the Gasoline Direct Injection Engine?* : SAE Technical Paper; **2019**. Report No.: 0148-7191.
[218] Cabié M., Gailhanou M., Ferry D., editors. Electron tomography: influence of defocus on the determination of reconstructed soot aggregates' surface and volume. European Microscopy Congress 2016: Proceedings; 2016: Wiley Online Library.
[219] Koelmans A.A., Jonker M.T., Cornelissen G., Bucheli T.D., Van Noort P.C., Gustafsson Ö. *Black carbon: the reverse of its dark side*. Chemosphere. **2006**;63(3):365-77.
[220] Crowther R.A., Derosier D., Klug A. *The reconstruction of a three-dimensional structure from projections and its application to electron microscopy*. Proceedings of the Royal Society of London A Mathematical and Physical Sciences. **1970**;317(1530):319-40.
[221] Fernandez J., Agulleiro J., Bilbao-Castro J., Martínez A., García I., Chichón F., Martín-Benito J., Carrascosa J. *Image processing in electron tomography*. Microscopy: science, technology, applications and education. **2010**:19-28.
[222] Adachi K., Buseck P.R. *Internally mixed soot, sulfates, and organic matter in aerosol particles from Mexico City*. Atmos Chem Phys. **2008**;8(21):6469-81.
[223] Kook S., Zhang R., Chan Q.N., Aizawa T., Kondo K., Pickett L.M., Cenker E., Bruneaux G., Andersson O., Pagels J. *Automated detection of primary particles from transmission electron microscope (TEM) images of soot aggregates in diesel engine environments*. SAE International Journal of Engines. **2016**;9(1):279-96.

[224] Anderson P.M., Guo H., Sunderland P.B. *Repeatability and reproducibility of TEM soot primary particle size measurements and comparison of automated methods*. J Aerosol Sci. **2017**;114:317-26.
[225] Gontard L.C., Ozkaya D., Dunin-Borkowski R.E. *A simple algorithm for measuring particle size distributions on an uneven background from TEM images*. Ultramicroscopy. **2011**;111(2):101-6.
[226] Huffman G.P., Shah N., Cprek N., Huggins F.E., Casuccio G., Ramer E., Hicks J.B. *CCSEM investigation of respirable quartz in air samples collected during power plant maintenance activities*. Fuel. **2012**;95:365-70.
[227] Hermann G., Coudray N., Buessler J.-L., Caujolle-Bert D., Rémigy H.-W., Urban J.-P. *ANIMATED-TEM: a toolbox for electron microscope automation based on image analysis*. Machine Vision and Applications. **2012**;23(4):691-711.
[228] Cheng A., Leung A., Fellmann D., Quispe J., Suloway C., Pulokas J., Abeyrathne P.D., Lam J.S., Carragher B., Potter C.S. *Towards automated screening of two-dimensional crystals*. J Struct Biol. **2007**;160(3):324-31.
[229] Preibisch S., Saalfeld S., Tomancak P. *Globally optimal stitching of tiled 3D microscopic image acquisitions*. Bioinformatics. **2009**;25(11):1463-5.
[230] Martos F.J., Lapuerta M., Expósito J.J., Sanmiguel-Rojas E. *Overestimation of the fractal dimension from projections of soot agglomerates*. Powder Technol. **2017**;311:528-36.
[231] Radermacher M., Hoppe W., editors. Properties of 3-D reconstruction from projections by conical tilting compared to single-axis tilting. Proceedings of the 7th European Congress on Electron Microscopy; 1980.
[232] Penczek P., Frank J. Resolution in Electron Tomography. Electron Tomography Methods for Three-Dimensional Visualization of Structures in the Cell. 2 ed. New York: Springer; 2008. p. 307-30.
[233] Garduño E., Wong-Barnum M., Volkmann N., Ellisman M.H. *Segmentation of electron tomographic data sets using fuzzy set theory principles*. J Struct Biol. **2008**;162(3):368-79.
[234] Chalana V., Kim Y. *A methodology for evaluation of boundary detection algorithms on medical images*. Ieee T Med Imaging. **1997**;16(5):642-52.
[235] Mairhofer S., Sturrock C., Wells D.M., Bennett M.J., Mooney S.J., Pridmore T.P. *On the evaluation of methods for the recovery of plant root systems from X-ray computed tomography images*. Funct Plant Biol. **2015**;42(5):460-70.
[236] Mairhofer S., Zappala S., Tracy S.R., Sturrock C., Bennett M., Mooney S.J., Pridmore T. *RooTrak: automated recovery of three-dimensional plant root architecture in soil from X-ray microcomputed tomography images using visual tracking*. Plant physiology. **2012**;158(2):561-9.
[237] Kubota K. *From tumor biology to clinical PET: a review of positron emission tomography (PET) in oncology*. Annals of nuclear medicine. **2001**;15(6):471-86.
[238] Hatt M., Le Rest C.C., Descourt P., Dekker A., De Ruysscher D., Oellers M., Lambin P., Pradier O., Visvikis D. *Accurate automatic delineation of heterogeneous functional volumes in positron emission tomography for oncology applications*. International Journal of Radiation Oncology* Biology* Physics. **2010**;77(1):301-8.
[239] Mol A., Balasundaram A. *In vitro cone beam computed tomography imaging of periodontal bone*. Dentomaxillofacial Radiology. **2008**;37(6):319-24.
[240] Heeraman D.A., Hopmans J.W., Clausnitzer V. *Three dimensional imaging of plant roots in situ with X-ray computed tomography*. Plant and soil. **1997**;189(2):167-79.
[241] Perret J., Al-Belushi M., Deadman M. *Non-destructive visualization and quantification of roots using computed tomography*. Soil Biology and Biochemistry. **2007**;39(2):391-9.
[242] Ali R.A., Landsberg M.J., Knauth E., Morgan G.P., Marsh B.J., Hankamer B. *A 3D Image Filter for Parameter-Free Segmentation of Macromolecular Structures from Electron Tomograms*. PLOS ONE. **2012**;7(3):e33697.
[243] Mezerji H.H., Van Den Broek W., Bals S. *A practical method to determine the effective resolution in incoherent experimental electron tomography*. Ultramicroscopy. **2011**;111(5):330-6.
[244] Hamarneh G., Jassi P. *VascuSynth: Simulating vascular trees for generating volumetric image data with ground-truth segmentation and tree analysis*. Computerized medical imaging and graphics. **2010**;34(8):605-16.
[245] Haffner-Staton E., La Rocca A., Fay M.W. *Progress towards a methodology for high throughput 3D reconstruction of soot nanoparticles via electron tomography*. Journal of microscopy. **2018**;270(3):272-89.
[246] Mikhailov E., Vlasenko S., Podgorny I., Ramanathan V., Corrigan C. *Optical properties of soot–water drop agglomerates: An experimental study*. Journal of Geophysical Research: Atmospheres. **2006**;111(D7).
[247] Hu E., Hu X., Liu T., Fang L., Dearn K.D., Xu H. *The role of soot particles in the tribological behavior of engine lubricating oils*. Wear. **2013**;304(1):152-61.

Appendix

A1 - Propagation of Missing Wedge Error: Fast Fourier Transforms of 2D shapes

The concept of the missing wedge and its associated error is unquestioned in ET. The emphasis for the development of many advanced reconstruction algorithms is improved quality in spite of the missing wedge, but few studies take the time to consider how this source of error actually impacts their reconstructions.

The lack of projections in Z-direction in a typical ±60° tilt-series results in a loss of resolution in the Z-axis [1]. The elongation in the Z-direction was described by Radermacher in terms of a ratio of resolution in the XY-plane and the Z-direction, resulting in equation-A1 [2, 3]:

$$e_{xz} = \sqrt{\frac{\alpha + \sin(\alpha)\cos(\alpha)}{\alpha - \sin(\alpha)\cos(\alpha)}} \qquad \textbf{(A.1)}$$

Following this equation, the ratio of Z:X resolution (and elongation) for a ±60° single-axis tilt-series is expected to be 1.55 (55%).

However, Penczek and Frank [4] considered that while true for small spherical objects, the effects of the missing wedge will be 'object dependent' for more complicated structures. Hence, we are in a position where we know there is at least some degree of missing wedge elongation, and it is likely *not* to be 55%. Certainly, observing the 3D model produced for the FG soot nanoparticle in chapter-4 it is difficult to observe an obvious elongation as large as 55%. Also, it is somewhat uncertain how this elongation is expected to propagate. Is the whole tomogram stretched evenly in the Z-direction, or is it just the edges of the particle?

To get a better understanding of the propagation of missing wedge effects, some short tests were performed using 2D objects in Fiji. In Fiji, it is easy to apply fast Fourier transform (FFT) filters to images, including the inverse filter. As such, we can essentially directly create the equivalent of the 'full set' of projections of an object that is required for tomographic reconstruction. In a ±60° tilt-series, we have missing information in the 3D-FT of the object in the shape of a wedge. In the FFT of a 2D

image, we can directly exclude this data. We can then perform an inverse FFT to observe the effects of that missing wedge.

This test was performed using a variety of different shapes, to better understand how object complexity may affect the propagation of missing wedge effects.

A1.1 - Example-1: Circle

A binary image of a circle was used as the first example. The FFT was created, and the content removed in form of a missing wedge equivalent to a ±60° tilt-series. An inverse FFT was then performed to illustrate missing wedge propagation.

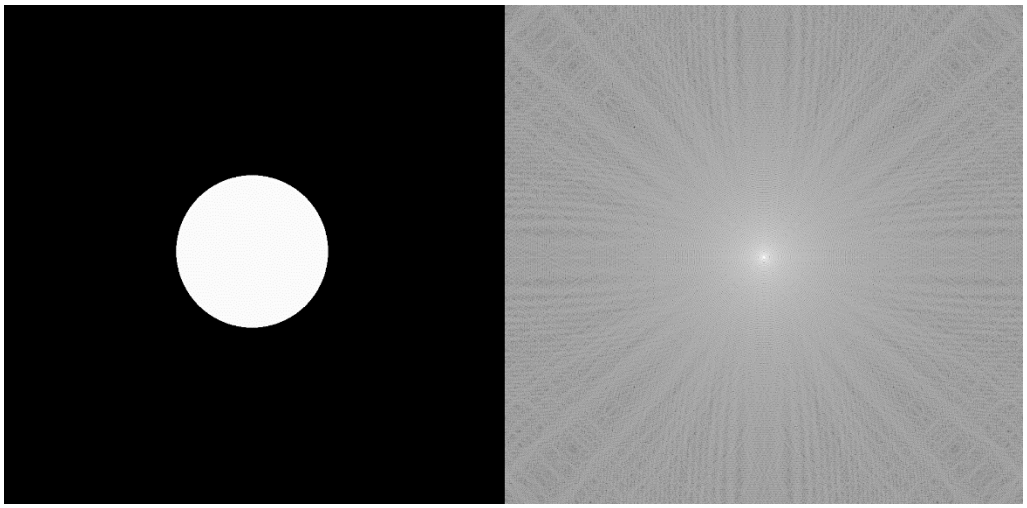


Figure-A.1: Original image and FFT

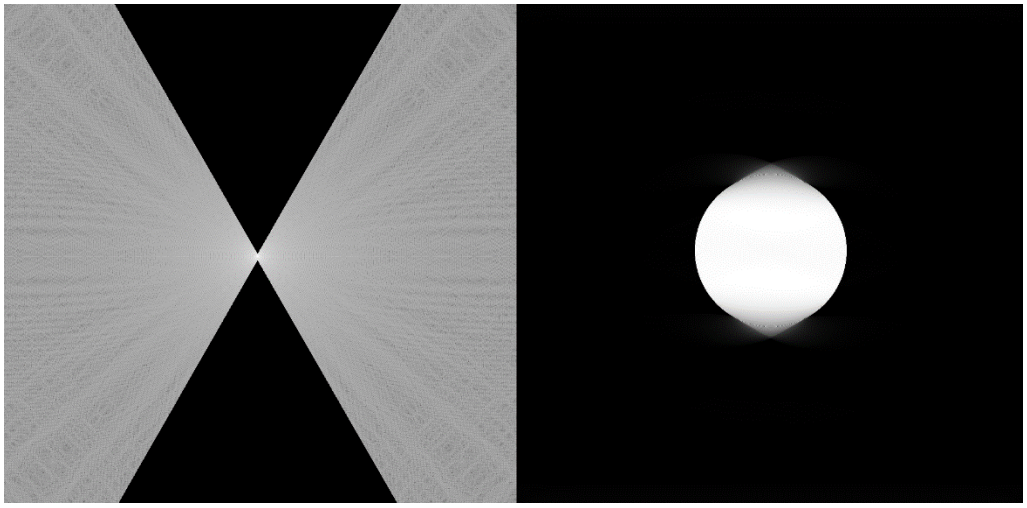


Figure-A.2: FFT with missing wedge, and result of inverse FFT

For this example, the missing edge elongation is clear to see in the Z-direction. The original circle was 300 px in diameter. After the missing wedge is applied, the circle was stretched by around 22 pixels at the top and bottom. This is equivalent to approx. 15% stretch in the Z-direction. Including the elongated sections, the area of the shape measured is only 3% > the area of the original circle.

The shape of the elongation is also interesting to see. Rather than being applied evenly and resulting in an ellipsoid shape, a small conical section is added to the original circle. By superimposing the limits of the missing wedge (in red, figure-3), it is clear to see that the missing wedge propagates perpendicularly to those angles.

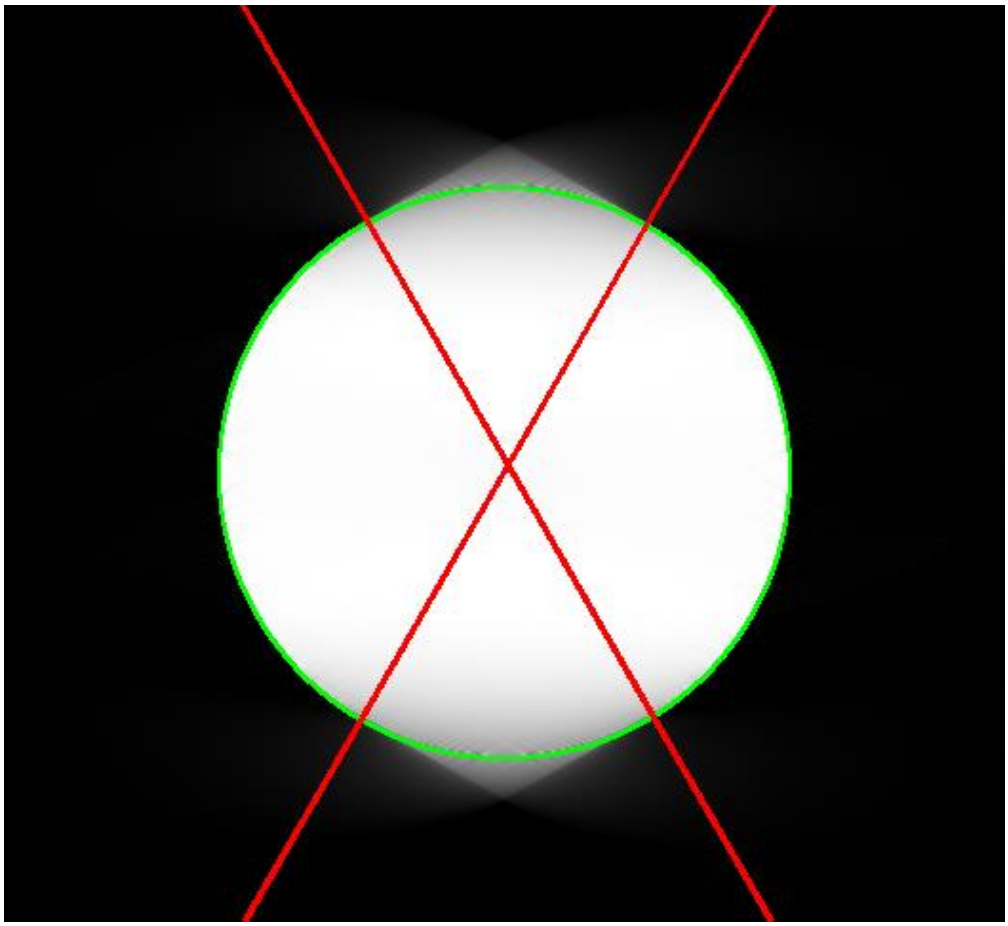


Figure-A.3: 'Post-reconstruction' (inverse FFT) of circle. Showing in green the outline of the original circle, and in red the limits of the missing wedge (±60°).

A1.2 - Example-2: Ellipses at different angles

The next consideration was the effect of the objects shape, and its angle to the direction of the missing wedge. An ellipse was used to investigate whether the aspect ratio affects the propagation of the missing wedge. The same ellipse shape was positioned at 4 angles from 0-90° to the missing wedge.

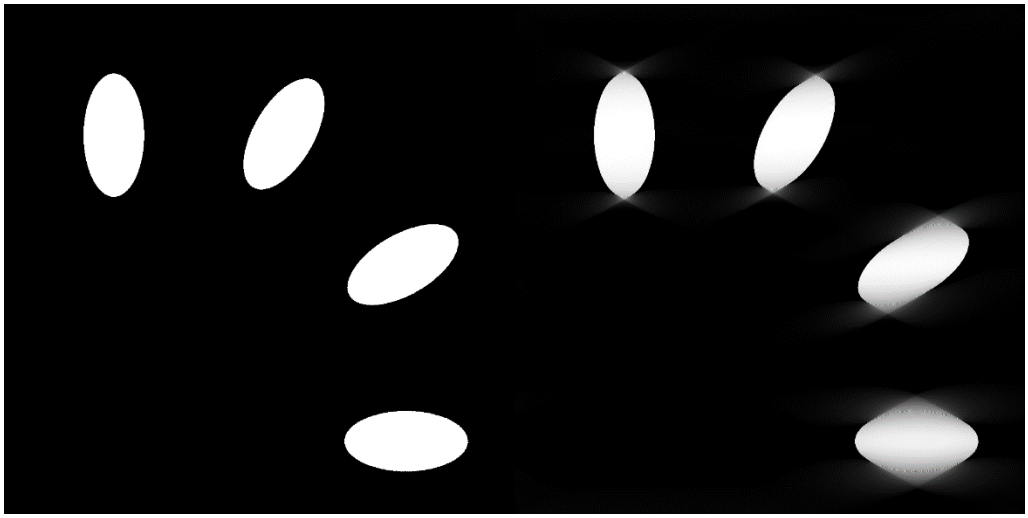


Figure-A.4: Showing the original, and post-missing wedge ellipses.

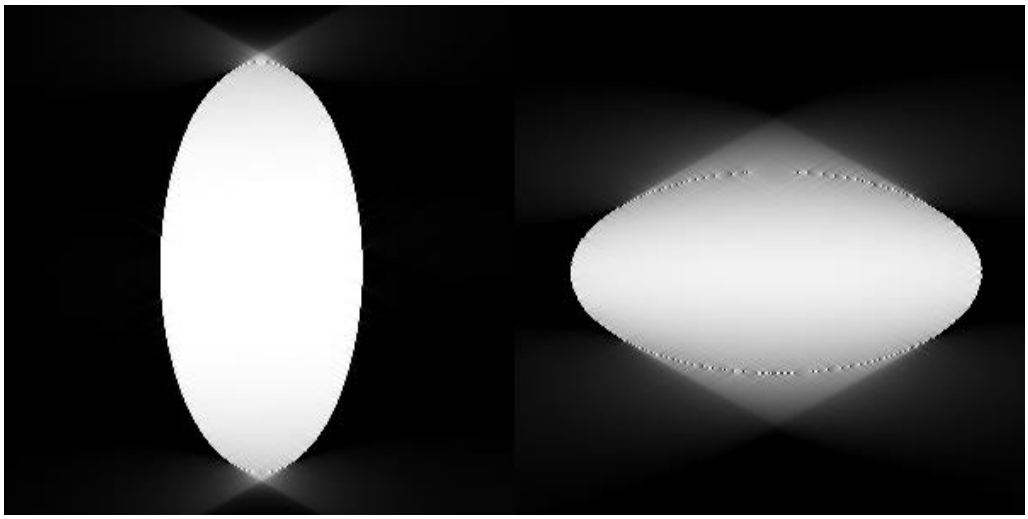


Figure-A.5: Comparison of missing wedge elongation when major axis of the ellipse is parallel to the missing wedge (left), and perpendicular to missing wedge (right).

The first observation is that when the major axis of the ellipse is vertical, and parallel to the missing wedge, the effect of elongation is very small and much less noticeable in comparison to the circle example. As the ellipse is rotated through 90°, the missing

wedge elongation becomes more prominent as it occurs over a greater proportion of the shape.

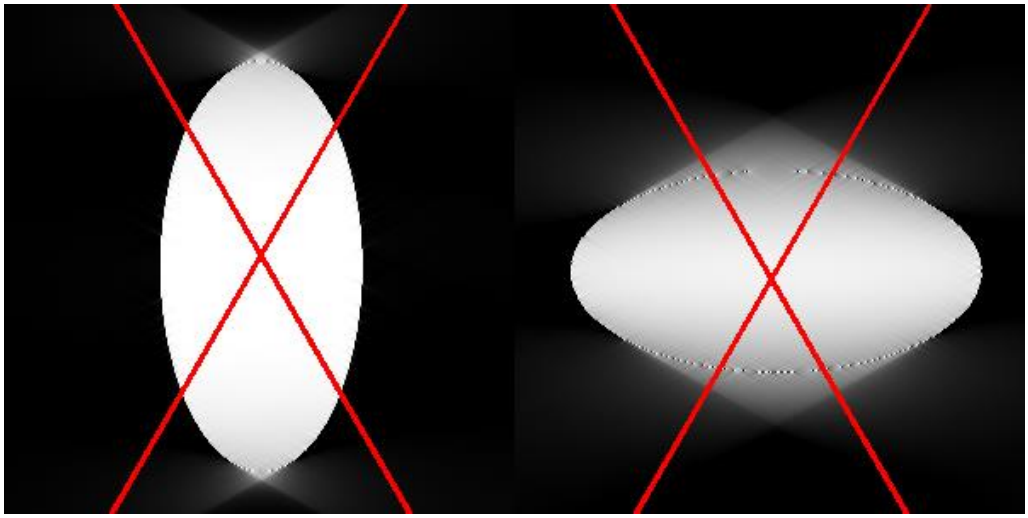


Figure-A.6: Tilt-series limits superimposed onto the centre of the ellipses

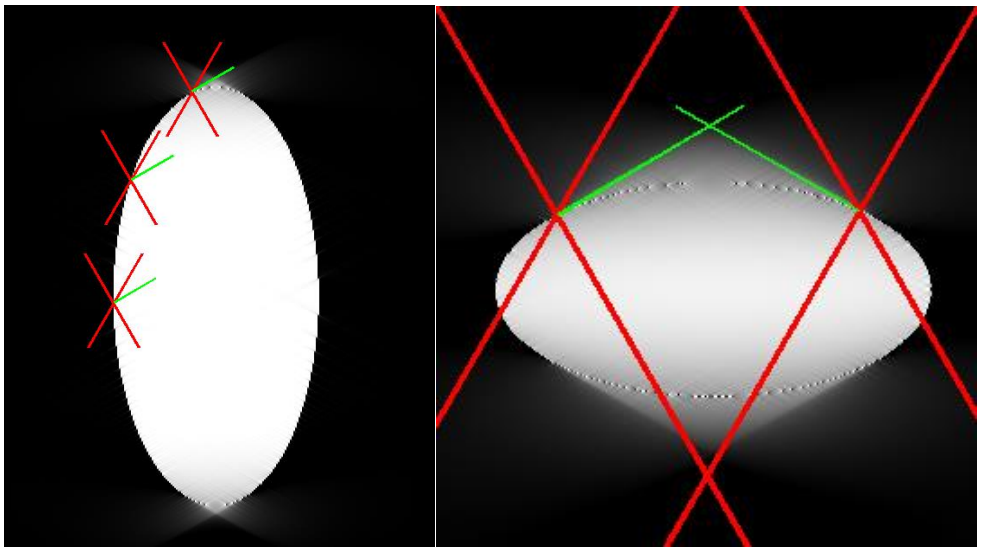


Figure-A.7: Application of tilt-limits (red) to edge contours of ellipses, and perpendicular angle following path of missing wedge blurring/elongation (green).

In contrast to the circle example, when superimposing the missing wedge limits onto the centre of the objects they do not align perpendicularly with the elongation. However, by repositioning these limits onto the edges of the shape do reveal that this perpendicular behaviour can still be observed. Instead of thinking of the missing wedge elongation as occurring from the centre of the object, it actually occurs at each point in the tomogram. This is not unexpected, as the nature of the FFT does **not** directly correspond to the

spatial arrangement of matter in the original image. The observations of the data from the ellipses is that the blurring only occurs when the angle of blurring (*i.e.* perpendicular to the tilt-series limits) is more extreme than the contour of the object. As such, missing wedge elongation should only occur over very small areas, and therefore be relatively insignificant, for more complex and irregular contours. However, the blurring itself (aside from elongation) will still be able to alter the shape of the reconstruction from the true structure.

A1.3 - Example 3: Nanoparticle Shape

The last example studied was a soot-like shape. This was a 2D projection of one of the simulated aggregated models used in chapter-7. This was to provide an example of (a 2D representation of) the effect of missing wedge elongation on a more soot-like contour.

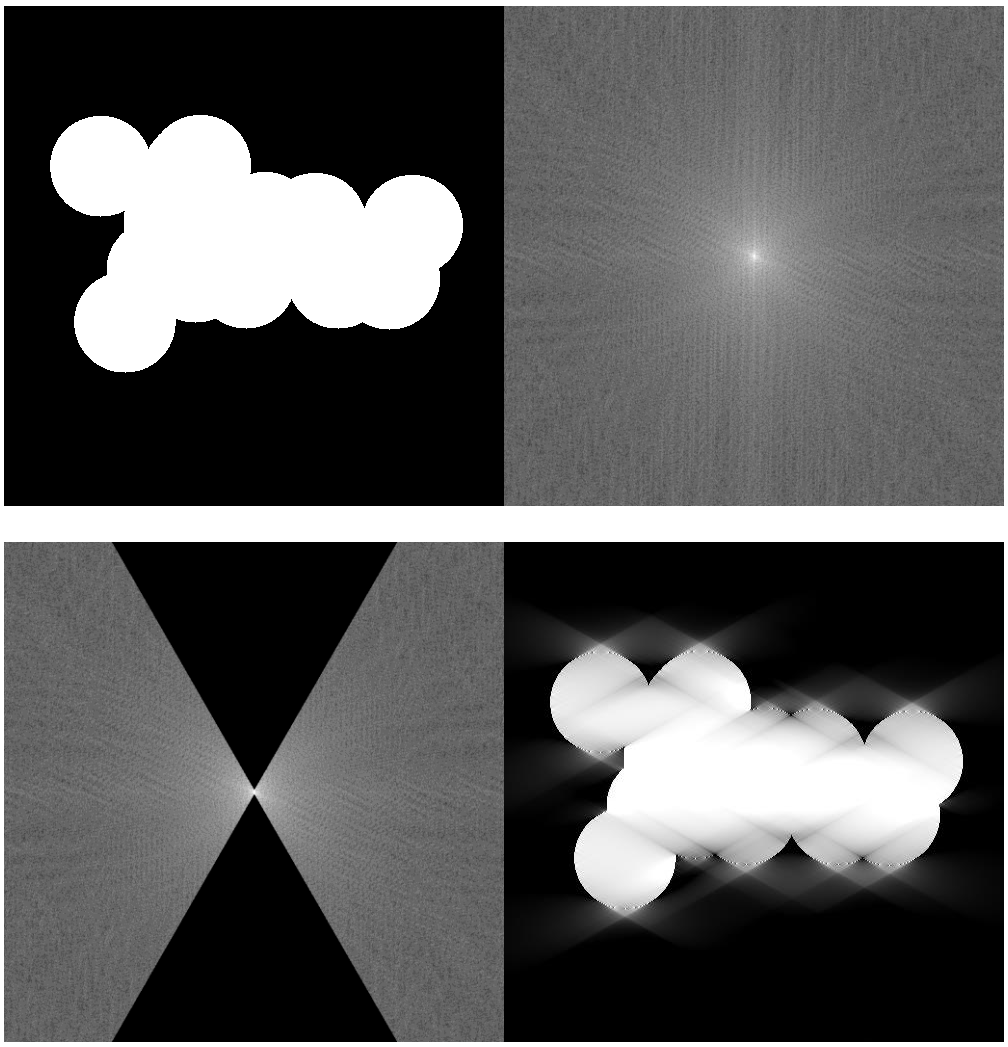


Figure-A.8: (Above) Showing soot-like contour and associated FFT. (Below) Showing FFT with missing-wedge and result of inverse FFT.

For this structure, the elongation again occurs only relatively small areas at the tips of the particle in the Z-direction. However, there is also some visible degradation on the quality of the contour. This is most prominent where the contour is broad, for example on the lower-right underside. The elongated shape was segmented and measured in terms of area to quantify the effect of elongation. While the original shape possessed an area of 65,900 pixels, the area of the elongated shape was 2.7% larger at 67,700 pixels. The circularity of the shape was 0.41 originally, and 0.38 post-elongation (7.9 % larger).

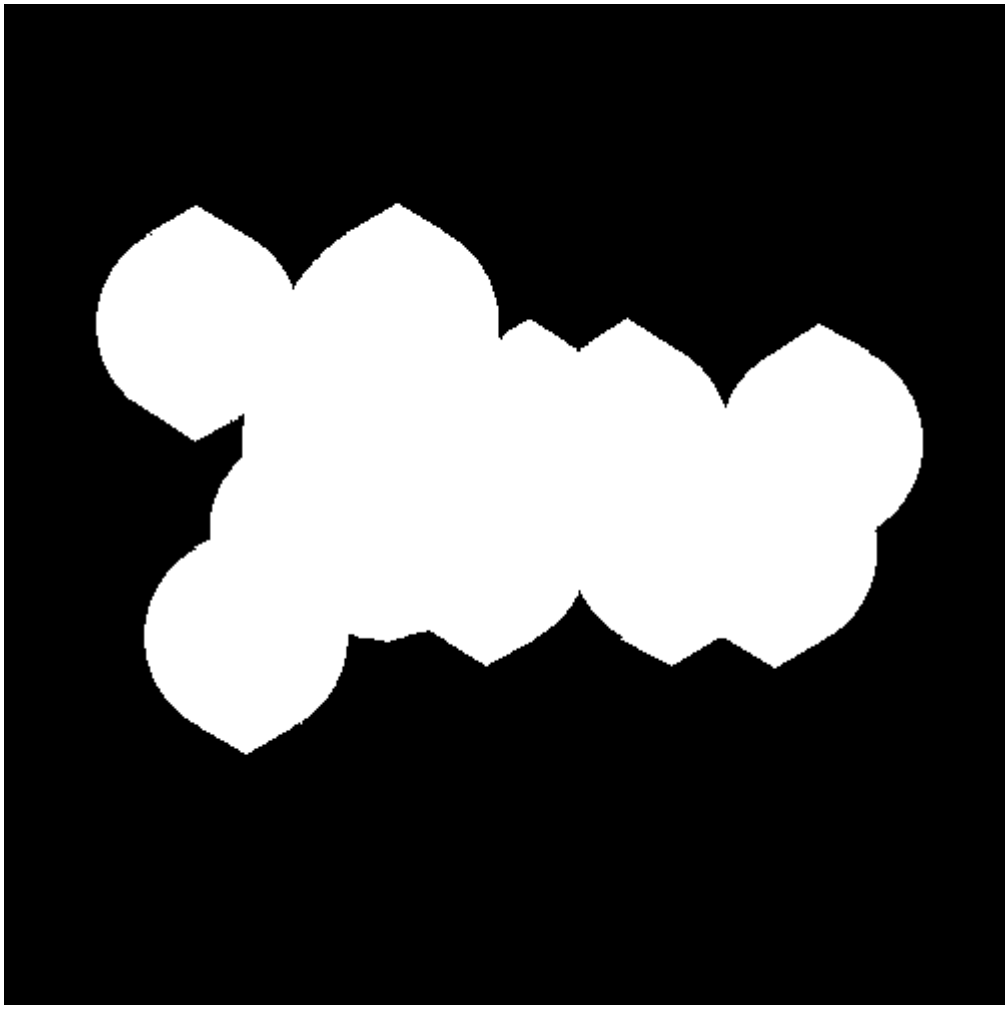


Figure-A.9: The area measured based on the 'reconstruction' of the particle-like contour.

The very final test carried out was to apply TEM-like appearance to this particle-style contour. This was performed in a similar method as for the soot-like aggregate models in chapter-7. This was performed to check how the missing wedge blurring may alter depending on the contrast and resolution of the structure.

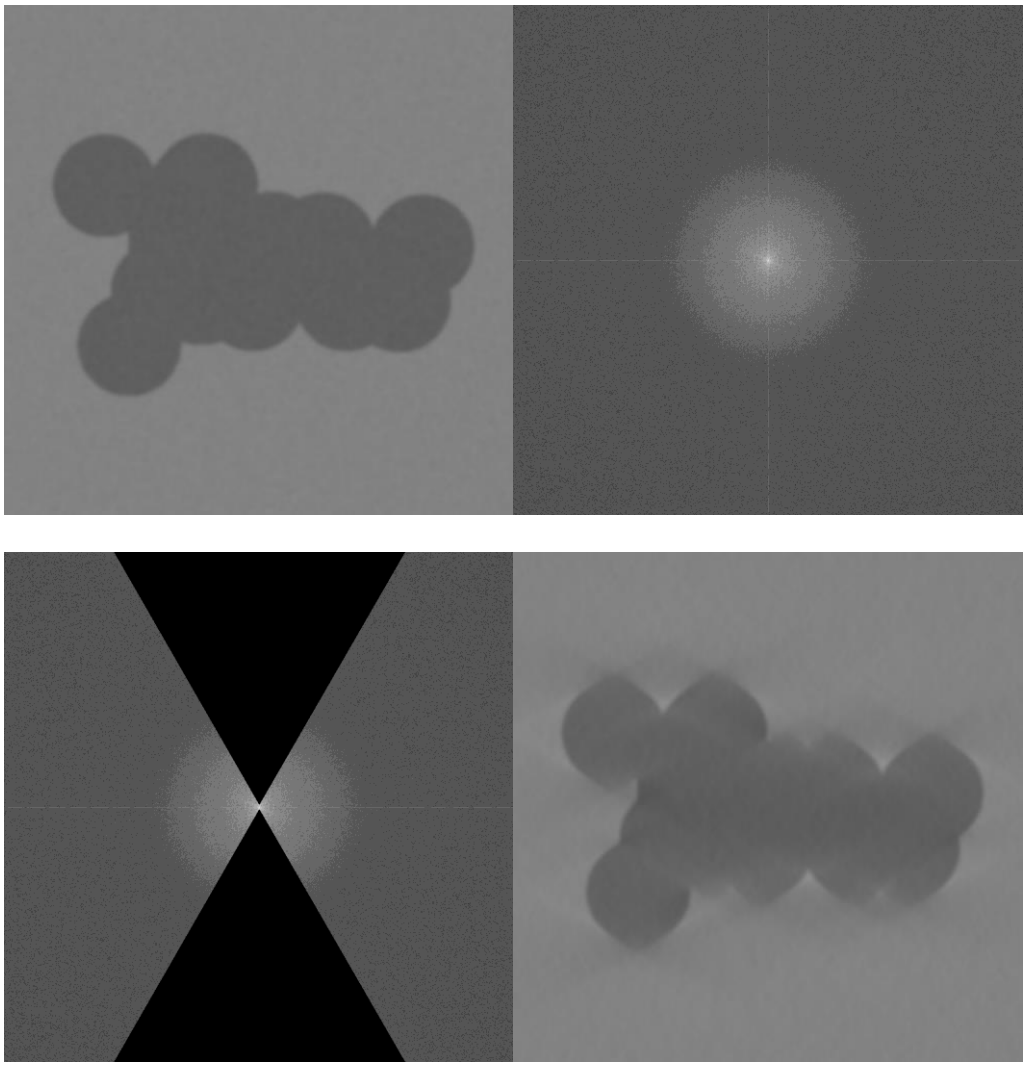


Figure-A.10: Particle-like contour with application of soot-like TEM contrast, noise, and blurring.

From observing the images in figure-A.10, the propagation of the missing wedge is somewhat different to that in figure-A.8. While for the binary case the furthest extents of the fanning effects are clear to see against the black background, they are somewhat obscured in the case of the TEM-style image. However, the main elongation is very similar, as highlighted in figure-A.11 by superimposing the contour of the post-elongation shape for the binary version on to the TEM-style image.

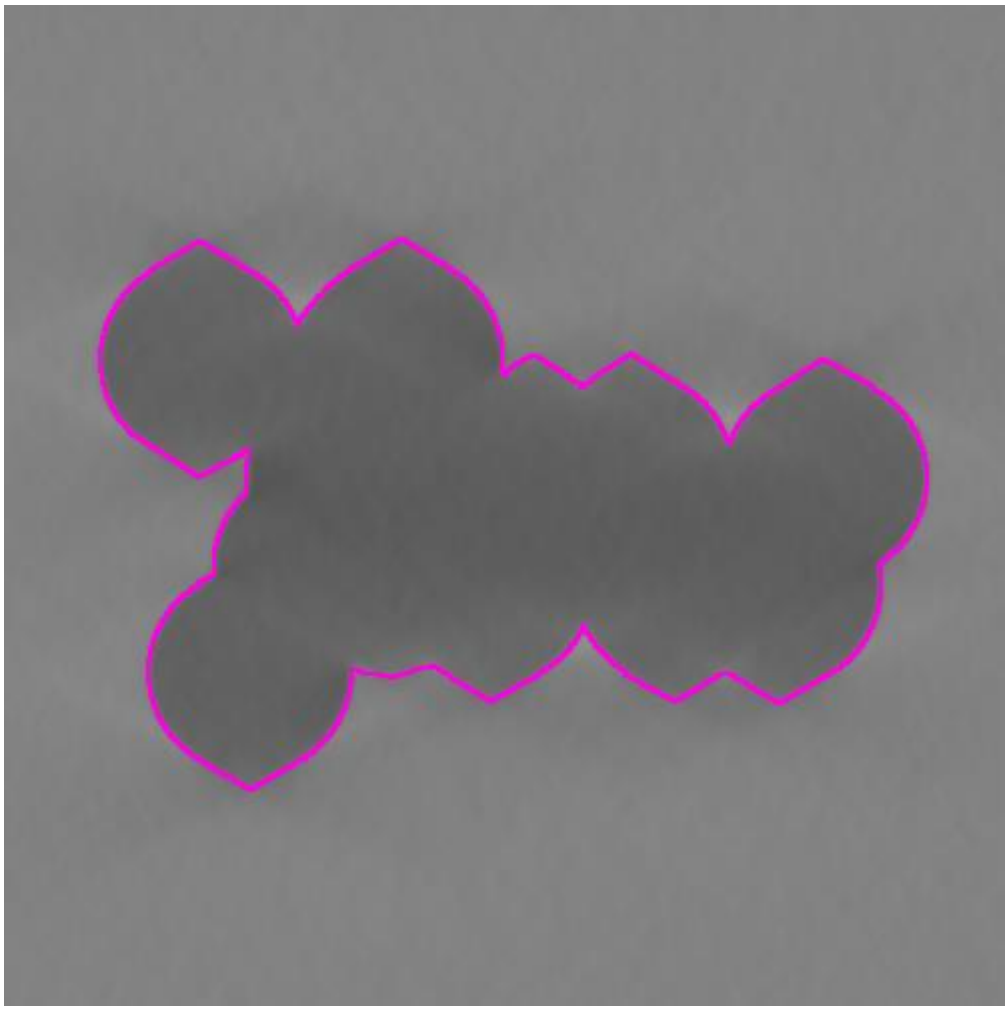


Figure-A.11: ROI from binary version (figure-A.9) superimposed onto result of elongated shape with TEM-stylings.

A.1.4 - Summary

A 2-dimensional surrogate was used to further understand the propagation of missing wedge elongation. It was observed that elongation was occurred only at the very vertical limits of the structures, and only where the angle of the contour was less than blurring angle. The absolute vertical length of a sphere was seen to elongate by 15%, but differences in overall area were less pronounced (3% increase). By using ellipsoid shapes it was observed that missing wedge elongation was more prominent over broader areas of the contour, so would be stronger for smoother objects. A soot-like shape was used to observe the effects of elongation on a more realistic structure. Some definition was lost in smoother areas leading to a change in circularity of around 8%, but overall change in area was again very small (<3%). TEM-like contrast reduced the prominence

of the outer limits of the blurring, but in terms of elongation the effect was very similar to the case of a binary image.

A.1.5 - References

[1] Radermacher M. Weighted Back-Projection Methods. In: Frank J, editor. Electron Tomography Methods for three-Dimensional Visualization of Structures in the Cell. 2 ed. New York: Springer; 2008. p. 245-73.

[2] Radermacher M. *Three-dimensional reconstruction of single particles from random and nonrandom tilt series*. J Electron Microsc Tech. **1988**;9.

[3] Radermacher M., Hoppe W., editors. Properties of 3-D reconstruction from projections by conical tilting compared to single-axis tilting. Proceedings of the 7th European Congress on Electron Microscopy; 1980.

[4] Penczek P., Frank J. Resolution in Electron Tomography. Electron Tomography Methods for Three-Dimensional Visualization of Structures in the Cell. 2 ed. New York: Springer; 2008. p. 307-30.

A.2 - Choice of Resampling Factor in BoneJ Surface Area Calculations

A.2.1 - Introduction

The calculation of surface area in BoneJ is performed *via* the application of a surface mesh to the 3D particle model [1]. This mesh is formed from triangular faces, and the number of triangles comprising the mesh is used to calculate the surface area. This calculation involves the choice of a 'resampling factor', which determines how large the mesh triangles are compared to the pixels of the model. The lowest resampling factor (= 1) considers every single surface of each pixel in the model, while high resampling factors simplify the surface. The default resampling factor in BoneJ = 6, but some consideration was required to account for the different resolutions of the 3D models and ensure a consistency in surface area calculations.

There was concern over inappropriate choice of resampling factor, both in terms of being too high and too low. A very low resampling factor accounts for all outer surfaces of the individual surface pixels. This is not a real irregularity of the soot nanoparticle, however, but merely a consequence of working using digitized images. As such, low resampling factors will tend over-estimate the true surface area. Of course, too high resampling will simplify the surfaces too much and lead to underestimation of the true surface area. In order to guide the choice of resampling factor, it was considered that the primary particle represents the major source of surface irregularities in the soot nanoparticles. As long as the roughly spherical structure is retained, then the resampling factor would be considered appropriate.

In this section, acceptable resampling factors were determined by producing 3D models of spheres of different sizes, to represent different scales of resolution in 3D soot models. The surface area of the spheres is known inherently (SA = $4\pi r^2$), and different resampling factors were used to measure surface area using the 'isosurface' function in BoneJ. Comparison of the expected and observed values were used to determine acceptable resampling factors.

A.2.2 – Results: Surface Area of Spheres as a Function of Resampling Factor

For the GTDI soot-in-oil sample used in this work, the mean primary particle diameter was determined as 33 nm. Based on the scale of the tilt-series images, this equates to primary particle diameters of approximately 50 to 150 pixels. For the FG soot nanoparticle the mean primary particle diameter was 20 nm and around 19 pixels, based on the scale of 1.068 nm per pixel. The resampling factors tested in the work were = 1, 2, 4, and 6. Results are summarised in table-A.1 below:

Model	Known Surface Area (px^2)	Resampling factor	Resampled Surface Area (px^2)	% difference *vs.* known Surface Area
150px Sphere	70,686	6	70,648	-0.1
		4	70,868	0.3
		2	71,347	0.9
		1	76,842	8.7
100px Sphere	31,416	6	31,607	0.6
		4	31,410	-0.02
		2	31,676	0.8
		1	34,140	8.7
50px Sphere	7,854	6	7,631	-2.8
		4	7,768	-1.1
		2	7,884	0.4
		1	8,537	8.7
20px Sphere	1,257	6	1,103	-12.3
		4	1,175	-6.5
		2	1,240	-1.4
		1	1,371	9.1

Table-A.1: Values of surface area of sphere models calculated using the BoneJ 'isosurface' function

These results indicate that, as expected, the use of the highest resampling factors causes an overestimation of the surface area of a curved shaped. This is typically around 9% larger than the expected value, and is due to the sharp voxel edges being into account.

The results also highlight the effect of scale in the tilt-series/tomogram images. For the FG soot particle, the scale is relatively coarse. Using a sphere model only 20 px in

diameter shows that with resampling factor of 6, we will experience a relatively high level of under-appreciation of the real particle surface area. For this particle it appears that a resampling factor of 2 is most appropriate, at least in terms of preserving the spherical shape of a single primary particle.

For the GTDI soot-in-oil sample, the finer scale in the images means that resampling remains accurate at higher levels. While for the lower resolution tomograms (*cf.* the 50 px diameter sphere) a resampling factor of 6 results in under-estimation of around 3%, for the higher resolution tomograms (*cf.* the 150 px diameter sphere) this level of resampling was actually the most accurate (though it must be noted that all resampling factors > 1 were extremely accurate and within 1%). As higher resampling factors are quicker to compute, and given the small levels of underestimation expected from the results of this test, we conclude that a broad resampling factor of 6 is appropriate for the whole set of GTDI soot-in-oil particles.

A.2.3 - References

[1] Doube M., Klosowski M.M., Arganda-Carreras I., Cordelieres F.P., Dougherty R.P., Jackson J.S., Schmid B., Hutchinson J.R., Shefelbine S.J. *BoneJ Free and extensible bone image analysis in ImageJ*. Bone. **2010**;47(6):1076-9.